Università degli Studi di Napoli 'Federico II'

DOTTORATO DI RICERCA IN

FISICA

XXXIII Ciclo

Coordinatore: prof. Salvatore Capozziello

Searches for an invisible Z' and for the dark Higgsstrahlung $A'h'$ process in $\mu^+\mu^-$ plus missing energy final states at Belle II

Dottorando
Marcello Campajola

Tutors
Prof. Guglielmo De Nardo
Dott. Francesco Di Capua

Anni 2018/2021

Abstract

The work presented in this thesis concerns two searches for dark sector mediators in e^+e^- annihilations at the center-of-mass energy of 10.58 GeV with the Belle II experiment. Two different processes have been investigated in the same final state, consisting of two muons plus missing energy, by using the first data collected by the experiment so far.

The first search presented in this work investigates an invisibly decaying Z' boson (in the framework of a $L_\mu - L_\tau$ symmetry) produced radiatively by muons in the process $e^+e^- \to \mu^+\mu^- Z'$; $Z' \to$ invisible. The only previous measurements in the same theoretical framework have been performed by the BaBar and CMS experiments for a Z' decaying to muons, while no results for an invisible decay have been reported before. For this measure, the data-set collected by Belle II during the so-called Phase 2 commissioning run in 2018 has been used, corresponding to an integrated luminosity of 276 pb^{-1}. No anomalies have been observed in data, and upper limits on the coupling constant g' in the range $[5 \times 10^{-2} - 1]$ have been placed for a Z' mass less than 6 GeV/c^2. As an extension of the above search, the existence of a LFV Z' boson has been investigated in the process $e^+e^- \to e^\pm\mu^\mp Z'$, $Z' \to$ invisible. Even in that case, no anomalies have been observed, and model independent upper limits on the cross section (times efficiency) have been computed.

The search for a different process is also presented, consisting in the simultaneous production of a dark photon A' and a dark Higgs h' boson via the so-called dark Higgstrahlung process $e^+e^- \to A'h'$; $A' \to \mu^+\mu^-$, $h' \to$ invisible. The only similar measurement was performed by the KLOE experiment, for A' masses up to $\simeq 1$ GeV/c^2. Therefore, Belle II would be able to produce a sizeable enlargement of the explored region. The analysis flow, optimized for the data collected by the experiment during 2019, corresponding to an integrated luminosity of $\sim 9\,\text{fb}^{-1}$, is described and the expected upper limits on the cross section and in terms of the coupling constants product $\epsilon^2 \times \alpha_D$ are provided.

Contents

Introduction

Understanding the nature of Dark Matter (DM) is one of the main open questions in fundamental physics today: what are its constituents, and how do they interact with each other and with the ordinary matter particles? Answering these questions would provide us the key to deepening our understanding of the laws of the Universe.

The evidence for dark matter derives essentially from cosmological and astrophysical measurements in different contexts and over a wide range of scales, from the galactic rotation curves, up to the Cosmic Microwave Background (CMB) power spectrum behaviour. It has been estimated that DM accounts for $\sim 27\%$ of the total energy density of the Universe and for about 85% of its matter density. However, these data are essentially gravitational, and therefore tell us little about the particle nature of dark matter. In the last decades, many experiments have been designed and built to probe the DM constituents. Most of these have been focused on the hypothesis that dark matter is made of massive particles, called Weakly Interacting Massive Particles (WIMPs): these hypothetical particles with a GeV–TeV mass are electrically neutral and interact with ordinary matter through the weak force. This hypothesis elegantly allows to explain the estimated density of dark matter observed in the Universe and it is in agreement with most of the constraints deriving from astrophysics and cosmological observations. Several experiments, both on the ground and in space, are trying to reveal WIMP signals using various techniques. However, to date, no pieces of evidence have been confirmed.

In recent times, theories with new light dark matter candidates gained much interest from the scientific community. Dark matter candidates could be states of a new Hidden or Dark Sector (DS), whose constituents are neutral under Standard Model (SM) forces and interact through new dark forces. DS models are often invoked to solve many experimental anomalies. Moreover, they open to different experimental implications. Indeed, dark sector models remove most of the WIMP assumption on the DM composition and thus provide larger model independence with a huge discovery potential. As a result, DM particles and new mediators with GeV or sub-GeV masses become well motivated candidates, beyond the reach of the majority of past DM experiments. In this scenario, low energy e^+e^- colliders, like flavour factories, have unique capabilities to fully explore DS models in the MeV – 10 GeV/c^2 mass range. Through the use of extremely large data samples, current and past experiments such as KLOE, CLEO, BABAR, Belle and BESIII have explored a broad spectrum of dark sector models, placing stringent limits on their

parameter space, while the Belle II next generation B-factory experiment is starting to show its incredible discovery potential, already with the first data collected.

The work presented in this thesis concerns two searches for dark sector mediators in e^+e^- annihilation at the Belle II experiment, installed at the SuperKEKB electron-positron collider at the KEK laboratory in Tsukuba (Japan). Specifically, searches for two different processes in the same final state with two muons plus missing energy have been performed by using the first data collected so far.

The first search presented in this work investigates an invisibly decaying Z' boson (in the framework of a $L_\mu - L_\tau$ symmetry) produced radiatively by muons in the process $e^+e^- \rightarrow \mu^+\mu^- Z'$; $Z' \rightarrow$ invisible. The only previous measurements in the same theoretical framework have been performed by the BaBar and CMS experiments for a Z' decaying to muons, while no results for an invisible decay have been reported before. The data-set collected by Belle II during the so-called Phase 2 commissioning run in 2018 has been used for this analysis, corresponding to an integrated luminosity of 276 pb^{-1}. No anomalies have been observed in data, and upper limits on the Z' coupling constant in the range $[5 \times 10^{-2} - 1]$ have been placed for a Z' mass less than 6 GeV/c^2. As an extension of the above search, the existence of a LFV Z' boson has been investigated in the process $e^+e^- \rightarrow e^\pm\mu^\mp Z'$, $Z' \rightarrow$ invisible. Even in that case, no anomalies have been observed, and the model independent upper limits on the cross section (times efficiency) have been computed.

The search for a different process is also presented, consisting in the simultaneous production of a dark photon A' and a dark Higgs h' boson in the so-called dark Higgstrahlung process $e^+e^- \rightarrow A'h'$; $A' \rightarrow \mu^+\mu^-$, $h' \rightarrow$ invisible. The only similar measurement was performed by the KLOE experiment, for A' masses up to $\simeq 1$ GeV/c^2. Therefore, Belle II would be able to produce a sizeable enlargement of the explored region. The analysis flow, optimized for the data collected by the experiment during 2019, corresponding to an integrated luminosity of $\sim 9\,\mathrm{fb}^{-1}$, has been shown and expected upper limits on the cross section and in terms of the coupling constants product $\epsilon^2 \times \alpha$ have been provided.

The thesis is organized as follows. In Chapter 1, an overview of the dark matter puzzle is given. The astrophysical and cosmological observations motivating the speculation about dark matter are presented, and the theoretical framework able to take it into account is presented. The main DS models are reviewed, with a particular focus on the vector portal model, which postulates the existence of a new spin-1 massive boson (dark photon or Z') coupling to both standard model and dark sector particles. A description of the kinetic mixing mechanism and the theoretical framework related to the $L_\mu - L_\tau$ symmetry, both used to interpret the results presented in this thesis, are described. The detection methods currently exploited for DM searches are then briefly described, and an overview of the state of the art for dark sector searches at low energy e^+e^- colliders is given.

In Chapter 2 the experimental environment used in the framework of this work is fully

described: the second generation B-factory experiment Belle II at the superKEKB collider. A brief description of the SuperKEKB machine operation and the main upgrades with respect to the predecessor facility KEKB is given. The Belle II sub-detectors are then described, with a focus on the improvements with respect to Belle necessary to meet the high luminosity requirements. Furthermore, the main phases of the experiment operations and its data-taking schedule are presented.

The search for an invisibly decaying Z' boson in the process $e^+e^- \rightarrow \mu^+\mu^- Z'$; $Z' \rightarrow$ invisible is then presented in Chapter 3. The final state can be reconstructed by knowing the energy of the initial e^+e^- state and the properties of the muon tracks in the center-of-mass system (CMS) with high accuracy. The analysis relies on searching for a peak of the mass distribution of the system recoiling against the muon pair, which coincides with the Z' mass in case of signal events. The signal extraction strategy is based on a Poisson counting experiment technique, motivated by the low statistics of the expected yields. The selection criteria to suppress the main backgrounds have been optimized using simulated events prior to examining data, and are fully described here. The dominant backgrounds are SM final states with two tracks identified as muons and missing energy due to undetected particles. Following, a full simulation study of the signal shape for the extrapolation of the signal widths to setup the binning scheme is illustrated. A study on control samples on data used to check background rates predicted by simulation and to estimate correction factors and related uncertainties is then presented. The expected yields from simulation have been compared to the Belle II 2018 data, and no anomalies have been observed, with all results below 3σ local significance. The 90% credibility level upper limits on the cross section have been computed using a Bayesian procedure, and results have been translated in terms of the coupling constant g'. Upper limits stay in the range $[5 \times 10^{-2} - 1]$ for $M_{Z'} \leq 6$ GeV/c^2. As an extension of the above search, the existence of a Lepton Flavour Violating (LFV) Z' boson has been investigated in the process $e^+e^- \rightarrow e^\pm\mu^\mp Z'$, $Z' \rightarrow$ invisible. The same analysis chain, except for the particle identification requirements, has been applied. Also in that case, no anomalies have been observed above 3σ local significance, and model-independent upper limits on the LFV Z' efficiency times cross section have been computed. A paper reporting the results from these analyses achieved with the Belle II 2018 data has been published on *Physical Review Letters* [1].

In Chapter 4, the search for a simultaneous production of a dark photon A' and a dark Higgs h' bosons into the dark Higgsstrahlung process $e^+e^- \rightarrow A'h'$, $A' \rightarrow \mu^+\mu^-$, $h' \rightarrow$ invisible is presented. The final state is given by a pair of opposite charge muons plus missing energy. For signal events, the presence of simultaneous peaks both in the distribution of the invariant mass of the two muons and in the distribution of the mass of the system recoiling against the two muons is expected. The same background sources as for the invisible Z' analysis are expected and similar selection criteria to the aforementioned analysis have been used. The analysis strategy relies on a mass scan plus counting technique within mass windows of size proportional to the experimental resolution into the two-dimensional mass phase space. The signal shape study

and the optimization of the background suppression are presented. Data validation studies on control samples to measure the agreement between data and simulations and to compute the systematic uncertainty on the expected background yields and signal efficiencies are illustrated. The strategy for the statistical interpretation was defined in Appendix B, based on a completely Bayesian approach. Following, the expected 90% CL upper limits to cross section have been computed and then translated in terms of the coupling constant product $\epsilon^2 \times \alpha_D$. With the 2019 data-set, Belle II is expected to constrain $\epsilon^2 \times \alpha_D$ down to $\mathcal{O}(10^{-7})$, as illustrated in [2, 3]. As the analysis is still in a blinded phase, results on data couldn't be achieved so far and therefore shown in this work.

Future updates of both analyses are foreseen as it has been shown throughout this thesis, with the goal to improve current bounds by using larger statistics and detector/analysis improvements. Particularly relevant is the possibility to use more inclusive trigger lines, which have been recently activated. In Appendix A it is discussed the case of the CDC-KLM based Level 1 trigger, i.e., the Belle II single-muon trigger, whose performances measured on the 2020 data-set are reported.

Chapter 1

The Dark Matter puzzle

Understanding the nature of Dark Matter (DM) is still one of the most important open problems in science nowadays, requiring both theoretical and experimental efforts to resolve it. All evidence for DM comes from its gravitational interactions with ordinary matter. While important clues have been inferred from those observations, many questions about its particle nature, such as its mass and its interaction strength with ordinary matter, remain open.

In this Chapter, the main experimental observations that motivate the existence of DM, as well as the different theoretical frameworks able to take it into account, will be presented. The main detection methods currently exploited for DM searches are then briefly described, and an overview of the state of the art for dark sector searches at low e^+e^- colliders is given.

1.1 Evidences for Dark Matter

At present, the evidence for dark matter comes from the impact of its gravitational interactions on astrophysical and cosmological measurements in many different contexts and over a wide range of scales, from dwarf galaxies to the largest cosmological scales. In this Section, some of the main observations for dark matter are presented.

1.1.1 Velocity dispersion of galaxy clusters

The earliest suggestion for the existence of DM was found by Fritz Zwicky in the 1930's, by studying the radial velocity of galaxies in the *Coma cluster* [4, 5]. Zwicky observed that the velocity dispersion of galaxies was far too large with respect to what the virial theorem predicts for the observed luminous matter. This brought him to the conclusion that those galaxies couldn't be bound to the cluster by the gravitational attraction of the visible matter (stars, gas, dust) alone. The only way the observed velocities would reconcile with the virial theorem was to postulate that the cluster also contained a large 'dark' (i.e., non luminous) matter component.
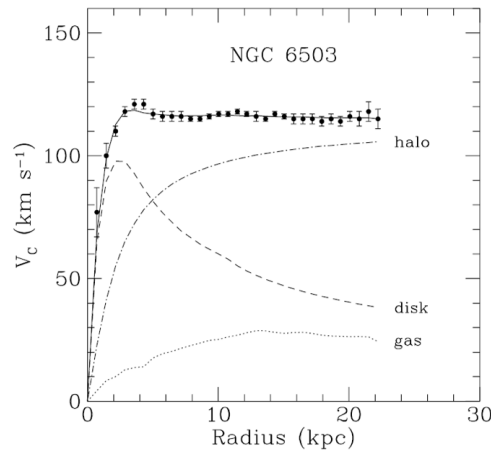
Figure 1.1: Rotation curve for the spiral galaxy NGC6503. The points are the measured circular rotation velocities as a function of distance from the center of the galaxy compared to theoretical prediction for the rotational velocity due to the observed disk and gas (dashed and dotted curves) and the estimated contribution from the *dark* halo (dot-dash curve) needed to fit the data. Figure from Ref. [7]

1.1.2   Rotation curves of spiral galaxies

The concept of dark matter was resurrected in 1970s as an explanation for the anomaly observed in the measurements of galactic rotation curves, performed by Vera Rubin and collaborators [6]. In the approximation of circular orbits, the velocity of stars within a galaxy is expected to be $v(r) = \sqrt{G_N M(r)/r}$, where G_N in the Newton's gravitational constant and $M(r)$ is the mass contained inside a sphere of radius r. Most of the visible material in galaxies is concentrated in the central part, thus the rotation velocity of stars is expected to slow down at large radii as $v(r) \propto \sqrt{1/r}$. However, Rubin and collaborators measuring the rotational velocity from the analysis of the spectral lines (by means of Doppler effects) over more than 60 galaxies, observed an almost constant rotation speed: objects in the outer region of galaxies were moving as fast as those in the inner region. As an example, the measurement of the spiral galaxy NGC6503 rotation curve is shown in Figure 1.1.

A possible explanation to this anomaly relies on the presence of an additional dark massive halo, filling all the space surrounding the galaxies with density $\rho = 1/r^2$ and consequently accounting for an effective mass at a distance r which is linearly growing with the radius itself: $M(r) \propto r$.

1.1.3   Gravitational Lensing effects

Modern experimental evidence of the existence of DM comes from gravitational lensing [8]. The curvature of space–time near any mass (including dark matter) deflects passing rays of light, distorting and magnifying as a lens the images of background galaxies (see for example
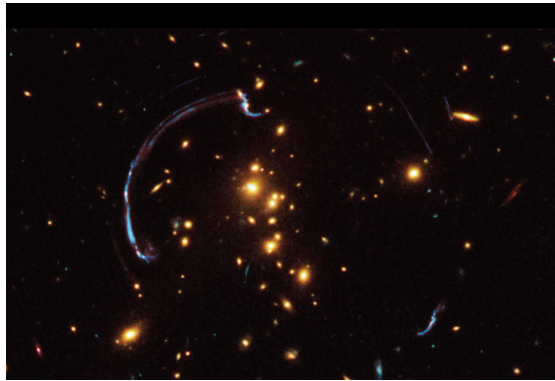
Figure 1.2: Giant Lensed Galaxy Arc behind a foreground galaxy cluster. Credits to NASA, ESA, and A. Gonzalez, A. Stanford, and M. Brodwin.

Figure 1.2). The mass distribution of the lens can then be reconstructed by measuring the distortion of the light coming from the source. Comparing the measured mass of the lens with the one inferred by its luminosity over a variety of astrophysical sources, a mismatch is found again. A variety of studies on several galaxy clusters over the years has confirmed much more lensing than those expected by the luminous matter only. A summary of such studies as well as the benchmark measurements is reported in Ref. [9].

Perhaps the most suggestive evidence for DM comes from the observation of the galaxy cluster 1E 0657-56, also known as the "Bullet Cluster", as shown in Figure 1.3. This cluster was formed after the violent collision of two large clusters of galaxies moving at great speed almost perpendicularly to the line of sight. The name refers to the smaller sub-cluster, which moves away from the larger one, like a bullet. The figure shows a composite image: hot gas, detected by Chandra in X-ray emission, is seen as two pink clumps and it constitutes the dominant baryonic mass of in the two clusters, while the blue areas show where most of the mass is expected by gravitational lensing observations. This latter is found to not trace the baryonic distribution (pink), giving direct evidence that nearly most of the matter in the clusters is 'dark'. The figure also shows how the hot gas in each cluster was slowed down during the collision. Conversely, the dark matter was not slowed down by the impact, resulting in the separation of the dark and normal matter seen in the image. This suggests that the DM component does not interact strongly with either gas or itself, and thus it is effectively collisionless.

1.1.4   Cosmological scale observations

The advancement of cosmology over the past two decades led to a variety of evidences for DM existence and has now made it possible to precisely determine its amount in the Universe, as discussed below.
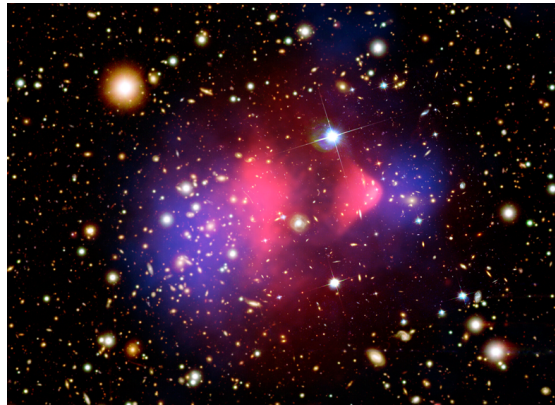
Figure 1.3: Composite image of the Bullet Cluster 1E 0657-56. The background image shows the location of optical galaxies, with most of the larger yellow galaxies associated with one of the two colliding clusters. The overlaid pink distribution shows the X-ray emission from hot intra-cluster gas. The overlaid blue areas show a reconstruction of the total mass from measurements of gravitational lensing. Image from /www.esa.int/. Credits to NASA/CXC/CfA/M.Markevitch (X-ray); NASA/STScI, Magellan/U.Arizona/D.Clowe (Optical and Lensing), ESO WFI (Lensing).

The Large Scale Structure

On large scales, the Universe exhibits a hierarchical structure with galaxies grouped into clusters, clusters as part of super-clusters, and super-clusters arranged into large-scale sheets, filaments and voids, as revealed by large-scale surveys such as 2-degree Field Galaxy Redshift Survey [10], and the Sloan Digital Sky Survey [11].

Large-scale cosmological N-body simulations, like the Millennium simulation [12], show that the observed Large Scale Structure (LSS) of luminous matter could have been formed only if a substantial amount of dark matter was present. In the early Universe, structures in baryons cannot grow until recombination, when atoms become stable. Indeed, the photon pressure in the plasma prevents it. However, there would not be enough time to form the structures we observe now. On the contrary, since DM interacts only gravitationally, it would collapse into halos well before ordinary matter. In this scenario, at the recombination time, baryons would fall into already formed potential wells of DM, giving rise to the major features of the large-scale structure of the Universe. DM had to be 'cold' or non-relativistic at the time when galaxies could just start to form. Indeed, relativistic ('hot') DM would have a very large free-streaming length, so that it would escape from galaxy-sized dense regions [13]. This would imply that only very large structures can form early, while smaller structures arise from fragmentation of larger ones, but it does not reproduce the observation of the past Universe in very high redshift.

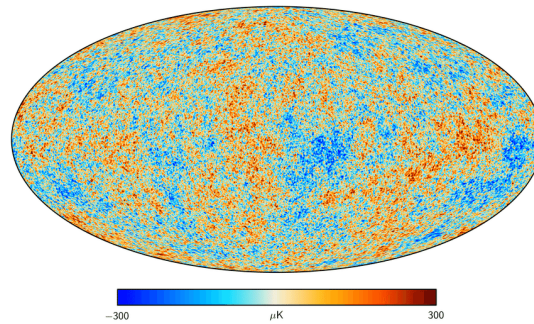Figure 1.4: The CMB temperature perturbation spectrum as viewed by the Planck telescope. Colors represent the relative change of temperature with respect to 2.7 K (red color indicates warmer regions, blue color colder areas) [18].

The Cosmic Microwave Background and the ΛCDM model

Another fundamental observation that supports the dark matter hypothesis comes from the study of the Cosmic Microwave Background Radiation (CMB). The CMB is a very nearly uniform background of photons in all directions of the sky, whose spectral distribution follows a 'black body' spectrum for a temperature of 2.73 K. It was first discovered by Wilson and Penzias in 1964 [14]. CMB photons arise from the recombination phase when the Universe was about 378.000 years old: at that stage, free protons and electrons composing the primordial hot plasma became bound to form electromagnetically neutral hydrogen atoms, thus allowing photons to freely propagate across the Universe. As the Universe expanded, photons have then red-shifted to microwave wavelengths, and now constitute what we call CMB. Three main space telescopes were launched in order to study the CMB, starting with the Cosmic Background Explorer (COBE) in 1989 [15], followed by WMAP [16] and Planck [17].

CMB is a very powerful tool to probe the early Universe: from CMB anisotropies, information on the distribution of baryon and matter in the Universe at the time of recombination, can be obtained. DM over-densities and under-densities in the primordial plasma before recombination translated into anisotropies ($\delta T/T \sim 10^{-5}$) in the angular distribution of temperatures in the CMB, as shown in Figure 1.4. The power spectrum associated to these anisotropies reveals information on the total energy density ρ_{tot} of the Universe and allows us to constrain non-baryonic dark matter density ρ_{DM}.

Fits to the CMB power spectrum allow to determine the parameters of the so-called ΛCDM model, which is considered nowadays the standard cosmological model and is almost universally thought to be the best description of the present experimental results. This model relies on the following assumptions: the Universe is assumed to be homogeneous, isotropic and flat on cosmological scales, to be governed by the laws of Einstein's General Relativity and to be composed by stable particles known in the SM of particle physics, plus two additional ingredients: cold dark matter, which only interacts gravitationally, plus "dark energy", which is responsible for the observed acceleration in the Universe expansion. Dark energy is assumed to take the form

of a constant vacuum energy density, referred to as the cosmological constant (Λ). Defining the density parameter, or relic density Ω as the total energy density ρ_{tot} of the Universe divided by the critical energy density ρ_C, i.e., the value needed for making up a flat Universe, and neglecting smaller order terms, one have by definition: $\Omega_\Lambda + \Omega_{CMD} + \Omega_b = 1$, where Ω_Λ, Ω_{CDM} and Ω_b represent the dark energy, the cold DM and the baryon contributions to the total energy density.

The last results from Planck mission showed that the total energy-matter density is consistent with a good precision with the inflationary paradigm of a flat geometry space time. Based on the latest measurements, the current values for the relative densities of dark energy, DM and baryonic matter are $\Omega_\Lambda \sim 68.3\%$, $\Omega_{DM} \sim 26.8\%$ and $\Omega_b \sim 4.9\%$ [17].

This represents the ultimate and strongest confirmation of the large discrepancy between the baryon and the total density of matter of the Universe, suggesting the existence of a component of dark matter.

1.2   Theoretical scenarios

In the previous section of this Chapter, important clues from astrophysical and cosmological observations about the dark matter evidence have been described. However, many questions about the nature of DM remain open, such as the cosmological origin of the DM abundance observed nowadays, the DM particles content and their interaction, both with each other and with SM constituents.

1.2.1   Dark Matter properties constraints

Besides being a piece of evidence for the dark matter existence, the observations mentioned in the previous Section also constrain the properties that any dark matter candidate must have. These can be summarized as follows:

- DM candidates must be neutral or at least must couple via QED significantly weaker than conventional astrophysical SM matter. This is usually argued by to the fact that DM existence can not be directly inferred by astronomical observations of photons. However, the strongest constraint comes from the requirement to not couple too strongly to photons during the recombination epoch, avoiding disruption of the CMB perturbations [19];

- DM must be very stable with a lifetime comparable to that of the Universe, to be conform with LSS and CMB observation [20];

- Cosmological history studies indicate that DM must be cold, in order to collapse under gravity and form small-scale structure like cluster or galaxy halos after it has decoupled from the thermal bath in the early Universe [13];

- The DM self-interaction strength must be weak, according to astronomical observations. The strongest constraint comes from merging clusters, that put an upper bound of the

ratio of the DM-DM cross section and the DM mass $\sigma_{DM-DM}/m_{DM} < 0.47\,\mathrm{cm}^2/\mathrm{g} \simeq 0.84\,\mathrm{barn}/\mathrm{GeV}$ [21].

Based on these properties, one might wonder whether dark matter could be composed of SM particles. Based on the first two properties, most of the content of the standard model must be excluded. The only massive, neutral and stable particle candidates in the SM are neutrinos. They interact through weak and gravitational forces only. However, even if most of the neutrinos are non-relativistic today, deep within the radiation-dominated epoch, when the temperature was above a few MeV, neutrinos were relativistic. According to what discussed in Sec 1.1.4, they would not be able to explain the observed small clustering scale of galaxies, and therefore cannot be considered suitable dark matter candidates.

From these considerations, one can reasonably conclude that dark matter has to be primarily made of particles Beyond the Standard Model (BSM). On the other hand, the BSM physics case is larger than just the DM puzzle. For instance, the SM predicts massless neutrinos, but the observation of neutrino flavor oscillation proved the opposite. It is thus needed to introduce in the SM a right-handed sterile neutrino or other mechanisms to generate the neutrino mass. Furthermore, SM does not provide a satisfying explanation for the matter/antimatter asymmetry we observe in the Universe. Other problems suggesting the evidence of new physics beyond SM are related to apparently unnatural choices of parameters, i.e., the so-called hierarchy problem, which highlights the discrepancy between the weak and gravitational energy scale.
In the following Sections, many models for DM particles will be presented, with a focus on candidates that are motivated not only by cosmology, but also by robust problems in particle physics.

1.2.2   Thermal production in the early Universe

Before going into the details of the possible DM candidate models, it is useful to address in a general way the problem of the genesis of the observed DM abundance. It may be produced in a simple and predictive manner as a thermal relic of the Big Bang as explained through the *freeze-out* mechanism. It is derived from the Boltzmann equations, and relies on the thermal equilibrium between dark matter particles χ and the plasma in the early Universe through dark matter annihilation processes.

The evolution of the density of DM particles χ and antiparticles $\bar{\chi}$ interacting with SM particles in a thermal bath is given by the Bolzmann transport equation (see e.g. Ref. [22]):

$$\frac{dn}{dt} = -3H_0 n - \langle \sigma_A v \rangle (n^2 - n_{eq}^2) \tag{1.1}$$

where n is the number density of the dark matter particle χ, t is the time, H_0 is the expansion rate of the Universe (i.e., the Hubble constant), $\langle \sigma_A v \rangle$ is the thermally averaged annihilation cross section for the processes $\chi\chi \to \mathrm{SM}\,\mathrm{SM}$, where here SM here denotes standard model particles,
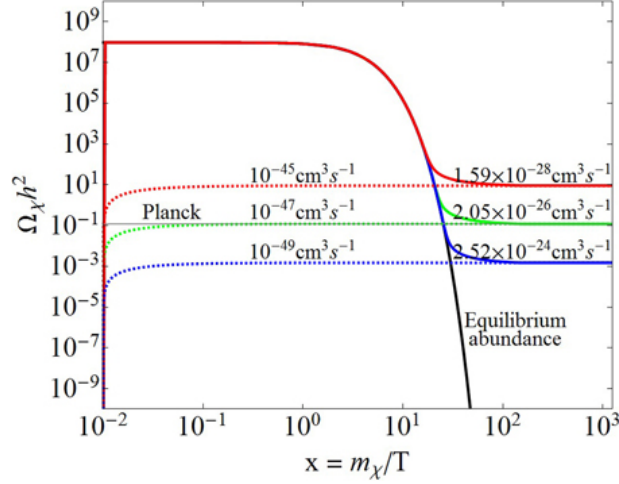
Figure 1.5: Illustration of the freeze-out mechanisms in the evolution of thermal DM abundance as a function of $x = m_\chi/T$ for different annihilation rates [23]. Here a DM mass $m_\chi = 100$ GeV has been considered.

and n_{eq} is the dark matter number density in thermal equilibrium. The three terms on the right-hand side of eq. 1.1, account respectively for density dilution due to the Universe expansion and the particle annihilation (n^2 term) and creation (n_{eq}^2 term).

According to the freeze-out mechanisms, the evolution of a thermal relic number density proceeds as follow. Initially, when the early Universe is dense and hot, all particles are in thermal equilibrium. Then the Universe expands and the plasma temperature decreases to a temperatures T below the dark matter particle mass m_χ: the DM number density is then exponentially suppressed as $e^{-m_\chi/T}$. However, while the Universe expands, the DM density decrease at a level that the interaction rate becomes too small. The dark matter particles then *freeze out*, with their number asymptotically approaching a constant: their thermal relic density. A visualization of such a process is given in Figure 1.5.

The standard approximate solution to eq. 1.1 in the freeze-out regime, yields the present DM relic density:

$$\Omega_{DM}h^2 \sim \frac{3 \cdot 10^{-27}\text{cm}^3\text{s}^{-1}}{\langle \sigma_A v \rangle}. \tag{1.2}$$

The final abundance is then inversely proportional to the thermal annihilation rate. Thus, the larger the cross section, the longer the DM particles stay in equilibrium with the thermal bath, and hence the lower the final abundance [23].

If however the DM was never in thermal equilibrium with the SM due to a small coupling, and interactions were not strong enough for the freeze-out to happen, the relic abundance can be explained by a *freeze-in* mechanism. In this alternative scenario the DM particle density slowly

increase until the production rate becomes negligible due to Boltzmann suppression. At this point the number density becomes constant and the DM abundance freezes in.

1.2.3   Weakly Interactive Massive Particles

The DM paradigm mainly investigated nowadays assumes that dark matter is made up of WIMPs: particles with a mass in the 10 GeV/c^2 to 10 TeV/c^2 range, typically interacting with SM particles through the electro-weak sector. These are the natural mass scales for any particle involved in solving the hierarchy problem, or for a particle whose mass shares a common origin with the SM Higgs. WIMPs are excellent dark matter candidates due to the naturalness with which they can predict the present day dark matter density, through the *freeze out* mechanisms. Indeed, following eq. 1.2, it can be probed that for a DM candidate with $m_\chi \sim \mathcal{O}(100)$ GeV/c^2 and a weak-scale cross section ($\langle \sigma_A v \rangle \simeq 1\text{pb} \times \text{c}$) the freeze-out process is able to predict the observed dark matter relic density. This is usually referred to as the "WIMP miracle".

The WIMP miracle thus provides naturally a model-independent motivation for new physics at the weak scale out of the theories designed to address the gauge hierarchy problem. Moreover, it also has strong implications on dark matter detection experiments. It requires that DM interactions must exist, and also implies that the DM-SM interactions must be efficient. Note that after freeze out, even though interactions that change the number of DM particles are negligible, interactions that can efficiently exchange energy between DM and other SM particles may still be active. Furthermore, it provides the lower bounds on interaction rates, and thus a highly motivated target for experimental searches that may be able to detect WIMPs and constrain their properties [24].

Among the most studied WIMP candidates in the literature there are particles belonging to super-symmetric models. Super-symmetry [25] has been proposed as extensions of the SM to solve the hierarchy problem as well as the unification of weak, strong and electromagnetic interactions. In this model, a whole new set of particles are postulated as super-symmetric partner of the SM contents. Among these, the neutralino is the lightest neutral particle which appears as a superposition of the partners of the standard model bosons and constitutes an example of a good WIMP candidate. The panel of WIMPs candidates is very wide and it would be beyond the scope of this work to make an exhaustive discussion.

1.2.4   Dark Sector models

Most of the searches performed during the last decades focused on the hypothesis of a WIMP-like dark matter. A significant portion of the parameter space for these candidates has been explored and no evidences have been found. Furthermore, even with the present highest energy reached at the collider experiments no indication of new physics has been observed up to the TeV scale. On the other hand all these searches focused on the hypothesis of heavy dark matter. On the contrary, the parameter space of light dark matter (LDM) is less explored. As it will be

explained in Sec. 1.3.1, part of the reason is due to higher sensitivity requirement of the direct detection experiments. But another reason is due to theoretical prejudice: there is a lower bound on the mass of a thermal relic dark matter candidate whose interactions with the Standard Model are mediated by particles of weak scale mass and coupling strength, as first noted by Lee and Weinberg [26]. It is possible to break this lower limit if a lighter mediator is responsible for DM to SM annihilation. However, below a certain DM mass threshold, the required mediator mass is lighter than any other known SM gauge boson masses, therefore requiring the existence of a new mediator. One can therefore address the DM puzzles, by introducing new mediators, and more in general an entire new model which assumes the existence of a new gauge group of symmetry consisting of particles not charged under SM forces (i.e. the dark matter) and their own *dark* gauge interactions. This is referred to as *Hidden* or *Dark Sector*.

That of the Dark Sector is a natural generalization of the WIMP idea to account for SM-DM interactions through new forces rather than just SM forces. The high-mass parameter space for hidden sector DM, above several GeV, overlaps WIMP parameter space and has similar phenomenology. However the low-mass parameter space, below a few GeV mass, offers very different scenarios. Indeed, this is not accounted within the WIMPs framework, and not explored by most of traditional WIMP searches. This strongly motivates new experimental efforts for probing low mass DS candidates.

External motivations which suggest a great interest into DS models, arise from a number of experimental results which point indirectly to the existence of new light bosons with small couplings to the SM. Many astrophysical observation could potentially be explained by the annihilation of DS candidates with a mass of a few MeV into electron-positron pairs (see Sect. 1.3.2). Another low-energy new physics indication comes from the measurement of the anomalous magnetic moment of the muon, $(g - 2)_\mu$, whose experimental determination famously shows a $\sim 3\sigma$ discrepancy with the most sophisticated available theoretical predictions [27, 28].

The connection between the SM and the dark sector is usually made through a 'mediator', i.e., a particle which possesses both Standard Model and dark sector quantum numbers, and interacts with SM particles either directly or indirectly through loop diagrams or mixing. Depending on the type of the mediator few "portals" to the hidden sector could be identified [29, 30]. Below is a description of the most common portals that can be introduced:

- Scalar portal: such scenario employs an additional scalar particle S coupled which interacts with the Standard Model Higgs boson H, as described by the phenomenological Lagrangian:

$$\mathcal{L} \sim \mu S H^+ H + \lambda S^2 H^+ H;$$

- Pseudoscalar portal: a possible solution to the strong CP problem is the introduction of a new Peccei-Quinn global U(1) symmetry which is broken spontaneously. The pseudo Nambu-Goldstone boson of this breaking is the axion. The interaction between the axion

a and the SM fermion field Ψ_f is given by the:

$$\mathcal{L} \sim \frac{\partial_\mu a}{f_a} \bar{\psi}_f \gamma^\mu \gamma_5 \psi_f.$$

While the parameters of the axion, namely, its mass m_a and coupling g_a to SM are functions of the breaking scale f_a of the Peccei-Quinn symmetry, other axion-like particles (ALPs) may well exist and their parameters are free;

- Neutrino portal: the neutrino mass puzzle provides input for few interesting models accounting for a rich DM-neutrinos scenario. The possible existence of a sterile neutrino may lead to the addition of Yukawa term:

$$\mathcal{L} \sim y_L LHN.$$

where N is the fermionic field associated to the right-handed sterile neutrino portal, which mixes with the SM leptonic field L through the SM Higgs H, with interactions proportional to the Yukawa coupling y_L;

- Vector portal: the most general interaction of a neutral vector particle A' with the Standard Model fermions can be written in the form:

$$\mathcal{L} \sim g' q_f \bar{\psi}_f \gamma^\mu \psi_f A'_\mu$$

where g' is the universal coupling constant of the new interaction and q_f is the corresponding charge of the interacting fermions. The new boson A' is often referred to as *dark photon*. It could itself be the mediator between SM and the dark sector but the link can also be realized in different ways.

All these gauge groups have four dimensions and are renormalizable, with the exception of thenon-renormalizable five-dimensional axion one.

It must be noted how dark sector models are often the answer to other SM challenges. Indeed, axions in the pseudo-scaar portal, sterile neutrinos in the neutrino portal, and light Higgs bosons in the Higgs portal are themselves well-motivated BSM particles aiming to solve SM challenges such as strong CP problem, the Higgs hierarchy and baryogenesis.

Below the discussion focuses in greater detail on two models of the vector portal, of which in Chapter 3 and Chapter 4 the experimental results from their investigation at the Belle II experiment will be given.

The kinetic mixing model

One of the most motivated vector portal model is the so-called *kinetic mixing* model. It introduces an additional $U(1)_D$ gauge group which mirrors the hyper-charge interactions of the SM particles. Its interaction carrier is a massive spin-1 boson A' called *dark photon* (sometimes also referred to as *U-boson*, *dark boson* or *secluded photon*). This model has been studied extensively in the literature since the 1980's [31, 32, 33, 34]. The dark photon can interact with SM photons through the so-called kinetic mixing mechanism, described by the following Lagrangian mixing term:

$$\mathcal{L}_{mix} = \frac{1}{2}\epsilon F^{\mu\nu}F'_{\mu\nu} \tag{1.3}$$

where $F^{\mu\nu}$ and $F'^{\mu\nu}$ are field strength tensors of the SM $U(1)_{em}$ and the dark sector $U(1)_D$ groups, respectively, and ϵ is a dimensionless parameter characterizing the kinetic mixing strength.

The physical consequences of the kinetic mixing are best understood in the basis where the kinetic terms are canonical. Here two gauge bosons arise: the ordinary photon A and the dark photon A'. As a result of the kinetic mixing the dark photon acquires a coupling of strength ϵ with the electromagnetic current J_{em}, described by the following interaction term:

$$\mathcal{L}_{int} = \epsilon e A'_\mu J^\mu_{em}. \tag{1.4}$$

The mixing parameter ϵ can be understood as the suppression factor relative to the dark photon coupling with the electron charge e. This coupling can arise, for example, as loops of heavy particles in theories that include new fields charged under both $U(1)_D$ and $U(1)_{em}$. In such a case, perturbative theory can account for ϵ in the range $10^{-8} - 10^{-2}$ [32].

Note that the dark photon actually couples to the hypercharge. As a consequence, it can mix even with the Z^0 boson in addition to the photon, but the suppression of most processes due to the mass of the Z^0 make the mixing too weak to have a noticeable effect at the energy scales much smaller than the mass of the Z^0.

In the kinetic mixing model, all the processes are determined by a single parameter: the mixing strength ϵ. Under the assumption that no dark state particles exist below the dark photon mass, it decays exclusively to SM particles via kinetic mixing [35]. In the mass range $m_{A'} \geq 2m_e$, the dark photon decays to leptons with the following partial decay width:

$$\Gamma_{A' \to l^+l^-} = \frac{1}{3}\alpha\epsilon^2 m_{A'}\sqrt{1 - \frac{4m_l^2}{m_{A'}^2}}\left(1 + \frac{2m_l^2}{m_{A'}^2}\right) \tag{1.5}$$

For masses $m_{A'} > 2m_\pi$ hadronic decays are also allowed with a partial decay width:

$$\Gamma_{A' \to had} = \frac{1}{3}\alpha\epsilon^2 m_{A'}\sqrt{1 - \frac{4m_\mu^2}{m_{A'}^2}}\left(1 + \frac{2m_\mu^2}{m_{A'}^2}\right) \times \left.\frac{\Gamma(e^+e^- \to \text{hadrons})}{\Gamma(e^+e^- \to \mu^+\mu^-)}\right|_{s=m_{A'}^2} \tag{1.6}$$

Neutrino decays are neglected since they are heavily suppressed by a factor $m_{A'}^4/m_Z^4 \sim 10^{-8}$.
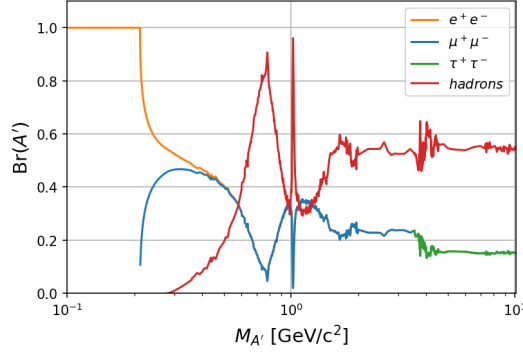
Figure 1.6: Dark photons decay modes and their branching fractions for different dark photon mass values. Reproduced from [35].

The decay fraction of the dark photon into SM particles is shown in Figure 1.6.

In a non-minimal scenario, the dark photon might not be the only accessible state from the dark sector. In its simplest form, the interaction term of a dark fermion χ, with the dark photon would be similar to QED case:

$$\mathcal{L}_D \sim \sqrt{4\pi\alpha_D}\,\bar{\chi}\gamma^\mu\chi A'_\mu \tag{1.7}$$

where α_D is the coupling constant associated with the $U(1)_D$ gauge group in the dark sector. In such a case, if kinematically allowed ($m_{A'} > 2m_\chi$) the dark photon would decay to DM pairs with the decay rate:

$$\Gamma_{A'\to\chi\bar{\chi}} = \frac{1}{3}\alpha_D m_{A'}\sqrt{1 - \frac{4m_\chi^2}{m_{A'}^2}}\left(1 + \frac{2m_\chi^2}{m_{A'}^2}\right) \tag{1.8}$$

An interesting possibility appears when $\alpha_D \gg \alpha\epsilon^2$: the dark photon will not decay to visible particles at all, thus resulting in an effectively *invisible* decay.

As the mass term of the dark photon breaks the gauge invariance of the $U(1)_D$ group, one can implement, in close analogy with the SM, a spontaneous breaking mechanism of the $U(1)_D$ gauge group: a Higgs-like particle h', called *dark Higgs* is therefore introduced [35]. The masses of the dark Higgs and the dark photon arising through spontaneous symmetry breaking of the $U(1)_D$ would be of similar order. Then the additional terms to the dark sector part of the Lagrangian would be:

$$\mathcal{L} \sim \frac{1}{2}m_{A'}^2 A'_\mu A'^\mu + g_D m_{A'} h' A'_\mu A'^\mu + \frac{1}{2}g_D^2 h'^2 A'^2. \tag{1.9}$$

As an experimental consequence, the interactions and the parameters of the dark photon

could also be probed through the searches of the hidden Higgs fields.

Theoretically, the values of the kinetic mixing and the dark photon mass can take on a wide range of values. However, much attention has given on the MeV–GeV mass range where the dark photon could explain the $(g-2)_\mu$ anomaly. Indeed, the exchange of a dark photon via a triangular diagram could be responsible for such a disagreement. There are many experimental probes of MeV–GeV mass dark photons. These include productions in collider experiments, beam dumps, rare meson decays, and precision measurements. Existing constraints have almost disfavored the entire mass and coupling range in which dark photons could explain it, assuming the dark photon decays directly to SM particles with a branching ratio close to 100%. In Section 1.4 more details on dark photon searches at low energy e^+e^- will be presented.

The $L_\mu - L_\tau$ model

Beyond the kinetic mixing mechanism, other types of vector couplings can be foreseen, which still require dark sectors containing a new massive gauge boson. Additional possibilities arise for instance, from couplings to accidental symmetries of the SM, like those related to baryon or lepton numbers: other $U(1)$ anomaly-free gauge group can be easily constructed, like $U(1)_{B-L}$, $U(1)_{L_e-L_\tau}$, $U(1)_{L_\mu-L_\tau}$ and $U(1)_{L_e-L_\mu}$.

A particularly interesting model is the one that gauges the $L_\mu - L_\tau$ current [36, 37, 38]. It predicts a massive gauge boson called Z', which couples only to the heaviest generations of leptons (μ, τ and their corresponding neutrinos), with a new coupling constant g'. The interaction Lagrangian in such a model is given by:

$$\mathcal{L} = \sum_\ell \theta g' \bar{\ell} \gamma^\mu Z'_\mu \ell \tag{1.10}$$

where the sum is extended to $\ell = \mu, \tau, \nu_{\mu,L}, \nu_{\tau,L}$ including the heavy leptons and their relative (left-handed) neutrino species, with $\theta = -1$ if $\ell = \mu, \nu_{\mu,L}$ and $\theta = 1$ if $\ell = \tau, \nu_{\tau,L}$.

Such a model may solve many open issues in particle physics, like the well-known discrepancy associated with the muon anomalous magnetic moment, which points into the direction of a lepton flavour non-universality. Furthermore, it has been invoked to explain the high energy cosmic neutrino spectrum, and the problem of DM abundance by providing a way to balance the annihilation rate to sterile neutrinos in the early universe [36]. In addition, some works use it to explain the rare B decay anomalies [37] observed in the $B \to K l^+ l^-$ analyses [38].

The decay partial widths to SM particles obtained from [39], are:

$$\Gamma(Z' \to l^+l^-) = \frac{(g')^2 M_{Z'}}{12\pi} \left(1 + \frac{2M_l^2}{M_{Z'}^2}\right) \sqrt{1 - \frac{4M_l^2}{M_{Z'}^2}} \tag{1.11}$$

and

$$\Gamma(Z' \to \nu_l \bar{\nu}_l) = \frac{(g')^2 M_{Z'}}{24\pi} \ . \tag{1.12}$$

This gauge interaction is well-hidden from most experiments due to its lack of coupling to first-generation leptons. Thus only a limited phase space region has been probed so far. Limits on the Z' coupling constant derive form low-energy e^+e^- colliders and neutrino beam-dump experiments. In Section 1.4, more details on the Z' searches at low energy e^+e^- will be presented.

1.3 Detection methods

The possibility that dark matter has other than gravitational interactions with standard model particles potentially allows for detectable signals in both space and terrestrial experiments. Usually, dark matter detection experiments are grouped into three main categories, depending on the different strategy used to reveal it:

- direct detection: look for recoil energy of SM nuclei after a DM-SM interaction;

- indirect detection: look for SM products of DM-DM annihilation;

- direct production: look for hints in SM-SM particle collisions at accelerators/colliders.

A schematic representation of the aforementioned processes that each detection method aims to probe is given in Figure 1.7.

The common purpose of these experiments is to measure or at least constrain the properties of DM, as its mass and the cross sections of self or with SM interactions. Once measured, such properties can then be used to determine or at least exclude any particular DM model. Each of the previously mentioned methods has advantages and shortcomings, often complementary to the others. Thus the synergy of experiments based on different detection techniques allows to test for a wide range of models.

To date, the majority of these experiments has not provided DM evidence. However, anomalies that may have been induced by DM have been reported in some cases. A brief description of the three methods is given below, showing the significant results or the discovery potential of the main experiments.

1.3.1 Direct detection

Direct detection experiments are based on the assumption that, as the Earth passes through our galaxy's DM halo, dark matter could interact with the ordinary matter particles in some detection apparatus. Specifically, it would be possible to detect the SM particles scattered by the incoming dark matter. This technique mainly targets the DM interactions with ordinary matter nucleons, but also DM-electron interaction can be probed, depending on the properties of the DM
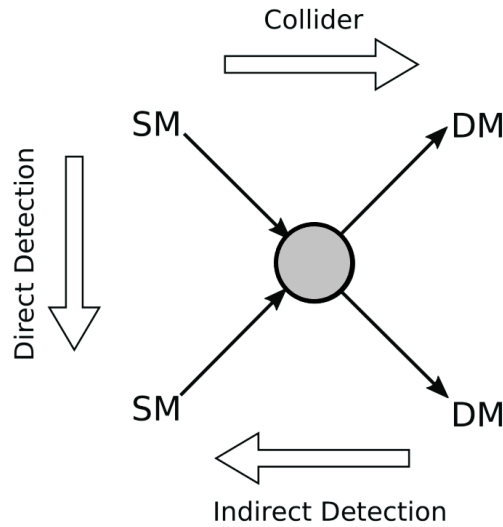
Figure 1.7: Schematic representation the possible dark matter detection channels. The direction in which the diagram is read determines the physical process that can be exploited. If the diagram is read from top to bottom, this involves the DM-SM scattering suitable for DM direct detection. Right to left direction represents DM annihilation to SM particles suitable for indirect detection experiments. Left to right represents the SM annihilation into DM particles process, investigated from SM collisions in particle colliders.

particles under investigation. The expected rate of interactions per unit mass of detector material depends on the DM density and velocity distribution in the galaxy and on the interaction cross section. The DM interaction with the detector's nuclei can have different features: it could be either elastic or inelastic, spin-dependent or spin-independent. The DM-nucleon interaction sign is the energy released by the nuclear recoil in the detector medium, usually in the range from some to hundreds of keV, depending on the DM mass and type of nuclei in the detector. It can be computed assuming a Boltzmann velocity distribution for the DM candidate which transfers a momentum q, corresponding to a recoil energy of $E_r = \frac{|q|^2}{2m_N}$, where m_N is the nucleus mass. For light dark matter, the exchanged momentum q becomes quickly small at the point which dark matter experiments cannot detect it anymore. Therefore, direct search methods are suited to investigate mainly heavy DM, as is the case with WIMPs. The challenge of most of the nowadays experiments is to push the recoil threshold required for detection to lower energies, and thus light DM. To detect the DM-SM interaction, the main experimental techniques exploit the ionization induced by the nuclear recoil through the medium, the scintillation light produced in crystal scintillators or in noble gas detectors and the detection of phonons produced by DM-SM particle interactions in cryogenic solid state detectors.

Of course, the larger is the time of exposure and the quantity of target material, the larger will be the number of observed events. Thus, direct search experiments setup usually include a huge detector which has to be optimized to minimize the background contamination. The most
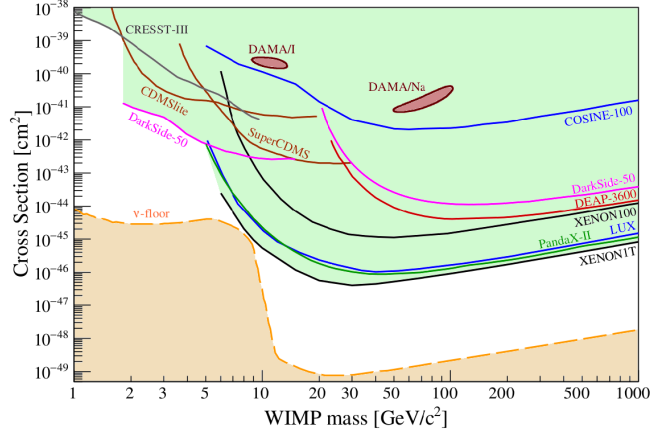
Figure 1.8: Current experimental limits on spin-independent dark matter-nucleon cross section. Parameter combinations above the lines (i.e., the green shaded area) are disfavoured at 90% confidence level. The dashed orange line represents the neutrino floor. The regions labeled "DAMA" mark the preferred parameter space if the annual modulation seen by DAMA/LIBRA would be interpreted as originating from dark matter interactions. Figure from Ref. [43].

important backgrounds usually come from natural radioactivity, intrinsic radioactivity of the detector and cosmic rays. For this reason, direct detection experiments are based underground in order to block cosmic rays, and every component, including the target material, are cautiously selected to reduce radioactive background.

Up to now, experiments of direct detection provided the strongest constraints on the WIMP-SM interaction cross section, without revealing their nature. A summary of the most important results of the many direct searches experiment is shown in Figure 1.8, where the WIMP-nucleon cross section is plotted versus the WIMP mass for a spin independent interaction. The current strongest bounds are from LUX [40], PANDAX II [41] and XENON1T [42].

Even if new experiments are under-construction in order to have detectors with larger fiduciary masses and exposures, as well as enhanced background veto and target sensitivity, there is a limit below which it is no longer possible to explore the WIMP phase space, due to the irreducible background due to coherent neutrino scattering. This lower bound is known as the neutrino floor and is shown in Figure 1.8. A way around this is to have a detector sensitive to the incoming WIMP direction, since neutrinos will scatter isotropically while the DM is expected to be directional. Other interesting handles include searches for modulation in the dark matter signal: an annual modulation of the observed signal rate may be expected, due to the earth relative motion with respect to a WIMP wind coming uniformly from the galactic halo. This modulation can be exploited to reject background in direct detection experiments. Results from DAMA/LIBRA experiment, which exploits the equivalent of ~ 250 kg of radio-pure Na(Tl) target detectors, report about the observation of an annual DM modulation at a confidence level that exceeds 9σ, over the 14 year cycles of data collected [44]. However, no other direct search

experiments have been able to confirm those results yet. A simple hypothesis that explains the spectrum and magnitude of the signal, and reconciles it with the null results of other experiments, is that dark matter-nucleus scattering is dominated by an inelastic process, in which the dark matter χ scatters off a nucleus N into an excited state χ^* with mass splitting of 100 keV [45].

1.3.2   Indirect detection

Indirect detection of dark matter involves searching for products of DM-DM self-annihilation (or decay) far in the Universe. Indeed, stable SM particles may be the end product of the annihilation, or decay, of DM in high density space regions. The indirect strategy, thus, focuses on finding an excess in the flux of the annihilation products of known sources regions. The most favoured regions to search for indirect signals are the galactic centre and halo close galaxy clusters or dwarf galaxies. The latter are very popular locations due to their large measured mass to light ratio and their small background.

Depending on the mass of the DM, as well as its interactions, the DM can annihilate to a variety of SM leptons, quarks or gauge bosons. As a result of subsequent decays of the primary annihilation products, many kinds of particles will be further created. The SM particles giving the best information are photons, neutrinos and stable anti-particles, i.e., positrons and anti-protons.

Antiparticles usually deliver good information because there is very little abundance in the Universe and known astrophysical sources are expected to produce very small amounts of it. Since dark matter annihilation would produce both particle and antiparticle in equal number, we can gain some interesting hints from the energy distribution of the relative fluxes of particle and antiparticle. The main experiments looking for antimatter fluxes are currently satellite based, namely AMS-02 [46], Fermi-LAT [47] and PAMELA [48, 49]. An excess of the measured positron fraction in cosmic rays, not accompanied by a visible excess of the anti-proton flux has been observed for the energy range 20∼200 GeV by both FERMI and PAMELA experiments and also confirmed by AMS (Figure 1.9). This anomaly implies the existence of a source of primary e^+ (and e^-) other than the known astrophysical ones. The new source can be either of astrophysical nature, i.e., one or more pulsars, or supernova remnants, or annihilating light DM. DM annihilation to a dark photons which subsequently decay to electron-positron pairs, naturally yields an enhanced signal and a sufficiently hard positron spectrum to match the observations. Furthermore, it would forbid the production of anti-protons, if the dark photon is lighter than twice the proton mass.

The main limitation of using antimatter as a probe for DM annihilation is the fact that the propagation of charged particles is affected by the interstellar medium, magnetic field and other energy loss processes. On the contrary, neutrinos can freely propagate in the galaxy, and also through dense matter of stars and planets. However, neutrinos detection is difficult. Their fluxes can be measured indirectly via the detection of charged particles, like muons, produced
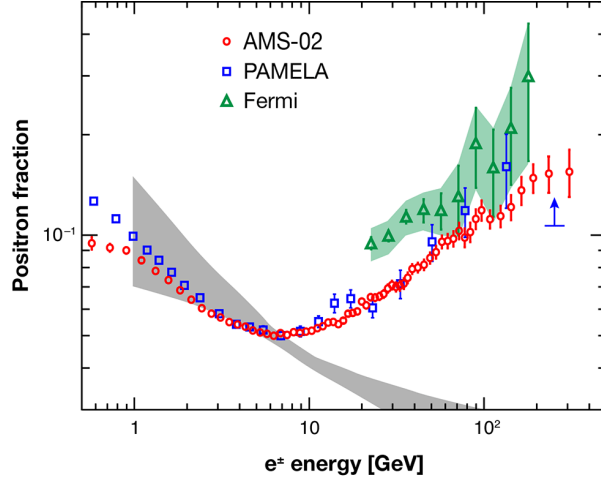
Figure 1.9: The positron fraction in high-energy cosmic rays reported by PAMELA and Fermi-LAT and AMS satellites. The grey band indicates the expected range in the positron fraction [50]. Image from Ref. [51].

by a neutrino interaction in the surroundings of the detector. The detector can partially then reconstruct the original energy of the incoming neutrino. Large neutrino detectors like Ice Cube [52], ANTARES [53] or Super-Kamiokande [54] searched for dark matter annihilations into neutrinos. To date, no evidence for such a signal has been observed, resulting in constraints on the cross-section.

The detection of photons could give a very accurate hint on the DM annihilation that created them. Unlike charged final states, photons propagate in the galaxy without any appreciable deflection due to the magnetic field, and unlike neutrinos, they are easy to detect. However, they can be affected by absorption in the interstellar medium over the large galactic distance scales. If photons are promptly produced as primary products of the DM-annihilation, then one will observe a line feature in the energy spectrum with a kinematic cut-off at the DM mass. Such a signature, if observed, would be a clear hint for DM annihilation, due to the low astrophysical background able to replicate such a signal [55]. If the photons are produced further down the decay tree, then one will observe an extended diffuse energy spectrum [56].

Imaging atmospheric Cherenkov telescopes for TeV γ-ray detection can look specifically in the direction of objects where a large amount of dark matter is expected. So far no significant anomalies have been observed, and upper limits are derived by the MAGIC [57], HESS [58] and VERITAS [59] telescopes. Gamma-ray searches can be also performed by satellite-based instruments capable of detecting low-energy γ-rays (approximately 20 MeV to $\sim$ 300 GeV) like Fermi-LAT. The INTEGRAL telescope [60] has reported a 511 keV photon signal near the Galactic center. This excess could be explained by annihilation of light dark matter or by heavy dark matter with MeV excited states. In the latter case, dark matter excited by scattering decays back to the ground state by emitting a soft e^+e^- pair. In the energy region of $0.1 - 10$ keV,

X-ray satellites as XMM-Newton [61] and Chandra [62] provided data to search for indirect dark matter signals. An unexpected line at 3.5 keV was found in the data recorded by both satellites [63]. This signal can be interpreted by a decay of dark matter candidates, for instance, from sterile neutrinos or axions [64]. Other astrophysical explanations have been, however, proposed and thus, the origin of the signal remains controversial.

1.3.3   Direct production

Experiments at particle colliders/accelerators are ideally well suited for searching for new physics hints, by either attempting to directly produce new particles or by searching for deviations in precision measurements of otherwise well-understood SM phenomena. There are two basic frontiers in particle physics, namely, the energy and the intensity frontiers. A primary goal of the Large Hadron Collider (LHC) and other "energy frontier" experiments is the exploration of new particle above the electro-weak scale. Thus, such experiments can be used to search for new particles predicted by BSM models with masses at or above several hundreds of GeV, by directly producing them in high-energy collisions. On the contrary, the "intensity frontier" experiments could search for new particles below the electro-weak scale not yet detected due to their small coupling with the SM particles. A major drawback of direct production experiment, is that such searches are by necessity highly model dependent, requiring both specific dark matter mass ranges and couplings.

Dark matter candidates produced in a collider experiment would not interact with the detector as by definition they interact very weakly with SM particles. However, the presence of a DM particles would leave a distinctive signature inside the detector: as DM escapes detection, an energy/momentum inbalance is expected to be measured. Thus, direct detection experiments usually search for missing energy/momentum signature, that is, visible particles recoiling against DM invisible particles.

Given the energy at the Tevatron and the LHC colliders and the properties of WIMP candidates (mass and coupling at the electro-weak scale) one can certainly attempt to produce them. The best targets are mono-jet or mono-photon signals from $\chi\bar{\chi}j$ and $\chi\bar{\chi}\gamma$ production (see as an example [65, 66]), respectively, where the jet j or the photon come from initial state radiation. The caveats to this type of search is that the DM particle may be too heavy to be produced (above a few TeV) or its signal may be hidden by backgrounds. In fact, an unfavorable point at hadron colliders, is that, beside initial state protons have fixed energy, the quarks and gluons do not, thus hardening the final state reconstruction. As a result, at the Tevatron and LHC, the mono-jet and mono-photon signals are easily obscured by backgrounds. More details on DM searches at LHC experiments can be found here [67, 68, 69].

Direct production experiments can investigate not only WIMPs candidates but even lower mass matter candidates. In this region, the most promising candidates are related to Dark Sector models. Usually, DS searches target the portal mediator rather the DM itself, assuming the existence of a non-gravitational coupling with SM and without any hypothesis on the DM

structure. Such mediators may have sizeable couplings to the SM, thus may be potentially probed at the intensity-frontier experiments, like e^+e^- colliders. Since DS mediators necessarily have hidden charge, their decays may be non-standard. Specifically, once produced, the mediator can have two different decay mode: an invisible decay to DM resulting in a missing momentum signature; if invisible decay is kinematically forbidden, decay to SM particles is expected. As it will be discussed in the following Section, low-energy e^+e^- colliders as KLOE, CLEO, BABAR, Belle, and BESIII provided a very good environment to test dark sector and LDM candidates, because of the high luminosity, clean environment and the favorable production cross section for low mass scenario.

On the other hand, direct production experiments are not confined to colliders. Even fixed-target experiments using beams of protons or electrons can extended the sensitivity to light dark matter at sub-GeV scales. Fixed-target experiments attempt to produce DS particles in beam collision with nuclei in the target material and then detected downstream of the target. Specifically, new mediators may be produced either radiated from beam particles or in the decay of mesons produced in beam-target interaction. The advantages of fixed-target experiments compared to lepton colliders are the larger luminosity, the scattering cross section enhancement due to the nuclear charge of the target and a resulting boosted final state that can be revealed by compact special-purpose detectors. Some examples of fixed-target experiments are the HPS and APEX at the JLAB, PADME, NA64 [70]. As the experimental principle in this case is similar to that of neutrino experiments, several neutrino experiments can also be used to probe DS, for example, CHARM, LSND, MINOS, and MiniBooNE [71].

So far no significant excess has been observed in direct production experiments, placing significant constrain on a large number of dark matter models and masses.

1.4 Dark Sector searches at low energy e^+e^- colliders

While in the past, most of the direct production dark matter searches have been performed at high-energy colliders (such as LEP, Tevatron, LHC) with the aim of looking for heavy DM candidates, in recent times much attention has been devoted to the low-mass dark sector candidates. As previously observed, searches for new particles with a $\sim \mathrm{GeV}/c^2$ mass are particularly motivated by many independent observations of anomalies explainable with a same dark sector framework.

Low-energy colliders such as B meson factories (and more in general flavour factories) are ideally suited to probe dark-sector particles [72, 73, 35, 74, 75, 76, 77]. While the primary purpose of such experiments is to study flavour physics, their experimental environment allows a wide range of new-physics searches, including dark sector. Indeed, by working at the so-called intensity frontier, they are expected to collect such a huge data-set to have an unprecedented sensitivity to probe small couplings and rare physics processes. Furthermore, the low-mass DS production rate at a low energy e^+e^- collider is larger than those expected at the energy frontier

experiment, since, over a large amount of DS production processes, the cross section is inversely proportional to the center-of-mass energy $\sqrt{s}$. Moreover, low energy e^+e^- colliders provide a clean and well controlled environment with a well defined initial state, allowing to search for new particles both in decay to SM particles and in missing energy/momentum final states.

During the past two decades, high luminosity flavour factories, like KLOE, CLEO, BABAR, Belle, and BESIII produced an enormous amount of data at different center-of-mass energies useful to test for many dark sector scenarios. Most of the results for dark sector searches comes BaBar, Belle and KLOE. The BABAR experiment at the SLAC National Accelerator Center collected an integrated luminosity of $\sim$430 fb^{-1} on the $\Upsilon(4S)$ resonance at a center-of-mass energy of $\sqrt{s}$ =10.58 GeV. The Belle experiment at the KEK laboratory in Japan obtained an integrated luminosity of 725 fb^{-1} on the $\Upsilon(4S)$. The two experiments also acquired data on the $\Upsilon(3S)$ and $\Upsilon(2S)$ resonances, and at nearby energies. The KLOE experiment at the DAΦNE collider, collected events mainly at $\sqrt{s} \sim m_\Phi \sim 1.02$ GeV. Operating at lower energies, it required much lower integrated luminosity to reach sensitivities similar to the B-factories. For example, the $\sim$2.5 fb^{-1} of data collected by KLOE makes this experiment competitive with Belle and BaBar searches for sub-GeV mass dark sectors. Of course the signatures of dark sector models were quite different, resulting in better sensitivities depending on the particular case. Despite such a large amount of data collected by these flavour factories, the parameters space of interesting dark sector models still to be investigated is large. Furthermore, it is pointed out that often only a fraction of the data was useful to test dark sector models because of the absence of dedicated triggers for low-multiplicity events. Therefore, the development of new experiments capable of testing dark sector models with greater sensitivity is more than motivated. This is the case of the the Belle II experiment at the SuperKEKB energy-asymmetric e^+e^- collider, which is a substantial upgrade of the Belle experiment at KEKB (see Chapter 2). It started operations in 2018 and aims to record within the next years about 50 ab^{-1} of data, a factor of 50 more than its predecessor. Thanks to this large data-set and by using dedicated triggers, Belle II is expected to explore dark sector candidates with an unprecedented sensitivity in a mass range up to 10 GeV/c^2.

In this Section, the production mechanisms of dark-sector particles through the vector portal at e^+e^- colliders will be discussed. The main dark sector searches performed at past experiments and the current constraints on the model parameters will be discussed. Furthermore, considerations on the Belle II potential discovery will be addressed.

1.4.1   Signatures and current bounds

As previously described, dark sector searches usually target the portal mediator rather the DM itself. Depending on the model, mediators can couple to boson or fermion particles, to both quarks and leptons, only to quarks (leptophobic) or only to leptons (leptophilic). If new mediators are scalar or pseudoscalar it is furthermore expected a coupling to fermions proportional to their mass.
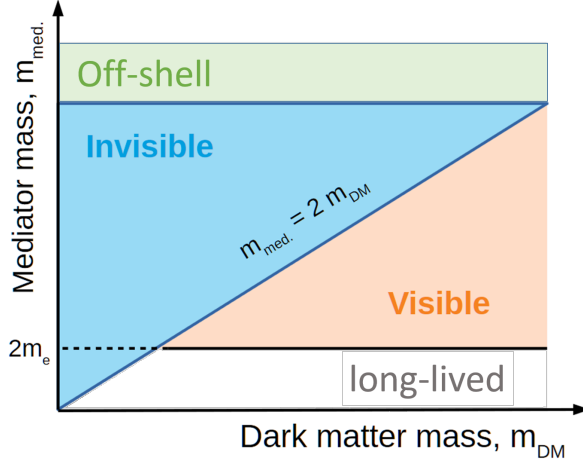
Figure 1.10: Regions in the $m_{med} - m_{DM}$ plane with different expected signatures due to kinematical constraints.

The phenomenology of dark sector candidates produced in e^+e^- collision is quite rich, and depends on the different models and the particles content. Here, we will assume a minimal dark sector scenario, with a spin-1 neutral light mediator, like a dark photon or a Z'. Depending on the mass relationship between the DM candidates and the portal mediator several signatures can be depicted based on kinematic considerations. In general, the mediator vs DM masses plane ($m_{med} - m_{DM}$) can be divided into four regions with distinct kinematics [75], as illustrated in Figure 1.10. Specifically, four different cases can be distinguished:

- $m_{med} > \sqrt{s}$: the mediator is too heavy to be produced on-shell, and DM production proceeds through an off-shell mediator;

- $2m_{DM} < m_{med} < \sqrt{s}$: the mediator decay promptly and dominantly to DM, thus being invisible;

- $2m_e < m_{med} < 2m_{DM}$: the mediator is produced on-shell, but the decay to DM is kinematically forbidden. It would decay into a SM particle resulting into a visible signature;

- $m_{med} < 2m_e$ and $m_{med} < 2m_{DM}$: the mediator is too light to decay to either DM or SM particle, thus it is long-lived decaying eventually outside the detector.

Different production mechanisms are suitable for vector portal dark sector searches at low energy e^+e^- colliders. The most exploited consist of:

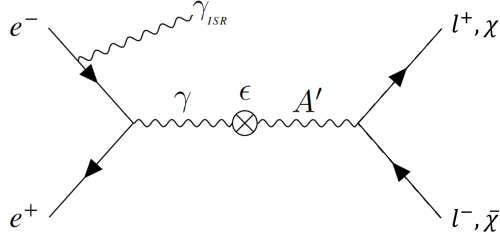- Initial State Radiation (ISR) processes;

- Mesons decay;

Figure 1.11: Feynman diagram representing the dark photon production in the ISR process $e^+e^- \to \gamma_{ISR}\,A'$. Different final-states are possible depending on the dark photon mass relationship with hypothetical dark matter particles.

- Dark Higgsstrahlung process;

In this Section a review of the main results achieved at low energy at e^+e^- colliders constraining the kinetic mixing parameter ϵ is provided, focusing mainly on direct production in ISR processes. In addition, the discovery potential of Belle II will also be discussed. Finally, the two searches on which this thesis focuses, i.e., a non-minimal dark photon model with an additional dark Higgs boson and a Z' boson coupled to heavy flavours leptons according to the $L_\mu - L_\tau$ symmetry will be presented.

Note that other models and signatures are also under investigation at Belle II (see as an example [78, 79, 80]) and first results have already been achieved (like for the ALPs search [81]), however their discussion is beyond the work of this thesis. For a mini-review of recent DS searches at Belle II see Ref. [2, 3, 82].

Dark photon direct production

A simple way to search for a dark photon at an e^+e^- collider is in the resonant process with initial state radiation (ISR) $e^+e^- \to \gamma_{ISR}\,A'$. The process is depicted in Figure 1.11. Its cross section is proportional to $\epsilon^2\alpha^2/s$ where α is the electromagnetic coupling.

As previously discussed, the decay modes of the dark photon depend on its mass and couplings, as well as on the particle spectrum of the dark sector. If the dark photon is the lighter DS state, it would decay dominantly into SM final states $A' \to l^+l^-$ or $A' \to h^+h^-$ (l=leptons, h=hadrons) with an expected branching ratio equal to that of a virtual photon of mass $m_{A'}$, as shown in Figure 1.6. In such a scenario, the dark photon search proceeds by looking for a resonance in the invariant mass distribution of the reconstructed daughter particles. This is rather challenging experimentally as it suffers for high SM backgrounds. As this process is predominantly used to search for decay into a lepton-pair, the QED main background is $e^+e^- \to \gamma\gamma^* \to \gamma l^+l^-$.

On the other hand, if a sufficiently low mass dark matter state χ exists (such that $m\chi < 1/2\,m_{A'}$), one can assume that the dominant decay mode of the dark photon is into DM via

$A' \rightarrow \chi\bar{\chi}$. Since the interaction probability of dark matter with the detector is negligible, this case is referred to as *invisible* decay (while the former case is referred to as *visible* decay). The experimental signature of the process $e^+e^- \rightarrow \gamma_{ISR} A'$, $A' \rightarrow \chi\bar{\chi}$ would be only a mono–energetic ISR photon, accompanied by significant missing energy and momentum. In such a case, the energy of the ISR photon is related to the dark photon mass $m_{A'}$ through the relationship $E_\gamma = \frac{s - m_{A'}^2}{2\sqrt{s}}$. The search, then, occurs as a scan of the squared mass distribution of the recoiling system against the ISR photon. The backgrounds expected for this search are due to high cross section QED processes $e^+e^- \rightarrow e^+e^-\gamma(\gamma)$ and $e^+e^- \rightarrow \gamma\gamma(\gamma)$ where all but one photon are undetected, being out of acceptance, or due to gaps or inefficiently regions. It is therefore needed a rather good knowledge of the detector efficiencies to perform such analysis.

An additional possible signature derives from the dark photon lifetime; in fact, in the case of long-lived A', the decay can happen far from the production point. In such a case, the two tracks vertex would be significantly displaced with respect to the interaction region, providing a clear signature of the process.

BaBar searched for the visible dark photon in e^+e^- and $\mu^+\mu^-$ final states using a data-set of 514 fb^{-1} [83]. Constraints on the mixing parameter ϵ have been set to the level of $\mathcal{O}(10^{-3})$ in a mass region $0.02 < m_{A'} < 10.20$ GeV/c^2. Also KLOE searched for an A' direct production in e^+e^-, $\mu^+\mu^-$ and $\pi^+\pi^-$ final states [84, 85, 86]. The decay into pion-pair is particularly interesting in order to recover sensitivity in the mass range of the $\rho - \omega$ resonances region, which is not covered by BaBar: the mixing of the γ to the ρ meson makes the decay into hadrons more probable. Other searches looking for the dark photon in meson decay were also carried out by BaBar, KLOE and Belle, but the limits obtained are less stringent than the current ones. A compilation of all exclusion limits obtained in the last years and future projections is reported in Figure 1.12. Constraints from old axion searches (experiments E141 and E774) as well as a constraint from the precision observables $(g-2)$ of the electron, are also shown. They cover the lower and the upper left corner, respectively. The best limits in the low mass region $\sim 10 - 100$ MeV/c^2 have been computed the NA48 collaboration at the SPS/CERN looking for a dark photon production in the $\pi_0 \rightarrow \gamma A'$ decay [87], while for higher masses the best current limits are from BaBar. Recently LHCb searched for a dark photon in *proton-proton* collisions, placing the most stringent limits on ϵ for the mass range $10.6 < m(A') < 70$ GeV/c^2 [88] (not shown here). The $(g-2)_\mu \pm 2\sigma$ band depicts the parameter range, in which the dark photon could explain the presently seen deviation of 3.6 standard deviations between the SM prediction and the direct measurement of the anomalous muon magnetic momentum. Currents limits completely exclude such a hypothesis.

Visible dark photon searches are also planned at Belle II. Preliminary studies for the visible search at Belle II have been performed in Ref. [89]. Results of the BaBar experiment for the visible decay of an A' via e^+e^-, $\mu^+\mu^-$ final states have been used to extract expected sensitivities. Taking into account the better invariant mass resolution ($\sim$ a factor 2) of Belle II due to the
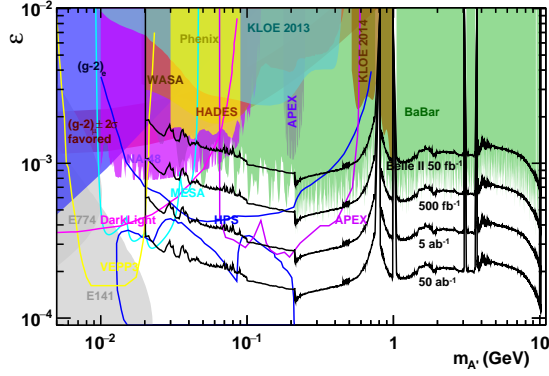
Figure 1.12: Existing constraints and future projection on the dark photon kinetic mixing parameter ϵ and mass $m_{A'}$ via the visible decay process $e^+e^- \to \gamma_{ISR} A'$, $A' \to l\bar{l}$ with projected limits for Belle II and other future experiments [89].

larger drift chamber radius and a better trigger efficiency for both muons ($\sim$ a factor 1.1) and electrons ($\sim$ a factor 2), the projected sensitivities for different values of integrated luminosity are shown in Figure 1.12. Belle II is expected to be competitive with Babar at 500 fb^{-1}, while is expected to constrain ϵ down to $\mathcal{O}(10^{-4})$ at the target luminosity of 50 ab^{-1}.

BaBar searched also for an invisible dark photon. This analysis requires the implementation of a dedicated first level (L1) trigger sensitive to a single photon, which was not available at the Belle experiment, and only partially available at the BaBar experiment. Specifically, BaBar recorded only 53 fb^{-1} of data with the single-photon trigger on. The main difficulty in realizing such a trigger is due to the high rate mainly due to radiative Bhabba and $e^+e^- \to \gamma\gamma$ events in which only a single photon is produced within the detector acceptance. The BaBar upper limits on the mixing strength are shown in Figure 1.14.

Belle II searches for a dark photon in the invisible process are expected too [89]. Here, setting new stringent upper limits is already possible with the data collected so far. The expected sensitivities of Belle II to the mixing parameter ϵ is shown in Figure 1.14. With an integrated luminosity of 20 fb^{-1}, Belle II should be able to set a limit considerably lower than the equivalent of BaBar. The better expected sensitivity compared to BaBar is due to the more homogeneous electromagnetic calorimeter of Belle II, whose barrel part has no projective gaps to the interaction point. In BaBar, this caused a large irreducible background of $e^+e^- \to \gamma\gamma(\gamma)$ events, due to one or more photons escaping the detection by passing through projective cracks between adjacent crystals. Furthermore, the usage of the Belle II KLM (see Chapter 2 for a Belle II detector description) detector can be used to veto photons not detected by the electromagnetic calorimeter. Additionally, SuperKEKB beam energies provide a smaller boost and larger electromagnetic calorimeter angular coverage, allowing for a larger acceptance of signal events.
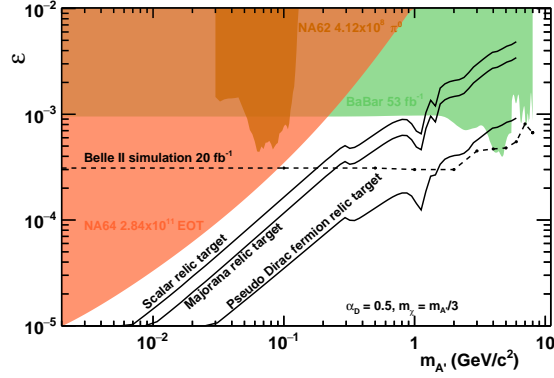
Figure 1.13

Figure 1.14: Existing constrain on the dark photon kinetic mixing parameter ϵ and mass $m_{A'}$ via the invisible decay process $e^+e^- \to \gamma_{\mathrm{ISR}}\, A'$, $A' \to$ invisible and the Belle II expected sensitivity for the early data-set. Figure updated from [89].
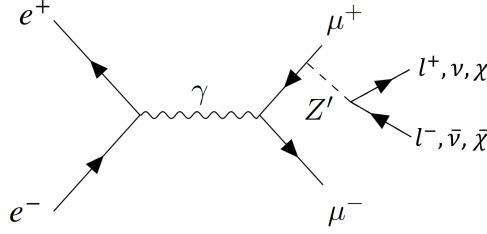

Figure 1.15: Feynman diagram representing a Z' production in the process $e^+e^- \to \mu^+\mu^- Z'$. Different final states are possible depending on the $L_\mu - L_\tau$ model branching ratios or if DM kinematically accessible exists

Z' searches

An interesting scenario belonging to the vector portal case is provided by the so called $L_\mu - L_\tau$, which introduces a new massive gauge boson Z', coupling only to the second and third generation of leptons (see Sect. 1.2.4).

At an e^+e^- collider it can be produced in processes such as $e^+e^- \to \mu^+\mu^- Z'$ or $e^+e^- \to \tau^+\tau^- Z'$, thus being radiated from one of the final state muons or taus and then eventually decaying either visibly into a muon or tau pair, or invisibly to neutrinos or dark matter. The process is depicted in Figure 1.15.

Searches can be performed into a four charged lepton final state or by looking for the invisible decay. This latter case allows to constrain the parameter space and mass regions lower than the dimuon threshold. According to eq. 1.11 and 1.12 the expected branching ratios to neutrinos are:
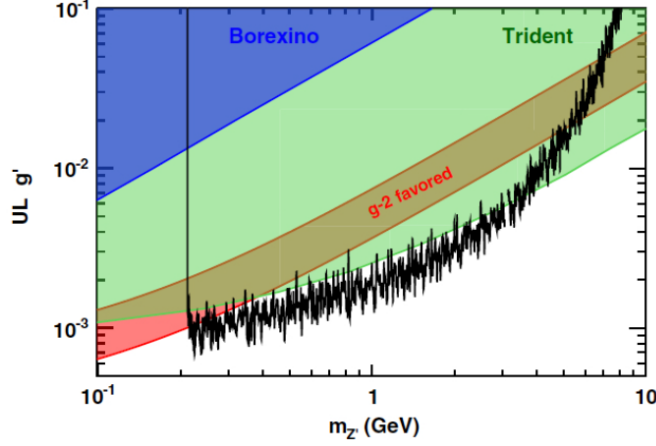
Figure 1.16: The 90% CL upper limits on the Z' coupling constant g' as a function of the mass $m_{Z'}$ [90], together with the derived constraints from other experiments. The region consistent with the discrepancy between the calculated and measured anomalous magnetic moment of the muon within 2σ is shaded in red.

$$m_{Z'} < 2m_\mu \quad \implies \quad BF[Z' \to \text{invisible}] = 1, \qquad (1.13)$$

$$2m_\mu < m_{Z'} < 2m_\tau \quad \implies \quad BF[Z' \to \text{invisible}] \simeq 1/2, \qquad (1.14)$$

$$m_{Z'} > 2m_\tau \quad \implies \quad BF[Z' \to \text{invisible}] \simeq 1/3. \qquad (1.15)$$

Of course, in the case of kinematic accessible decays of Z' to dark matter particles χ one can expect that $BF(Z' \to \chi\bar{\chi}) = 1$, i.e., all the branching fraction for SM final states would turn out to be largely suppressed. Consequently, the invisible search is not directly comparable to the visible decay search and rather complementary to it.

BaBar searched for a Z' (in the $L_\mu - L_\tau$ framework) decaying into a pair of muons in a four-muon final state [90]. The Z' coupling constant g' parameter space constrained by the this search is shown in Figure 1.16. A similar search for four-muon events production at $\sqrt{s} = 13$ TeV has been performed also by the CMS experiment [91] for a Z' mass between 5 and 70 GeV/c^2 (not shown here). Limits on the visible Z' derived also from neutrino-nucleus scattering processes at neutrino beam dump experiments (neutrino trident production processes [92]), as measured, for instance, by the CCFR experiment [93], as shown in Figure 1.16.

The first search for an invisible decaying Z' was performed by the Belle II experiment with the 2018 pilot run data-set, corresponding to an integrated luminosity of $\sim$276 pb^{-1}. This analysis is an integral part of the work done in this thesis and it is presented in more detail in Chapter 3.
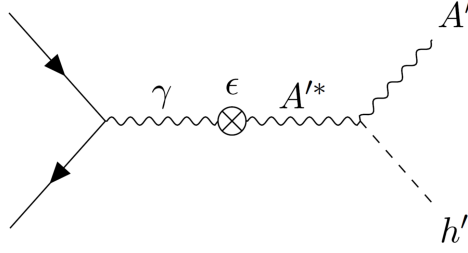
Figure 1.17: Feynman diagram representing the dark Higgsstrahlung process $e^+e^- \to A'^* \to$ $A'h'$. Depending on the to the dark photon and dark higgs mass relation, different final states are possible.

Dark Higgsstrahlung

As discussed in Section 1.3.3, a new Higgs-like particle h', called *dark Higgs*, can be implemented into the dark photon theoretical framework. The dark Higgsstrahlung process $e^+e^- \to$ $A'\,h'$ (shown in Figure 1.17), with A' decaying into lepton or hadron pairs, is then an interesting reaction to be studied at an e^+e^- collider in order to probe both dark candidates. The production cross section of such a process is proportional to the product $\epsilon^2 \times \alpha_D$, where α_D is the unknown dark coupling constant.

There are two very different scenarios depending on the masses of the dark photon $m_{A'}$ and of the dark Higgs boson $m_{h'}$. For $m_{h'}$ larger than $2m_{A'}$, the dark Higgs boson would decay dominantly and promptly to a dark photon pair, thus giving rise to a six charged particle final state. A peak is expected in the invariant mass of each of the three pairs of particles to the mass of the dark photon. In addition, a peak is expected around $m_{h'}$ in four-particles invariant mass. A different scenario happens if the h' is lighter than the dark photon: it would be long-lived for most of the parameter phase space, thus escaping the detection (*invisible dark Higgs* scenario). The signature would be given by the dark photon decay products plus missing energy.

Many searches looked for a simultaneous dark photon and dark Higgs production through the dark Higgsstrahlung process. BaBar investigated the six charged particles final state in the $0.8 < m_{h'} < 10$ GeV/c^2 and $0.25 < m_{A'} < 3$ GeV/c^2 masse range, with the constrain that $m_{h'} > 2m_{A'}$ [94]. The search was performed either in exclusive final states $3(l^+l^-)$, $2(l^+l^-)\pi^+\pi^-$, and $2(\pi^+\pi^-)l^+l^-$, or in inclusive modes $2(\mu^+\mu^-) + X$ and $e^+e^-\mu^+\mu^- + X$, where X denotes any final state other than a pair of pions or leptons. Upper limits have been set on $\alpha_D \times \epsilon^2$ in the range $10^{-10} - 10^{-8}$, which for $\alpha_D = \alpha$ translate into a limit on ϵ of $10^{-4} - 10^{-3}$. Also Belle performed a similar search [95] with $977\,\text{fb}^{-1}$ of data. These limits improve upon and explore slightly wider mass ranges than the BaBar as shown in Figure 1.18.

The invisible Higgs case was investigated by the KLOE experiment only which looked both into a two-muons and two-electron plus missing energy final states [96] for A' masses up to $\simeq$
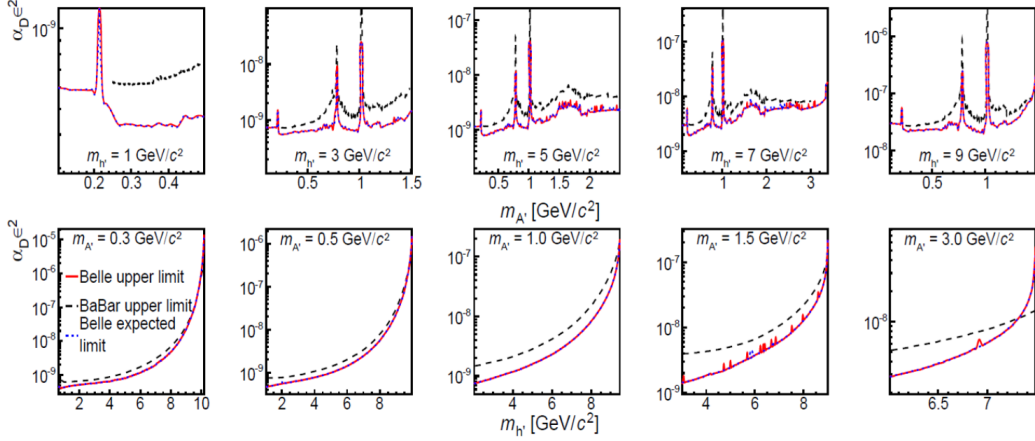
Figure 1.18: 90% CL upper limit on the product $\alpha_D \times \epsilon^2$ versus dark photon mass (top row) and dark Higgs boson mass (bottom row) for Belle (solid pink curve) and BaBar (dashed black curve) in the dark Higgsstrahlung process. The blue dotted curve shows the expected Belle limit. From Ref. [95]

1 GeV/c^2. The upper limits on the product $\alpha_D \times \epsilon^2$ were in the range $10^{-9} - 10^{-8}$ for a large range of the masses. These limits are complementary to the Belle and BaBar results as they refer to the same process in a different final state and phase space region.

Belle II is competitive in this latter search even with the first data collected. With a center-of-mass energy of 10.58 GeV, it would result in a significant extension of the covered phase space by KLOE. The full analysis flow to search for the A' and h' production via the $e^+e^- \rightarrow A'h'$, $A' \rightarrow \mu^+\mu^-$, $h' \rightarrow$ invisible process, by using data collected by Belle II during 2019 ($\sim 9\,\text{fb}^{-1}$) is a substantial part of this Thesis and will be further described in Chapter 4.

Chapter 2

The Belle II detector at the SuperKEKB collider

Belle II at the SuperKEKB collider is a new generation of B-factory experiment, which is going to collect an integrated luminosity of 50 ab^{-1} at the center-of-mass energy of $\sqrt{s} = 10.58\,\text{GeV}$ within the next decade. With such a hige data-set, Belle II aspires to have the best sensitivity on several measurements in heavy flavour physics as well as for many BSM signatures, including dark sector searches. In this Chapter, a general picture of the Belle II experiment is given, ranging from the SuperKEKB collider to the Belle II detectors structure, and the trigger and data acquisition system description. In the last part of this Chapter a description of three running phases of Belle II and SuperKEKB is provided, concluding with the luminosity prospects for the next data-taking years.

2.1 The $B-$factory experiments

Experiments at the B-factories have been built with the primary purpose of measuring the time-dependent CP asymmetries in B-meson systems as predicted by the CKM mechanism [97]. In addition, they are also capable of performing precise measurements of the CKM matrix elements and several branching fractions of rare B meson decays, allowing to constrain the SM parameters with the highest experimental precision. Furthermore, B-factories experiments allow the study of the charm, τ lepton and two-photon physics, and to search for new physics beyond the SM [98]. Such experiments are performed at e^+e^- colliders, which provide an extremely clean environment and a well known and coherent initial state. In order to have a large amount of $B\bar{B}$ mesons, these colliders operate at a center-of-mass energy of 10.58 GeV/c^2, corresponding to the invariant mass of the $\Upsilon(4S)$ resonance (see Fig. 2.1). This is a bound state (called *bottomonium*) of a beauty quark b and its antiparticle, with quantum number $J^{CP} = 1^{--}$. Specifically, it is the first state of the *bottomonium* family above the threshold for B-meson pair
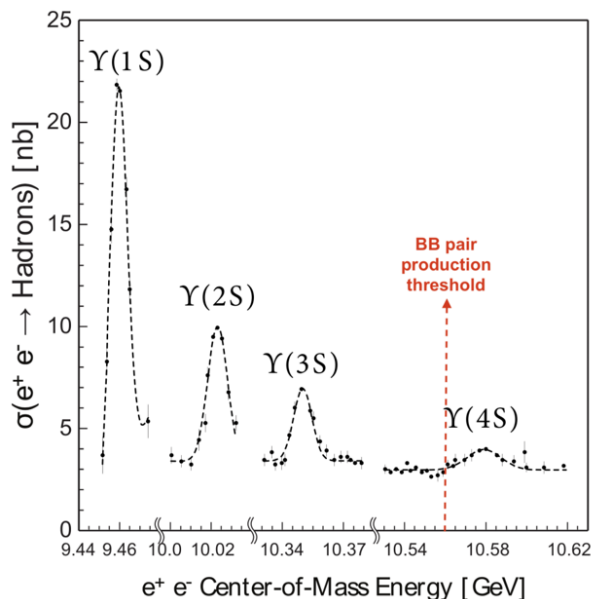
Figure 2.1: Hadronic cross section for e^+e^- collisions as a function of the center-of-mass energy in the region of the first four S-wave Υ resonances. The vertical red line indicates the $B\bar{B}$ production threshold.

production ($2m_B \sim 10.56\,\text{GeV/c}^2$) and mainly decays to neutral or charged $B\bar{B}$ pairs (roughly in the same proportion) with a branching ratio of $\sim 96\%$ [99]. The B mesons are produced almost at rest in the CMS frame and because of their short lifetime ($\tau = 1.519 \times 10^{-12}\,\text{s}$ [99]), they travel a very reduced distance in the laboratory. Therefore, given the typical resolution of the vertex detectors, of the order of 10μm, the measurement of their decay vertices separation which is needed for CP violation measurement would be hardly achievable. In order to solve this problem, an asymmetric beam energy collider can be exploited. By using different energies for the electron and positron beams the Υ(4S) acquires a boost in the laboratory frame and the decay products are pushed forward in the direction of the electron beam. In such a way, a proper B-decay vertices separations resolvable with current vertex detectors is achievable.

As interesting processes to be studied are *rare*, a data-set equivalent to millions of $B\bar{B}$ pairs is needed. Thus B-factories machines typically operate at unprecedented luminosities, of order $10^{34} - 10^{35}\,\text{cm}^{-2}\,\text{s}^{-1}$. There are unique features in a B-factory that make it an attractive and competitive alternative to the energy frontier approach. Specifically, the high signal-to-background ratio, the cleaner environment with respect to hadron colliders, which implies lower track multiplicity and detector occupancy, the possibility to build hermetic detectors with excellent reconstruction of neutrals and consequently in the possibility to close the event kinematics. This last feature is crucial to perform missing energy searches and look for invisible particles that may be hint of new physics, including dark sectors.

The experiments Belle at the KEKB collider (KEK laboratory, Japan) and BaBar at the

PEP II collider (SLAC National Accelerator Laboratory, USA) were the first B-factories to be built [98]. Both are asymmetric energy e^+e^- colliders with detectors that have almost 4π coverage at the interaction point of the collider. They were constructed and operated on similar time scales. The BaBar experiment finished taking data in 2008 accumulating $\sim 0.5\,\mathrm{ab}^{-1}$ of data, while Belle stopped in 2010 with a total integrated luminosity of $\sim 1\mathrm{ab}^{-1}$. They operated at all the Υ resonances, but most of that data was accumulated while operating at a centre-of-mass energy corresponding to the $\Upsilon(4S)$ resonance in order to perform the primary measurements of these experiments. With such huge samples, these B-factory experiments observed the CP violation into the B-meson system [100, 101] which experimentally confirmed the CKM mechanism and led to the 2008 Nobel Prize in Physics awarded to Kobayashi and Maskawa. The measurement of the direct CP violation in $B \to K\pi$ decays followed, and also the charm mixing [102] and several B and τ rare decays were measured, as well as many predicted and unexpected new states. In addition, a large number of searches for BSM physics, including dark sector, have been performed and stringent limits on their parameter space have been set, as discussed in Section 1.4.1.

Beyond these remarkable successes, many recent experimental measurements indicated several hints of discrepancies with the SM predictions. Accordingly, a much larger data sample is required to investigate further whether these are truly indicative of New Physics effects. With this purpose, the second generation of B-factory experiment Belle II at SuperKEKB collider was built.

2.2 The SuperKEKB accelerator

SuperKEKB is an asymmetric e^+e^- collider located at the KEK laboratory in Tsukuba (Japan). It is the successor of the KEKB collider [103], which was shut down in 2010. With respect to KEKB, a substantial upgrade of the machine was performed in order to reach the target instantaneous luminosity of $8 \times 10^{35}\,\mathrm{cm}^{-2}\mathrm{s}^{-1}$, a factor 40 times higher compared to predecessor[1] [104, 105]. Such a value will be the world highest instantaneous luminosity ever achieved, compared to previous colliders, as shown in Figure 2.2.

In Figure 2.3 a schematic overview of the SuperKEKB accelerator is reported. It consists of two major parts: the linear accelerator and a double-ring structure formed by the High Energy Ring (HER) storing electrons and the Low Energy Ring (LER) for positron storage. The electrons are produced in a pre-injector by a pulsed laser directed on a cold cathode target. Then they are accelerated by a linear accelerator (LINAC) to 7 GeV and injected in the HER of SuperKEKB. The positrons are produced by the collision of electrons with a tungsten target and then they are injected in a damping ring to reduce their emittance. When the positrons reach the required emittance they are accelerated to 4 GeV in the LINAC and then injected into the LER. The two main storage rings have a 3 km circumference. They are divided into four arc sections, which host

---

[1]A more realistic prediction, based on the feedback obtained with operation in the early stages, is to achieve a maximum instantaneous luminosity of $6.5 \times 10^{35}\,\mathrm{cm}^{-2}\mathrm{s}^{-1}$.
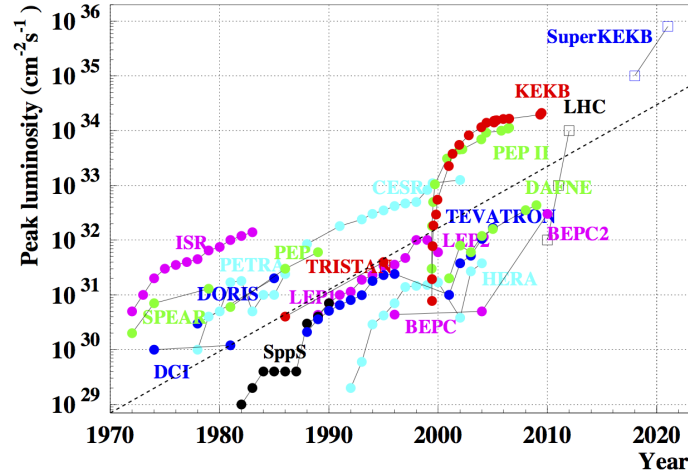
Figure 2.2: Comparison of the luminosity achieved and planned by different particle physics experiment.

normal conducting dipole bending magnets in order to guide the particles around the ring, and four straight sections. Both straight and bent sections are equipped with focusing magnets and collimators to maintain a small diameter of the beam. Superconducting and normal conducting Radio-Frequency (RF) cavities are installed along the straight sections to mitigate the energy loss due to synchrotron radiation. The RF frequency of these devices is 508.887 MHz.

When the circulating beams are sufficiently intense, they are brought to a collision at the Interaction Point (IP), which is surrounded by the Belle II detector. The Interaction Region (IR) is defined as the area around the IP with an extension of $\sim 4\,$m along the storage rings. It hosts the quadrupole magnets for the final focusing of the beams. The increased design luminosity required a larger crossing angle and a smaller energy asymmetry compared to KEKB. The increase in the beam energy of the LER from 3.5 to 4.0 GeV helps mitigate the emittance growth due to intra-beam scattering and the short beam lifetime due to Touschek effect. The decrease in the beam energy of the HER from 8.0 to 7.0 GeV is beneficial in obtaining a lower power consumption. The asymmetric energies of electrons and positrons provide a boost in the laboratory system equal to $\beta\gamma \sim 0.28$, necessary in order to allow vertex determination of short-lived particles decay. This condition results into an increased detector hermeticity, but also into a reduced flight distance for B mesons which is $\sim$130 μm, the 35% smaller than the 200μm of KEKB. However, the smaller beam pipe at the interaction region with the closer innermost layer of Belle II vertex detector lead to an improvement of a factor ~ 2 on the impact parameter resolution with respect to Belle. The beams are tilted with respect to each other by 83 mrad in order to avoid a head-on collision, which would introduce various difficulties and disadvantages due to beam optical effects. The nominal center-of-mass energy of the collision is at the $\Upsilon(4S)$ resonance but it can still be tuned in a small energy regime ranging from the $\Upsilon(1S)$ mass up to
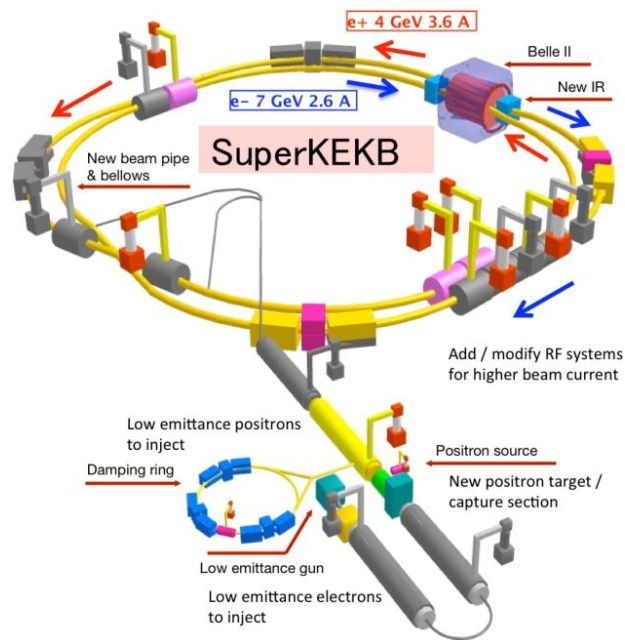
Figure 2.3: A schematic representation of the SuperKEKB asymmetric energy e^+e^- collider at the KEK Laboratory, in Tsukuba (Japan). Electrons and positrons are accelerated in the linear accelerator at the bottom of the image before entering the HER (blue) and the LER (red). Image from [106].
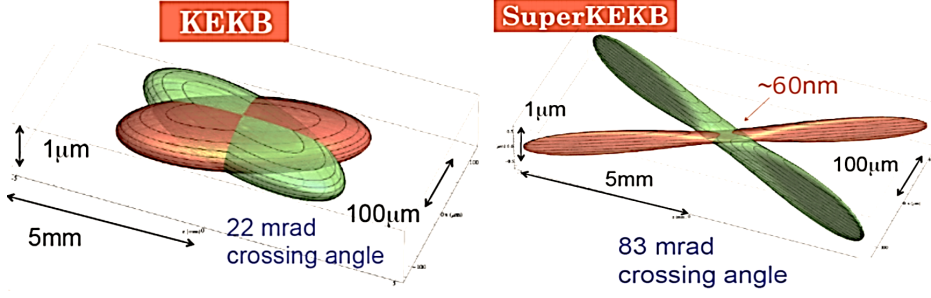
Figure 2.4: Two-dimensional sketch of the *nano-beam scheme* mechanism implemented at SuperKEKB (right) compared with the previous KEKB collision scheme (left).

the $\Upsilon(6S)$ mass.

Particles in the beams are grouped into bunches. Each ring can store 2506 bunches with roughly 10^{11} particles per bunch with a revolution frequency of 99.4 kHZ and bunch spacing of 4 ns. Newly accelerated bunches are continuously injected from the linear accelerator into the main storage rings with the help of electromagnets with fast-varying magnetic fields. The rate of injection is 25 Hz.

2.2.1   The machine upgrade and nano-beam scheme

The luminosity $\mathcal{L}$ is a key factor in determining the performance of an experiment, since it is related to the the production rate R for a process with cross section σ thought $R = \mathcal{L} \cdot \sigma$. In order to achieve the much larger luminosity with respect to the KEKB apparatus, many parts of the machine had to be upgraded and their operation improved. At an e^+e^- collider the instantaneous luminosity can be parametrised as follow:

$$\mathcal{L} = \frac{\gamma_\pm}{2er_e}\left(1 + \frac{\sigma_y^*}{\sigma_x^*}\right)\frac{I_\pm\xi_{y\pm}}{\beta_{y\pm}^+}\cdot\frac{R_L}{R_{\xi_y\pm}} \tag{2.1}$$

where γ is the relativistic Lorentz factor, e is the absolute value of the electron charge, r_e is the classical radius of electron, σ_x^* and σ_y^* are the widths of the bunch at IP on the transverse plane, $I_\pm$ is the beam current, β_y^* is the vertical betatron function at the IP which is correlated with the vertical beam size σ_y^*, $\xi_{y\pm}$ is the vertical beam-beam parameter, R_L and R_{ξ_y} are the reduction factors of the luminosity and the vertical beam-beam parameter due to not-vanishing crossing angle and '$\pm$' refer to the charge of the particles in the beam. For a more detailed description of the parameters refer to [104].

In order to reach the luminosity increase, SuperKEKB is going to use a larger beam current and a smaller beam dimension at the IP, with the use of the so called *nano-beam scheme* [107]. This aims to strongly reduce the vertical betatron function with the minimization of the longitudinal size of the beam overlap at IP. Specifically, this innovative configuration is based on keeping small horizontal and vertical emittance and use a large crossing angle, as shown in Figure 2.4.

	KEKB (LER / HER)	SuperKEKB (LER / HER)
Energy [GeV]	3.5/8.0	4.0/7.0
σ_x^* [μm]	90	9
σ_y^* [nm]	1900	60
Cross. Angle [mrad]	22	0.83
β_y^* [mm]	5.9/5.9	0.27/0.41
I [A]	1.64/1.19	3.6/2.62
Luminosity [10^{35} cm^{-2} s^{-1}]	0.211	8.0

Table 2.1: Fundamental design parameters of SuperKEKB and the values achieved by KEKB.

This is obtained with a specially designed final-focus superconducting-quadrupole-magnet system, made of magnets, corrector coils, and compensation solenoids installed at each longitudinal end of the interaction region. As a result, the vertical beta function is expected to be $20\times$ lower compared to KEKB. Additionally, the beam currents will be increased with respect to KEKB of about a factor 2, leading to a luminosity increase of a factor 40. The proposed improvements compared to the KEKB design and are presented in Table 2.1.

The luminosity requirement imposed several other modifications to the accelerator structure: the electron injection and positron target have been modified; furthermore, the damping ring, the radio-frequency system, the optics, the beam pipe and the vacuum system have been renewed. The SuperKEKB upgrade needed to increase the luminosity had a counter effect appearing as a higher beam-induced background rate of a factor 10 to 20, compared to KEKB. There are essentially two types of background at SuperKEKB [108]: single-beam backgrounds and luminosity-dependent ones. The first processes can originate from the interaction between a particle of a bunch with residual gas in the beam pipe or other particles within the same bunch, whereas luminosity-dependent backgrounds are induced by beam collisions and include QED processes, such as (radiative) Bhabha scattering $e^+e^- \rightarrow e^+e^-(\gamma)$ or two-photon processes $e^+e^- \rightarrow e^+e^-e^+e^-$. Thus, to maintain the good performances of the detector, mitigate the effects of higher background level is a necessary point.

2.3 The Belle II detector

The Belle II detector is a multi-purpose detector with cylindrical geometry located at the interaction point of the SuperKEKB accelerator. It is an upgrade of the Belle detector [109], with a substantial renewal of many systems in order to guarantee an equal or better performance than those achieved by Belle with KEKB. Specifically, a better resolution in the reconstruction of the decay positions (vertices) of long lived particles is achieved, to enhance background suppression and sensitivity in measurements of decay-time dependent quantities; a more efficient charged hadron identification is implemented in order to obtain an increased separation of final-state

charged hadrons, a reduction of the backgrounds, and an improved flavor-tagging; and a more hermetic acceptance is achieved thanks to the smaller boost of the center of mass of the collision. These improvements are achieved through technologies designed to sustain the side-effects of higher SuperKEKB luminosity, which include high occupancy and radiation damage, associated with higher beam-induced backgrounds on the detector and an increased pile-up noise on the electromagnetic calorimeter. Furthermore, a faster and more efficient trigger system, as well as data acquisition system capable of processing large quantities of data is needed too.

2.3.1   Detector overview

A detailed description of the Belle II detector is reported into the Technical Design Report (TDR) [110]. In this section, a general description of each sub-detector is given.

The Belle II detector is conventionally described by a right-handed Cartesian coordinate system with the origin located at the nominal IP. The z axis is parallel to the beam pipe, with the positive direction pointing to approximately the direction of the electron beam. The positive part of the y axis points to the top of the detector and the orientation of the x axis is parallel to the radial direction towards the outside of the storage ring. The Belle II detector is about 8 meters in length, width, and height, and weighs 1400 tons. A picture of the experiment is given in Figure 2.5.

The detector has an approximate cylindrical symmetry around the z-axis, while it has a significant forward-backward asymmetry to improve the solid angle acceptance in the boost (forward) direction. The angular acceptance of Belle II amounts to $17° < \theta < 150°$ for the polar angle and 2π for the azimuthal angle. With regard to the polar angle the detector is divided into three regions:

- the forward region ($17° < \theta < 30°$);

- the barrel region ($30° < \theta < 125°$);

- the backward region ($125° < \theta < 150°$).

The detailed structure of the detector is shown in Figure 2.6, with the main sub-systems highlighted.

The operation of Belle II in a nutshell is as follows. The particles produced by the interactions of electrons with positrons at the interaction point propagate outwards passing through successive layers of detectors designed specifically to measure their properties. The inner layers provide precise spatial tracking of charged particles, which can be used for reconstruction of primary and secondary vertex positions. The 1.5 T solenoid magnet causes charged particles to bend, enabling the determination of their momenta by measuring the tracks curvature within a gaseous drift chamber. Denser outer detectors stop and measure the energy of electrons and photons, while muons are identified by their ability to penetrate into the outermost layers. Furthermore, Cherenkov radiators provide additional particle identification information.
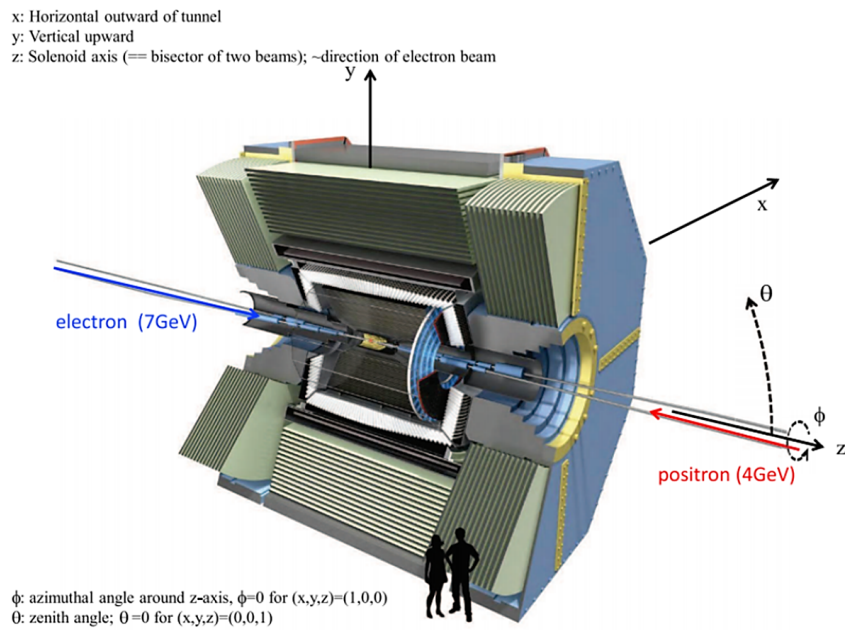
x: Horizontal outward of tunnel
y: Vertical upward
z: Solenoid axis (== bisector of two beams); ~direction of electron beam

Figure 2.5: A representation of the Belle II detector. Here the axes of the reference frame have been highlighted: the x axis points along the radial direction towards the outside the ring while the y axis indicates the vertical upward direction. The positive z axis points approximately towards the electron beam direction. Positive z coordinates correspond to the 'forward' region, those with negative z belong to the 'backward' region.
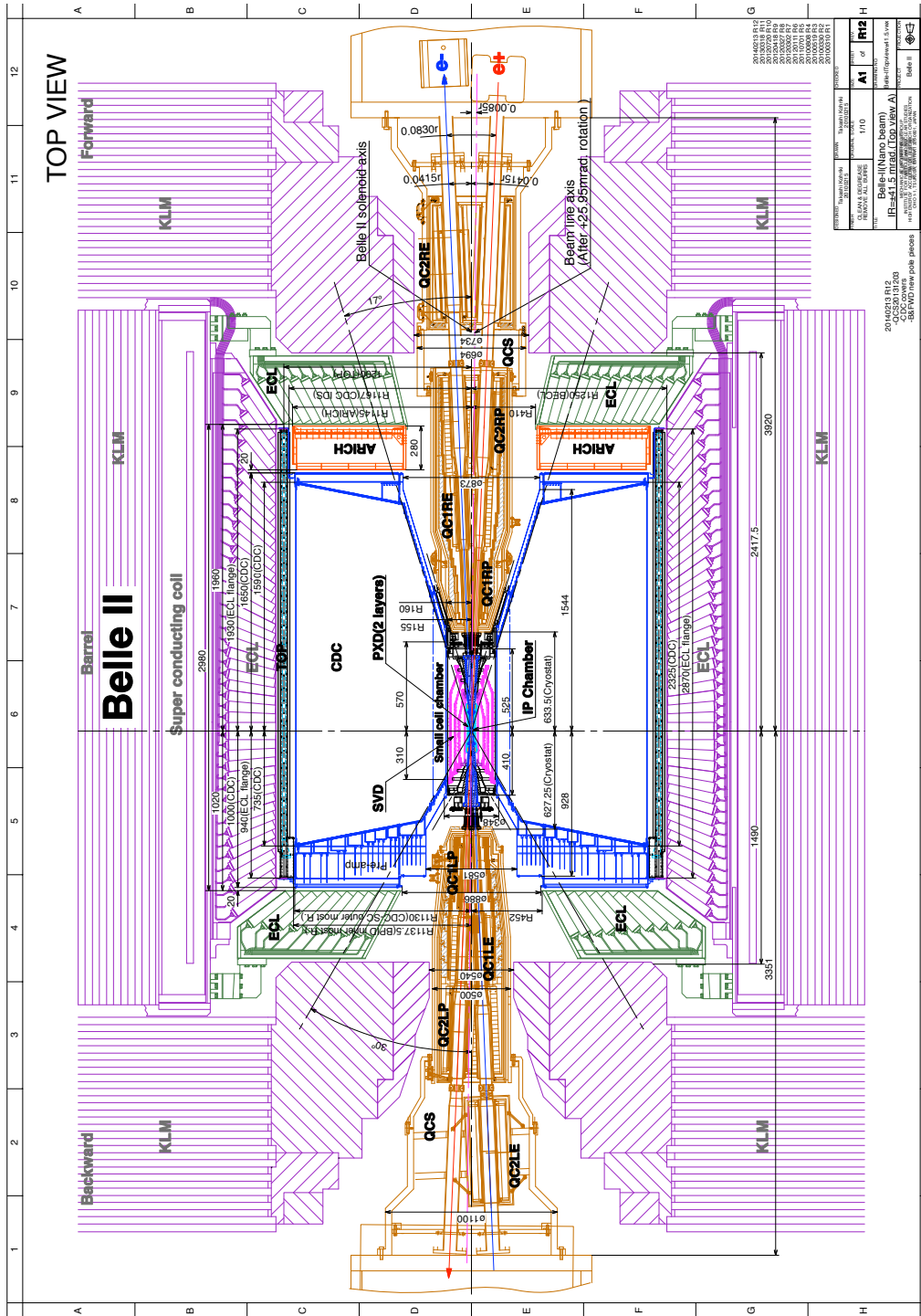
Figure 2.6: The Belle II detector horizontal cross section at the level of the interaction point, with all the sub-detctors highlighted, as designed in [110].
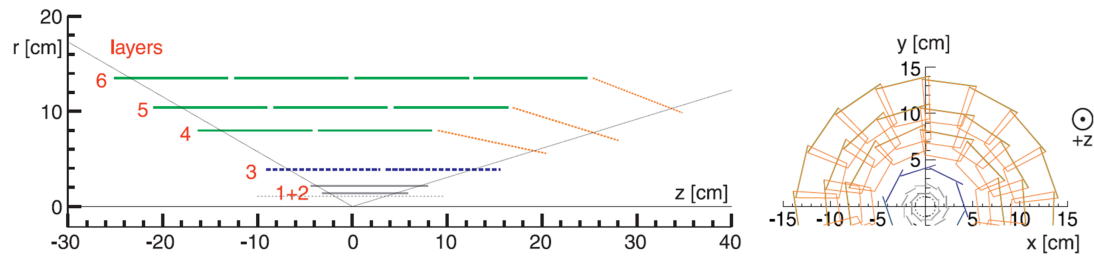
Figure 2.7: View of the Silicon Vertex Detector in the $r - z$ (left) and $x - y$ (right) planes. The PXD is in gray, while the remaining layer are from the SVD. Picture adapted from [110].

This brief introduction is followed by an overview of the various sub-detectors, from the innermost to the outermost sub-detector.

2.3.2 The Vertex Detector

The innermost sub-detector is the Vertex Detector (VXD), which consists of a Pixel Detector (PXD) and a Silicon Vertex Detector (SVD), as shown in Figure 2.7. Both PXD and SVD have an excellent space resolution and serve to identify secondary vertices and charged particle tracks. The VXD is a completely new device with respect to the Belle case, in order to achieve a significant improvement is expected in the vertex resolution. To ensure a good performance of the VXD, for both the detectors a very low material budget and short shaping time in order to limit the occupancy is required.

The Pixel Detector

The PXD the closest sub-detector to the IP [111]. It consists of two layers of pixelated DEPleted Field Effect Transistor (DEPFET) sensors. The DEPFET technology allows for very thin ($\sim 50 \mu$m) sensors in order to obtain a low material budget of $0.2X_0$ in the detection region. The two layers are placed around the beam pipe on a cilindrical layout at 14 mm and 22 mm from IP. The longitudinal extension of the outer is 174 mm and the polar angle ranges from 17° to 150°. The total amount of pixels composing the PXD is around 8 million organized into arrays with pixels size of $50 \times 50 \, \mu$m^2 and $50 \times 75 \, \mu$m^2 for the inner and outer layers, respectively. The transverse impact-parameter resolution is $12 \, \mu$m, achieved by weighting the charge deposited in neighbouring pixels. At the moment only the inner PXD layer and part of the second layer is installed; the full outer layer will be added in 2022. The readout electronics, which is cooled by means of the evaporative CO_2 cooling technique, is located outside the acceptance region and therefore does not contribute to the multiple-scattering material budget. PXD has to meet the requirement of being a inherently radiation-hard detector. Another challenging requirement is the short frame readout time, that is achieved by splitting the readout on both sides of the pixel matrix and introducing high level of parallelization.

The Silicon Vertex Detector

The outermost detector of the vertex detector is the SVD [112]. It is composed by a silicon bulk sandwiched between a p-type and n-type doped layer, which is segmented into strips. The strips are oriented orthogonal to each other. These devices simultaneously measure two coordinates of the traversing charged particle. The SVD is composed of four layers positioned at radii between 38mm to 135mm from the IP in a cylindrical geometry, and covers the full Belle II angular acceptance $17° < \theta < 150°$. As shown in Figure 2.7, SVD has a polar-asymmetric geometry with the most forward sensors slanted towards z-axis, in order to take into account the asymmetry in particle density resulting from the center-of-mass boost. The average material budget per layer is approximately $300\,\mu$m, and the separation between adjacent sensing strips ranges from $50\,\mu$m to $240\,\mu$m. SVD uses several shape and strip pitch sensors. While the innermost layer is entirely covered with small rectangular sensors, the outer layers host large rectangular (barrel sensors) and trapezoidal-shaped (slanted sensors) sensors for improving acceptance and precision of forward boosted particles.

2.3.3   The Central Drift Chamber

Surrounding the VXD detector there is the Central Drift Chamber (CDC): a wire drift chamber designed to reconstructs the trajectories of charged particles to precisely determine their momentum from the bending radius due to the magnetic solenoid field of Belle II. Additionally, the CDC provides PID information by measuring the energy loss of particles in the gas volume, and it generates trigger information for charged particles. The CDC has a hollow cylindrical geometry extending over a radial region between 160 cm to 1130 cm. It is filled with a mixture of helium and ethane (50% He, 50% C_2H_6). The low atomic number of the gas mixture is needed to suppress multiple scattering. The radiation length of the mixture is approximately 640 m. The entire volume is closed by two carbon cylinder and 2 aluminium end-plates. The angular acceptance is the same of the VXD ($17° < \theta < 150°$) to be able to merge all the tracks of the two sub-detectors.

The chamber is composed of 8 super-layers formed by 6 layers of wires each, and an innermost super-layer formed by 8 layers, as illustrated in Figure 2.8. Two classes of wires are present: the field wires producing the accelerating electric field, and the sense wires collecting the released charge. Sense wires are gold plated tungsten wires with a thickness of 30 μm. Each of the sense wires is surrounded by 8 aluminum field wires. The wire orientation between the super-layers alternates between parallel to the beam axis (axial layers) and skewed by an angle of -74 mrad to 70 mrad (stereo layers). When a charged particle crosses the CDC ionize the gas mixture of the chamber producing electrons and ions. The electrons are accelerated by the electric field and produce a charge avalanche that induces a signal on the sense wires. Spatial information about the incident position in the $x - y$ plane is obtained by timing measurements combined with the known drift velocity of electrons. The tilted stereo layers provide additional information about
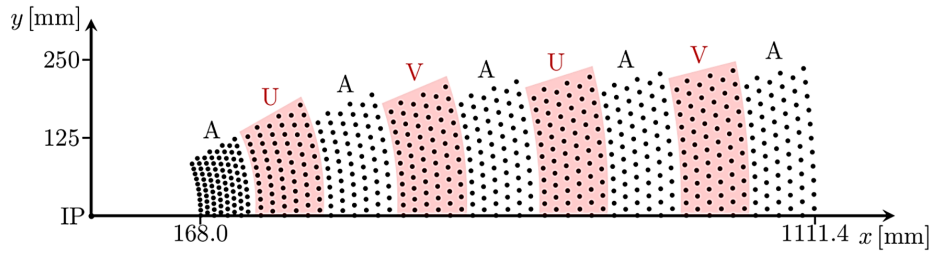
Figure 2.8: Layer configuration of the Central Drift Chamber. The letter A stays for axial super-layers; the letter U for stereo super-layers with positive stereo angle; and the letter V for stereo super-layers with negative stereo angle

the position in z direction. The electric pulse induced at the sense wires is proportional to the deposited energy of the incident particle, which allows for energy loss measurements. The spatial resolution of CDC is about $100\,\mu$m in r while $2\,$mm in z. The resolution on the energy loss by a charged particle inside the chamber is 12 %, for incoming particles at an incident angle of $90°$.

The front-end electronics is located near the backward end-plate, and it uses an ASIC chip to amplify, shape and discriminate the signal. A Time to Digital Converter (TDC) is used to measure the drift time and a Fast Analog to Digital converter (FADC) to measure the signal charge.

2.3.4   The Particle Identification system

Two detectors are used specifically for particle-identification purpose, namely the Time-of-Propagation counter (TOP) in the the barrel region, and the Areogel Ring-Imaging Cherenkov (ARICH) in the forward end-cap region. Both systems are based on Cherenkov light detection, but the operating principles are substantially different, thus they are described separately.

The Time of Propagation counter

The TOP is located in the barrel region of the detector just outside the CDC at $1.2\,$m radius from the IP and consists of 16 rectangular $2.5\,$m long and $2\,$cm thick quartz radiators. The polar angular acceptance ranges from $31°$ to $128°$. The end of the modules is equipped with a spherical mirror which focuses the light and reduces the chromatic error in the forward region and an array of photo-sensors in the backward region, as represented in Figure 2.9. Cherenkov photons, generated by the passage of a charged particle through the radiator, are internally reflected at the radiator walls confining their propagation to the interior of the quartz modules until they are detected by the photo-sensors at the end of each quartz module. The photons emitted in the forward directions are first reflected by the mirror at the end of the quartz bar and directed to backward end. By measuring the time of propagation of the Cherenkov photons internally reflected in the quartz bar, together with the arriving position along the quartz bar,
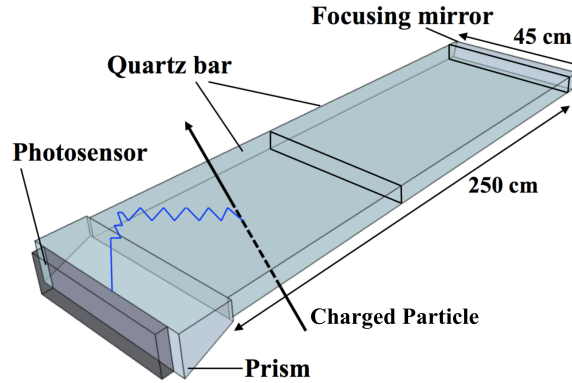
Figure 2.9: Representation a module of the Time-of-Propagation detector. A charged particle is shown passing through the radiator and emitting a Cherenkov photon.

the Cherenkov emission angle θ_C can be reconstructed. Knowing this, the particle velocity v can be inferred and the likelihood for different mass assignment hypothesis is calculated.

The TOP counter requires photo-sensors with an excellent single-photon time resolution, which is achieved with a 16-channel MCP (Micro-Channel Plate) Photo-Multiplier Tube (PMT) specially developed for this purpose. The single-photon time resolution is about 100 ps, providing a good separation of pions and kaons in the $0.4 - 4$ GeV/c momentum range (kaon identification efficiency is about 95%, pion fake rate is about 10%).

The Aerogel Ring-Imaging Cherenkov counter

Charged-particle identification in the forward end-cap is provided by the ARICH counter, which measures the Cherenkov ring produced by the passage of charged particles through a radiator. It covers a polar region between $14.78° < \theta < 33.71°$. The ARICH consists of an an aerogel radiator, where Cherenkov photons are produced by charged particles followed by an expansion volume of 20 cm to allow the photons to form rings on the photon detector surface. This latter is composed by an array of Hybrid Avalanche Photon Detector (HAPD), that is capable of detecting single photons in a high magnetic field with high efficiency and with good resolution in two dimensions. The radius of the ring depends on the opening angle of the Cherenkov cone, which is determined by the incident particle's velocity. The resolution per track improves as $\sigma_{\theta_C}/\sqrt{N_{p.e.}}$, where $N_{p.e.}$ is the number of detected photons and σ_{θ_C} is the resolution on the Cherenkov angle. $N_{p.e.}$ increases with the thickness of the radiator but σ_{θ_C} degrades due to the uncertainty of the emission point, thus in order to optimize the performances a peculiar solution has been adopted: two layers of aerogel with different refractive indexes (n = 1.045 upstream and n = 1.055 downstream) and 2 cm thickness are used, so that the two produced rings are overlapped on the detection surface, giving the $N_{p.e.}$ equivalent to a double radiator thickness. This is schematically represented in Figure 2.10. The reached resolution is
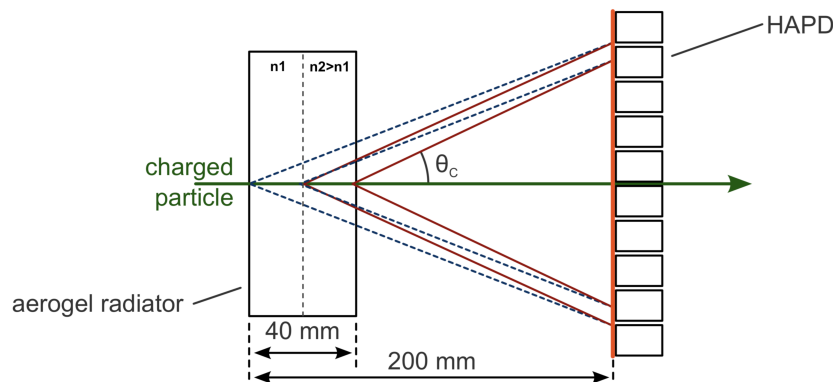
Figure 2.10: A schematic drawing of the Aerogel Ring-Imaging CHerenkov and the proximity focusing system with non-homogeneous dual-layer aerogel is shown. The two rings coming from the different aerogel layers, with an appropriate choice of the refractive indices totally overlap on the photon detector surface.

$\sigma_{\theta_C} \sim 16$ mrad, optimized for charged tracks with momentum larger than 3.5 GeV/c, but it doesn't show significant degradation also for lower momentum tracks. The observed ARICH performances allows for a 5σ separation between kaons and pions of $0.4 - 4$ GeV/c momenta, and a 4σ separation between pions, muons and electrons with momenta smaller than 1 GeV/c.

2.3.5   The Electromagnetic Calorimeter

The Electromagnetic Calorimeter (ECL) is a homogeneous highly segmented calorimeter, composed by Thallium-doped Caesium Iodine CsI(Tl) crystals. Belle II uses the same crystals of the Belle calorimeter, but has a complete upgraded readout electronics, needed to cope with the SuperKEKB increased luminosity.

The main tasks of the calorimeter are:

- detection of photons with high efficiency, and measuremnt of their energy and angular coordinates;

- particles identification;

- generation of the proper signal for trigger;

- on-line and off-line luminosity measurement.

Particles penetrating the crystals of the ECL generate photons either through direct ionization and excitation or electromagnetic/hadronic showers. Showers are associated with a neutral particle, if they are not matched to a track provided by the tracking detectors. The lateral extent of showers supplies an additional identification criterion, since showers generated by hadrons (hadronic showers) are broader compared to electromagnetic showers generated by photons or electrons.

The ECL is composed by an array of 8736 crystals, where each element has a size of 6 cm × 6 cm × 30 cm and a radiation length of $16.1X_0$. CsI(Tl) was chosen as the scintillation crystal material for the Belle calorimeter due to its high light output, relatively short radiation length, good mechanical properties and moderate price. The ECL is subdivided into three regions, the barrel region, the forward and the backward region, and covers about 90% of the solid angle in the center-of-mass system, with an angular acceptance of $12.4° < \theta < 155.1°$, as show in Figure 2.11. The barrel region is extended for 3 meters and has an inner radius of 1.25 m. The annular end-cap regions have the internal base at z = 1.96 m (forward) and z = -1.02 m (backward) from IP. Crystals are assembled in a non perfect projective geometry in order to avoid gaps between adjacent elements pointing to the interaction region, as shown in Figure 2.11. However, two gaps of $\sim 1°$ between the barrel and the endcaps regions to allow the passage of the cables of internal sub-detectors are present.

The scintillation light is detected by a pair of 10 mm × 20 mm Hamamatsu S2744-08 photodiodes are glued at the external basis of each crystals with a 1 mm plexiglass plate. Each photodiode terminates in a preamplifier producing an independent signal and the two pulses are then summed at an external shaper board. The relatively long decay time of scintillation in CsI(Tl), roughly 1 μs, in presence of the much higher background level with respect to Belle produces a not negligible overlapping of pulses from neighbouring background events (pile-up). In order to deal with this issue, a new read-out electronic has been implemented, which samples the photodiode signals in 16 points and then fits the signal shape with a predefined proper function.

The overall structure is flushed with dry air to provide a low humidity (5%) environment for the crystals, while the heat generated by the preamplifiers (about 3 kW in total) is extracted by a water cooling system.

The light output yield of the crystals is roughly 5000 photo-electrons per 1 MeV of deposited energy, while the average equivalent noise is at the level of 200 keV. The energy resolution of the ECL is given by:

$$\frac{\sigma_E}{E} = \sqrt{\left(\frac{0.066\%}{E}\right)^2 + \left(\frac{0.81\%}{\sqrt[4]{E}}\right)^2 + (1.34\%)^2}$$

where E is the energy in GeV [113]. For instance, it means $\sigma_E/E \sim 2\%$ at 100 MeV and $\sigma_E/E \sim 1.4\%$ at 4 GeV. The angular resolution is $\sigma_\theta \sim 13$mrad at low energy and $\sigma_\theta \sim 3$mrad at high energies.

2.3.6 The K_L and Muon Detector

The K_L and muon detector (KLM) is located outside the superconducting coil, and it is used to identify particles that are not absorbed into the inner detectors. The barrel region covers the polar angle range of $(37° < \theta < 130°$, measured at the level of the innermost layer. Adding the endcaps, it extend from 20° to 155°.

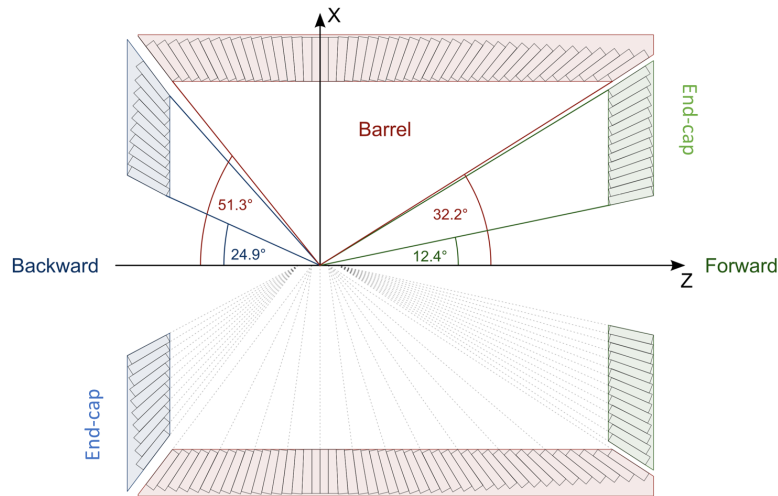It is composed of an alternating sandwich of 4.7 cm thick iron plates and active detector

Figure 2.11: Overview of the ECL. Green and blue regions are the forward and backward end-caps, respectively, while in red is the barrel part. The non projecting geometry pointing to the IP is illustrated in the half bottom part. Figure adapted from [114]

elements, as shown in Figure 2.12. The iron structure of the KLM provides 3.9 interaction lengths λ_0 in addition to the 0.8 interaction lengths X_0 of the calorimeter, in which K_L mesons can shower hadronically. Iron elements act also as magnetic flux returns for the tracking solenoid. The outermost barrel detector layers of KLM are Resistive Plate Chambers (RPC): a proportional gas chamber used in streamer mode with a dielectric plate between the electrodes to prevent the propagation of sparks and so increase the spatial resolution. The signal is read by metallic strips on one side of the chamber. Each KLM module is made of two coupled RPC, with independent power supply and orthogonal strips configuration. Differently from Belle, as the RPCs have a too long dead time to sustain the higher expected background rate, in the endcaps region and in the two innermost barrel layers of the KLM, two orthogonal layers of scintillator strips coupled with silicon photo-multiplier (SiPM) are used as they are tolerant to higher rates [115].

The KLM is used to identify K_L mesons and muons with a momentum above ~ 0.6 GeV. To reconstructs K_L, all the KLM hits within a 5° opening angle cone from IP are clustered, and matched with eventual ECL clusters within a 15° cone. The information of the KLM cluster, the associated ECL clusters and any closest track are then passed as inputs to a Boosted Decision Tree (BDT) to determine the probability that the given KLM cluster is originated by a K_L. An identification efficiency of up to 80% at 3 GeV is achieved with this method.

The typical momentum range of muons produced at Belle II is such that they are most often low ionizing, and can traverse the ECL and even the KLM iron plates with minimal energy loss with no showers. Thus, the muon hits in the KLM matched to tracks in the CDC provide a useful feature for the discrimination between muons and other charged hadrons, particularly pions, that do generate hadronic showers within the KLM. The muon detection efficiency plateaus is about
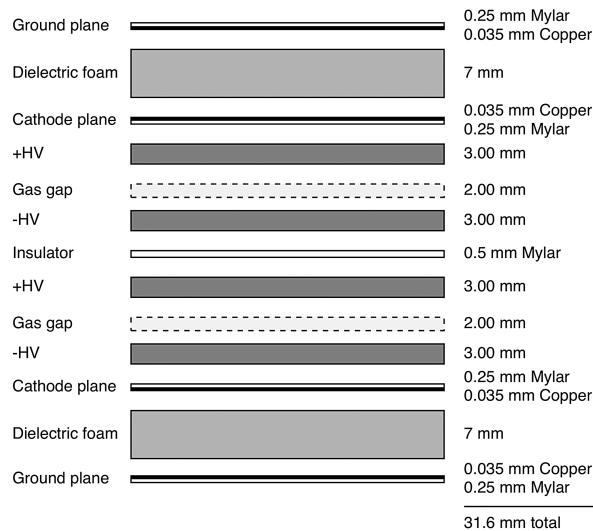
Figure 2.12: Exploded cross-section of an RPC superlayer of the KLM. Picture taken from [110].
.

90% above 1 GeV/c, with a hadron fake rate of about 1.3% due to pions that decay in flight in softer muons.

2.3.7 The solenoid

All of the sub-detectors except for the KLM are surrounded by a superconducting magnet made of NbTi/Cu. The internal volume is a cylinder of a diameter of 3.4 m and a length of 4.4 m. It operates with a 4400 A current and a liquid helium cryogenic system. The solenoid produces a constant solenoid field of 1.5 T, with the field lines parallel to the detector axis (z axis). Electrically charged particles are forced onto helical trajectories due to the Lorentz force generated by the magnetic field. The curvature of the trajectories is used to reconstruct the momentum of particles. The iron structure of the KLM provides the return yoke of the magnetic field, therefore in the region of KLM outside the coil the direction of the magnetic field, and thus the curvature of the tracks is inverted.

2.4 The Data Acquisition and Trigger system

The high luminosity expected at the Belle II experiment requires a robust Data Acquisition (DAQ) system and a flexible Trigger for discriminating the signal events from the background and identify interesting ones. Below, a brief description of how both work is given.
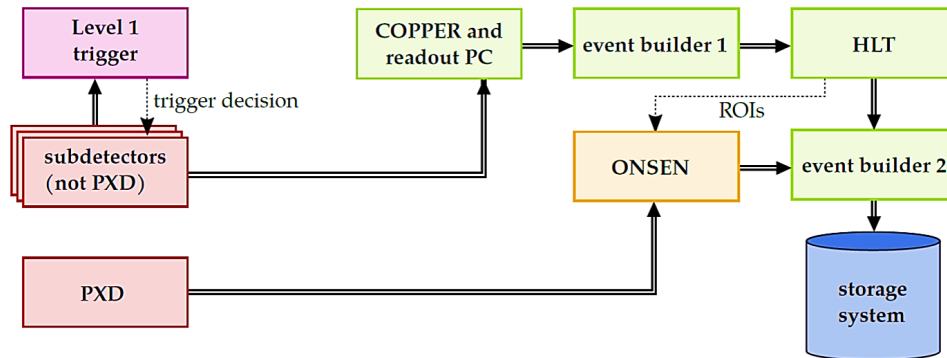
Figure 2.13: Schematic overview of the data flow from the detector readout up to the storage stage.

2.4.1 Data acquisition system

The DAQ system is responsible for transfers data from the detectors front-end electronics upon the trigger decision, through several steps of data processing and finally to the storage system. Figure 2.13 shows the global design of the Belle II DAQ system. The detector front-end boards with digitizers are placed near or inside the detector structure. Data selected by the hardware trigger or Level 1 (L1) trigger are transferred to the Common Pipeline Platform for Electronics Readout (COPPER) modules through long optical fibers using a communication protocol, called Belle2Link. Due to considerations of readout, bandwidth, and latency, the PXD data readout is treated separately from the other sub-detectors until the final event building and storage. Read-out PCs aggregate the data from COPPER modules and forward them to the event builder 1. Here, the data of the sub-detectors are merged to an event. For further filtering the the software High Level Trigger (HLT) performs a full event reconstruction on each event, using the same software as for offline reconstruction. Within that reconstruction without PXD data, particle tracks are extrapolated into the PXD volume and so-called regions-of-interest (ROIs) are defined. The HLT sends the ROI information of the selected events to the PXD online selection nodes (ONSEN) and forwards these events to the event builder 2. Here, the PXD data are received and added to the events. Finally, the events are sent to the online storage system from where they are copied to the offline storage system for data processing and offline analysis. A detailed description of the readout and online selection can be found in [116].

2.4.2 Trigger

The Belle II trigger system is responsible for selecting events of interest and reducing the data rate to a technically manageable level, by rejecting the large background from intra-beam scattering and Bhabha scattering. It is subdivided into the hardware Level 1 trigger and the software-based HLT. The first one removes most of the background events with the use of raw

information from the faster sub-detectors, the second trigger refine the selection with a more exhaustive analysis.

The primary purpose of the Belle II trigger is to select $B\bar{B}$ events with an high efficiency. Considering the high charged track multiplicity in $B\bar{B}$ event final states, the trigger logic is easily implemented based on the number of tracks in the event. However, there are physics processes, e.g., τ leptonic decays and typically dark matter processes, that have a low track number in the final state, and thus are much more challenging in the signal over background selection. In addition, some of these low-multiplicity processes have the same topology as the Bhabha scattering and two-photon $\gamma\gamma$ events, which have a huge cross section compared to the typical signal cross sections (1 nb) at the $\Upsilon(4s)$ center-of-mass energy. On the other hand, even if Bhabha scattering and $\gamma\gamma$ processes are not of particular interest for most of the Belle II physics studies, they are needed to measure the luminosity and to calibrate the detector response. Since the large cross sections and thus the events rates of these processes, a pre-scale factor of 100 or more is applied to these triggers. The total cross sections and the expected trigger rates of several physical processes of interest at the target luminosity of $8 \times 10^{35}\,\mathrm{cm}^{-2}\mathrm{s}^{-1}$ are listed in Table 2.2.

Compared to Belle, the Belle II trigger shows a substantial improvement, giving a better sensitivity and reduced systematic uncertainty for low multiplicity final states. In the following two sub-sections, the two trigger systems are introduced and their working principles are explained.

Physics process	Cross section (nb)	Rate (Hz)
$\Upsilon(4S) \to B\bar{B}$	1.2	960
continuum	2.8	2200
$\mu^+\mu^-$	0.8	640
$\tau^+\tau^-$	0.8	640
Bhabha $(\theta_{lab} > 17°)$	44	350*
$\gamma\gamma$ $(\theta_{lab} > 17°)$	2.4	19*
Total	130	20000

*rate is pre-scaled by a factor of 1/100

Table 2.2: Total cross section and trigger rates with $\mathcal{L} = 8 \times 10^{35}\,\mathrm{cm}^{-2}\mathrm{s}^{-1}$ from various physics processes at $\sqrt{s} = \Upsilon(4S)$.

Level 1 Trigger

The L1 trigger uses various signal from four sub-detectors at low resolution and implements multiple trigger lines [117]. Its implementation follows the same principle adopted for Belle, but with totally new technologies able to support the increased event rates. Furthermore, each component has a Field Programmable Gate Array (FPGA) so that the trigger logic is configurable rather than hard-wired.

The trigger consists of four sub-trigger systems based on the CDC, ECL, TOP, and KLM data. Each sub-trigger system sends information to the Global Reconstruction Logic (GRL) where
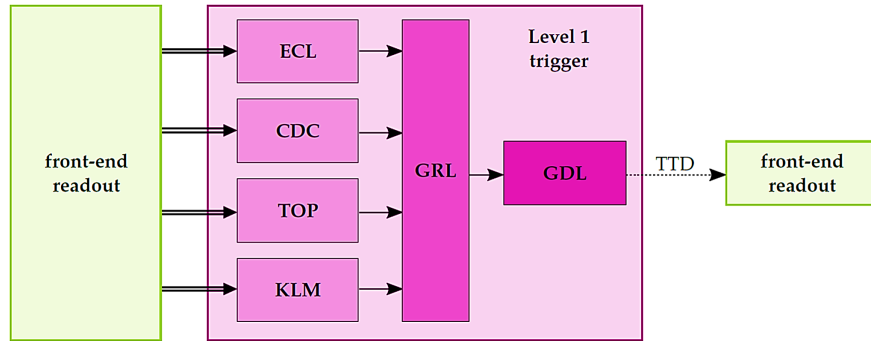
Figure 2.14: The Level 1 trigger system with the four sub-trigger systems map.

.

information of several sub-detector are combined. Its output is sent to the Global Decision Logic (GDL), which is responsible for issuing the trigger signal final-decision logic, when its criteria are satisfied. If the Level 1 trigger decision is positive, the trigger signal is distributed via the Trigger and Timing Distribution (TTD) system back to the front-end readout system of the sub-detectors. Triggered by that signal, the detector readout process for the event is started as described in Sec. 2.4.1. In Figure 2.14 a schematic overview of the L1 trigger logic is represented.

The main sub-detectors that contribute to the L1 trigger decision are the CDC and ECL, although TOP and KLM are also used. The CDC provide two-dimensional and three-dimensional tracking information. The z-position of the main vertex of the events is a strong discriminant for background events with vertices far away from the IP. The ECL provides a trigger signals mainly based on the total energy released in the calorimeter and on the number of the isolated shower. Moreover, the ECL trigger is able to recognize the back-to-back topology of Bhabha scattering with a high purity, which is fundamental for ensuring a high trigger efficiency of low multiplicity processes. The PID sub-triggers give precise timing and hit topology information. The KLM sub-trigger gives muon track information.

The latency of the L1 trigger is about 5 μs. The L1 trigger can sustain a maximum instantaneous rate of 30 kHz. According to Table 2.2, such a rate limit ensures a high efficiency for most of physics targets, mainly hadronic events.

The analyses presented in this work, make use of data selected by using the low-multiplicity Level 1 CDC trigger, also called `ffo` trigger. This trigger selects events with at least two tracks in the CDC acceptance with an opening angle in ϕ-plane of at least 90°.

Starting from the 2020 data-taking period, new Level 1 triggers which include information from the KLM detector have been activated. Among those, particularly interesting for future updates of the analyses described in this work are the `cdcklmX` lines, where `X` is the number of CDC tracks matched with fired barrel KLM (BKLM) sectors, with `X=1,2,3,4`. A KLM sector is fired if the number of layers with hits>0 is greater than 7. The matching is performed

only by the ϕ information of the CDC 2D track and fired KLM sector. As part of this work, the measurement of the efficiency of the Level 1 `cdcklm1` trigger, i.e., the single-muon Belle II trigger, has been performed on the 2020 collision data-set, as described in Appendix A. The use of this and other recently activated triggers, will allow a significant upgrade of the dark Higgsstrahlung analysis, improving considerably the sensitivity in the low mass phase space region, as discussed in Sect. 4.8.

High Level Trigger

The L1 output is forwarded to the HLT for further background rejection based on fully reconstructed objects. The HLT is a software trigger developed to improve the background suppression and to reduce the load of data to be written on permanent storage at a maximum output event rate of 10 kHz. It uses the full information of all sub-detectors except the PXD and performs a fast reconstruction: the events are completely reconstructed with the same software used in the offline analysis (except the PXD information). Then the trigger applies physics requirement to the reconstructed events thus reducing the event rate. After the HLT reduction, the tracks parameter estimate reconstructed with the SVD and the CDC in the fast reconstruction are extrapolated to the PXD layers and the ROI is evaluated. Only the pixels belonging to that region are readout and the selected PXD hits are used to complete the event reconstruction. In conclusion, the full events are build by combining the fast reconstruction events with the PXD data before the definitive storage.

During the early operations of Belle II, the HLT was in pass-through and no software filter was applied to the triggered events, resulting in a very favorable condition to collect events with topologies interesting for dark sector searches, that may be suppressed by the HLT filtering necessary for the higher luminosity runs.

2.5   Software

To process the events recorded by the Belle II detector the Belle II Analysis Software Framework (`basf2`) is used. This analysis package offers a collection of tools to extract physically relevant information from reconstructed particle tracks, particle identification (PID) likelihoods, calorimeter clusters and informations from KLM. The architecture of `basf2` follows a modular set-up. A data processing chain is constructed by defining so-called paths serving as containers for modules. Each module is designed to fulfill a specific task (e.g. reading/writing data, tracking, performing a full detector simulation etc.). The modules inside a path are processed in a linear order one after another. The data is stored in a common storage called DataStore in order to transfer it between modules. Input data is processed on an event by event basis. For each event all modules specified in the path are executed, while input and generated data are stored in the DataStore. When the last module has been executed, the DataStore is cleared and the next event is processed independently from the former one. The output of the offline reconstruction

is a summary of the reconstructed particles suitable for physics analyses known as mDST.

A relevant part of all physics analyses at Belle II requires the generation and analysis of simulated Monte Carlo events in addition to the analysis of the real detector data. This task involves the creation of physics events by means of a set of decay tables listing all the possible decay processes, their branching ratios and amplitudes. Those events are then passed to a full detector simulation, simulating the passage of the particles through the detector material of the various sub-detectors. Each subdetector has a digitizer assigned, that uses the input of the full detector simulation in order to perform a realistic detector response simulation. The digitized data is then passed to the reconstruction stage, where the input data for the physics analyses is created. The Monte Carlo chain and the real data chain share the same reconstruction and analysis procedures. The full detector simulation in `basf2` is based on Geant4, the standard toolkit for the simulation of particles traversing matter in the high energy physics community [118].

In the reconstruction phase, information on the detector conditions (alignment and calibration constants) during the data acquisition is taken into account. Those constants are calculated on the data itself by using well-known physics processes with a distinct topology that allows to measure, e.g., the displacement of the different detector layers among each other. The process of calibration and alignment is repeated regularly on the recorded data and the result is fed into a database, which is used for the reprocessing of the data.

2.6   The Belle II operations

The SuperKEKB and Belle II operations schedule can be subdivided in three main phases:

Phase 1 During the 2016 the accelerator rings have been commissioned without the final focusing system at the interaction point and without the Belle II detector placed in. Single beam studies were performed with the main goal to ensure that beam background levels are safe to install Belle II, and to provide feedback for the accelerator optimization on how the machine parameters affect background levels;

Phase 2 A second commissioning phase was performed during the 2018, with the final focusing and the Belle II detector in place, but without the full vertex detector installed. Only two ladders of the PXD and four ladders of the SVD were installed, one for each layer. Furthermore, additional background monitors were installed at the core of the Belle II detector in order to measure the beam backgrounds. The first physics collisions were detected on April 26th 2018, and the data taking continued until July 2018, with a maximum achieved instantaneous luminosity of $\sim 0.5 \times 10^{34}\,\mathrm{cm}^{-2}\,\mathrm{s}^{-1}$. A total integrated luminosity of $\sim$0.5 fb^{-1} was collected [119], as shown in Figure 2.15. This data-set has been used to prove the understanding of the detector through performance measurements and several rediscoveries. Furthermore, Phase 2 data have been used for dark sector searches as it is the case for
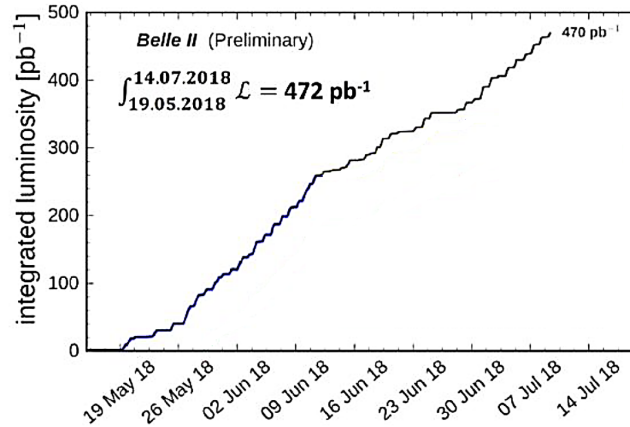
Figure 2.15: The integrated luminosity collected during the Phase 2 commissioning run in 2018.

the work presented in this thesis in Chapter 3 for the invisible Z' search.

Phase 3 In March 2019, collisions started with an almost complete detector[2]. On June 2020, the new world record for a colliding-beam accelerator instantaneous luminosity has reached with a value of $2.2 \times 10^{34} \, \mathrm{cm^{-2} \, s^{-1}}$. During the 2019 Belle II collected an integrated luminosity of $\sim 10 \, \mathrm{fb^{-1}}$, while at the end of 2020 it reach a total value of $\sim 90 \, \mathrm{fb^{-1}}$, as shown in Figure 2.16. The 2019 data-set has been used for the work presented in this thesis in Chapter 4 on the Dark Higgstrahlung search. Starting on the 2020 more inclusive L1 trigger lines have been activated, which would allow to significantly increase the signal efficiency for the analyzes presented in this work. In Appendix A, the study of the efficiency of the new CDC-KLM line, i.e., the Belle II single muon trigger, is presented. Currently, a part of the PXD is still missing and a a shutdown in 2022 is foreseen in order to install the full PXD. A total integrated luminosity of $\sim 500 \, \mathrm{fb^{-1}}$ is foreseen by the 2022 shutdown. The final goal of Belle II is to take physics data, while steadily increasing the instantaneous luminosity with the application of the final nano-beam scheme, and collect $50 \, \mathrm{ab^{-1}}$ of data within the next ten years. Such a large dataset will be the main ingredient in reaching the benchmarks physics of flavor and BSM searches.

---

[2]The PXD inner layer has one broken module the outer one has just two ladders, in such a way that the whole azimuthal angle is covered.
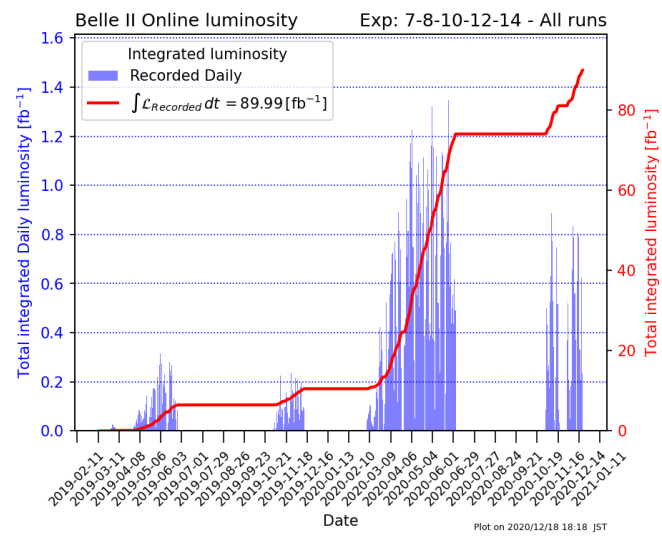
Figure 2.16: The integrated luminosity collected during the early Phase 3 operations.

Chapter 3

Search for an invisible Z' in $e^+e^- \rightarrow \mu^+\mu^-$ and missing energy events

In this Chapter, the search for an invisibly decaying Z' boson produced in the $e^+e^- \rightarrow \mu^+\mu^-Z'$, $Z' \rightarrow$ invisible process by using the data collected by the Belle II experiment during the 2018 data-taking period is presented. As an extension of this measurement a Lepton Flavour Violating (LFV) Z' has been searched into the $e^+e^- \rightarrow \mu^{\pm}e^{\mp}Z'$, $Z' \rightarrow$ invisible process, too. No anomalies have been observed in data, and 90% CL upper limits on the cross section and the coupling constants have been set.

3.1 Analysis overview

One of the simplest ways to extend the SM content and include new physics is by adding an extra $U(1)'$ group according to the $L_\mu - L_\tau$ symmetry (see Sect. 1.2.4). Such a $U(1)'$ group of symmetry would give rise to an extra gauge boson, called Z'. Within the SM content, it would couple only to μ and τ (and the respective neutrinos ν_μ and ν_τ), with a new coupling constant indicated with g'. Such a boson could be produced at an e^+e^- collider in the process $e^+e^- \rightarrow \mu^+\mu^-Z'$ (see Fig. 1.15), thus being radiated from one of the final state muons. Among the possible decay modes, the case of a Z' invisible decay, i.e., to SM neutrinos or DM if kinematically accessible, is investigated here. The state of the art for similar searches has already been presented in Sect. 1.4.1: the only similar measurements for a low mass Z' boson related to the $L_\mu - L_\tau$ symmetry was performed by the BaBar experiment for a Z' decaying into muons [90], while the invisible decay topology is being investigated here for the first time.

The search presented in this Chapter has been performed on the data-set collected by the

Belle II experiment at the nominal center-of-mass energy ($\sqrt{s} = 10.58\,\text{GeV/c}^2$) during the 2018 data-taking period, so-called Phase 2. The data-set useful for the analysis corresponds to an integrated luminosity of $276.5\,\text{pb}^{-1}$. The final state consists of only two opposite charge muons plus missing energy. A signal production would result in a bump in the distribution of the mass recoiling against the two-muon system M_{rec}, defined as:

$$M_{rec} = -\sqrt{-M_{rec}^2}, \text{ if } M_{rec}^2 < 0 \quad \text{or} \quad M_{rec} = \sqrt{M_{rec}^2}, \text{ if } M_{rec}^2 > 0 \tag{3.1}$$

with:

$$M_{rec}^2 = s + M_{\mu\mu}^2 - 2\sqrt{s}E_{\mu\mu} \tag{3.2}$$

where $M_{\mu\mu}$ is the invariant mass of the two-muon system and $E_{\mu\mu}$ is the sum of the two muon energy in the CMS. Indeed, for signal events, the four-momentum of the recoiling system coincides with the four-momentum of the Z' boson, so the invariant mass of the recoiling system would peak at the value of the Z' mass. In the following, the invariant mass of the recoiling system is simply referred to as "recoil mass" while the mass of the two-muon system is called "dimuon mass".

Assuming the $L_\mu - L_\tau$ model the predicted cross section for the signal process is quadratic in the coupling constant g' and decreases at higher Z' masses, vanishing when approaching $\sqrt{s}$. The expected decay branching ratio to invisible, according to the $L_\mu - L_\tau$ model, has been discussed already in Sect. 1.2.4. In case of kinematic accessible decay modes to dark matter particles χ ($\bar{\chi}$), such as $Z' \to \chi\bar{\chi}$, one can expect that $BF(Z' \to \chi\bar{\chi}) = 1$. The simulated signal cross section as a function of the Z' mass, assuming a coupling constant of $g' = 0.01$, is shown in Figure 3.1.

The main backgrounds for the analysis come from SM processes producing final states with two muons and missing energy that can mimic the signal signature, namely $e^+e^- \to \mu^+\mu^-(\gamma)$ with one or more photons lost due to inefficiency or being out of acceptance, $e^+e^- \to \tau^+\tau^-(\gamma)$ with $\tau \to \mu\bar{\nu}_\mu\nu_\tau$ or $\tau \to \pi\nu_\tau$ (due to pions misidentification in muons) where the missing momentum comes from neutrinos, and $e^+e^- \to e^+e^-\mu^+\mu^-$ (i.e., two-photon processes) where electron and positron usually are outside the detector acceptance. The interesting events are selected as those with two identified muons and no reconstructed photons above a minimum energy in the direction opposite to the dimuon momentum. Furthermore, the transverse momentum of the dimuon system is required to be above some threshold, as this selection is very effective against $\mu^+\mu^-(\gamma)$ and $e^+e^-\mu^+\mu^-$ backgrounds. Finally, an additional selection, referred to as "τ suppression" is performed in order to further suppress the $\tau\tau(\gamma)$ background, which is found to be dominant for most of the mass range. Details of the event selection and the background suppression optimization are given in Sect. 3.3 and 3.5.

Due to the smallness of the expected background at the end of the selections, a counting procedure, as opposed to a fitting technique, has been chosen. Indeed, over a large part of the recoil mass range there is no enough statistics to evaluate the background size and shape. The procedure, consists of the definition of a set of mass windows in the recoil mass distribution as
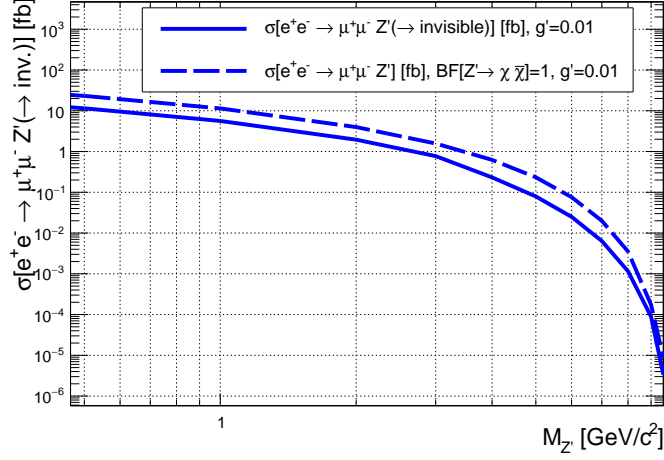
Figure 3.1: Numerical cross sections for $e^+e^- \to \mu^+\mu^- Z'(\to \text{invisible})$ obtained with MadGraph. The solid line assumes the $L_\mu - L_\tau$ predicted rates for $Z' \to$ invisible while the dashed line assumes $BF[Z' \to \text{invisible}]=1$. For Z' masses approaching the CMS energy $\sqrt{s}$, the cross section vanishes, limiting the sensitivity to the parameter space region for $M_{Z'} > 8$ GeV/c^2.

described in Sect. 3.4, in which the number of the observed events and of expected background can be computed.

As a blinded analysis strategy has been adopted, in order to avoid the experimenter's bias, the selections optimization has been performed by using only simulated samples and control samples. The Monte Carlo predictions have been checked before unblinding data with an extensive use of control samples, from which correction factors and related systematic uncertainties to both the background and the signal efficiency have been inferred, as shown in Sect. 3.6.

After the unblinding, no anomalies have been observed in data, with all the results being below 3σ local significance. The 90% credibility level (CL) upper limits on the cross section have been computed using a Bayesian procedure as described in Sect. 3.7, and results have been translated into 90% CL upper limits on the coupling constant g'.

As an extension of the above search, the existence of a LFV Z' boson has been investigated too. Specifically, this search focused on a LFV Z' produced in the process $e^+e^- \to e^\pm\mu^\mp Z'$, $Z' \to$ invisible. The experimental signature consists of two oppositely charged tracks with different flavours plus missing energy. Due to the non-availability of a robust signal generator, a model-independent search has been performed by using the same selection criteria of the above ($L_\mu - L_\tau$) Z' search, aside from the obvious requirement to have an electron instead of a muon in the final state. The search for a LFV final state is expected to have a small SM background: the dominant contribution after the final selection is $e^+e^- \to \tau^+\tau^-(\gamma)$ with taus going to one-prong muon and one-prong electron. In the case of signal events, a bump in the

distribution of the mass recoiling against the $e\mu$ system is expected at the mass value of the LFV Z' boson. In the rest of this Chapter, the Z' produced in association with a $\mu\mu$ pair is denoted with " standard Z' " , while the Z' produced with a $e\mu$ pair is denoted as " LFV Z' ".

The results obtained in this work using the data-set collected by Belle II during 2018 have been published in Ref. [1].

3.2   Data sets

The results presented in this Chapter are based on the data collected by Belle II during the 2018 commissioning run, also referred to as Phase 2. As mentioned in Sect. 2.6, during Phase 2 the accelerator instantaneous luminosity was well below the design one and the VXD was not fully installed. A total integrated luminosity of $479.8\,\mathrm{pb}^{-1}$ (measured by using with Bhabha events [119]) was achieved during this period. The interesting events to the standard Z' analysis have been selected by the low-multiplicity Level 1 CDC trigger, also called `ffo` trigger (see Sect. 3.6.2). Differently, for the LFV Z' analysis, the ECL based `hie` trigger has been used (see Sect. 3.6.2). Because of the trigger configuration and the data quality selections used for the analyses, the effective available integrated luminosity was reduced to $276\ \mathrm{pb}^{-1}$.

As mentioned in the previous Section, a blind analysis strategy has been adopted. Therefore, the selection optimization has been performed by using only simulated Monte Carlo samples. For the standard Z' search, samples with Phase 2 geometry and beam background, produced with the 02-00-01 `basf2` release and with the MadGraph generator [120] according to the model described in Sect. 1.2.4 have been used. A total of 16 samples of 20k events each for Z' boson masses from $0.5\ \mathrm{GeV}/c^2$ up to $8\ \mathrm{GeV}/c^2$, with a mass step size of $0.5\ \mathrm{GeV}/c^2$, has been produced. For the LFV Z' case a robust signal generator was not available, thus a model-independent search has been performed, as explained later.

For the background related studies the MC samples with Phase 2 geometry and beam background listed in Table 3.1 were used. Such samples are used for both standard and LFV Z' searches.

Table 3.1: Phase 2 MC samples used for background studies and the equivalent integrated luminosity.

Process	$\int L\,dt\ [\mathrm{fb}^{-1}]$
$e^+e^- \to \mu^+\mu^-(\gamma)$	8.711
$e^+e^- \to \tau^+\tau^-(\gamma)$	40.044
$e^+e^- \to e^+e^-\mu^+\mu^-$	2.116
$e^+e^- \to \pi^+\pi^-\gamma$	65.359
$e^+e^- \to e^+e^-$	0.033
$e^+e^- \to e^+e^-e^+e^-$	1.259

3.3   Event reconstruction

The interesting events have been reconstructed by requiring two opposite charge tracks coming from IP, satisfying the following criteria which define the *CleanedTracks* selection:

- the longitudinal distance dz of the perigee of the track helix from the origin must satisfy the condition: $|dz| < 2$ cm;

- the distance dr of the perigee of the track helix from the origin in the transverse plane $r - \phi$ must be: $|dr| < 0.5$ cm;

- the track must have at least one hit in the CDC: $nCDCHits > 0$.

The reconstruction proceeds by performing a muon identification by applying a loose selection based on the ECL information:

- as the muons are not expected to produce electromagnetic showers, the energy deposition within the ECL *clusterE* must be low: $clusterE < 0.75$ GeV;

- the ratio of the energy deposit and the muon momentum p in the laboratory frame must satisfy the condition $clusterE/p < 0.5$

These two requirements are necessary in order to reject the electron candidates. Since the KLM was still in a commissioning phase during the 2018 data-taking period, it wasn't possible to use it to further select the muon candidates and distinguish them from pions.

The selected tracks are then combined to form a dimuon candidate and the event is accepted only if the total number of *cleanedTracks* in the event is less than 4. Then, the recoil system against the dimuon candidate with respect to the center-of-mass momentum is reconstructed, being the Z' candidate for that event.

Additionally, the Rest Of Event (ROE) with respect to the dimuon candidate is reconstructed. It is defined as the set of tracks and ECL clusters that are not used to reconstruct the dimuon particle. In order to clean the ROE from the beam background, a track in the ROE is required to have at least 1 hit in the CDC, while an ECL cluster in the ROE is required to have an energy larger than 100 MeV.

As a last step, the kinematic information of the photon closest to the recoil momentum are computed: the angle with respect to the Z' candidate momentum, the polar angle and the energy in both the laboratory and CM frames are computed. This is needed in order to be able to veto events in which the recoil momentum can be associated to a photon, as it will be described in Sect. 3.5. Furthermore, the information on the most plausible π^0 candidate in the event are computed.

LFV Z' to invisible

For LFV Z', the same event reconstruction is applied as far as the *CleanedTracks* selection is concerned. For the particle identification, one track is required to be identified as a muon, as

explained for the standard Z' case, and a second track to be identified as an electron according to the following ECL-based selection:

- $clusterE > 1$ GeV

- $0.7 < clusterE/p < 1.3$

Then the $e\mu$ candidate is obtained by combining the electron and muon tracks (requiring that the two tracks have an opposite charge) and the reconstruction chain continues as for the standard Z' case.

After reconstruction, the events undergo a further selection as described in Sect. 3.5.

3.4   Signal studies

This search relies on a counting experiment technique: the number of events are counted in recoil mass windows corresponding to a given Z' mass hypotheses and compared to the background yield expectations. In order to do that, a binning scheme was defined on the basis of the recoil mass distributions of the simulated signal samples. As opposed, a different approach would be fitting the recoil mass distribution. This would have improved the sensitivity to a hypothetical observed signal; however, due to the low statistics expected after the final selections (see Sect. 3.5), this option had to be discarded.

The binning scheme on which the counting technique is applied has been optimized as a function of the signal recoil mass resolution. To find the width of the signal distribution an unbinned maximum likelihood fit has been performed on the recoil mass distribution of the signal samples generated for various Z' masses. The signal shape is modeled by a Probability Density Function (PDF) which includes two contributions:

- a Crystal Ball (CB) shape function [121], which allows to describe the rightmost tail of the recoil mass distribution due to Initial State Radiation (ISR) contribution;

- a Gaussian, added to model the remaining part of the distribution and to account for the reconstruction resolution effect.

The resulting PDF consists of five parameters: σ_{CB} and σ_{Gauss}, being the width of the CB and the Gaussian respectively; α_{CB} and n_{CB}, being the remaining CB parameters; and $frac$, the fraction of each function with respect to the normalized sum of both. The mean of both CB and Gaussian have been set to a fixed value. The recoil mass distribution for some generated signal sample and the corresponding fitted PDF can be observed in Figure 3.2. To cope with the negative values and the double-peaked profile (due to a dip at zero, as a consequence of eq. 3.2; see an an example Fig. 3.4, left side) obtained for the signed recoil mass distribution in case of the $M_{Z'} = 0.5$ GeV/c^2 mass hypothesis, for this value the squared recoil mass M_{rec}^2 has been used.

An overall width for every recoil mass distribution has been computed by taking into account the different contributions of CB and Gaussian as:

$$\sigma_w = \sqrt{frac \times \sigma_{\mathrm{CB}}^2 + (1 - frac) \times \sigma_{\mathrm{Gauss}}^2} \tag{3.3}$$

The resulting weighted widths for every generated Z' mass point are shown in Figure 3.3.

As the recoil mass resolution may differ in real data from what observed in the simulation due to unknown detector effect, it has been validated on data by means of control samples, as will be shown in Sect. 3.6.2.

Then, the mass windows scheme has been computed as a set of contiguous bins of size proportional to the mass resolution values before computed. The optimal bin width is found to be
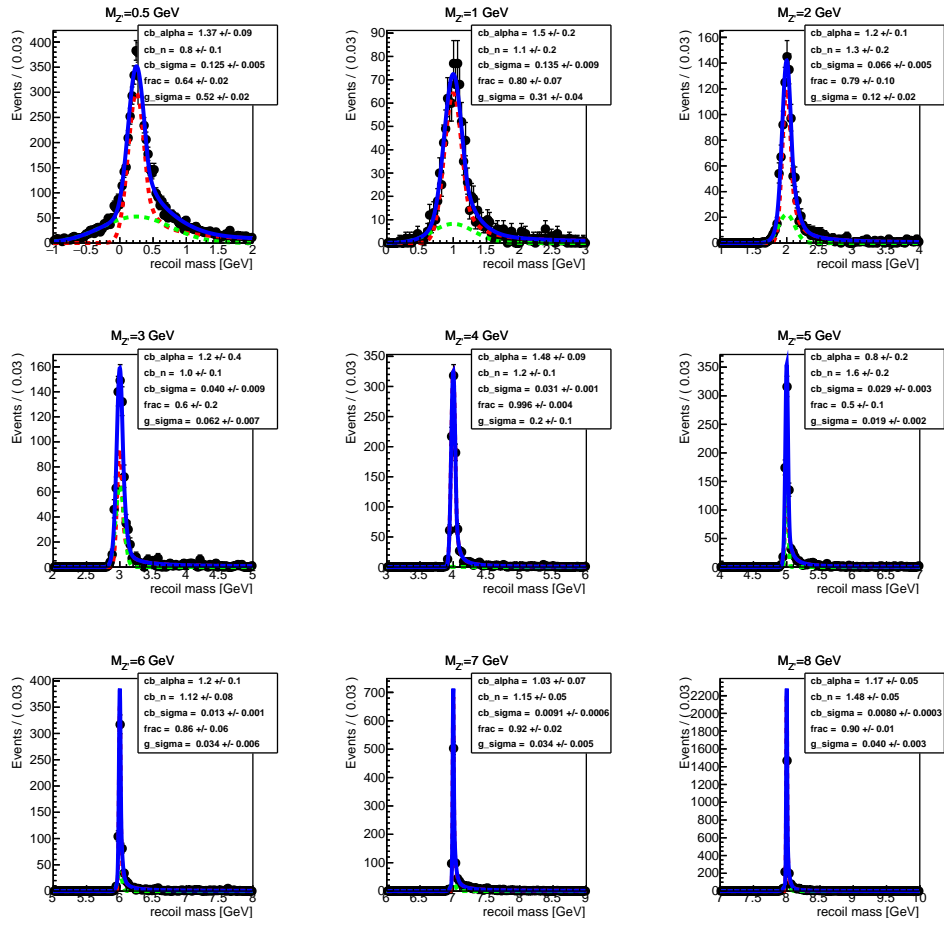
Figure 3.2: Recoil mass distribution and fitted PDF (blue line) for different generated signal samples. The contribution of the CB and the Gaussian function are shown with a red and green dotted line, respectively. The resulting fit parameters are shown in the top right corner of each plot.

a $\pm 2\sigma_w$, as described in Sect. 3.5.2. Mass window widths vary from 1300 MeV/c² at $M_{Z'} = 0.5$ GeV/c² to 53 MeV/c² at $M_{Z'} = 7$ GeV/c², due to the different recoil mass resolution. An additional binning scheme is defined, with a half bin shift on the right with respect to standard one, as a final measurement cross check in order to conveniently cover hypothetical signals located at the border of two contiguous bins.
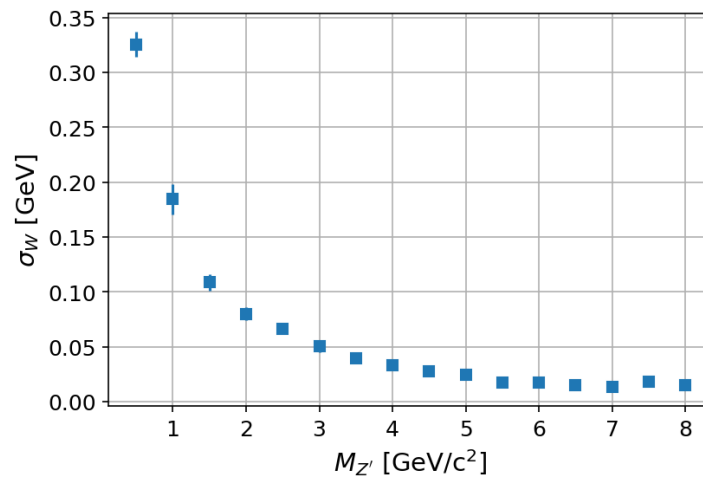
Figure 3.3: Recoil mass resolution computed according to eq. 3.3 as a function of the Z' mass.

3.5   Event selection

To suppress the background sources, a two-level selection has been implemented, as described in this Section. First, a tighter selection, called "generic selection" in the following, then a stronger selection specifically optimized as a function of the candidates mass are applied to each reconstructed event.

3.5.1   Generic selection

Each reconstructed candidate has to satisfy the following criteria:

1. the number of *CleanedTracks* must be exactly two and the opening angle between the two muon candidates in the transverse plane must exceed 90°, in order to emulate the functionality of the CDC trigger: its logical implementation requires two tracks with an opening angle $\Delta\phi$ in the transverse plane larger than 90°. As it is not simulated in the MC samples, this additional selection requirement has to be satisfied to correctly reproduce the data. Furthermore, the same opening angle is required to be less than 172°, in order to have a good control of the systematic effects (see Sect. 3.6.2);

2. a tighter ECL-based muon selection: $0.15 < clusterE < 0.4$ GeV and $clusterE/p < 0.4$;

3. all events with the closest reconstructed photon within a 15° cone from the recoil momentum direction are discarded;

4. the ROE must not contain any physical objects as follows:

   - it must have no additional good tracks; only very poor quality tracks not coming from the IP and not detected by the CDC are tolerated, since they are mainly remnants of beam-induced backgrounds not associated to any physics event;

   - as most of the physical background comes from τ pair production and π^0 are among them the most common τ decay products, a π^0 veto has been setup. Photons in the ROE which pass the beam-background rejection are used to reconstruct the decay $\pi^0 \to \gamma\gamma$. Then, only one π^0 candidate per event is selected by choosing the one with the invariant mass closest to the nominal π^0 mass. The event is then discarded if the following conditions are both satisfied: the mass of the candidate is in the range $125 < M_{\pi^0} < 145\,\mathrm{MeV/c^2}$ and the remaining energy detected in the ROE exceeds 0.20 GeV;

   - the extra energy in the ECL, which is the energy deposit not associated to any particles in the cleaned ROE, is required to be below 0.4 GeV;

5. the polar angle of the muon tracks must be within a restricted barrel ECL angular acceptance for a good cluster-matching efficiency and for a good control of the systematics $(37° < \theta_\mu < 120°)$;

6. the recoil momentum must point to the barrel ECL acceptance region ($33° < \theta_{\text{rec}} < 128°$), to exclude inefficient regions of the detector where photons can pass undetected and mimic the signal recoil. This selection is applied only for recoil masses below 3 GeV/c^2, as for larger masses the photon hypothesis is unlikely;

7. the transverse momentum of the dimuon candidate in the CMS frame must satisfy the requirement $p^T_{\mu\mu} > p^T_{cut}$, where p^T_{cut} is a linearly decreasing function with the recoil mass and its value is 1.03 GeV/c at a recoil mass of 0.5 GeV/c^2 and 0.43 GeV/c at a recoil mass of 9 GeV/c^2. This requirement is efficient in removing the dominating background at very low recoil mass coming from radiative dimuon events $e^+e^- \rightarrow \mu^+\mu^-(\gamma)$ which presents a low $p^T_{\mu\mu}$ behaviour. This cut is anyway superseded by further selection described in Sect. 3.5.2.

The number of background events as a function of the analysis cut number and the background spectrum achieved after the generic selection cuts, as a function of the recoil mass, are shown in Figure 3.4. All the backgrounds are normalized to the integrated luminosity of 276 pb^{-1} and scaled by a trigger efficiency of 0.79 (estimated as discussed in Sect. 3.6). After applying the above selections, it turns out that τ pair events ($\tau^+\tau^-(\gamma)$) are the main source of background for a large part of the available phase space. Radiative dimuon events ($\mu^+\mu^-(\gamma)$) contribute at very low recoil masses, while four lepton final state events ($\mu^+\mu^-e^+e^-$) dominate above 7 GeV/c^2. The other sources of background are found to be negligible.

The signal efficiency for each generated Z' mass hypothesis, computed as the ratio between selected and generated events and also multiplied by the measured trigger efficiency (79%), is shown in Figure 3.5 as a function of the analysis cuts listed above.
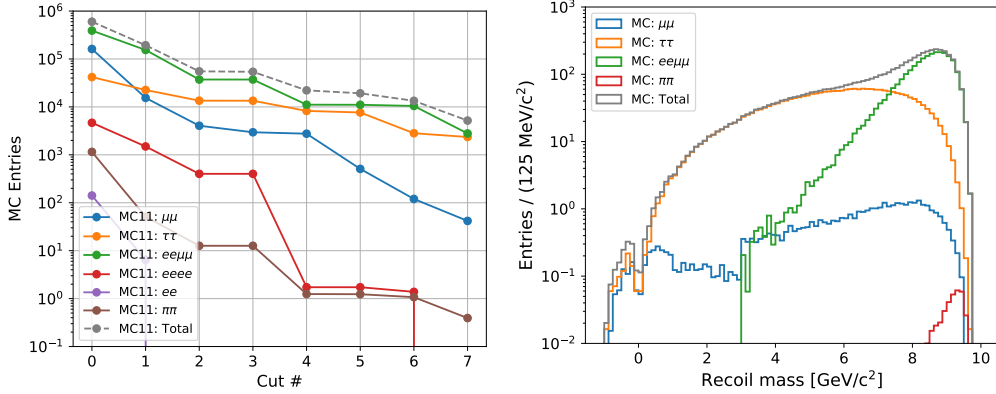
Figure 3.4: Left: Surviving background events as a function of the cut number. Cut 0 corresponds to having applied the reconstruction selection, only. Right: Background spectrum achieved after the generic selection cuts as a function of the recoil mass. The background has been normalized to an integrated luminosity of 276 pb^{-1} and scaled by a trigger efficiency of 0.79.
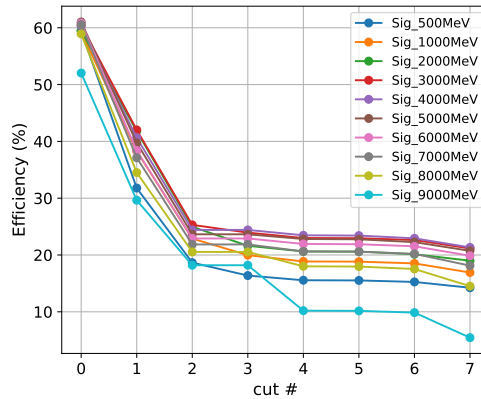
Figure 3.5: Signal efficiencies for different Z' masses as a function of the cut number. Cut 0 corresponds to having applied the reconstruction selection, only. Signal efficiencies take into account the trigger efficiency (79%).

3.5.2 τ suppression and selection optimization

In order to suppress the surviving τ pair background, a further selection strategy, called "τ suppression", has been setup. The selection has been optimized with events grouped according to the mass windows scheme described in Sect. 3.4: recoil mass windows width have been computed as multiples of the recoil mass resolution, according to the results from Sect. 3.4. Optimal window size values turn out to be $\pm 2\sigma$, as verified later.

In order to discriminate signal from background, it was exploited the fact that the Z' production is a Final State Radiation (FSR) process from a muon leg (see Figure 1.15), while the invisible momentum in τ pair events, which can mimic the presence of the signal, comes from neutrinos from τ decays on both muon legs. Kinematic variables that can quantify this behaviour in the event topology have been searched and used to suppress background. An MVA software package (`scikit-learn` Python library [122]) was used to only rank the variables in order of signal/background discriminating power. Being this a very initial stage of the Belle II experiment life, a more intensive use of MVA algorithms was avoided in order to allow a more easy evaluation of systematic uncertainties and detector effects. The most discriminating variables and easiest to use in terms of linear cuts turn out to be the transverse component of the recoil momentum (which coincides with the Z' momentum in the signal case) with respect to the maximum and minimum momentum muon directions p_{max}^{T}, p_{min}^{T}, and the transverse momentum of the dimuon candidate $p_{\mu\mu}^{T}$. All these variables are computed in the CMS frame. Bidimensional distributions of p_{max}^{T} versus p_{min}^{T} and distributions of $p_{\mu\mu}^{T}$ for three sample mass windows (centered at 2, 5 and 7 GeV/c^2 respectively) are shown in Figure 3.6 for signal and background. It must me remarked that a loose cut on $p_{\mu\mu}^{T}$ has already been applied at the level of the generic cuts.

An optimal separating line $y = mx + q$ in the $p_{max}^{T} - p_{min}^{T}$ plane and an optimal threshold cut on the $p_{\mu\mu}^{T}$ distribution were searched by independently varying the corresponding three
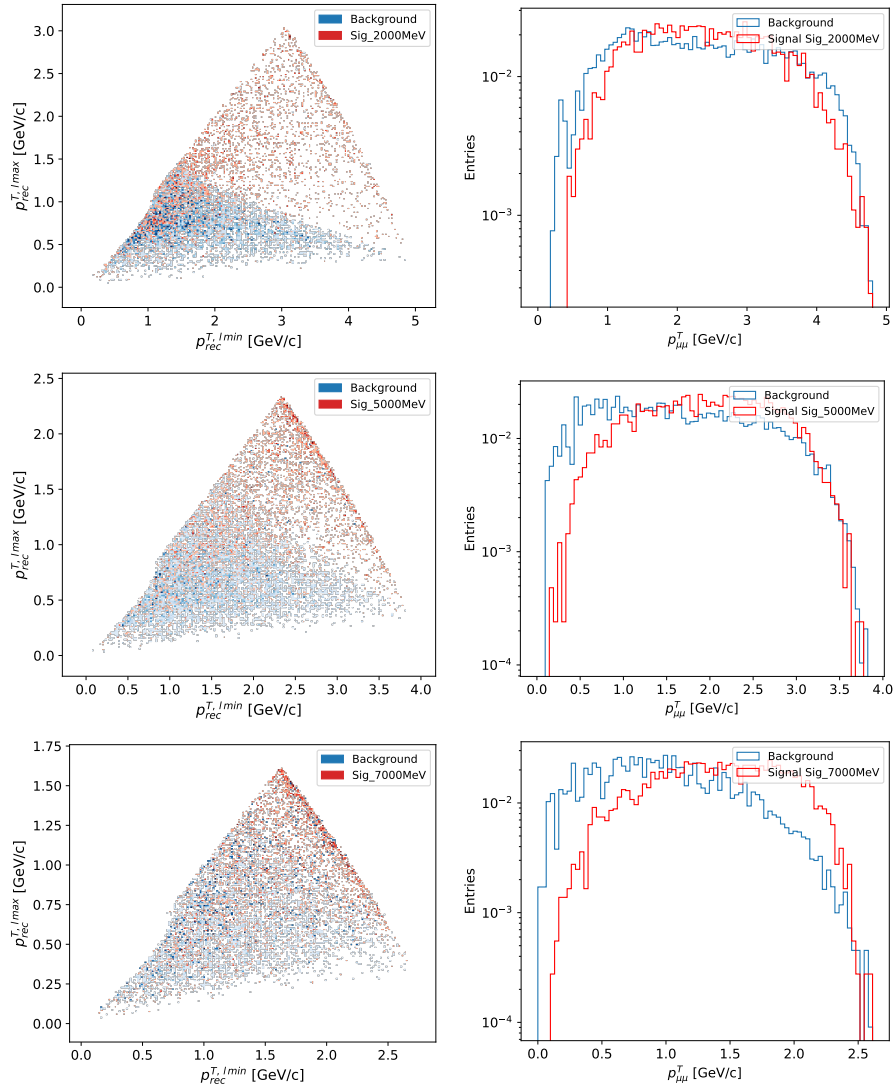
Figure 3.6: $p_{rec}^{T,lmax}$ vs $p_{rec}^{T,lmin}$ (left) and $p_{\mu\mu}^{T}$ (right) distributions for $M_{Z'}$=2, 5 and 7 GeV/c^2. The signal is in red and the background in blue.

parameters: two for the separating line (m and q) and the cut threshold on $p_{\mu\mu}^{T}$. The applied selection is then in the form: $p_{max}^{T} > m^{OPT} \cdot p_{min}^{T} + q^{OPT}$ and $p_{\mu\mu}^{T} > p_{\mu\mu}^{T}{}^{OPT}$ where the upscript "OPT" marks the optimal parameters. The optimization has been performed by varying the parameter values simultaneously in nested loops and looking, numerically, for the maximum Punzi Figure of Merit (FOM$_{\text{PUNZI}}$) [123]. The FOM$_{\text{PUNZI}}$ estimator takes into account the signal efficiency ϵ_{sig}, the number of surviving background events N_{bkg} and the desired Confidence Level (C.L.) for an exclusion limit (in terms of number of sigmas a corresponding to one-sided Gaussian tests at the given C.L.):

$$\text{FOM}_{\text{Punzi}} = \frac{\epsilon_{\text{sig}}}{a/2 + \sqrt{N_{\text{bkg}}}} \qquad (3.4)$$

where a was set to 1.64, as a 90% C.L. was chosen. With respect to other most common figures of merit, the Punzi FoM has the advantage to be independent from the unknown signal cross section on which the limit has to be measured.

Figure 3.7 shows, as an example, the bidimensional $p_{max}^T - p_{min}^T$ distributions after the optimal $p_{\mu\mu}^T$ cut, with the optimal separation line superimposed. Events above the optimal line were classified as signal, while below as background. The background rejection factor achieved by the τ suppression procedure only, and the Punzi FOM as a function of the recoil mass are displayed in Figure 3.8.
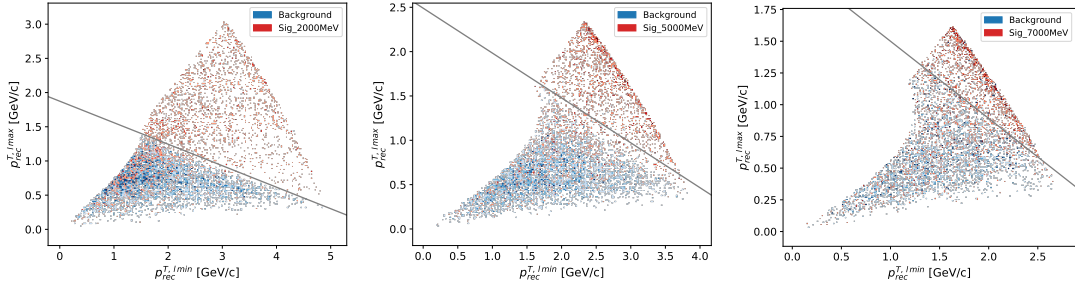
Figure 3.7: p_{max}^T vs p_{min}^T distributions after the optimal $p_{\mu\mu}^T$ cut for $M_{Z'} = 2, 5, 7$ GeV/c^2 signal (left, middle and right respectively, red) and for background (blue). The optimal separation line is superimposed.
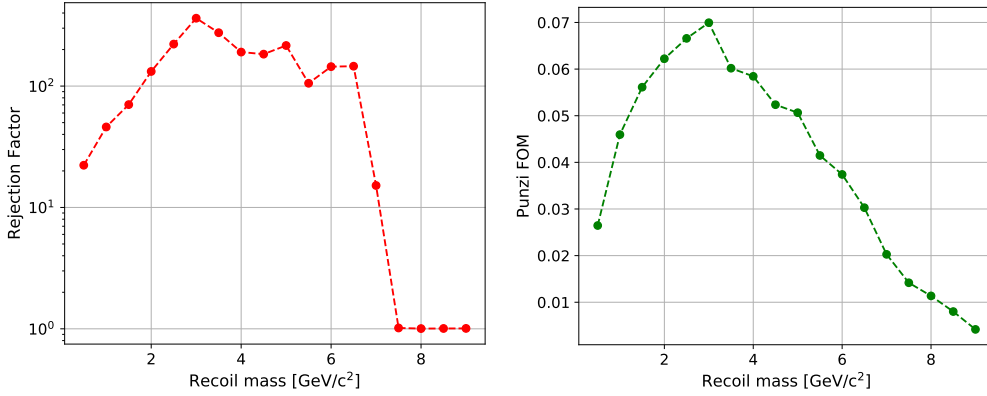
Figure 3.8: The background rejection factor from the τ suppression procedure only (left) and the Punzi FOM as a function of the recoil mass after the optimization process (right).

The optimization was performed only for the recoil mass within mass windows corresponding to the generated signal samples (see Sect. 3.2). In order to get the cut values for a generic recoil mass, the m and q parameters and the values of the $p_{\mu\mu}^T$ cut were independently fitted (neglecting

mutual correlations arising from the optimization procedure) with a linear spline technique as a function of the recoil mass. Figure 3.9 shows the separation line parameters and the $p_{\mu\mu}^T$ cuts determined by the optimization procedure, together with the interpolated values from the linear spline technique.
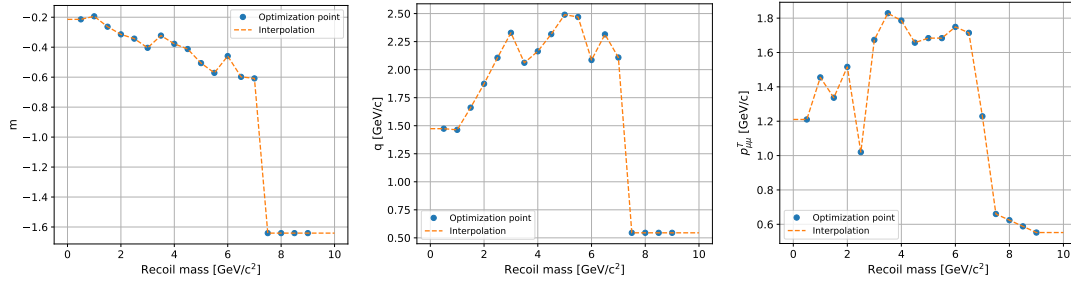
Figure 3.9: Optimal τ suppression parameters as a function of the recoil mass. The interpolated values (linear spline) are also shown.

Figure 3.10 shows the signal efficiency and the surviving background spectrum as a function of the recoil mass. After the selection, the background originating from τ pair production is composed by only 15% of events in which both τ's decay leptonically in muons, all the remaining fraction being dominated by τ decaying to pions. This opens to a potentially big margin of improvement of this analysis with the KLM based muon identification selection, available starting on Phase 3.
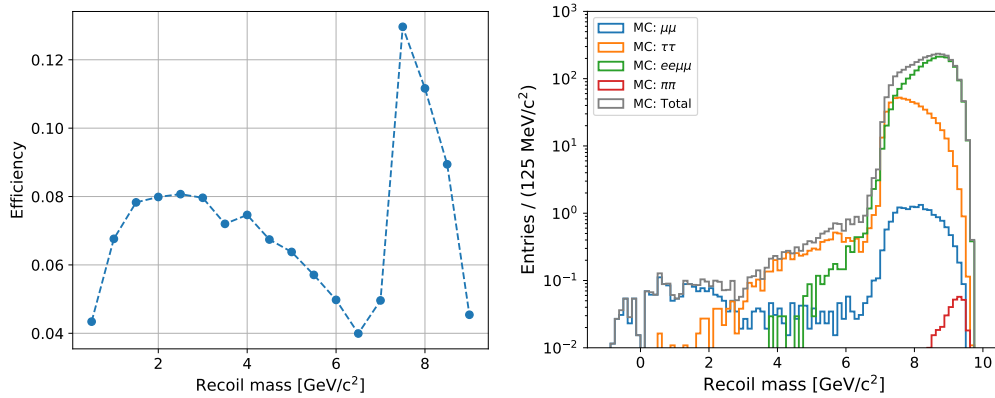
Figure 3.10: Signal efficiency (left) and background spectrum (right) after all the analysis cuts as a function of the recoil mass. Background is normalized to an integrated luminosity of 276 pb^{-1}.

For masses above 7 GeV/c^2 signal and background significantly overlaps in the $p_{max}^T - p_{min}^T$ plane and the optimization procedure stops finding an effective separating line. This is clearly seen in Figure 3.10 with both signal efficiency and background suddenly increasing for recoil masses larger then 7 GeV/c^2. The loss of rejection power is due to kinematics reasons and the

change of the dominant background source (being $e^+e^-\mu^+\mu^-$), against which the procedure is not effective.

The optimal mass window width has been checked, still by looking for the value which maximize the PUNZI FoM. The optimal choice turned out to be a mass window of $\pm2\sigma$, as shown in Figure 3.11. Only in the region above 7 GeV/c^2, due to the high background level, there would be a gain in tightening the size of the bin. However, the measure in this region is in any case strongly disadvantaged due to the cross section behaviours (see Fig. 3.1), thus a fixed width in terms of sigma (namely $\pm2\sigma$) across all the recoil mass range was considered for simplicity.
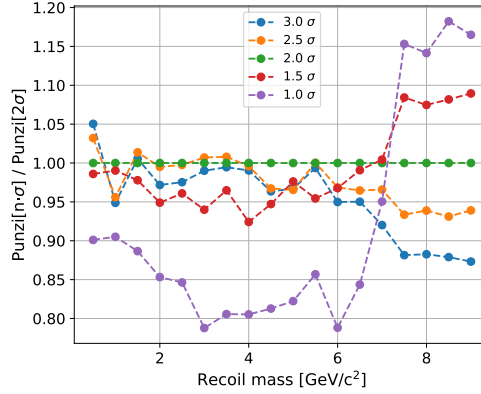
Figure 3.11: Ratio of the Punzi FOM at the end of the analysis computed for different recoil mass window widths with respect to that computed for mass windows of $\pm2\sigma$.

As a final step, the expected values in the continuous binning scheme, described in Sect. 3.4, have been calculated: signal efficiencies are interpolated at the center of each bin and the background yields are then recomputed. Results are shown in Figure 3.12. These values, as well as the one achieved on data after the unblinding will be used for the final statistical computation as described in Sect. 3.7.

LFV Z' to invisible

As a reliable LFV Z' signal simulation was not available, a proper selection optimization was not possible. Thus, this search was performed in the wake of the standard Z' analysis by applying a minimum set of changes to its selections. Same event selection has been performed, with the obvious requirement of one track to be identified as a muon and a second good track to be identified as an electron according to the following ECL-based selection:

1. the ECL-based muon selection, $0.15 < clusterE < 0.4$ and clusterE$/p < 0.4$ for the muon candidate and the ECL-based electron selection $0.8 < $ clusterE$/p < 1.2$ for the electron candidate;

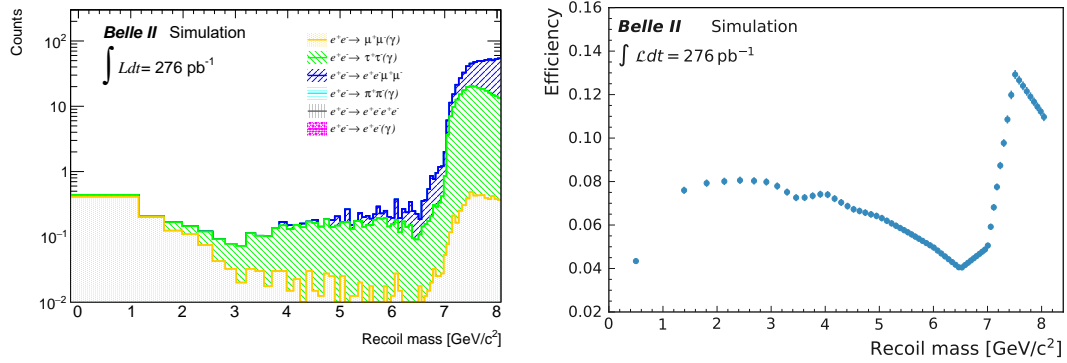2. the sum of the *clusterE* energies associated with the electron and muon candidates was

Figure 3.12: Left: Expected background yields after the τ suppression selection as a function of the recoil mass in the contiguous binning scheme for an integrated luminosity on $276\,\mathrm{pb}^{-1}$. Right: Signal efficiencies resulting from the interpolation procedure on the contiguous binning scheme as function of the recoil mass, after the τ suppression selection.

required to exceed 1.5 GeV, in order to fire the ECL trigger used for this analysis.

Then the event selection flow continues exactly in the same way as for the standard Z' case. The expected background events after the analysis cut number and the background spectrum achieved after event selection, as a function of the recoil mass, are shown in Figure 3.13.
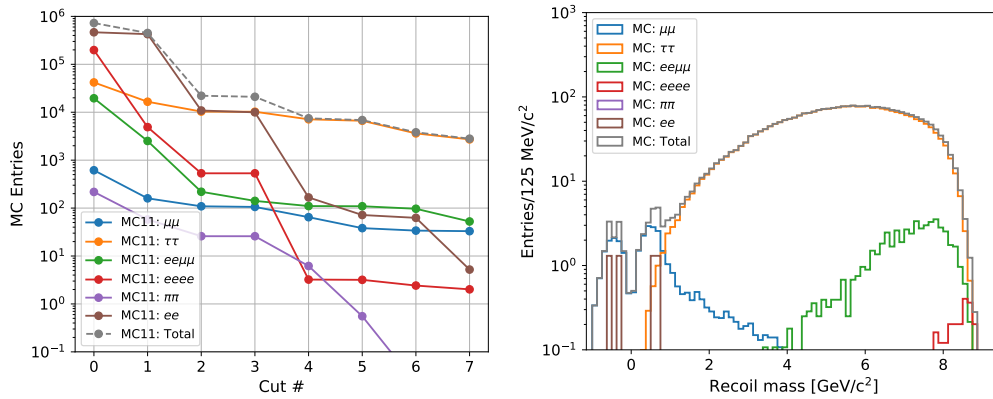
Figure 3.13: Left: Surviving background events as a function of the cut number. Cut 0 corresponds to having applied the reconstruction selection, only. Right: Background spectrum achieved after the generic selection cuts as a function of the recoil mass. The background has been normalized to an integrated luminosity of $276\,\mathrm{pb}^{-1}$ and scaled by a trigger efficiency of 0.79.

All the background sources are normalized to the same integrated luminosity as in the standard Z' analysis ($276\,\mathrm{pb}^{-1}$), but with a trigger efficiency assumed to be 96% (see Sect. 3.6.2). The main source of background for most of the available phase space is due to $\tau^{+}\tau^{-}(\gamma)$ events, while only for of a small region at low recoil masses radiative dimuon events $\mu^{+}\mu^{-}(\gamma)$ dominates.

To further suppress the surviving background, the same τ suppression selection as for the standard Z' was applied. Figure 3.14 shows, the bidimensional $p^T_{max} - p^T_{min}$ distributions after the $p^T_{e\mu}$ cut, with the separation line (as optimized in the standard Z' analysis) superimposed, for same sample masses for background only. Figure 3.15 shows the background rejection factor achieved by the τ suppression procedure only, and the surviving background spectrum as a function of the recoil mass.

As a final step, the expected values in the continuous binning scheme, have been calculated, as shown in Figure 3.16.
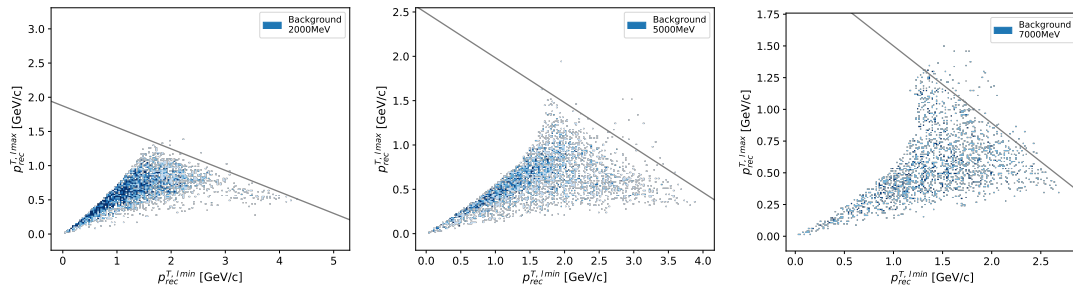
Figure 3.14: p^T_{max} vs p^T_{min} distributions after the $p^T_{e\mu}$ cut for background centered around recoil masses of 2, 5, 7 GeV/c^2 (left, middle and right respectively). The separation line (from standard Z' optimization) is also shown.
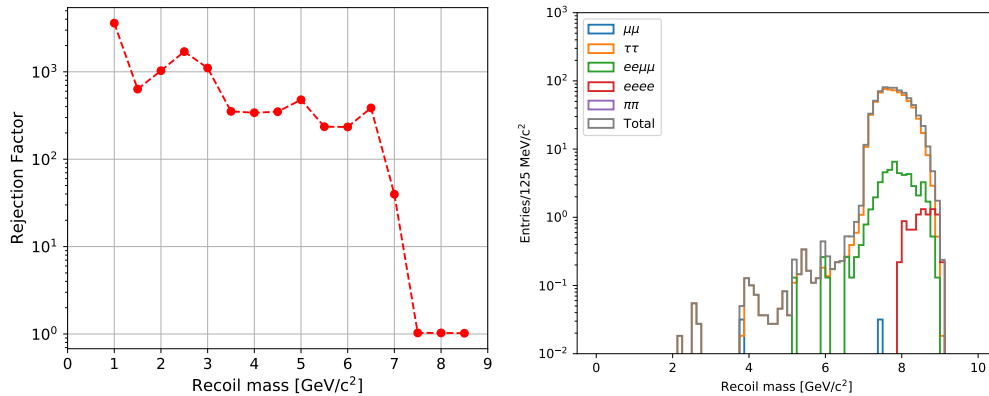
Figure 3.15: Left: Background rejection factor achieved by the τ suppression procedure only. The value at 0.5 GeV/c^2 could not be computed because no background events survived the selection. Right: background events after all the analysis cuts as a function of the recoil mass. The background is normalized to an integrated luminosity of 276 pb^{-1}
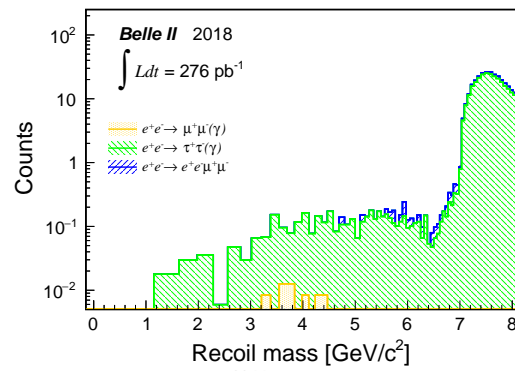
Figure 3.16: Expected background yields after the τ suppression selection as a function of the recoil mass in the contiguous binning scheme for an integrated luminosity on $276\,\mathrm{pb}^{-1}$.

3.6 Data validation and systematic uncertainties evaluation

In this Section, the main sources of systematic uncertainty which affect the invisible Z' analysis are discussed. Systematic uncertainties may come either from detector effects, as inefficiencies and resolutions that need to be measured on real data, and from the differences between the simulation, used for the analysis optimization, and data. Part of these systematic effects have been estimated in dedicated studies carried out by the Belle II collaboration and possibly verified in the context of this thesis in conditions as closer as possible to those of the analysis measurement. Further systematic uncertainties are derived from the data validation procedure, as illustrated below.

3.6.1 Data validation studies

The purpose of the validation procedure is to: have an estimate of the background from data and compare it with the one evaluated in MC simulation, and check the effect of analysis selections described in Sect. 3.5. As described below, this is done by means of control samples on which checks to ensure that the probability to reveal the signal is negligible have been performed.

Three different typologies of control samples have been used:

- ee sample. Beside the Bhabha and $eeee$ backgrounds, it is dominated by $\tau\tau(\gamma)$ events, with both τ's decaying to electrons, whose kinematics is almost identical to one of the $\tau\tau(\gamma)$ events in the Z' analysis ($\tau\tau(\gamma)$ events, with both τ's decaying to muons). All the analysis selections, with the exception of the PID ones, can be checked without any unblinding issue;

- radiative samples: $\mu\mu\gamma$ (and $e\mu\gamma$, $ee\gamma$). This sample is particularly useful in checking the low recoil mass region, being dominantly composed by the ISR $\mu\mu\gamma$ process. The $e\mu\gamma$ and $ee\gamma$ samples are used to cross check the $\mu\mu\gamma$ one and for the check on the LFV Z' search. The presence of a hard photon with a reconstructed energy above 1 GeV decreases the signal efficiency by $\approx \alpha_{QED}$, thus avoiding any unblinding issue;

- $\mu\mu$ (and $e\mu$) samples after the application of a partially reversed τ suppression procedure. This technique allows to strongly suppress hypothetical signal contributions, thus leaving an almost unbiased background sample with no unblinding issue.

The agreement between the number of events in data and Monte Carlo has been checked over the full recoil spectrum range and, separately, within three recoil mass regions corresponding to different sources of contributing background, as shown in Table 3.2. Furthermore, data vs Monte Carlo comparisons as a function of the most important analysis variables have been performed.

Table 3.2: Recoil mass regions used in control sample checks. For events with two identified muons they correspond to the different sources of contributing backgrounds.

Mass window [GeV/c^2]	dominant background source
-2 ÷ 3	$\mu\mu\gamma$
3 ÷ 6	$\tau\tau$
6 ÷ 11	$ee\mu\mu$

Unless differently stated, data events have been selected with the `ffo` trigger. Samples with electrons or photons with a reconstructed energy above 1 GeV can be triggered by the ECL `hie` line too, thus providing the possibility of cross checks.

Data validation with ee sample

In order to select an ee sample, all the cuts described in Sect. 3.5 were applied on data and MC, with the exception of the ECL-based muon ID, which was replaced by $0.8 < clusterE/p < 1.2$.

Recoil mass distributions for data and Monte Carlo after the generic cuts are shown in Figure 3.17: the agreement is very good, with an overall data/MC ratio of $\approx 0.97 \pm 0.01$. After the τ suppression selection, only 20 events are found in data (in the first two recoil mass windows) while 18.4 are expected in Monte Carlo. These numbers have been interpreted as a validation of the τ suppression procedure with a statistical precision of $\approx 22\%$. Thus, a 22% uncertainty has been quoted as a systematic error on the background level knowledge coming from the τ suppression procedure on both the standard Z' and the LFV Z' searches.
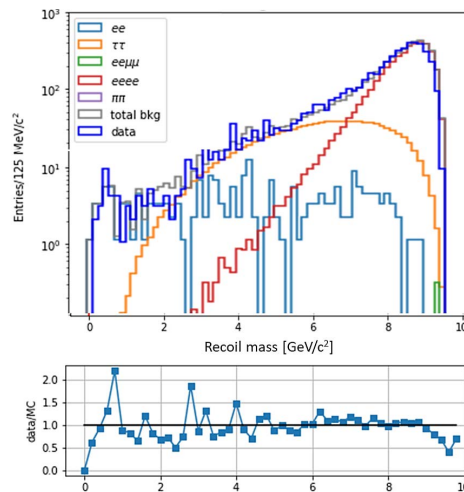
Figure 3.17: Recoil mass distribution of data and MC (on top) and ratio between data and MC (on bottom) for the ee sample before having applied the τ suppression.

Data validation with radiative samples

A $\mu\mu\gamma$ sample was required by applying the analysis flow in Sect. 3.5 with some modifications: it was required the presence in the barrel ECL of a photon with a reconstructed energy $clusterE_\gamma$ > 1 GeV; furthermore, the closest photon veto (cut 5) was dropped and the requirement on the extraEnergy in ROE (cut 6) was redefined with respect to the $\mu\mu\gamma$ system by requiring to have $extraEnergy\text{-}clusterE_\gamma$ <0.4 GeV.

The main sources of background are the same as in the standard Z' analysis. However, as the generator used to simulate the $ee\mu\mu$ background doesn't simulate ISR, a further cut was introduced on the direct dimuon mass $M_{\mu\mu} < 3$ GeV/c^2, being the $ee\mu\mu$ dominating at low dimuon masses, in order to reduce its importance. Data and Monte Carlo distributions have been compared after the generic selections, before applying the τ suppression procedure. This is shown in Figure 3.18, as a function of the squared recoil mass, for the three different mass intervals. Discrepancies of the order of 30% have been observed, with data consistently below Monte Carlo expectations, as reported in Table 3.3. Checks with a different $\mu\mu(\gamma)$ generator were performed but minor differences were observed with respect to the standard generated sample.
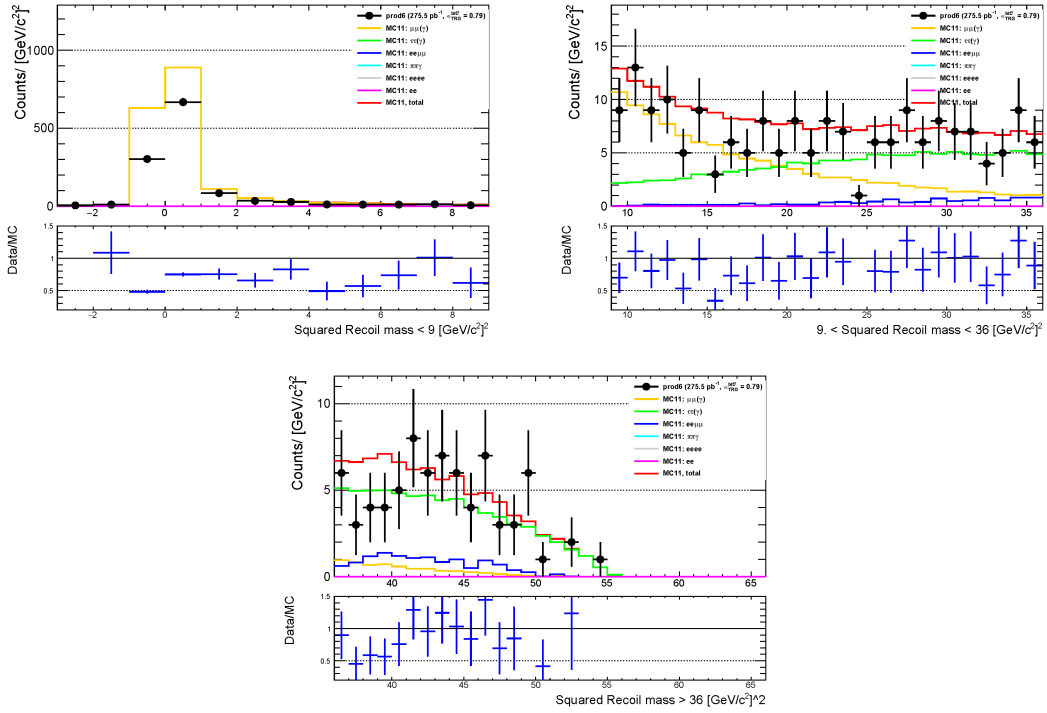
Figure 3.18: Data and MC comparison for the squared recoil mass distribution of the $\mu\mu\gamma$ validation sample in the three large recoil mass regions.

The effect of the individual selections was studied, as shown in Figure 3.19, which summarizes the data/MC ratio as a function of the cut.
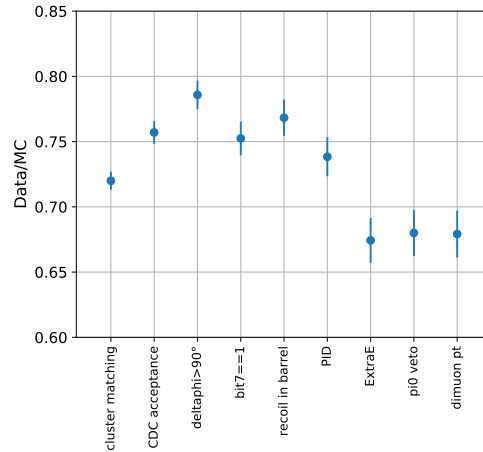
Figure 3.19: Data/MC ratio as a function of the cut number for the $\mu\mu\gamma$ control sample. The 0.79 efficiency correction due to the trigger was applied only when the requirement of having the `ffo` bit fired is effective (from the fourth point on).

The distributions of the relevant variables for the analysis have been checked, but no evident indication of a possible source of discrepancy comes out: most of the distributions look reasonably flat within the statistical fluctuations, with the exception of the data/MC comparison as a function of the azimuthal track angle (see Figure 3.20), which was due to hardware issues of the CDC trigger in Phase 2.
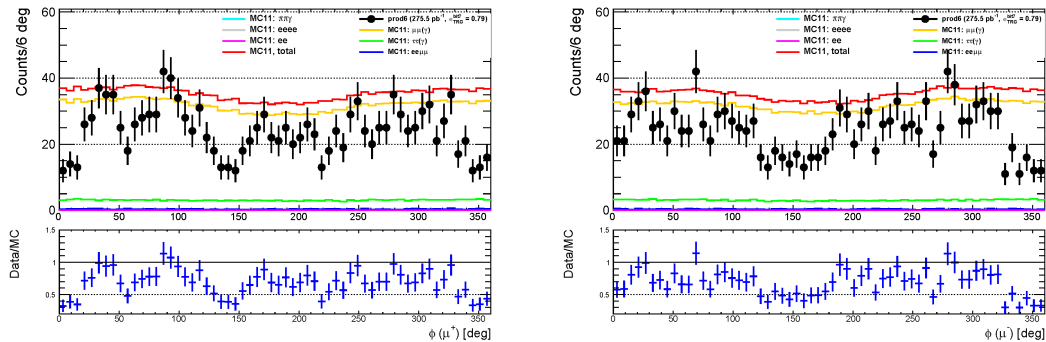
Figure 3.20: Azimuthal angle (LAB) of the two muons in the $\mu\mu\gamma$ validation sample: positive charge (left), negative charge (right).

The $\mu\mu\gamma$ sample, with the presence of the photon with energy above 1 GeV, allowed to measure the `ffo` trigger efficiency by using the calorimeter trigger line `hie` as reference, as described in Sect. 3.6.2. The entire data/MC validation checks with the $\mu\mu\gamma$ sample have been, also, repeated by requiring only the ECL `hie` trigger line to be fired, in order to check if the overall disagreement was imputable to the `ffo` trigger. The results are in agreement with that

obtained with the `ffo` CDC trigger (see Table 3.3).

Also the $e\mu\gamma$ and $ee\gamma$ final states have been studied, using both the CDC `ffo` trigger and the ECL `hie` trigger. The $e\mu\gamma$ sample is dominated by $\tau\tau\gamma$ events. For these validation samples, when the statistics is high enough, the agreement looks much better than for $\mu\mu\gamma$ (see Table 3.3), thus suggesting that the observed discrepancy is somehow related to muons.

Data validation with a reversed τ suppression procedure

A complementary validation procedure able to check the full interesting recoil mass region is achieved with a partially reversed τ suppression procedure: the selection on $p_{\mu\mu}^T$ was not considered, while the optimal separation line in the bidimensional $p_{rec}^{T,lmax} - p_{rec}^{T,lmin}$ plane was used in a reversed way, by accepting only events below it. This technique allows to strongly suppress hypothetical signal contributions, thus leaving an almost unbiased background sample with no unblinding issue. Figure 3.21 shows the Punzi FOM following the application of such a procedure compared with the one at the end of the analysis. The eventual distortion in the background induced by the reversed procedure, was studied on the ee sample and found to be negligible.
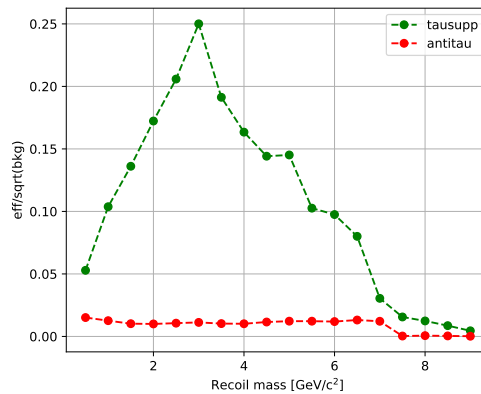

Figure 3.21: Punzi FOM as a function of the recoil mass for the normal τ suppression analysis (green) and with a partially reversed τ suppression procedure.

The squared recoil mass for the $\mu\mu$ sample for data and MC is shown in Figure 3.22, for the three different mass intervals. After applying the procedure, the data/MC ratio on the full recoil mass spectrum was 0.64 ± 0.02 for $\mu\mu$ and 0.90 ± 0.02 for the $e\mu$ sample. Such results confirm the data/MC discrepancies observed in the $\mu\mu\gamma$ sample (see also Table 3.3).

Distributions of the relevant variables for the analysis with a reversed τ suppression selection are shown in Figures 3.23 to 3.29. No evident indication of a possible source of discrepancy comes out: most of the distributions look reasonably flat within the statistical fluctuations, with the exception of the data/MC comparison as a function of the azimuthal track angle (see Figure 3.24).
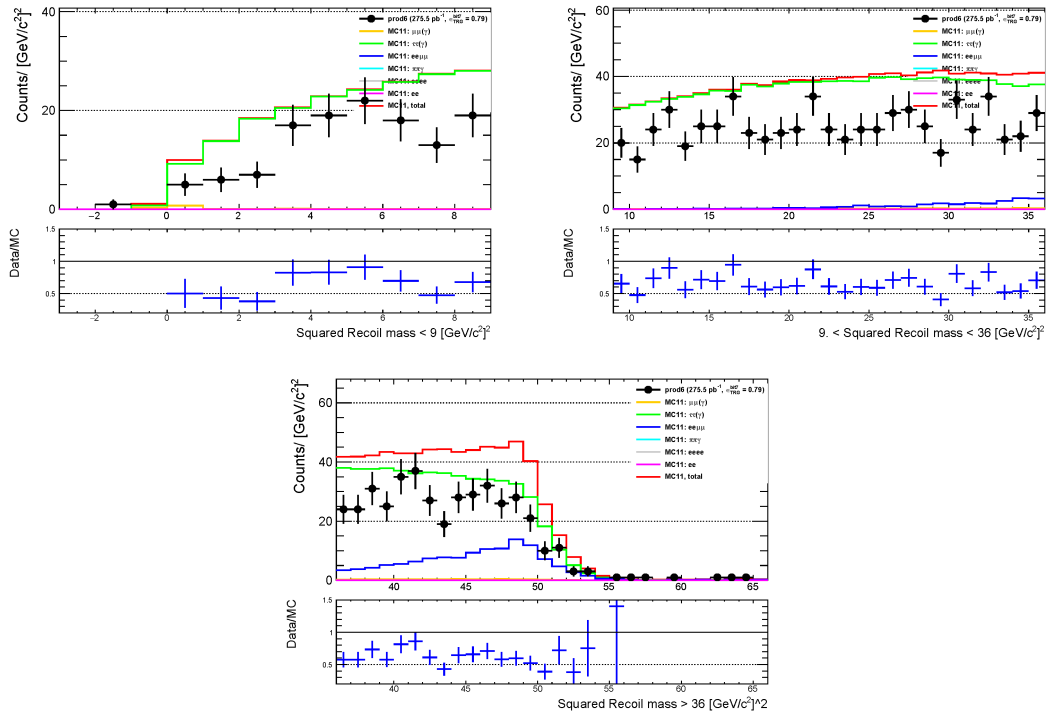
Figure 3.22: Squared recoil mass distribution for the $\mu\mu$ sample with a partially reversed τ suppression procedure and for three different intervals.
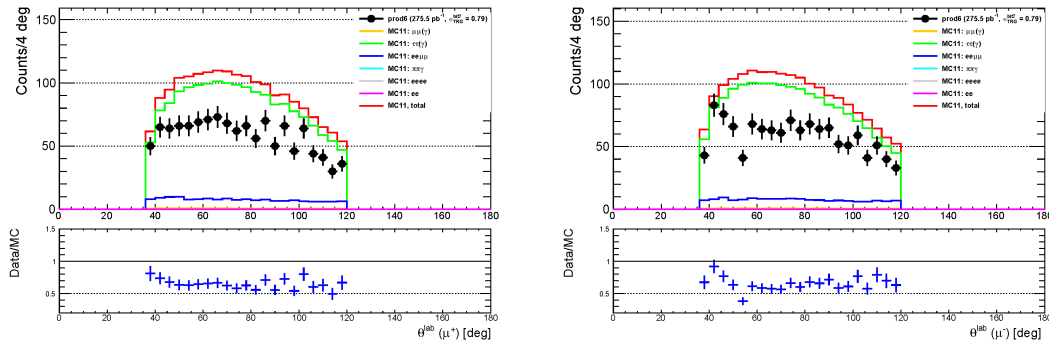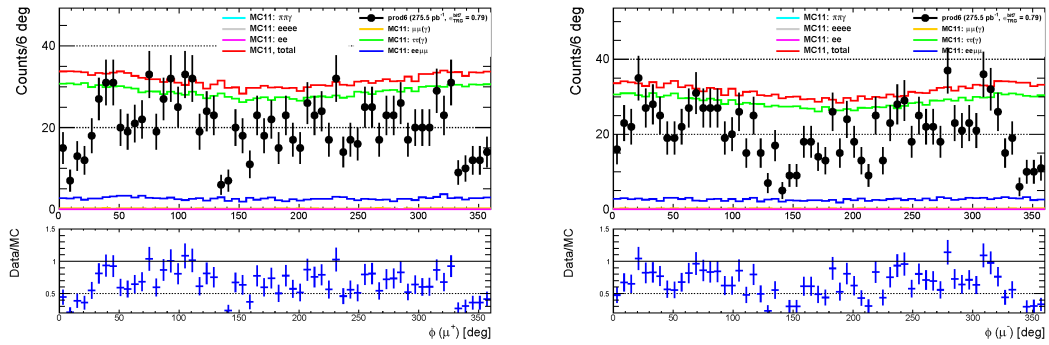

Figure 3.23: Polar angle (LAB) of the two muons in the $\mu\mu$ validation sample with a partially reversed τ suppression procedure: positive charge (left), negative charge (right).

Data validation summary

The results from the data validation procedure previously described are summarized in Table 3.3. They coherently point to a data/MC discrepancy of $\approx$-35% for $\mu\mu$ events and of $\approx$-10% for $e\mu$ events. A -10% discrepancy may be explained with tracking inefficiency, as evaluated in

Figure 3.24: Azimuthal angle (LAB) of the two muons in the $\mu\mu$ validation sample with a partially reversed τ suppression procedure: positive charge (left), negative charge (right).
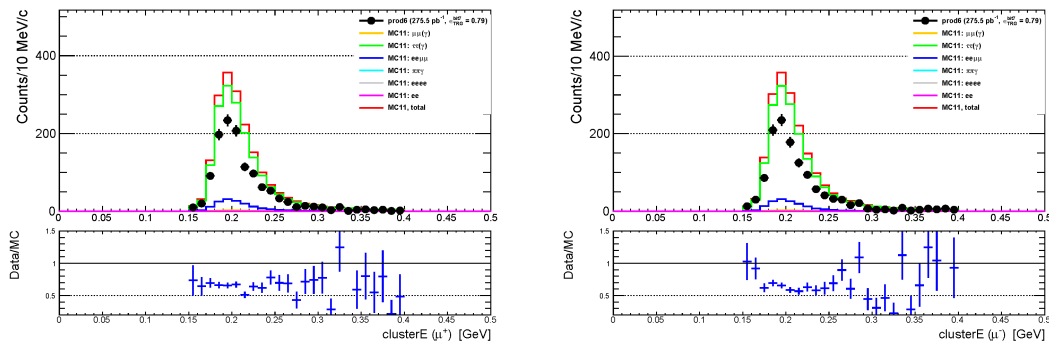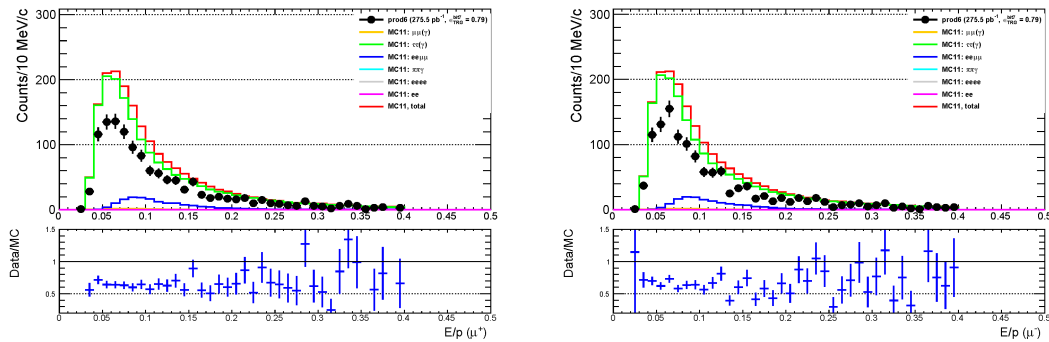

Figure 3.25: Cluster energy of the two muons in the $\mu\mu$ validation sample with a partially reversed τ suppression procedure: positive charge (left), negative charge (right).

Figure 3.26: Cluster energy over momentum ratio of the two muons in the $\mu\mu$ validation sample with a partially reversed τ suppression procedure: positive charge (left), negative charge (right).

Sect. 3.6.2. This allows to explain the $e\mu$ discrepancy and will be accounted by re-scaling by 0.90 the the expected background yields in the LFV Z' analysis. For what concerns the $\mu\mu$ sample,
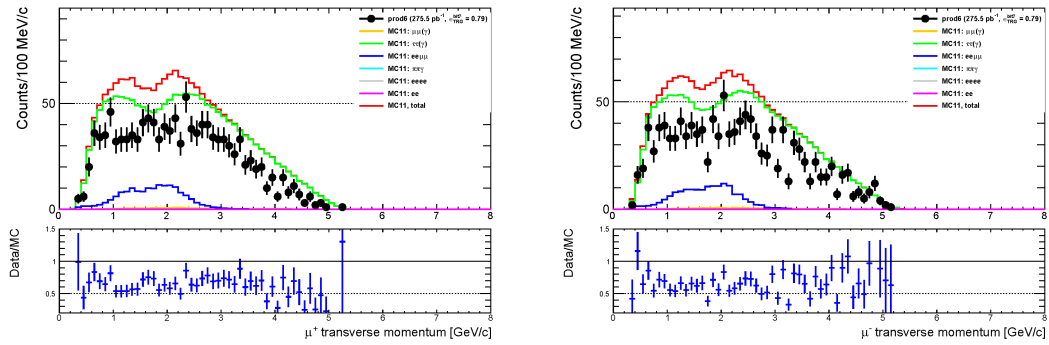
Figure 3.27: Transverse momentum of the two muons in the $\mu\mu$ validation sample with a partially reversed τ suppression procedure: positive charge (left), negative charge (right).
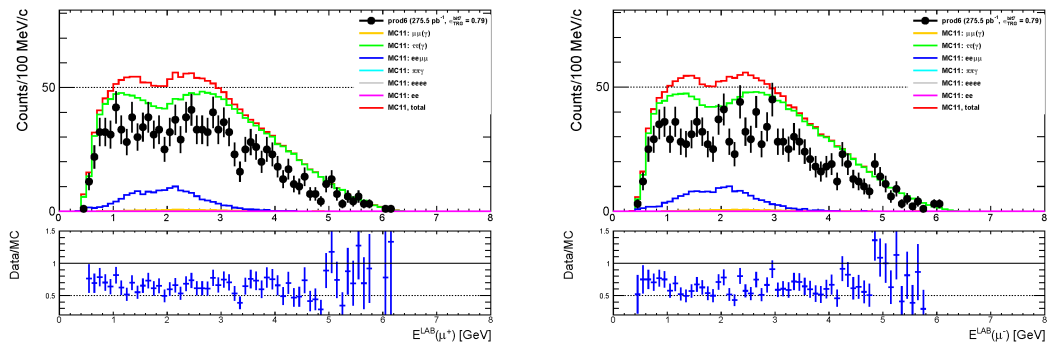

Figure 3.28: Energy (LAB) of the two muons in the $\mu\mu$ validation sample with a partially reversed τ suppression procedure: positive charge (left), negative charge (right).
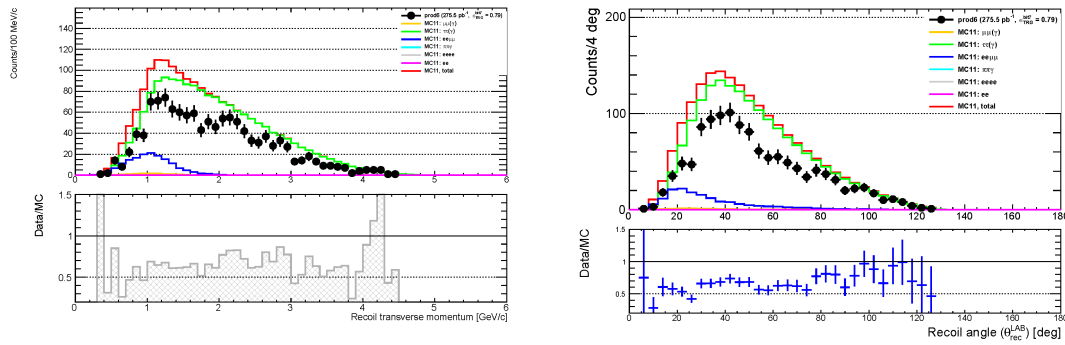

Figure 3.29: Transverse momentum (left) and polar angle (right) of the system recoiling against the two muons in the $\mu\mu$ validation sample with a partially reversed τ suppression procedure.

an unexplained -25% deficit in two muon events remains, which must be managed both in the background estimate and in the systematic uncertainty evaluation.

After re-scaling the expected background yield and the signal efficiency for the measured data/MC discrepancy, the following systematic uncertainties were assigned:

- an uncertainty of 2% to the background yields in both analysis, according to the statistical precision of the measurement of the background level before the τ suppression;

- an uncertainty of 22% to the background yields in both cases due to the τ suppression as discussed in Sect. 3.6.1. This value is driven by the low statistics of the control samples. It isn't considered for the signal efficiency, as the τ suppression selection is quite mild on the signal side and the distributions on which it is based are well reproduced in the simulation;

- an uncertainty of 12.5% (half of the fully unexplained discrepancy) to the signal efficiency because of the measured discrepancy.

Mass window [GeV/c^2]	$\mu\mu\gamma$	$\mu\mu\gamma$	$e\mu\gamma$	$e\mu\gamma$	$ee\gamma$	$ee\gamma$	$\mu\mu$+anti τ	$e\mu$+ anti τ
-	ffo	hie	ffo	hie	ffo	hie	ffo	ffo
-2 ÷ 3	0.65±0.02	0.67±0.02	0.8±0.3	1.3±0.3	0.88±0.01	0.99±0.01	0.66±0.06	0.94±0.07
3 ÷ 6	0.84±0.07	0.76±0.07	0.9±0.1	0.95±0.13	1.10±0.10	1.14±0.01	0.65±0.02	0.89±0.03
6 ÷ 11	0.9±0.1	0.72±0.13	0.9±0.2	0.93±0.15	2.13±0.12	1.3±0.1	0.63±0.03	0.89±0.03
Overall	0.68±0.02	0.68±0.02	0.92±0.09	0.96±0.10	0.90±0.01	0.99±0.01	0.64±0.02	0.90±0.02

Table 3.3: Summary of the validation checks for the data/Monte Carlo ratio on the various samples. The second row shows the trigger line used in the check. Data/MC ratios are shown for three different recoil mass intervals and for the total.

3.6.2   Further systematic uncertainties

The following systematic uncertainties have been furthermore taken into account.

Luminosity measurement

The luminosity measurement in Phase 2 was performed independently on two different samples: radiative Bhabha and two-photon events. The overall measurement strategy and the techniques to estimate the associated uncertainty are explained in Ref. [119]. The relative systematic uncertainty which is taken into account for the upper limit calculation is 0.7%.

Trigger efficiency

The standard Z' analysis is performed on data selected by the 2-track CDC trigger (`ffo` trigger). This trigger selects events with at least two tracks in the CDC acceptance with an opening angle in ϕ-plane of at least 90°. To emulate the effects of the trigger selection in simulations, the trigger requirement was added as a part of the selection cuts (see Sect. 3.5).

The efficiency of the `ffo` trigger has been measured in other Belle II collaboration studies [124]. It has been estimated by using the orthogonal ECL trigger line (`hie`) as a reference, which requires events with a total energy deposition in the barrel and part of the endcap ECL larger than 1 GeV: by using $e^+e^- \to e^+e^-$ events having a total energy deposition in the ECL larger then 1.5 GeV, the `ffo` efficiency ϵ_{trg} has been computed as the ratio between the number of events triggered simultaneously by both CDC and ECL and the number of events triggered by the ECL. During Phase 2, the `ffo` trigger efficiency strongly varied with runs. Thus, for this analysis measurement, only runs where the CDC trigger efficiency is validated and is higher than 50% have been used. The final trigger efficiency is defined as the average of efficiencies measured in such good runs weighted with the corresponding luminosity. In these conditions, the efficiency is found to be $79.0 \pm 0.1\%$ for a total integrated luminosity of 276 pb^{-1}. The systematic uncertainty in the trigger efficiency due to kinematic dependencies has also been evaluated as the relative variation of the average efficiency in bins of opening angle, polar angle, transverse momentum, and number of track hits in the CDC. In order to keep a low systematic effects, the opening angle is required to be less than 172°. In such a condition a 6% variation has been measured and assigned as systematic uncertainty.

As a crosscheck, the `ffo` trigger efficiency has also been measured in $\mu\mu\gamma$ events with photon energies above 1 GeV, thus able to fire the ECL trigger. This gave an efficiency $\epsilon_{ffo} = 0.747 \pm 0.007$(stat.), to be compared with 0.79 evaluated with e^+e^- events.

With the $\mu\mu\gamma$ sample, the azimuthal strong non uniformities induced by the `ffo` trigger were investigated. The trigger efficiency was measured as a function of the minimum and maximum track azimuth angle in the event: these are shown in Figure 3.30. Regions of better trigger efficiencies were selected, namely $\phi_{min} < -1$ and $0.5 < \phi_{max} < 2$, and efficiencies raised to ≈ 0.88. Repeating all the validation analysis with this angular selection (and using the corresponding

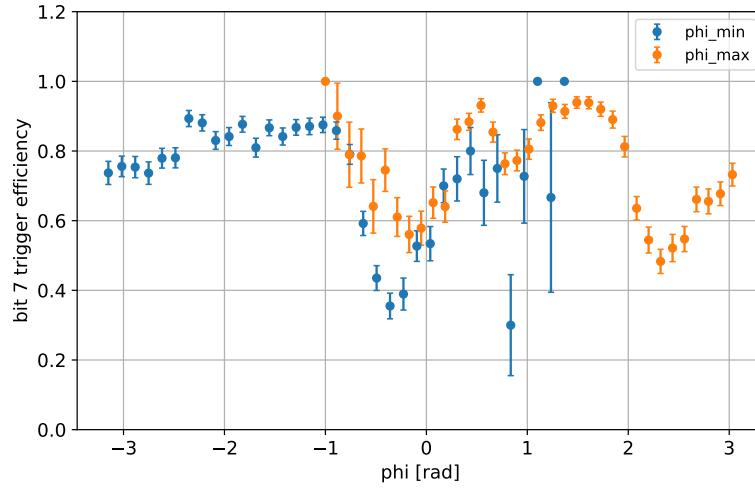trigger efficiency) finally gave the same data/MC discrepancies as in Table 3.3.

Figure 3.30: Trigger `ffo` efficiency as a function of the minimum (blue) track azimuth angle and of the maximum (orange) track azimuth angle in $\mu\mu\gamma$ events.

For the LFV Z' analysis, data were selected by the `hie` ECL trigger. The performances of the ECL trigger line have been studied on data by using the $e^+e^- \to \mu^+\mu^-\gamma$ control sample events selected with the CDC two-track trigger for photon energies larger than 1 GeV: the corresponding measured plateau efficiency is 96.0% with 1% of systematic uncertainties. As this was validated with the use of the 2-track CDC trigger, the same integrated luminosity of 276 pb^{-1} was considered for the LFV Z' analysis.

Tracking efficiency

The tracking efficiency has been measured on both Phase 2 data and MC simulated samples in other Belle II collaboration studies [125, 126] by using radiative Bhabha events and a tag-and-probe method: using the kinematics of one of the two tracks and of the radiated photon (tag), it is possible to find expected position of the other track (probe). As a result from this study, a tracking efficiency overestimated in simulations with respect to the real detector performance with dependencies on the track position has been observed. Due to this effect, an inefficiency of 10% ($\sim$ 5% for the track) between data and MC in this analysis is expected, with a 4% systematic uncertainty due to kinematic dependencies. This large discrepancy can be explained as the sum of several effects: a tracking algorithm not well optimized to operate with a partial VXD detector and a beam background in the CDC larger than expected.

Particle ID selection

In order to select muon events, a particle identification based on an ECL-based selection was used. The performance of these cuts has been measured on both Phase 2 data and MC samples

by using a self-tagging technique on $e^+e^- \to e^+e^-\mu^+\mu^-$ events [127]. For the ECL barrel region, an overall agreement was found to be at the level of 2% per track in the worst case. Thus a 4% systematic uncertainty due to particle ID selection was considered in this analysis.

Recoil mass resolution

The dimuon recoil mass resolution has been checked on data and then compared with the one from Monte Carlo simulation on the $e^+e^- \to \mu^+\mu^-\gamma$ control sample. The events have been selected according to the requirements described in Sect. 3.6.1. In addition, it was required that the sum of the energies of the two muons and of the photon lies between 10 and 12 GeV and that there are no additional detected photons with energy larger than 100 MeV in the event, to reject contamination from radiative τ pair events.

The selected events on both data and MC samples are then weighted to match the kinematic distribution expected for the signal. The weights have been computed in the bidimensional muon momentum distribution for different Z' mass hypotheses and then applied to the selected control samples on both MC and data events. The procedure works well only for low Z' masses, as, for high masses, it is harder to match the bidimensional dimuon momentum distributions with the $\mu^+\mu^-\gamma$ ones, due to kinematical reasons.

The weighted recoil mass distributions are expected to be centered at zero, as the recoil momentum is provided by a photon, while the difference in width between data and Monte Carlo can be used as a correction factor to the mass resolution. Distributions were fitted as in Sect. 3.4, with the sum of a Crystal Ball and a Gaussian. Figure 3.31 and Figure 3.32 show the results for Monte Carlo and $e^+e^- \to \mu^+\mu^-(\gamma)$ data, including the fitted PDF model distributions.

Correction factors, defined as the ratio of the values of the weighted widths for data (σ_w^{data}) and MC (σ_w^{MC}) recoil mass distributions from the fit are shown in Table 3.4. As they are smaller or compatible with 1, it was deduced that the effect of detector resolution is well described in simulations and systematic uncertainties have been neglected.

Table 3.4: The correction factor for detector resolution as a function of the Z' mass computed on the $\mu\mu\gamma$ control sample.

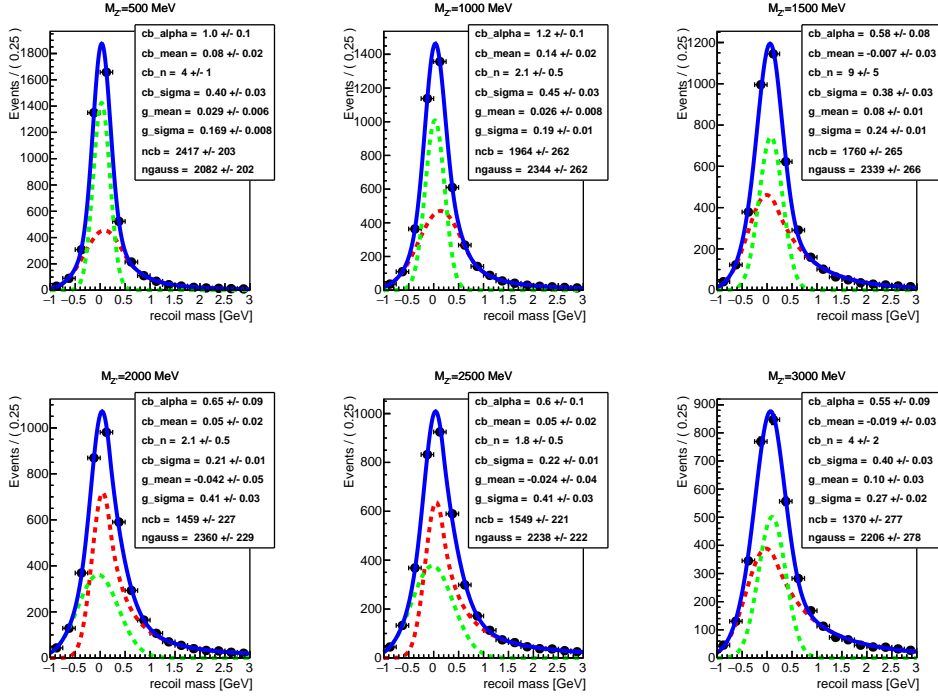| $M_{Z'}$ [GeV/c^2]	$\sigma_w^{\text{data}}/\sigma_w^{\text{MC}}$
0.5	0.883 ± 0.074
1	0.794 ± 0.084
1.5	0.938 ± 0.084
2	1.089 ± 0.105
2.5	1.048 ± 0.087
3	0.997 ± 0.081

Figure 3.31: Monte Carlo weighted recoil mass and fitted PDF model distribution (blue line) for different Z' mass point hypothesis. The contribution of the CB and the Gaussian function are shown with a red and green dotted line respectively. The resulting fit parameters are shown in the top right corner of each graph.

3.6.3   Systematic uncertainties summary

The main systematic uncertainties affecting the Standard and the LFV Z' measurement described before are summarized in Table 3.5. The systematic uncertainties due to trigger efficiency, tracking efficiency and particle ID selections are considered to affect in a completely correlated way the signal efficiency and the background yields.

Table 3.5: Relative systematic uncertainties affecting the $\mu\mu$ and $e\mu$ analyses. Where not specified, they apply to both signal and background.

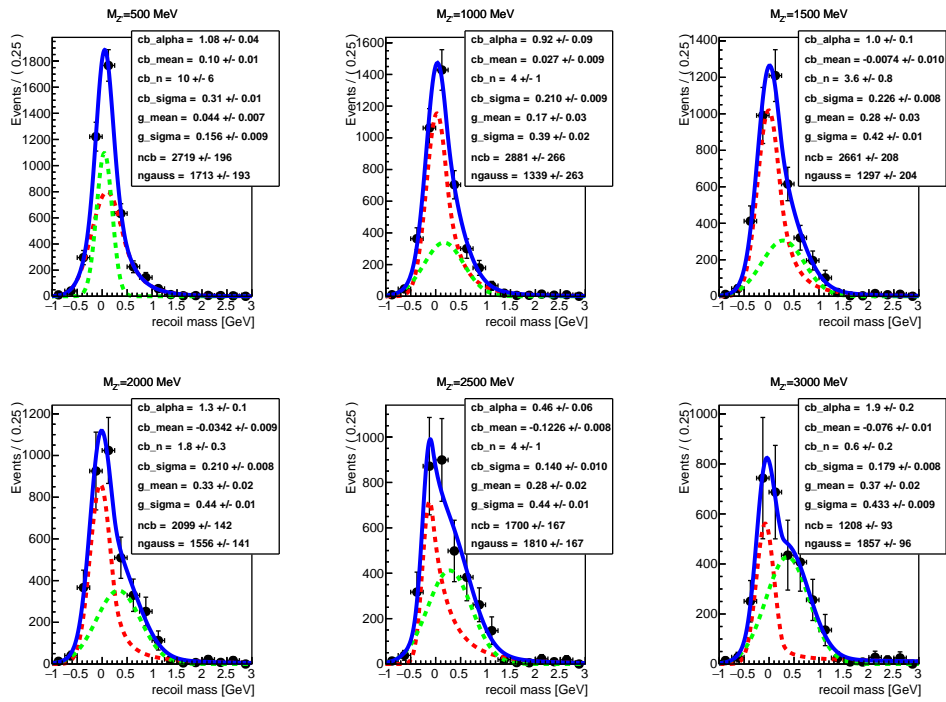| Source	$\mu^+\mu^-$	$e^\pm\mu^\mp$
Trigger efficiency	6%	1%
Tracking efficiency	4%	4%
PID	4%	4%
Luminosity	0.7%	0.7%
τ suppression (background)	22%	22%
Background before τ suppression	2%	2%
Discrepancy in $\mu\mu$ yield (signal)	12.5%	–

Figure 3.32: Weighted data recoil mass and fitted PDF model distribution (blue line) for different Z' mass point hypothesis. The contribution of the CB and the Gaussian function are shown with a red and green dotted line respectively. The resulting fit parameters are shown in the top right corner of each graph.

3.7   Results

In this Section, the statistical treatment of the yields found after the final selection in both MC and Phase 2 data is discussed. The statistical analysis of the selected events has been implemented in a frequentist approach for what concerns the significance test, while relies on a Bayesian approach for the upper limits computation. Details on the statistical procedure are reported in Appendix B. After the unblinding, no significant excess of events in neither the standard nor the LFV Z' cases has been observed and limits on the cross sections of both processes have been measured. For the standard Z' case only, the upper limits to the cross section have been then interpreted in terms of the coupling constant g'.

3.7.1   Standard Z'

After the checks on the control samples described in the previous section, the Phase 2 data were unblinded for both $\mu\mu$ and $e\mu$ samples. As a first step, the agreement between unblinded data and MC before applying the τ suppression procedure was verified. The MC simulated samples are normalized to an integrated luminosity of 276 pb^{-1} and scaled for the trigger efficiency (79%, see Sect. 3.6.2) and for the discrepancy measured on control samples (65%, see Table 3.3). The recoil mass spectra for $\mu\mu$ sample within the contiguous bin scheme (see Sect. 3.4) is shown in Figure 3.33 (Left), and a summary of the Data/MC check is reported in Table 3.6. The agreement between data and MC looks satisfactory over the entire spectrum.
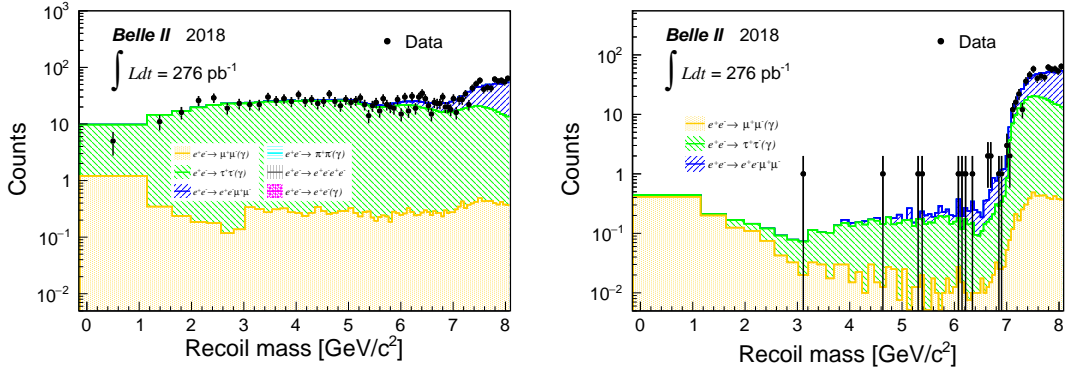

Figure 3.33: Recoil mass spectrum for the $\mu\mu$ sample before (left) and after (right) the τ suppression procedure. Monte Carlo values have been rescaled for luminosity, trigger efficiency (0.79) and validation procedure outcome (0.65).

Then, the τ suppression procedure was applied on both data and rescaled Monte Carlo. The final recoil mass spectrum is shown in Figure 3.33 (Right). Due to the smallness of the expected background at the end of the selections, a counting procedure was used, as opposed to a fitting technique. Indeed, over a large part of the mass plane there is not enough statistic to fit the background size and shape. The procedure adopted relies on comparing the number of observed

Table 3.6: Summary of the check for the data/Monte Carlo ratio before the τ suppression procedure on $\mu\mu$ and $e\mu$ samples. Data/MC ratios are shown for three different recoil mass intervals and for the total. Monte Carlo values have been rescaled for luminosity, trigger efficiency and validation procedure outcome.

Mass window [GeV/c^2]	$\mu\mu$	$e\mu$
-0.15 $\div$ 3	1.00 $\pm$0.09	0.91 $\pm$ 0.07
3 $\div$ 6	0.99 $\pm$0.04	1.01 $\pm$ 0.03
6 $\div$ 8	1.00 $\pm$0.03	1.11 $\pm$ 0.03
Overall	1.00 $\pm$0.02	1.04 $\pm$ 0.02

events with the expected background in mass windows. Following the procedure described in Appendix B, the background only hypothesis was checked, in order to look for possible anomalies in data, by computing the p-values for both the normal binning option and the half bin shifted one (see Sect. 3.4).

The p-values as a function of the recoil mass are shown in Figure 3.34. No outstanding anomaly is observed, with all results standing well below the 3σ equivalent level.
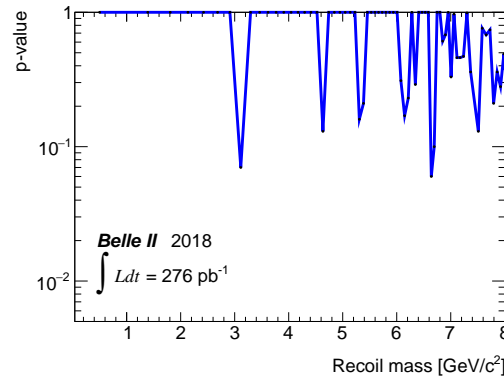

Figure 3.34: p-values as a function of the recoil mass. Results stay well below the 3σ equivalent level.

As no anomalies have been observed, the 90% credibility level upper limits to the signal cross section $\sigma[e^+e^- \to \mu^+\mu^- Z'(\to \text{invisible})]$ have been computed. As described in Appendix B, for each mass window, the following equation holds:

$$N = \sigma_{Z'} \times \mathcal{L} \times \epsilon_{\text{sig}} \times \epsilon_{\text{trigger}} + B \qquad (3.5)$$

where N is the observed number of events, ϵ_{sig} is the signal efficiency, B is the MC expected background and $\sigma_{Z'}$ is the cross section of the Z' process.

All the relevant prior distributions have been defined taking into account the following assumptions:

- the likelihood distribution for the model, given the observed number of events, was assumed to be Poissonian;

- the prior distribution for the Z' process cross section was assumed to be flat between 0 and $100 \cdot \sqrt{b}/(\mathcal{L} \times \epsilon_{\text{sig}})$ fb (with the luminosity expressed in fb^{-1});

- all the prior distributions related to systematic uncertainties were assumed to be Gaussian, with a width equal to the estimated size of the effect;

- the expected (Monte Carlo) background number of events was assumed to be Poissonian.

The size of the systematic effects is taken from the values in Table 3.5. All the sources are treated as uncorrelated and summed up in quadrature separately for signal and background, with the exception of the uncertainties coming from the trigger, luminosity, tracking efficiency, PID and the effect of generic cuts for which 100% correlation was assumed between signal and background. With the previous assumptions on the prior distributions, the BAT package [128] was setup to estimate a 90% CL upper limit on $\sigma_{Z'}$.

Results are shown in Figure 3.35 (left), where also sensitivities, i.e., the average upper limit obtained by an ensemble of pseudo-experiments with the expected background B only and no signal, are reported. Results have been translated in terms of upper limits on the coupling constant g' and shown in Figure 3.35 (right), together with the expected sensitivities. Both the branching ratio $BR(Z' \to \text{invisible})$ predicted by the $L_\mu - L_\tau$ model and and the enhanced $BR(Z' \to \text{invisible}) = 1$ due to kinematically accessible DM have been considered. Upper limits on the coupling constant stay in the range $[5 \times 10^{-2} - 1]$ for $M_{Z'} \leq 6$ GeV/c^2.

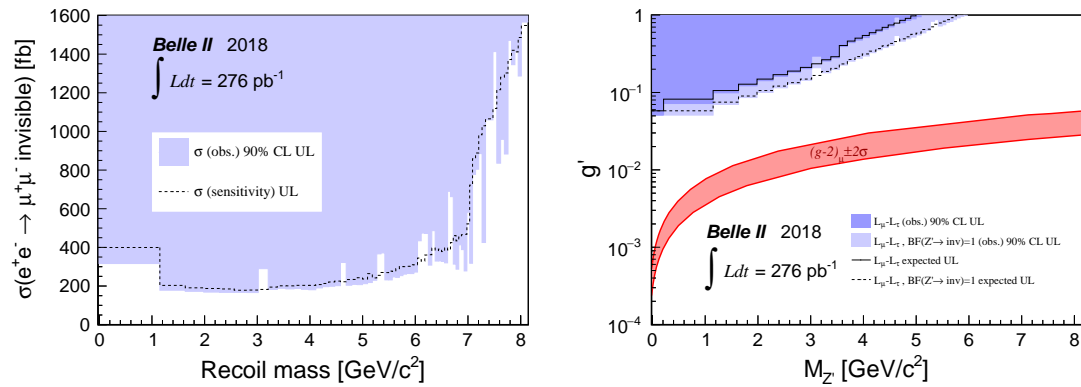Figure 3.35: Left: 90% CL upper limits to $\sigma[e^+e^- \to \mu^+\mu^- Z'(\to \text{invisible})]$ as a function of the recoil mass. The dashed line is the expected sensitivity. Right: 90% CL upper limits on the coupling constant g'. Dark blue filled areas show the exclusion regions assuming the branching ratio $BR(Z' \to \text{invisible})$ predicted by the $L_\mu - L_\tau$ model; light blue areas are for $BR(Z' \to \text{invisible}) = 1$. The solid and dashed lines are the expected sensitivities for the two hypotheses. The red band shows the region that could explain the muon anomalous magnetic moment $(g-2)_\mu \pm 2\sigma$.

3.7.2   Lepton Flavour Violating Z'

As for the previous case, the agreement between unblinded data and MC before to apply the τ suppression procedure was checked also for the LFV Z'. The MC simulated samples have been normalized to an integrated luminosity of 276 pb^{-1} and then scaled for the trigger efficiency (96%, see Sect. 3.6.2) and for the measured discrepancy (90%, see Table 3.3). The recoil mass spectrum for the $e\mu$ sample is shown in Figure 3.36(Left), and a summary of the Data/MC check is reported in Table 3.6. A good agreement between data and MC over the entire spectrum has been observed.
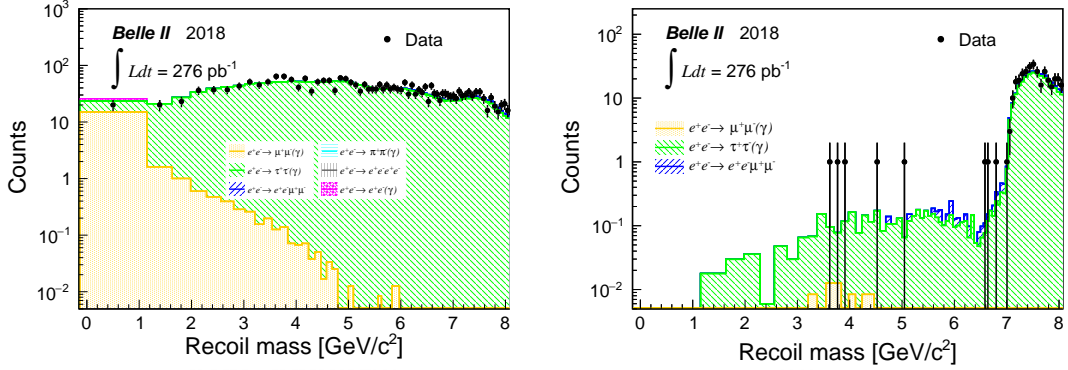

Figure 3.36: Recoil mass spectrum for the $e\mu$ sample before (left) and after (right) the τ suppression procedure. Monte Carlo values rescaled for luminosity, trigger efficiency (0.96) and validation procedure outcome (0.9).

The τ suppression procedure was then applied on data and rescaled Monte Carlo and the final recoil mass spectrum produced, as shown in Figure 3.36(Right). As for the standard Z', the background only hypothesis was checked, in order to look for possible anomalies in data by computing p-values for both the normal binning option and the half bin shifted one. No outstanding anomalies have been observed, with all results standing well below the 3σ equivalent level, as shown in Figure 3.37.

For the LFV Z' case, being at present impossible to estimate a signal efficiency in absence of a robust model, the product ($\sigma_{Z'} \times \epsilon_{\mathrm{sig}}$) in eq. 3.5 has been considered as a single parameter. Therefore, the 90% CL upper limits to $\epsilon \times \sigma[e^+e^- \rightarrow e\mu\, Z'(\rightarrow \mathrm{invisible})]$ were computed as a function of the recoil mass as shown in Figure 3.38. Due to the lack of a solid model for the LFV Z', the obtained results have not been further translated in upper limits to a coupling constant.

3.8   Future developments

The possibility to repeat the invisible Z' search on the data-set collected during the early Phase 3 period is currently under study. Many factors of improvement for the analysiss are
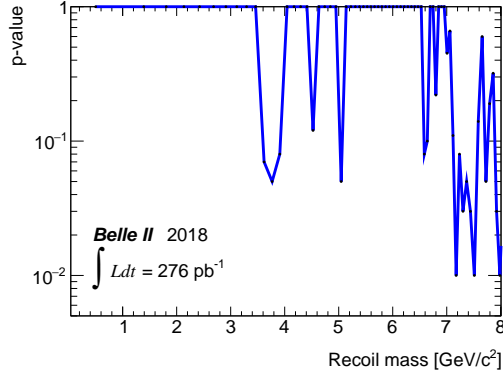
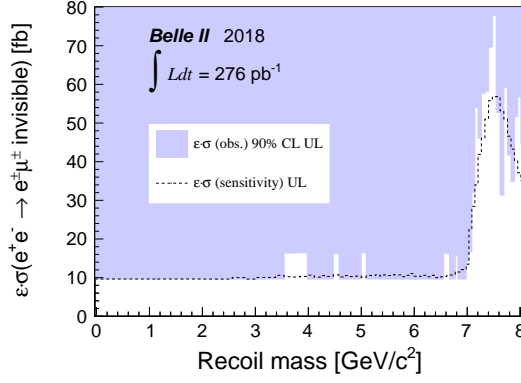Figure 3.37: p-values as a function of the recoil mass for the $e\mu$ sample.

Figure 3.38: 90% CL upper limits on efficiency times cross section $\epsilon \times \sigma(e^+e^- \to e^\pm\mu^\mp$ invisible) (light blue areas). The dashed line is the expected sensitivity

foreseen. First, the increased integrated luminosity: around 90 fb^{-1} of data have been collected during the 2019-2020 data-taking period, and ~ 500 fb^{-1} ar foreseen before the 2022 shut down (see Sect. 2.6). Second, starting from Phase 3, the muon identification is implemented with a KLM-based particle identification algorithm. The main benefit will be the ability to reduce the expected background due at the rate of particles misidentified as muons (mainly pions from tau decay). Finally, the presence of the full VXD provides a major impact on tracking performance and therefore on the mass resolution of recoil. Furthermore, as shown in Sect. 4.6, an overall better data/MC agreement has been observed on the early Phase 3 data-set. This implies a drastic reduction of the systematics on signal with respect to the Phase 2 analysis.

A further element of improvement derives from the use of more inclusive Level 1 triggers that have been activated starting from the 2020 data-taking period, specifically, the CDC trigger line `ff30` and the CDC-KLM lines (for more details see Sect. 4.8 and Appendix A).

First studies by using signal and background simulated samples with the early Phase 3 ge-

ometry and nominal beam background have been already performed. Specifically, the impact of more performing selection criteria based on Neural Network algorithms has been evaluated, whose description is outside the context of this thesis. More details are reported in the recent work [129]. From a preliminary study that takes into account the various improvement factors aforementioned the expected sensitivity on the cross section as a function of the recoil mass for an integrated luminosity of $50\,\mathrm{fb}^{-1}$ has been estimated. Only a preliminary and conservative systematic uncertainty on background (20%) and signal (10%) was assigned. Results have been translated also in terms of the coupling constant g', and are shown in Figure 3.39, compared to the results achieved in Phase 2.

A large improvement on the cross section upper limits is observed, being more than a simple scaling driven by the increased size of the data-set. With the data-set collected to date, and with the one to come in the coming years, there will be a serious possibility to exclude a good part of the region of the parameters able to explain the $(g-2)_\mu \pm 2\sigma$ anomaly.
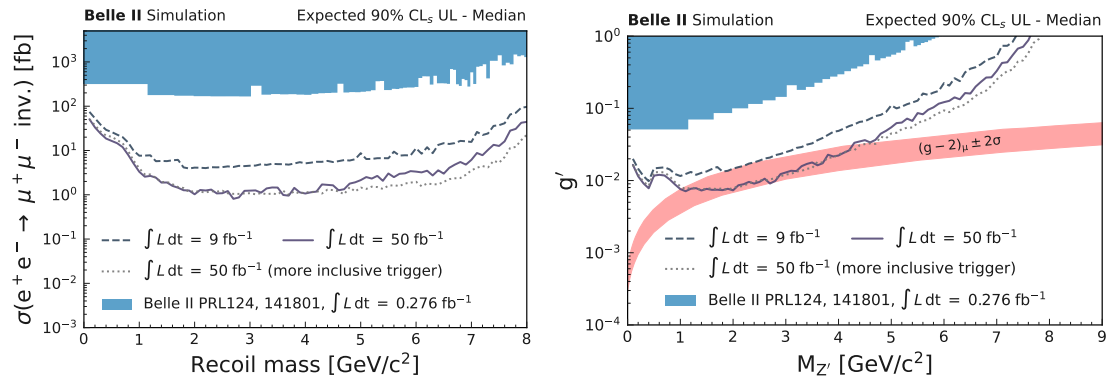

Figure 3.39: Left: Expected 90% CL UL on the Z' cross section (left) and of coupling constant g' (right) assuming a branching fraction $BR(Z' \to \mathrm{invisibe}) = 1$, for an integrated luminosity of $9\,\mathrm{fb}^{-1}$ and $50\,\mathrm{fb}^{-1}$. For the $50\,\mathrm{fb}^{-1}$ case, the effect of using the more inclusive $\mathtt{ff30}$ trigger is compared. The current 90% CL UL set with the Phase 2 data are shown too.

Chapter 4

Search for Dark Higgsstrahlung in $e^+e^- \to \mu^+\mu^-$ and missing energy events

In this Chapter, the search for a dark photon A' and dark Higgs h' simultaneously produced through the dark Higgsstrahlung process $e^+e^- \to A'h'$; $A' \to \mu^+\mu^-$, $h' \to$ invisible with the Belle II experiment is described. This analysis aims to achieve a result with the 2019 Belle II data-set. The entire analysis flow and the expected upper limits on the cross section and the coupling constants product are presented here.

4.1 Analysis overview

An interesting way to probe a non minimal dark sector scenario at an e^+e^- collider is through the dark Higgsstrahlung process $e^+e^- \to A^* \to A'h'$. As illustrated in Sect. 1.4.1, this process consists in the simultaneous production of a dark photon and a dark Higgs, according to the Feynman diagram shown in Figure 1.17. Of the possible experimental final states due to the several decay modes, here it has been investigated the case under the kinematical constraint $M_{h'} < M_{A'}$, i.e., the dark Higgs being the lightest particle: in such a case, the dark Higgs is long-lived and thus invisible to the Belle II detector, while the only detectable particles are the decay products of the dark photon. For this work, the search is limited to the A' decay into a muon pair through the process $e^+e^- \to A'h'$; $A' \to \mu^+\mu^-$, $h' \to$ invisible. The state of the art for similar searches has already been presented in Sect. 1.4.1. The only previous measurement in the same topology was performed by the KLOE experiment, for A' masses up to $\simeq 1$ GeV/c^2, with approximately 1.85 fb^{-1} of data.

In this Chapter, the analysis flow for the dark Higgsstrahlung search is shown, ranging from

the selection optimization up to the expected sensitivity computation on the cross section and on the coupling constant product. The final target is to perform the measurement with the data-set collected by the Belle II experiment at the nominal center-of-mass energy ($\sqrt{s} = 10.58\,\text{GeV/c}^2$) during the 2019 data-taking period, corresponding to an integrated luminosity of $\sim 9\,\text{fb}^{-1}$.

The final state consists of two opposite charge muons plus missing energy. In the case of signal production, the experimental signature would consists of simultaneous peaks both in the distribution of the dimuon invariant mass $M_{\mu\mu}$ (to the mass of the A' candidate) and in the distribution of the invariant mass of the system recoiling against the two muons M_{rec} (to the mass of the h' candidate). The measurement is thus performed in a two-dimensional mass phase space in the range $2\,m_\mu < M_{A'} < \sqrt{s}$ with the constraint $M_{h'} < M_{A'}$ and $(M'_A + M'_h) < \sqrt{s}$ due to energy conservation reason. Therefore, such a measurement would result in a sizeable enlargement of the region explored by KLOE. Most of the relevant analysis plots, shown in this Chapter, show variables as a function of the $M_{\mu\mu}$ and M_{rec} masses, with the interesting region having a triangular shape, being limited on the left by the constraint $M_{rec} < M_{\mu\mu}$ and on the right by energy conservation.

The production cross section of the dark Higgsstrahlung process is proportional to the coupling constants product $\epsilon^2 \times \alpha_D$ and depends on the boson masses. At lowest order it can be analytically expressed as (see Ref. [35]):

$$\sigma_{DH} = \frac{\pi\alpha\epsilon^2\alpha_D}{3s}\left(1 - \frac{M_{A'}^2}{s}\right)^{-2}\sqrt{\lambda\left(1, \frac{M_{h'}^2}{s}, \frac{M_{A'}^2}{s}\right)}\left[\lambda\left(1, \frac{M_{h'}^2}{s}, \frac{M_{A'}^2}{s}\right) + \frac{12M_{A'}^2}{s}\right] \quad (4.1)$$

where α is the electromagnetic coupling constant equal to $\simeq 1/137$ and

$$\lambda(A, B, C) = A^2 + B^2 + C^2 - 2AB - 2AC - 2BC \quad (4.2)$$

The branching ratio of the A' decay into muon pairs is predicted to be just below the 50% level for masses slightly above the kinematical threshold $M_{A'} = 2m_\mu$, then to decrease up to a minimum around 5%, for masses corresponding to the ρ resonance (due to the concurrent decay into hadrons), and then to increase to $\sim 30 \div 40\%$ up to $M_{A'} \simeq 1$ GeV/c^2. For masses above 4 GeV/c^2 the branching ratio into muon pairs stays approximately flat around 15% (see Figure 1.6). In Figure 4.1, the cross section (for $\epsilon^2 \times \alpha_D = 1$) times the branching ratio in muons is shown. Values as high as hundreds of femtobarns are reachable in this model if one assumes $\epsilon^2 \sim 5 \times 10^{-7}$, which is roughly the average limit set by BaBar [83].

This search has several similarities with the invisible Z' analysis described in Chapter 3. The final state is identical (two muons + missing energy), the expected background sources are the same and many of the initial selections are then very similar. A relevant difference is that the Dark Higgsstrahlung analysis is intrinsically two-dimensional, with the goal of looking for simultaneous bumps in both the dimuon and the recoil masses. This introduces non-trivial
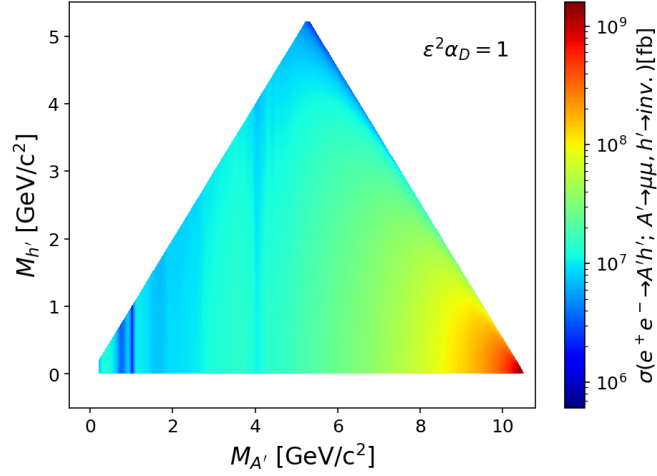
Figure 4.1: Cross-section for $e^+e^- \to A'h'$; $A' \to \mu^+\mu^-$, $h' \to$ invisible process, assuming $\epsilon^2 \times \alpha_D = 1$. The structures (vertical lines) visible for low dark photon masses correspond to hadronic resonances (particularly ρ and Φ whose presence lowers the branching ratio of A' to muons). The vertical line just below 4 GeV/c^2 corresponds to the threshold for the decay $A' \to \tau\tau$, which opens kinematically at $2m_\tau$ and lowers branching ratio of A' to muons.

difficulties into the analysis procedures but, at the same time, allows to drastically reduce the background, which is spread in two dimensions.

The main background sources are all the SM processes which give final states with two muons and missing energy, namely $e^+e^- \to \mu^+\mu^-(\gamma)$ with one or more photons lost due to inefficiency or being out of acceptance, $e^+e^- \to \tau^+\tau^-(\gamma)$ with $\tau \to \mu\bar{\nu}_\mu\nu_\tau$ or $\tau \to \pi\nu_\tau$ (due to pions misidentification in muons) where the missing momentum comes from neutrinos and $e^+e^- \to e^+e^-\mu^+\mu^-$ (two photon processes) with electrons and positrons usually outside the detector acceptance. Only events with two identified muons and no reconstructed photons above a minimum energy in the direction opposite to the dimuon momentum have been selected. Furthermore, the transverse momentum of the dimuon system has been required to be above some threshold, as this selection is very effective against $\mu^+\mu^-(\gamma)$ background. Then, a final background suppression to further improve the analysis sensitivity is presented in Sect. 4.5.

Due to the smallness of the expected background at the end of the selections, a counting procedure, as opposed to a fitting technique, has been chosen. Indeed, over a large part of the mass plane there is no enough statistics to evaluate the background size and shape. This implies the definition of a set of mass windows in a two-dimensional mass plane in which the number of observed events is compared to the expected background. As the the recoil and dimuon masses are kinematically related by eq. 3.2 and experimentally correlated by the fact that they are measured by using the same pair of muons, rotated signal windows, with a variable angle across the plane, are used in order adapt to the signal shape, as described in Sect. 4.4

A blind analysis strategy has been adopted in order to avoid the experimenter's bias. Thus

the selection optimization has been performed by using only simulated samples. The Monte Carlo predictions have been checked with extensive use of control samples, from which correction factors and related systematic uncertainties have been inferred, as described in Sect. 4.6.1.

The strategy for the statistical interpretation was defined in Sect. 4.7, based on a completely Bayesian approach. Then the expected 90% credibility level upper limits to the $e^+e^- \to A'h'$; $A' \to \mu^+\mu^-$, $h' \to$ invisible cross section have been computed, and the results have been translated in terms of the coupling constants product $\epsilon^2 \times \alpha_D$.

Those described here represent a complete version of the analysis flow relating to the dark Higgsstrahlung search. As soon as permission to unblind the 2019 collision data-set is provided by the Belle II collaboration, the full analysis chain will be performed on data.

4.2   Data sets

The analysis chain described in this Chapter has been optimized to be performed on the data-set collected by Belle II during the 2019 data-taking period, referred to as early Phase 3. The useful data-set corresponds to an integrated luminosity of $\int L dt = 8.339$ fb^{-1}, measured by means of Bhabha scattering events. Interesting events have been selected by the low-multiplicity Level 1 CDC trigger (`ffo` trigger logic), as for the invisible Z' analysis. It selects events with at least two tracks with an opening angle between the two candidates in the transverse plane $r - \theta$ exceeding 90°. A trigger efficiency of $\epsilon_{TRG} = 89.8\%$ has been evaluated for this data-set (see Sect. 4.6.2).

As a blind analysis strategy has been adopted, the selections have been optimized by using only simulated Monte Carlo samples. For the signal, Monte Carlo samples with Early Phase 3 geometry and nominal beam background, produced with `basf2` (release-04-00-03) and with the `MadGraph` generator [120], have been used. Different signal samples with and without ISR were produced for later specific uses in the analysis: a total of 9003 samples of 10k events each for signals with $M_{A'}$ ranging from the dimuon threshold up to 10.55 GeV/c^2 and with $M_{h'} < M_{A'}$ was generated. Mass points are located on a two-dimensional grid with spacing corresponding to the mass resolutions in the two directions (see Sect. 4.4). This mass grid was carefully tuned in view of a scanning technique for a hypothetical signal search.

For the background studies, the Monte Carlo samples with the Early Phase 3 geometry and nominal beam background listed in Table 4.1 have been used.

Table 4.1: Early Phase 3 samples used for background studies and the equivalent integrated luminosity $\int L dt$.

Process	$\int L dt$ [fb^{-1}]
$e^+e^- \to \mu^+\mu^-(\gamma)$	450
$e^+e^- \to \tau^+\tau^-(\gamma)$	3000
$e^+e^- \to e^+e^-\mu^+\mu^-$	600
$e^+e^- \to u\bar{u}$	100
$e^+e^- \to d\bar{d}$	100
$e^+e^- \to s\bar{s}$	100
$e^+e^- \to c\bar{c}$	100
$e^+e^- \to B^0\bar{B}^0$	100
$e^+e^- \to B^+B^-$	100
$e^+e^- \to \pi^+\pi^-(\gamma)$	65
$e^+e^- \to e^+e^-(\gamma)$	20
$e^+e^- \to e^+e^-e^+e^-$	300
$e^+e^- \to e^+e^-\pi^+\pi^-$	1000
$e^+e^- \to e^+e^-KK$	1000
$e^+e^- \to e^+e^-p\bar{p}$	1000
J/Ψ	164
$\Psi(2s)$	2500

4.3   Event reconstruction

The event reconstruction is mostly inherited from the invisible Z' analysis (see Sect. 3.3) and, therefore, only relevant differences are described here.

The events are reconstructed by requiring two opposite charge *CleanedTracks* coming from the IP, according to Sect. 3.3. Starting form Phase 3 a reliable particle ID for stable and long-lived charged particles (e, μ, π, K, p, d) based on a combination of measurements from the various sub-detectors is available. Information from each particle identification system (CDC, TOP, ARICH, ECL, KLM) is analysed independently to determine a likelihood $\mathcal{L}_{particle}$ for each charged particle hypothesis. These likelihoods are used to construct a combined global likelihood ratio, defined as: $particleID = \mathcal{L}_{particle}/\sum_i \mathcal{L}_i$ for i in $\{e, \mu, \pi, K, p, d\}$. Therefore, for this analysis tracks are identified as muons by applying a muonID selection requiring $muonID > 0.5$.

The selected tracks are then combined to form a dimuon candidate, being the A' candidate for that event. The recoil system against the dimuon candidate with respect to the center of mass momentum is also reconstructed, being the h' candidate for that event. Additionally, the Rest of Event is reconstructed by applying the same criteria as in Sect. 3.3, and furthermore the kinematic information of the photon closest to the recoil momentum and the kinematic information of the most energetic photon in the event are saved.

4.4   Signal studies

Due to the smallness of the expected background at the end of the selections, a scanning counting technique has been adopted: this implies the definition of a set of mass windows in a two-dimensional mass plane in which the number of observed events is compared to the expected background. Such windows have been built in the squared masses plane, in order to avoid the double-peaked profile (due to a dip at zero) obtained for the recoil mass distribution for signals with h' mass close to zero. The plots of relevant information (such as signal efficiency, expected events and events counted on data) will be shown, however, in the mass plane (not squared mass plane), as it is easier to be interpreted.

As a first step, the widths of the $M_{\mu\mu}^2$ and M_{rec}^2 distributions for different A' and h' mass hypotheses, covering all the interesting phase space, have been estimated. An unbinned maximum likelihood fit for each sample generated with no ISR contribution was performed: both the dimuon and recoil squared mass distributions were parametrized as the sum of two Gaussian functions. As the mean of both Gaussians was fixed to either the A' or h' squared mass value, the resulting PDF consists of three parameters: $\sigma_{\text{Gauss,1}}$ and $\sigma_{\text{Gauss,2}}$, being the width of the first and second Gaussian respectively; and $frac$, the fraction of each function with respect to the normalized sum of both. As an example, the dimuon and recoil squared mass distribution for a given mass point as well as the corresponding fitted PDF model distribution can be observed in Figure 4.2.
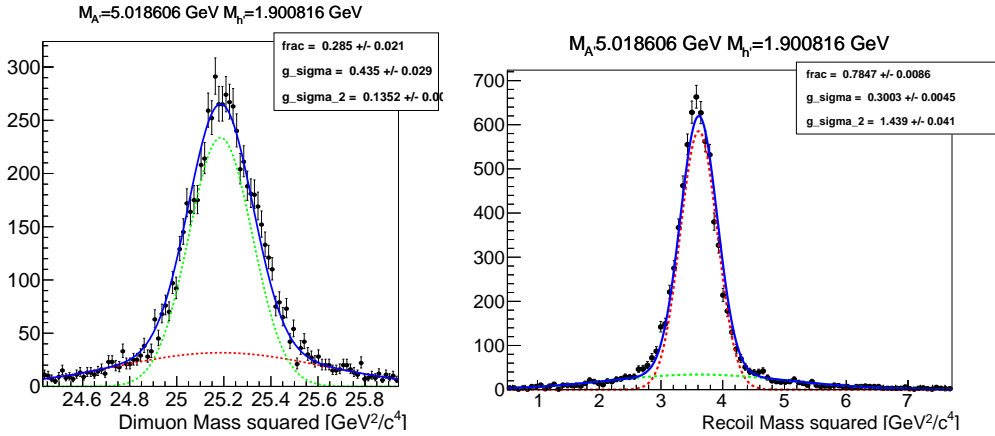

Figure 4.2: Dimuon (left) and recoil (right) squared mass distributions for a casual signal sample $M_{A'}$=3.885452 GeV/c^2 and $M_{h'}$=1.905020 GeV/c^2 with the fitted PDF model overlayed (blue). The contribution of the two Gaussian functions are shown with a red and green dotted line respectively. The resulting fit parameters are shown in the top right corner of every graph.

By taking into account the different contributions of the two Gaussians, a weighted width has been computed for both the distributions as:

$$\sigma_w = \sqrt{frac \times \sigma_{\text{Gauss,1}}^2 + (1 - frac) \times \sigma_{\text{Gauss,2}}^2} \qquad (4.3)$$

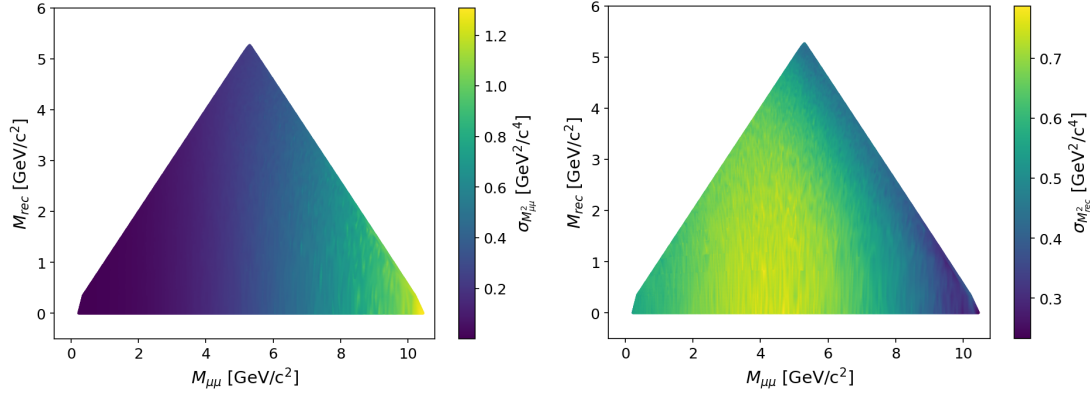The results of such procedure over different A' and h' mass hypotheses are reported in Figure 4.3.

Figure 4.3: Widths of the dimuon (left) and recoil (right) squared mass distributions for A' and h' mass values spanning the interesting mass phase space region.

As the recoil and the dimuon masses are measured by using the same pair of muons, they are experimentally correlated. Two examples of the signal distribution in the 2D mass plane are shown in Figure 4.4. Correlation is always negative and of variable amount across the plane.
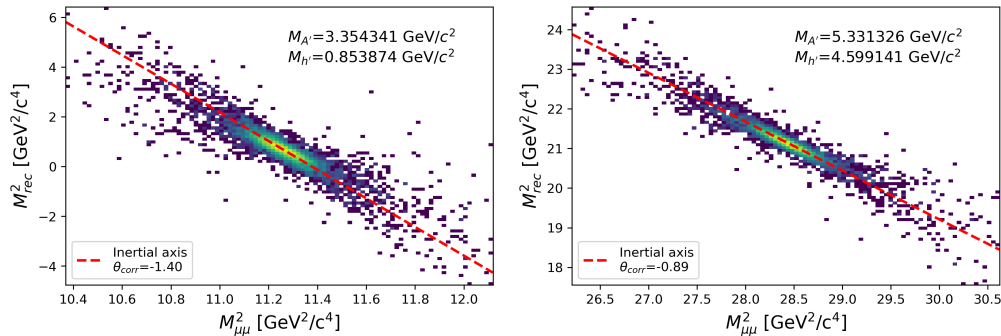

Figure 4.4: Examples of the correlation between the squared dimuon and the recoil mass in two generated signal samples without ISR.

Due to the correlation, a signal window defined by a rectangular cut on the dimuon and recoil mass axes would not be the optimal choice. In order to maximize the signal efficiency while keeping a small background yield, signal windows have been chosen as tilted elliptical windows with a variable angle across the plane. In order to correctly estimate their parameters, a decorrelation procedure was setup. The slope of the distribution in the squared mass plane was computed for each generated $A'h'$ simulated pair without ISR contribution, using the inertial momentum algorithm from rigid body classical mechanics. As an example, see Figure 4.4. The correlation angle magnitude across the plane is shown in Figure 4.5.
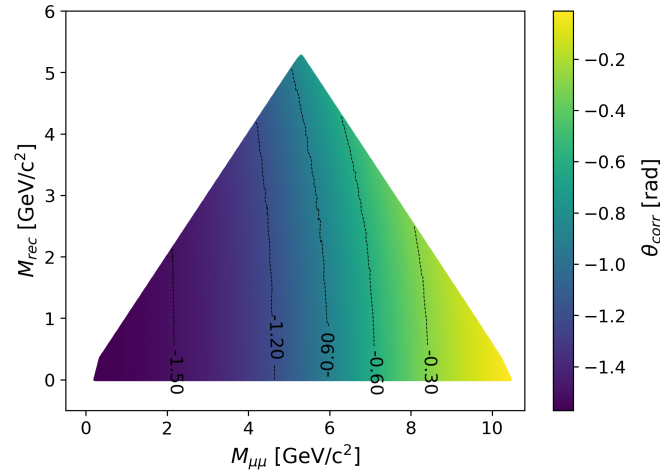
Figure 4.5: Rocoil and dimuon masses correlation angle, computed using the inertial momentum algorithm, as a function of the dimuon and recoil masses.

For each signal sample, a local rotation in the squared mass plane according to the previously computed slope has been performed and two new mass distribution, namely the projection along the correlation axis $M_\parallel^2$ and projection on its orthogonal axis $M_\perp^2$ have been defined. The 1D distributions of $M_\parallel^2$ and $M_\perp^2$ were then fitted separately for each generated $A'h'$ pair. Figure 4.6 shows an example of the fit procedure. The resulting weighted widths for every generated A' and h' mass point are shown in Figure 4.7.
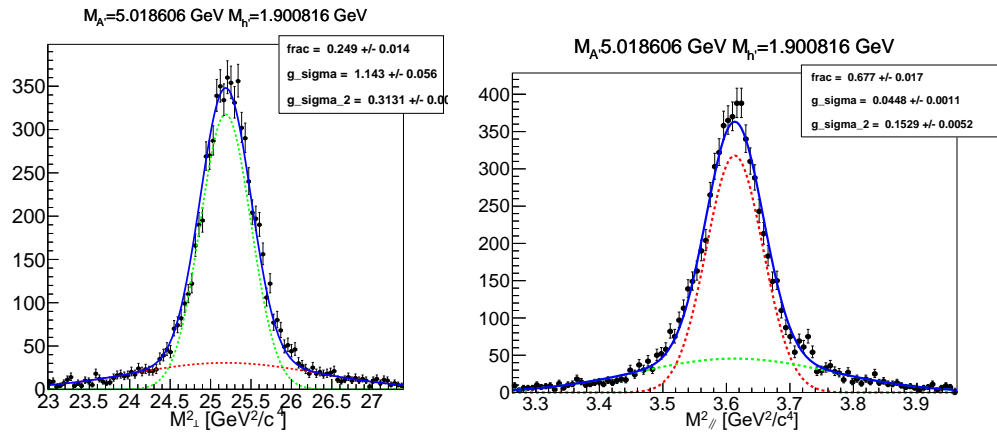

Figure 4.6: Dimuon (left) and recoil (right) squared mass distributions for $M_{A'}=3.885452$ GeV/c^2 and $M_{h'}=1.905020$ GeV/c^2 with the fitted PDF model overlayed (blue). The contribution of the two Gaussian functions are shown with a red and green dotted line respectively. The resulting fit parameters are shown in the top right corner of every graph.

Mass windows have been defined as ellipses centered at the nominal squared mass values, with
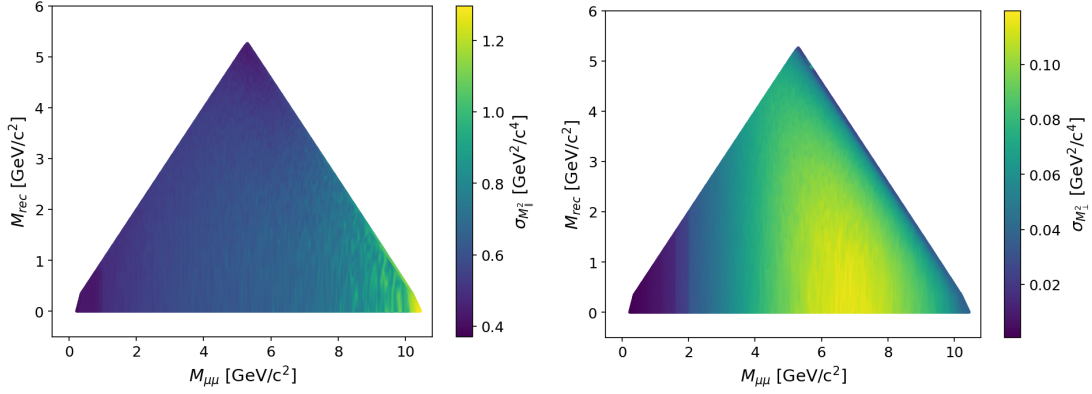
Figure 4.7: Weighted widths for the $M_\parallel^2$ (left) and $M_\perp^2$ (right) distributions for A' and h' mass values spanning the interesting phase space.

semi-axes equal to multiples of the $M_\parallel^2$ and $M_\perp^2$ distributions widths. Optimal values turned out to be widths of 2σ, for most of the phase space, while 1.5σ has been adopted in the right side of the triangle as will be shown in Sect. 4.5. As an example, the squared mass distribution of a given signal with superimposed the corresponding mass window is shown in Figure 4.8. The previously described procedure for estimating the correlation axis and the widths has been performed on samples without ISR generated. ISR introduces a tail in the recoil mass distribution (see, for example, Figure 4.8) only and its presence would introduce a non-trivial complication in the entire procedure described above, which has been therefore performed on samples without ISR. The slopes computed in the samples generated without ISR were checked to reproduce those in samples with ISR, and in any case, for the subsequent estimates of signal efficiency samples with the simulated ISR were used.

The impact of the decorrelation procedure was checked by comparing widths product (which is proportional to the mass window area) before and after the procedure, as shown for example in Figure 4.9. The decorrelation procedure allows to set a mass window that well adapts to the signal shape, with a reduction of the area, and thus the amount of background inside windows, by a factor ~ 3 (depending on the masses) with respect to the case where straight (unrotated) mass windows in $M_{\mu\mu}^2$ and M_{rec}^2 are used.

A total of 9003 overlapping elliptical squared mass windows, oriented according to the angles in Figure 4.5, have been defined. They cover all the interesting phase space region, with a distance between the centers of the ellipses corresponding to the squared mass resolutions in both directions. Figure 4.10 shows the mass windows scheme (the mass windows centers) in both the linear and squared mass planes.

A supplemental set of 9003 enlarged mass windows has also been defined for later use in the background suppression procedure and in the validation procedure (see Sect. 4.6.1). It is made of elliptical windows in the $M_{\mu\mu}^2$-M_{rec}^2 plane, similar to the above defined mass windows, but their semiaxes are set equal to 6σ, thus covering a surface 9 times larger.
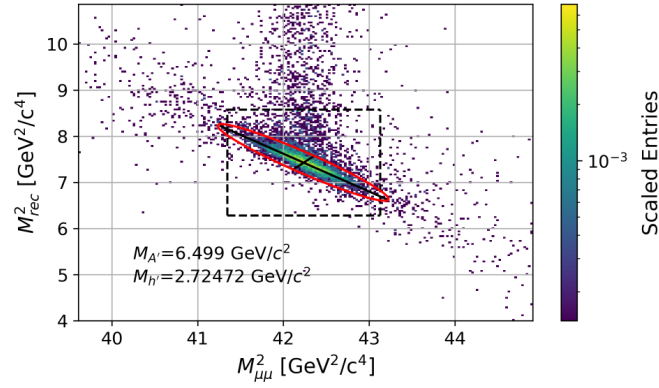
Figure 4.8: Squared mass distribution for a given signal hypothesis. In red, an elliptical mass window centered at the nominal signal squared mass values, with semi-axes equal to twice the widths of the $M_\parallel^2$ and $M_\perp^2$ distributions. As opposite, the dotted square black box represents a rectangular window with dimensions of 4 times the widths of the $M_{\mu\mu}^2$ and M_{rec}^2 distribution. The long tail in the recoil mass distribution is due to ISR contribution.

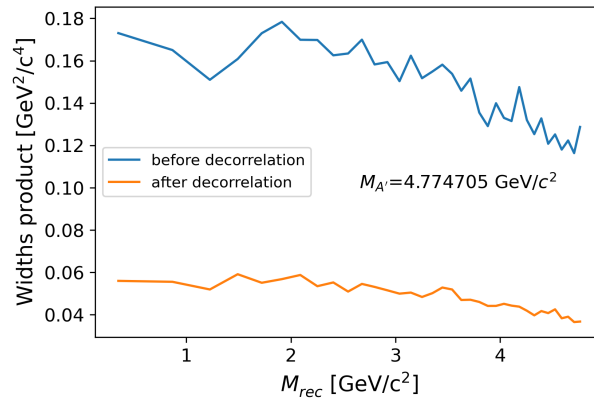Figure 4.9: Widths product before (blue) and after (orange) local rotation for every h' mass point associated to $M_{A'}$=4.774705 GeV/c^2.
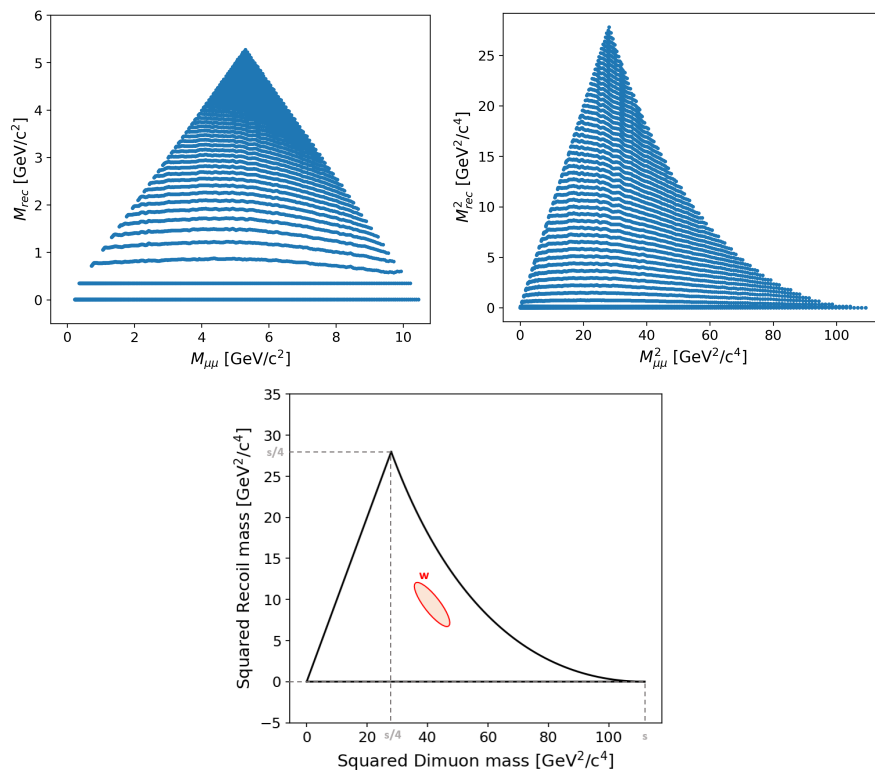
Figure 4.10: Top: Mass windows scheme in in both the linear and squared mass plane. Each point is the center of an elliptical mass window defined in the squared mass plane. Bottom: Squared mass plane, with a mass window W displayed for illustration only (not to scale).

4.5   Event selection

In order to suppress the background contamination, a two level selection has been applied. First tighter selections, called "preselections" in the following, then a stronger selection specifically optimized as function of the candidates mass are applied to each reconstructed event.

4.5.1   Pre-selections

The main background sources are SM processes whose final state is reconstructed as two muons and missing energy: $e^+e^- \rightarrow \mu^+\mu^-(\gamma)$ with one or more photons lost due to inefficiency or being out of acceptance, $e^+e^- \rightarrow \tau^+\tau^-(\gamma)$ with $\tau \rightarrow \mu$ or $\tau \rightarrow \pi$ (due to non optimal particle identification) where missing momentum comes from decay neutrinos and $e^+e^- \rightarrow e^+e^-\mu^+\mu^-$ (two photon processes) with electrons and positrons outside acceptance. The selections applied to suppress this background contamination are largely derived from the Z' analysis, and are re-proposed here for completeness. The following criteria have been implemented:

1. the number of "CleanedTracks" must be exactly 2 and the opening angle between the two muon candidates in the transverse plane must exceed $90°$, in order to emulate the functionality of the `ffo` trigger, that is not simulated in MC;

2. the polar angle of the muon tracks must be within a restricted barrel ECL angular acceptance for a good cluster-matching efficiency and for a good control of the systematics $(37° < \theta_\mu < 120°)$;

3. the recoil momentum must point to the barrel ECL acceptance region $(33° < \theta_{\rm rec} < 128°)$, to exclude inefficient regions where photons can pass undetected and mimic the signal recoil;

4. all events with the closest reconstructed photon within a $15°$ cone from the recoil momentum are discarded;

5. the ROE must have no additional "cdcTracks" and the extra energy in the ECL is required to be less than 0.4 GeV;

6. the transverse momentum of the dimuon candidate in the CMS frame must satisfy $p^T_{\mu\mu} > 0.1$ GeV/c;

7. a veto was setup in order to suppress cosmic tracks, whose reconstructed tracks are artificially split in two, thus passing the reconstruction selection: events with the ratio of the two muon momenta in the LAB frame $0.98 < p_0/p_1 < 1.02$ and with the opening angle (LAB frame) in the transverse plane $\Delta\phi > 179.7°$ were rejected;

8. the energy of the ECL cluster associated with the muon tracks must be below 1.5 GeV. This is effective in suppressing background events from the $\mu\mu(\gamma)$ process with Final State
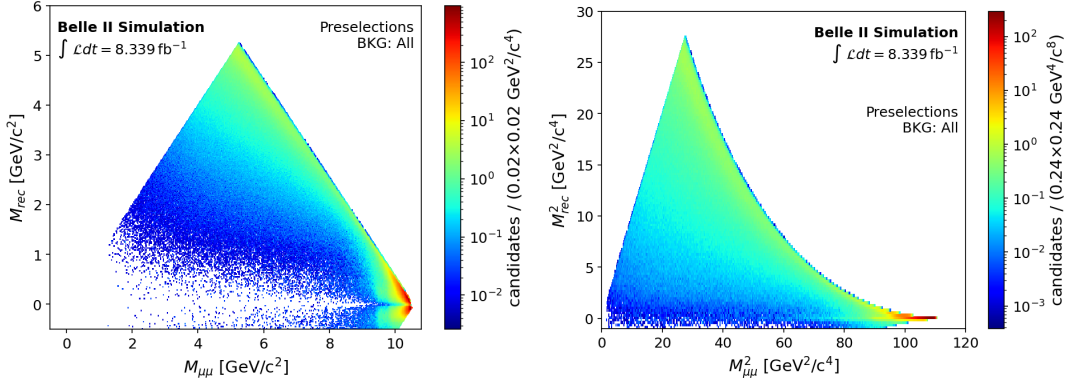
Figure 4.11: Mass distributions (Left) and squared mass distribution (Right) of the total background after the preselections, normalized to an integrated luminosity of 8.339 fb^{-1}.

Radiation (FSR), with an unresolved photon very close to the muon: FSR photons are typically emitted at very low angles with respect to the muon and can produce a cluster in ECL often associated with the track.

In addition to the above selections, the recoil and dimuon masses were required to satisfy the constraint $M_{rec} < M_{\mu\mu}$ and $(M_{\mu\mu} - \sqrt{s}) < M_{rec} < (\sqrt{s} - M_{\mu\mu})$ and $M_{rec} > -1\,\text{GeV}/c^2$, as no signal efficiency outside this region is expected.

The mass distributions of the total background after the preselections, normalized to a luminosity of 8.339 fb^{-1}, are shown in Figure 4.11. All the background sources but the three dominant ones shown in Figure 4.12 are negligible. The three main background sources populate distinct regions of the available phase space. As far as the $\mu\mu(\gamma)$ background source is concerned, this would be naturally expected to populate the low recoil mass region of the space phase due to the ISR photon. However, the above selections require no observed photons and a recoil momentum pointing in the very well equipped barrel region. Thus, for a hard ISR photon, this condition can be hardly satisfied, unless ECL inefficiencies. On the other hand, two hard ISR photons on opposite directions and at low angles (typically outside acceptance) can produce a total momentum pointing to the barrel. This condition typically corresponds to both a high diphoton invariant mass and recoil mass. This explains why most of the $\mu\mu(\gamma)$ contribution accumulates towards the right edge of the phase space triangle. The same mechanism is also the reason why a large part of the $J/\Psi\gamma(\gamma)$ and $\Psi(2S)\gamma(\gamma)$ backgrounds accumulate outside the mass triangle, at high recoil masses (not shown here).

These selections are mainly based on the experience gained in the search for the invisible Z', but their optimal values were checked anyway. As far as the muonID selection is concerned, two more options were investigated, namely, muonID>0.9 and muonID>0.95, as for these values corrections for efficiencies are available from Belle II collaboration studies. It must be noted that after pre-selections two out of the three main background sources ($\mu\mu$ and $ee\mu\mu$) produce real
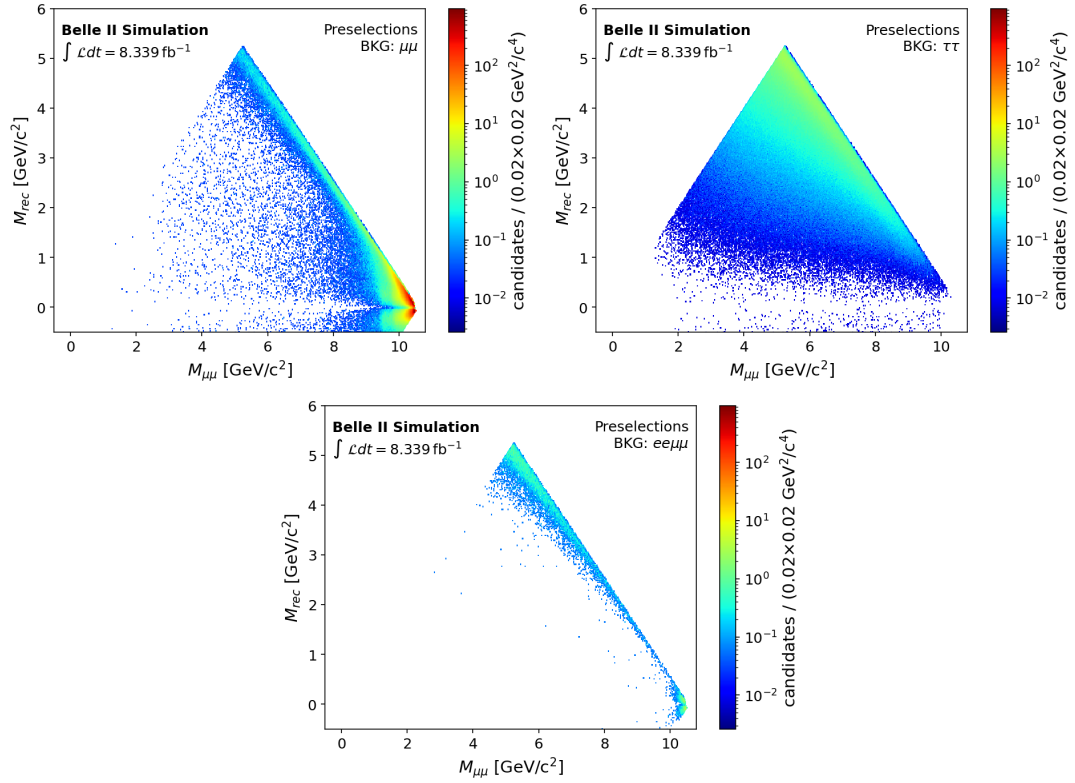
Figure 4.12: Mass distributions of the three main sources of background after the preselections, normalized to an integrated luminosity of 8.339 fb^{-1}. Top left: $e^+e^- \to \mu^+\mu^-(\gamma)$; top right: $e^+e^- \to \tau^+\tau^-(\gamma)$; bottom center: $e^+e^- \to \mu^+\mu^-e^+e^-$.

muons. Regarding the pion contamination due to $\tau \to \pi$ decay, it is found to slowly decrease with the increase of the muonID cut: it is 16.1%, 13.7% and 13.1% for muonID cuts of 0.5, 0.9 and 0.95, respectively. The reason is that pion contamination grows for increasing momentum due to the kinematics of the τ decay, as shown in Figure 4.13, and high momentum pions hardly can be distinguished by muons. As no particular gain in terms of background suppression was not observed in increasing the cut, while it would slightly decrease the signal efficiency, the reference selection muonID>0.5 was kept.

Also the dimuon transverse momentum $p_{\mu\mu}^T$ cut was checked by looking at distributions within many mass windows. It turned out that, on most of the mass plane, $p_{\mu\mu}^T$ distributions after preselections were very similar for signal and background, with minimum values starting approximately at 2 GeV/c. An exception to this situation holds for the region close to the kinematical limit, on the right edge of the mass triangle. This is shown in Figure 4.14. The $p_{\mu\mu}^T$ distributions for signal and background in that region can be easily understood. The background is dominated by the $\mu\mu(\gamma)$ contribution: the peak at $p_{\mu\mu}^T \simeq 0$ corresponds to ISR cases with the photon emitted at very low angles and thus carrying away no transverse momentum; the second peak corresponds to photons emitted at larger angles and coincides with that produced by the signal, which has a similar kinematics, as the dark Higgs has a very low mass in that region. Therefore a loose cut that rejects the $\mu\mu(\gamma)$ collinear background and preserves the signal efficiency as much as possible was set: $p_{\mu\mu}^T > 0.1$ GeV/c, shown as a vertical red line in Figure 4.14. Due to the above considerations, this selection was kept across the full mass plane.
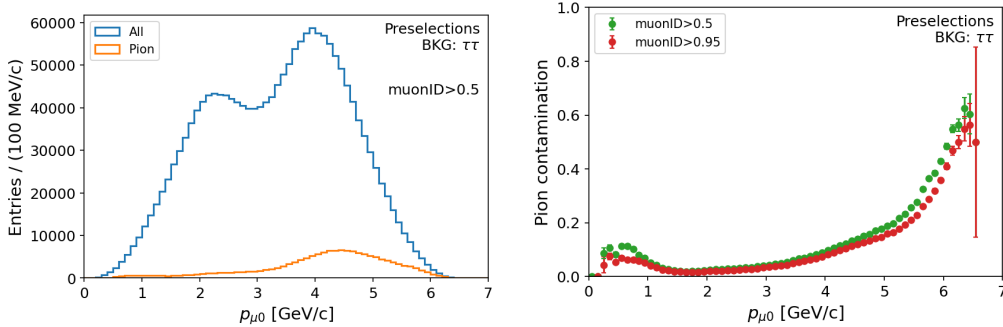

Figure 4.13: Left: Momentum distribution for the $\tau\tau$ background component after the preselection cuts. Right: Pion contamination in the $\tau\tau$ background component for different muonID selections.

The expected background yield and the signal efficiency within $\pm 2\sigma$ mass windows after the pre-selections have been computed, as shown in Figure 4.15 and in Figure 4.16. A luminosity of 8.339 fb^{-1} has been assumed, and a trigger efficiency of 0.898 has taken into account. As for the background within mass windows, it consists of up to few events for most of the plane, with the exception of the right side of the triangle region, where values from tens up to thousands of events at the right vertex of the triangle are expected. As far as the signal efficiency, a region
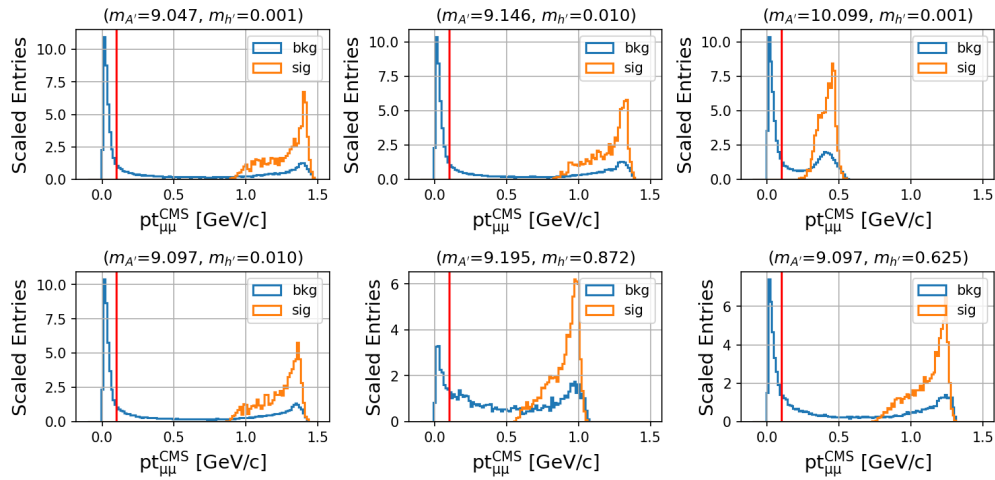
Figure 4.14: $p_{\mu\mu}^T$ distribution for the signal (orange) and background (blue) for mass windows close to the kinematical limit $M_{\mu\mu} = \sqrt{s}$. Not all the preselections have been applied. The vertical red line at $p_{\mu\mu}^T = 0.1$ GeV/c indicates the selection chosen.

with a very poor efficiency can be noted for $M_{A'}$ below approximately 4 GeV/c^2: this is due to the `ffo` trigger, which requires the opening angle between the two tracks in the transverse plane to be above 90°. A large part of this inefficiency will be recovered with the use of the KLM single-muon trigger activated during the 2020 data-taking runs, as it will be described in Sect. 4.8. For $M_{A'}$ above 5 GeV/c^2 the efficiency range from approximately 10% up to 20%.
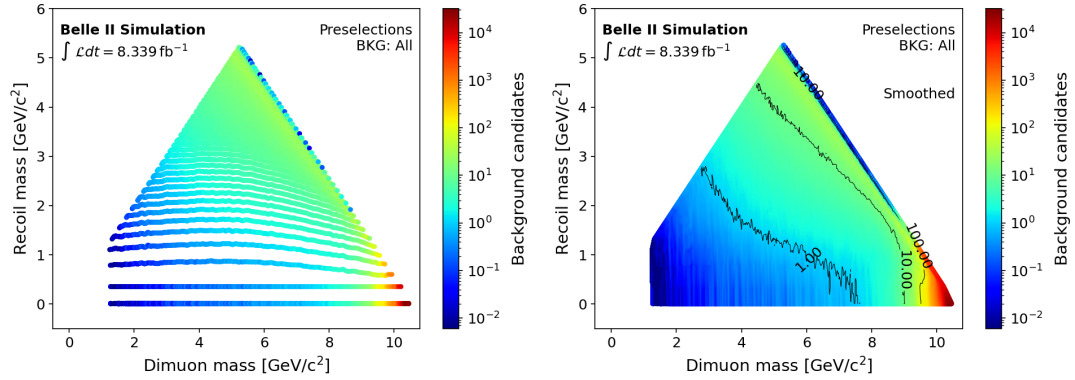
Figure 4.15: Left: Background candidates within mass windows after the preselections, as a function of the dimuon and recoil mass, normalized to an integrated luminosity of 8.339 fb^{-1}. Right: Smoothed version of the Left plot.

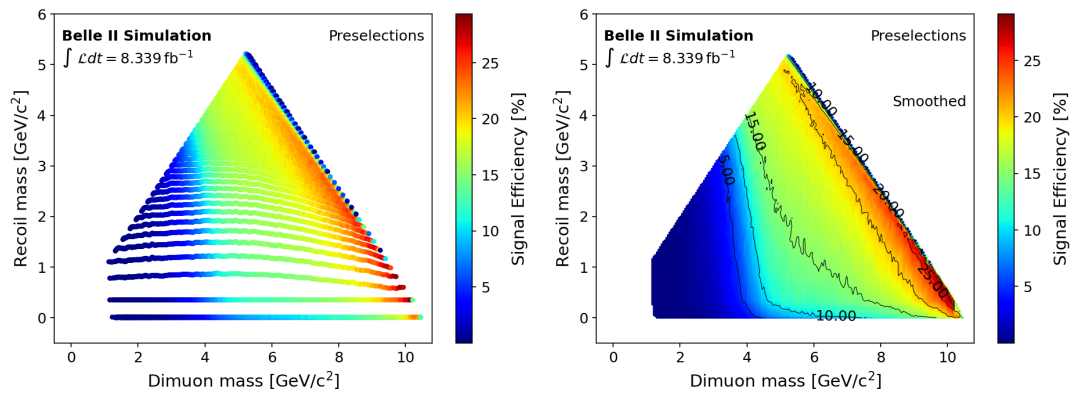Figure 4.16: Left: Signal efficiency within $\pm 2\sigma$ mass windows after the preselections, as a function of the dimuon and recoil mass. The `ffo` trigger efficiency ($\epsilon_{\mathrm{ffo}} = 89.8\%$) has been taken into account. Right: Smoothed version of the Left plot.

4.5.2   Final background suppression

In this subsection, the final background suppression procedure is described. It is based on the kinematic features of the selected events. Rearranging eq. 3.2, the following relation holds:

$$E_{\mu 0} + E_{\mu 1} = \frac{s + M_{\mu\mu}^2 - M_{rec}^2}{2\sqrt{s}} = E_k \tag{4.4}$$

where $E_{\mu 0} + E_{\mu 1}$ are the two muon energies in the CMS frame. The quantity E_k is approximately constant within mass windows, both for signal and background, because the squared dimuon and recoil masses are restricted within $\pm 2\sigma$ intervals (with the additional constraint, for the signal, of the on-shell condition). The relation $E_{\mu 0} + E_{\mu 1} = E_k$ defines a straight line with a slope of -45° and intercept E_k in the $E_{\mu 1}$ vs $E_{\mu 0}$ plane. Events populate a segment of variable length along the line, which depends on the minimum and maximum values that $E_{\mu 1}$ and $E_{\mu 0}$ can assume: they can be analytically computed, and, in the massless approximation, turn out to be:

$$E_{min} = (E_k - \sqrt{E_k^2 - M_{\mu\mu}^2})/2; \tag{4.5}$$

$$E_{max} = (E_k + \sqrt{E_k^2 - M_{\mu\mu}^2})/2. \tag{4.6}$$

Examples of distributions are shown in Figure 4.17 for various $M_{A'}$ and $M_{h'}$ combinations.

A clear signal to background separation can be observed: due to the different dynamical production properties, signals tend to cluster at the center of the segments, while backgrounds populate the ends preferentially.

In order to easily handle this behavior for a suppression of the backgrounds, a new variable called A_E has been constructed being the absolute value of the energy asymmetry of the two muons along the $E_{\mu 0} - E_{\mu 1}$ segment:

$$A_E = \frac{|E_{\mu 0} - E_{\mu 1}|}{\sqrt{E_k^2 - M_{\mu\mu}^2}} \tag{4.7}$$

A visual explanation of the A_E meaning is given in Figure 4.17 (bottom plot).

Distributions of A_E for various $M_{A'}$ and $M_{h'}$ combinations are shown in Figure 4.18. The A_E distribution extends from 0 to 1, with the background concentrated around 1 and the signal following a flat distribution. The A_E definition in eq. 4.7 turns out to be equal to the cosine of the so-called helicity angle θ_{hel}, which is defined as the angle between the flight direction of the A' in the center-of-mass system and the μ^- in the A' rest frame. The distribution of θ_{hel} is entirely determined by the general properties of a massive vector resonance decaying into two fermion particles. For an unpolarized A' the distribution of $\cos(\theta_{hel})$, is expected to be flat, a feature implied by the presence of the three polarization states (two transverse plus one longitudinal, as opposed to the case of the ordinary photon, where only the transverse degrees of freedom exist),
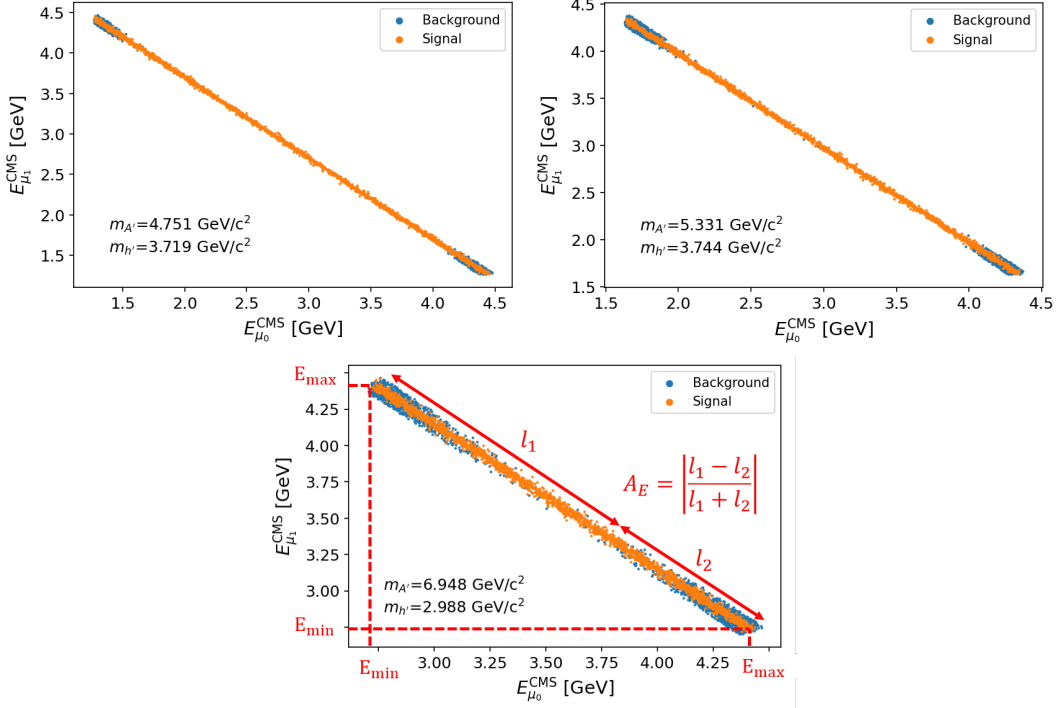
Figure 4.17: $E_{\mu 1}$ vs $E_{\mu 0}$ scatter plot for signal (orange) and background (blue) for three different mass hypothesis. On the bottom plot, the visual explanation of the A_E meaning.

due to the massive nature of the particle. This is not the case for the background, where the helicity angle θ_{hel} can be defined as well, but with no direct physical meaning, as the muons do not originate from a common resonance, coming either from different and independent decays $(\tau\tau(\gamma))$ or from different physics processes $(\mu\mu(\gamma)$ and $ee\mu\mu)$.

In order to suppress the background, a selection $A_E < A_E^{cut}$ was applied. The value of A_E^{cut} for each mass window was found as a result of an optimization procedure.

The optimal A_E^{OPT} cut value was chosen as the one which maximizes the Punzi Figure of Merit, which was introduced in Sect. 3.5 (see eq. 3.4). For the optimization procedure, an orthogonal MC sample with respect to the one used for final background estimation has been used in order to avoid over-fitting effects. In order to keep results as smooth as possible across the plane, the expected background has been estimated into the enlarged mass windows and then scaled to the area of the regular windows: this allows to reduce by a considerable amount the importance of statistical fluctuations. Figure 4.19 shows, as an example, the A_E cut optimization for a certain signal hypothesis.

The A_E cut optimization has been repeated over all the 9003 mass windows, resulting into a map of optimal cut values, shown in Figure 4.20. A_E^{OPT} is found to vary smoothly across the plane, with the exception of the region located at the extreme right of the phase space ($M_{\mu\mu} + M_{rec} > 9.5$ GeV/c^2), which reflects the fact that A_E distributions for signal and background
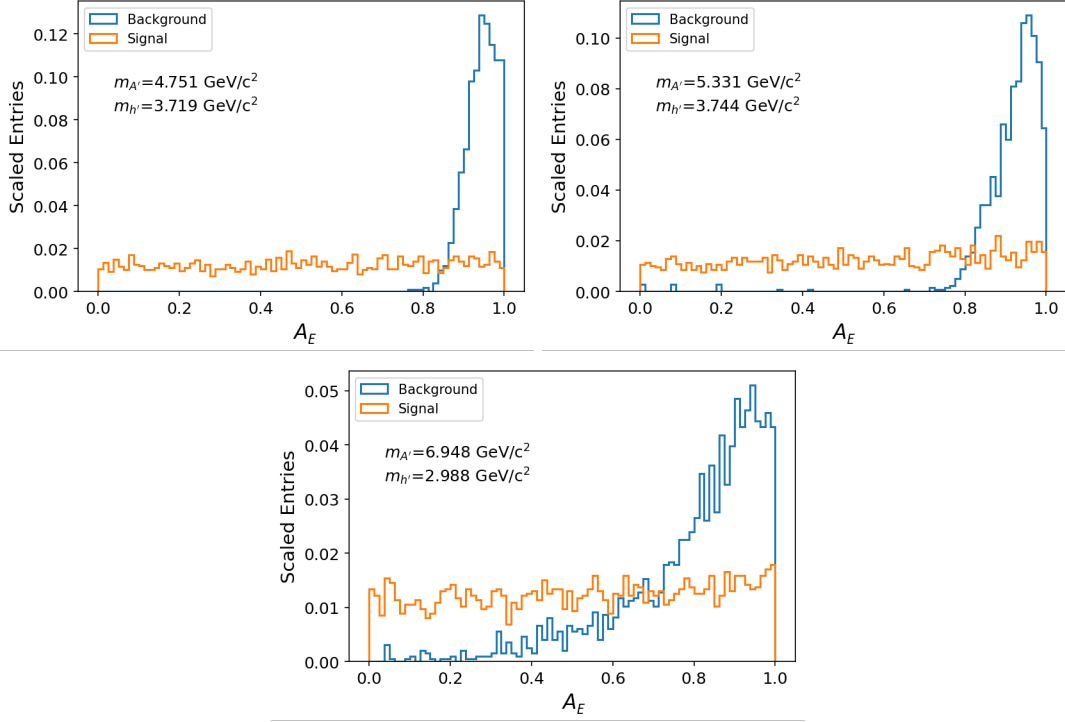
Figure 4.18: A_E distribution for signal (orange) and background (blue) for three different mass hypothesis.

overlap significantly when the sum of the dimuon and of the recoil masses approach $\sqrt{s}$.

While optimizing the A_E final selection, the optimal values of the signal window sizes were checked too. Cases of mass windows widths of ± 1, 1.5, 2.0, 2.5, 3 σ were investigated. It turned out that the $\pm 2\sigma$ choice is optimal for most of the plane, except in the right end region close to the kinematical limit, where the background is higher, being the final A_E selection less effective. Here mass windows of 1.5σ results in a Punzi FoM increase of $\simeq 25\%$ on average. Therefore such a choice was adopted in the region identified by the condition $M_{A'} + M_{h'} > 9.5$ GeV/c^2 or $M_{A'} > 8$ GeV/c^2.

The background and signal efficiencies after the final background suppression, by applying for each mass window the A_E selection which resulted from the optimization, have been then computed, as shown in Figure 4.21 and Figure 4.22. Apart from the area close to the right edge of the triangle, less than one event is expected within mass windows for most of the available phase space, while a signal efficiency of up to 15% is obtained.
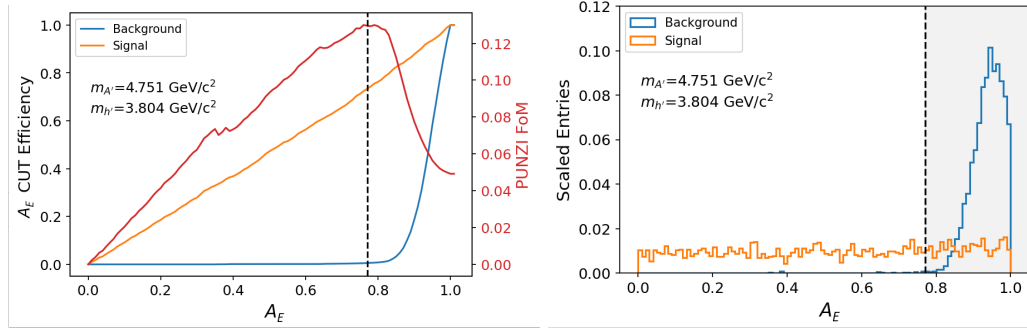
Figure 4.19: Left: Efficiency of the A_E selection for signal and background events as a function of the cut on A_E and the corresponding Punzi FoM. Right: A_E distribution for signal and background. The dashed vertical line mark the A_E value which maximize the Punzi FoM. Events above such a threshold are discarded.
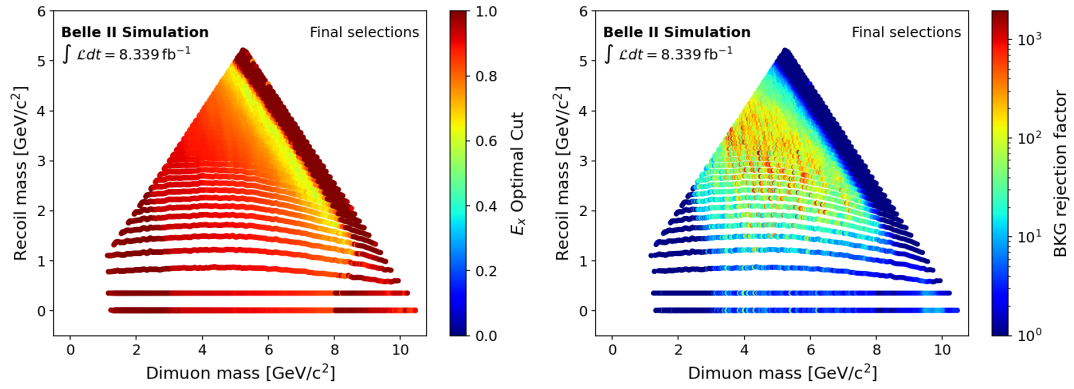
Figure 4.20: Left: Optimal A_E^{OPT} in mass windows as a function of the dimuon and recoil mass. Right: Punzi FoM in enlarged mass windows as a function of the dimuon and recoil mass.
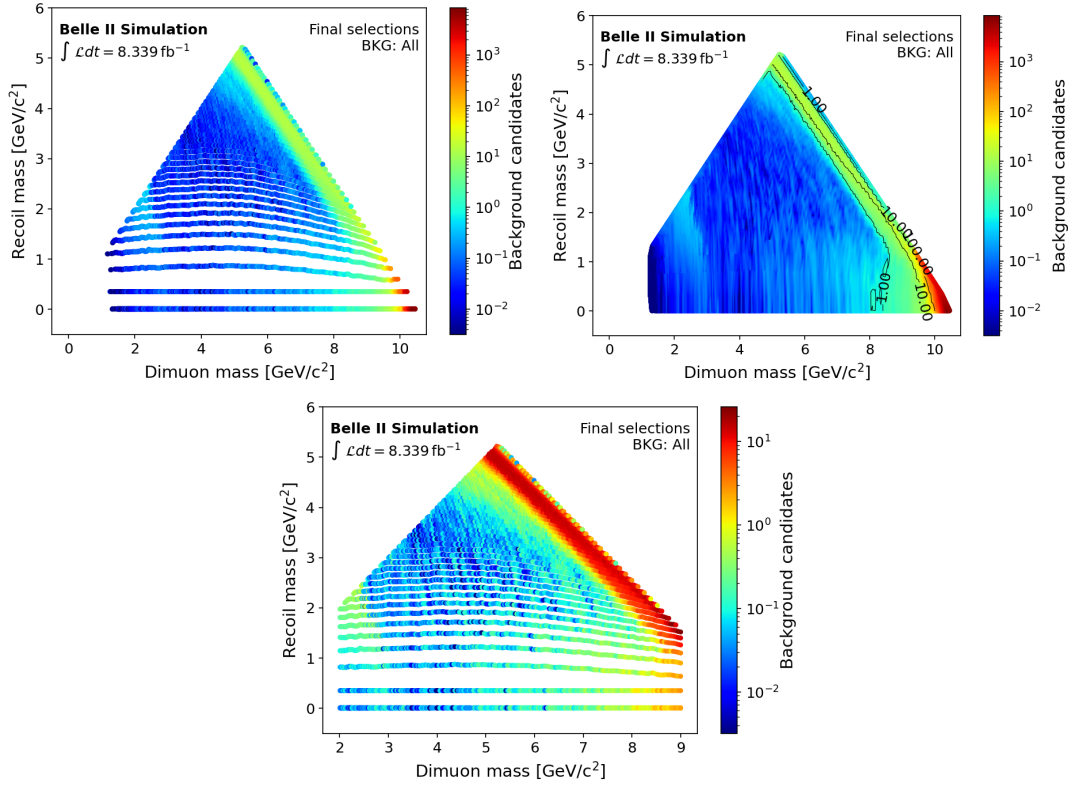
Figure 4.21: Left: Background candidates within mass windows after the A_E selection, as a function of the dimuon and recoil mass, normalized to an integrated luminosity of 8.339 fb^{-1}. Right: Smoothed version of the Left plot.
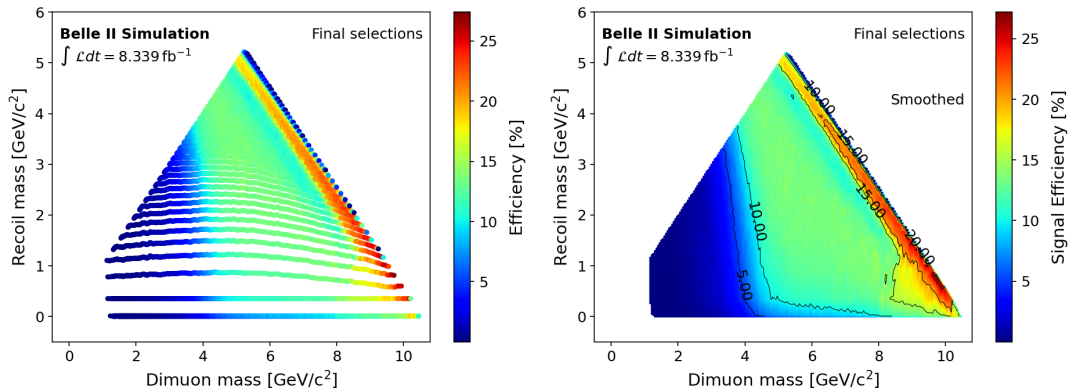
Figure 4.22: Left: Signal efficiency within windows after the A_E selection, as a function of the dimuon and recoil mass. Right: Smoothed version of the Left plot.

4.6 Data validation and systematic uncertainties evaluation

In this Section, data validation studies on control samples and the estimate of the main sources of systematic uncertainties which affect the analysis are discussed.

4.6.1 Data validation studies

Data validation studies on control samples allow to obtain an estimate of the total background yield based on real data and to compare it to the prediction form the Monte Carlo simulation. Furthermore, they permit to evaluate on real data the effect of the individual analysis selections optimized on MC samples as described in Sect. 4.5 for both the pre-selections and the final background suppression procedure, without risk of unblinding the signal in the data sample.

Data validation before unblinding is based on two control samples, where careful checks to ensure that the probability to accidentally reveal the signal is negligible have been performed. The chosen control samples are:

- $\mu\mu\gamma$ *sample.* This is selected by using the same cuts presented in Sect. 4.5, with few modifications. The veto on the recoil photon is dropped. On the contrary, the presence of a photon in the barrel region with a reconstructed ECL energy $E_\gamma > 1$ GeV is explicitly required; the requirement concerning the ECL extra energy, is replaced by the condition $extraE - E_\gamma < 0.4$ GeV. The presence of a photon with a reconstructed energy above 1 GeV decreases the signal efficiency by a factor α_{QED}, thus avoiding any unblinding issue. The resulting sample is dominated by the $\mu\mu(\gamma)$ process, with contributions from $\tau\tau(\gamma)$. The expected 2d background distribution is shown in Figure 4.23(Left).

- $e\mu$ *sample.* This is selected using the same cuts as in Sect. 4.5, with the obvious replacement in particle identification criteria: one track is required to have muonID>0.5 and the other to have eID>0.5. The resulting sample is largely dominated by the $\tau\tau(\gamma)$ process, with one τ decaying to an electron and the other to a muon (or pion, with misidentification). Other contributions, some involving particle misidentification, come from Bhabha, $\mu\mu(\gamma)$, $ee\mu\mu$, $eeee$. The expected 2d background distribution is shown in Figure 4.24(Right).

As opposed to these two final states, the sample being used for the Dark Higgsstrahlung search will be from now on named "measurement $\mu\mu$ sample".

The validation procedure is performed by comparing the number of selected events in data and MC in the $\mu\mu\gamma$ and $e\mu$ samples. They populate preferentially different regions of the mass phase space. In order to disentangle possible different effects and to take into account the background distribution in the measurement $\mu\mu$ sample, the 2d mass plane is split into 6+1 macro regions, as shown in Figure 4.25, which reflect approximately zones where single background sources are dominant: $\mu\mu(\gamma)$ contributes mostly in macro regions 2, 3, 7; $\tau\tau(\gamma)$ in macro regions 1, 3, 4, 5;
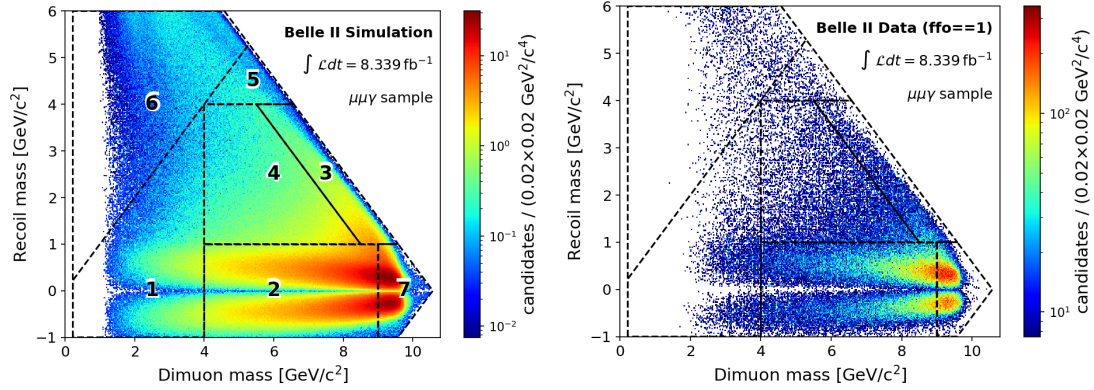
Figure 4.23: Background distribution for the $\mu\mu\gamma$ control sample in Monte Carlo sample (left) and data (right). Overlaid black lines show the macro regions and their numbering.
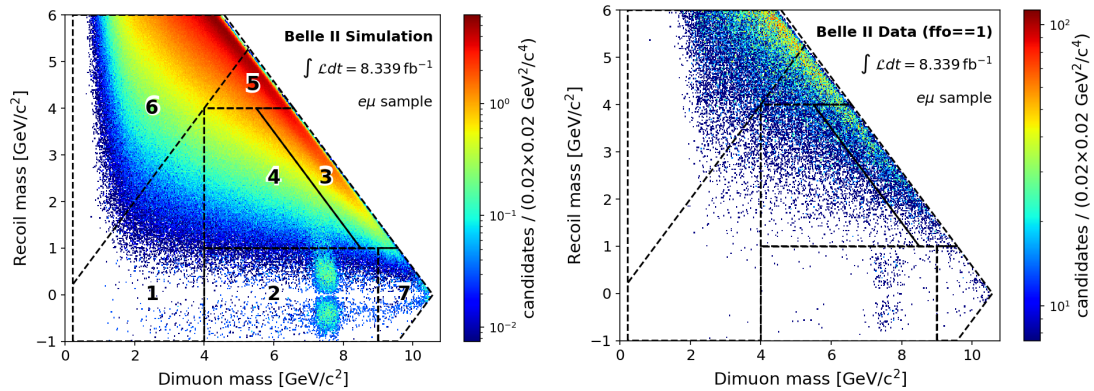
Figure 4.24: Background distribution for the $e\mu$ control sample in Monte Carlo sample (left) and data (right). Overlaid black lines show the macro regions and their numbering.

$ee\mu\mu$ in macro region 5. Macro region 3 is thus shared between the two control samples, but it is dominantly populated by $\tau\tau(\gamma)$ over $\mu\mu(\gamma)$. Macro region 6 is a sideband, being outside the search space, and is mostly populated by $\tau\tau(\gamma)$ and to a lesser extent by $ee\mu\mu$. Results from the $\mu\mu\gamma$ control sample will thus be particularly interesting for macro regions 2, 3, 7; those from $e\mu$ for macro regions 1, 3, 4, 5 (and 6).

The data/MC comparison is performed at three levels:

1. background normalization after preselections. Here data/MC ratios are measured for each macro region for the two control samples. Also effects of single selections are studied and taken into account for later systematics evaluation;

2. validation of background shapes the masses plane after preselections by checking data/MC ration in enlarged mass windows;

Figure 4.25: Background distribution (MC only) for the $\mu\mu$ final state. Overlaid black lines show the macro regions and their numbering.
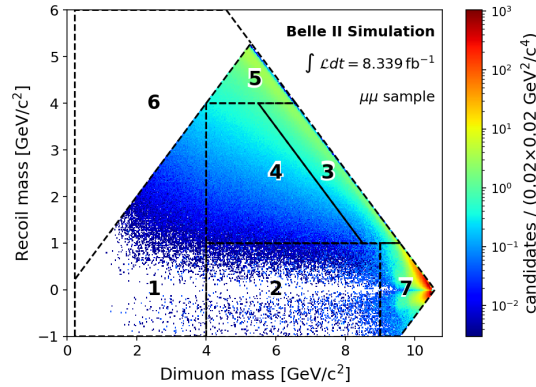
3. validation of the final background suppression variable A_E in enlarged mass windows. Here both the shapes of A_E distributions before the cut and the effect of the $A_E < A_E^{cut}$ cut itself in each macro region are studied.

Data validation in macro regions

Data/MC ratios after the preselections have been computed for the two control samples in each of the macro regions, as shown Table 4.2. Displayed values take into account correction factors for the muonID and eID efficiencies provided by other Belle II collaboration studies. There is a general good agreement, with numbers not too far from 1 and leaving the possibility of applying small corrections to the analysis. Averages in macro regions which are relevant for the two control samples are summarized in Table 4.3.

The entire procedure will be repeated on the measurement $\mu\mu$ sample after the unblinding.

Table 4.2: Data/MC ratios in macro regions for the $\mu\mu\gamma$ and $e\mu$ control samples. Errors are statistical only. MC normalized to an integrated luminosity of 8.339 fb^{-1}.

Macro region	$\mu\mu\gamma$ data/MC	$e\mu$ data/MC
1	0.851 ± 0.013	0.918 ± 0.039
2	0.980 ± 0.004	1.071 ± 0.061
3	1.026 ± 0.013	0.969 ± 0.012
4	1.050 ± 0.010	0.974 ± 0.014
5	1.070 ± 0.046	1.004 ± 0.011
6	0.885 ± 0.022	0.981 ± 0.007
7	0.989 ± 0.006	1.127 ± 0.100
total	0.986 ± 0.003	0.984 ± 0.007

Furthermore, data/MC comparisons as a function of the most important analysis variables have been performed, as shown in Figure 4.26 and Figure 4.27. The data/MC agreement is

Table 4.3: Data/MC ratios in macro regions or group of macro regions most relevant for the $\mu\mu\gamma$ and $e\mu$ control samples. Errors are statistical only. MC normalized to an integrated luminosity of 8.339 fb^{-1}.

Macro region(s)	control sample	data/MC
1,4,5,6	$e\mu$	0.984 ± 0.005
3	$e\mu$	0.969 ± 0.012
3	$\mu\mu\gamma$	1.026 ± 0.013
2,7	$\mu\mu\gamma$	0.983 ± 0.003
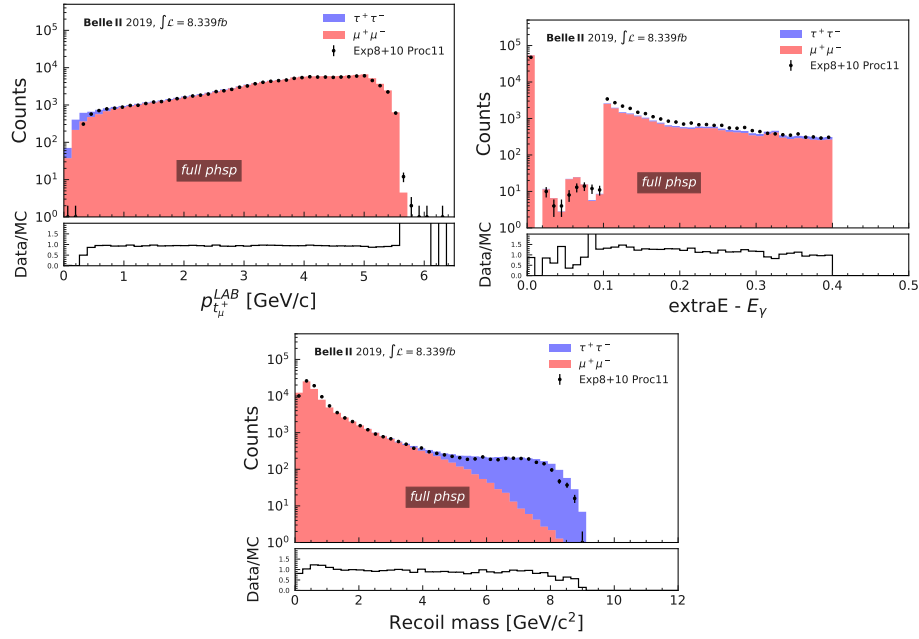
Figure 4.26: Distribution of transverse momentum of the μ^+ candidate, $extraE - E_\gamma$ and recoil mass for $\mu\mu\gamma$ control sample in case of selecting events from the full phase space.

always satisfactory.

As an additional check, the effect of the individual analysis selections based on the important variables for the analysis has been studied. The same selections previously described are applied on the two control samples, with the exception of four cuts whose individual impact on the Data/MC agreement is under check. The four cuts of interest are given below:

- $\mu\mu\gamma$ control sample

    - θ_γ: the polar angle of the photon is required to be in the ECL barrel region.

    - E_γ+ROE: the photon energy is required to be larger than 1 GeV and $extraE - E_\gamma <$ 0.4 GeV.

   - θ_{recoil}: the recoil momentum must pointing to the ECL barrel region.

Figure 4.27: Distribution of transverse momentum of the μ^- candidate, $extraE$ and recoil mass for the $e\mu$ control sample in case of selecting events from the full phase space.

> – $p_{\mu\mu}^T$: the transverse dimuon momentum must be larger than 0.1 GeV/c.

- $e\mu$ control sample

    – no close γ: events with a photon within a 15° cone are rejected.

    – ROE: low activity is required in the ROE with $extraE < 0.4$ GeV.

    – $\theta_{\rm recoil}$: The recoil momentum must pointing to the ECL barrel region.

    – $p_{e\mu}^T$: the transverse electron-muon momentum must be larger than 0.1 GeV/c.

The remaining set of selections applied during these checks is referred to as "baseline selection". For each of these cuts, the effect on the Data/MC agreement was checked by firstly excluding the cut and applying every other selection and then again with this cut applied on top. The resulting impact values for every cut are shown in Figure 4.28 for both control samples in the most relevant macro regions. Most of the values are close to 1 with the biggest discrepancy arising from the ROE cut in the $e\mu$ control sample.

Data validation of background shapes after preselections

The previous checks were aimed at validating the background normalization globally or in macro regions. The subject of this part is to validate the background shapes in the masses plane. In order to work with decent statistical sizes, the data vs. MC agreement has been checked on

Figure 4.28: Impact of individual cuts on Data/MC agreement defined as the ratio of the Data/MC values with and without the selected cut for both control samples $\mu\mu\gamma$ and $e\mu$ in the most relevant macro regions.

control samples at enlarged mass window level (see Sect. 4.4). Enlarged mass windows overlap widely and their contents are consequently ve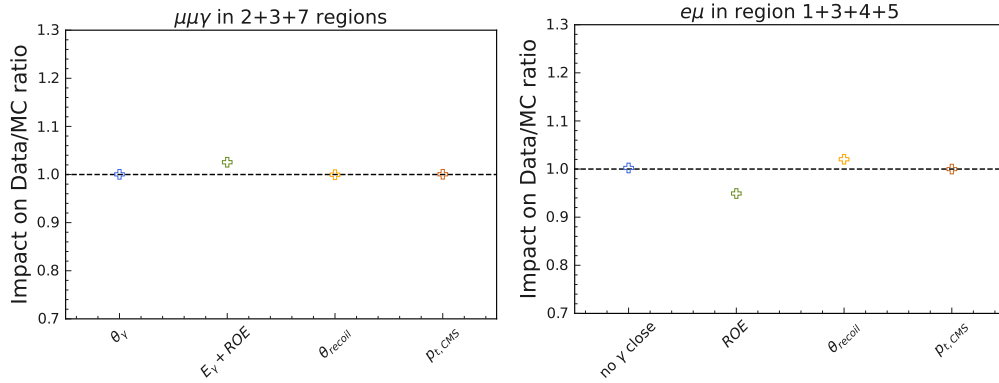ry correlated. This is a complication for the analysis, as fluctuations propagate through neighbouring windows. Thus, to limit this problem, a set of 300 out of 9003 enlarged mass windows was chosen, placed on a sub-grid with a 6σ step (to be compared with the regular grid with a 1σ step). From now on, by enlarged mass windows it is meant this reduced set. Data/MC ratios for such a set of enlarged mass windows for the two control samples were measured and expressed in terms of pulls with respect to the values computed in the macro region to which the enlarged mass window belongs to. In Figure 4.29, only mass windows whose absolute pull value exceeds 2 are shown. In the ideal case, one expects to find about 5% of the windows ($>2\sigma$ effects) in this situation, randomly spread across the plane. Clustering (not due to correlations) of contiguous windows in this situation may spot some local MC problems in correctly reproducing the background shape. Looking at Figure 4.29, while for the $e\mu$ case everything looks compatible with expectations, local effects can be clearly seen for the $\mu\mu\gamma$ one, suggesting some anomalies. However, the presence of the photon in the $\mu\mu\gamma$ control sample is a strong perturbation in the 2-dimensional mass distributions, compared to the $\mu\mu$ case. The study of pulls exceeding 2 points exactly to regions where the phase space of the control sample is greatly different from the measurement sample (as can be observed in Fig. 4.23 and 4.25). While the understanding of such discrepancies should be pursued, their existence is not guaranteed in the measurement $\mu\mu$ sample, implying that this entire study must be repeated on the final data sample after the unblinding.

Data validation of the A_E selection

In this subsection, the final suppression A_E variable distribution and the effects deriving from its use are investigated on control samples. This selection is very effective on most of the mass plane, bringing to a huge background suppression. Thus it is mandatory to check its variable
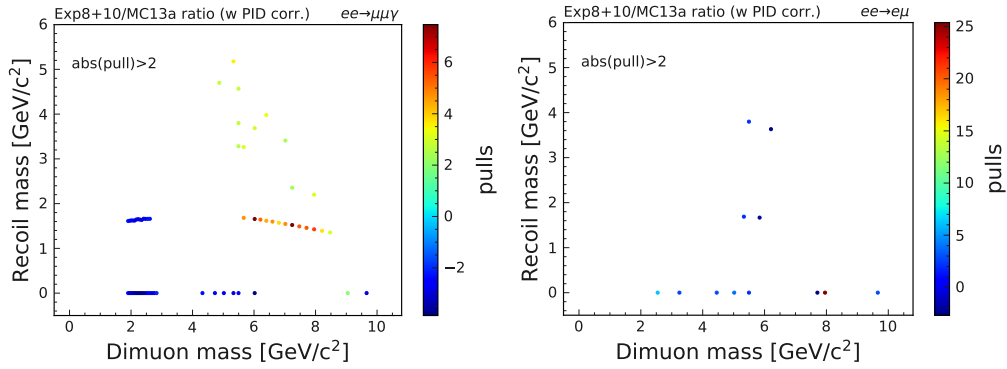
Figure 4.29: 2d distributions of pulls exceeding 2 in absolute value for the two control samples: $\mu\mu\gamma$ case on the left, $e\mu$ on the right.

distribution in MC to well reproduce those in data. At this purpose, the agreement of the shape of A_E distributions in data and MC after the preselections has been checked and then the data/MC ratios in enlarged mass windows after the selection $A_E < A_E^{OPT}$ have been computed.

An example of the shape of A_E in the MC only for measurement $\mu\mu$ sample and the two control samples is shown in Figure 4.30. As far as the shape comparison is concerned, it must be noted that A_E distributions in the $e\mu$ control sample reproduce almost exactly those of the measurement $\mu\mu$ sample apart for a scale factor, which is expected due to the taus decay modes. This is not necessarily true for the $\mu\mu\gamma$ control sample, due to the presence of the reconstructed photon. The data/MC comparison in the last case must thus be meant as a check on the validity of the methodology, rather than a quantitative measure of an expected effect.
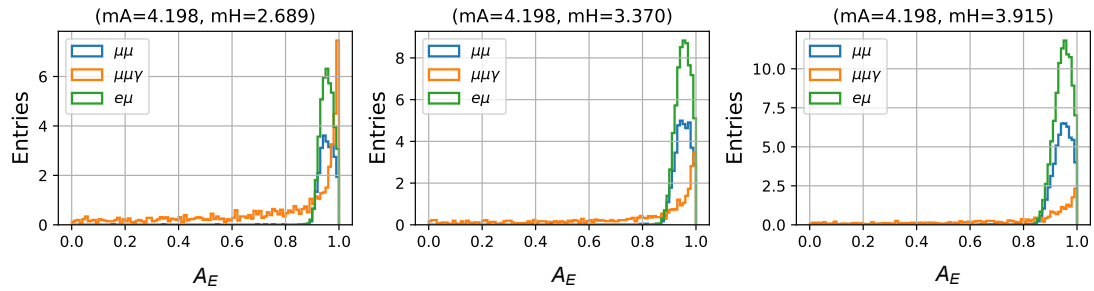
Figure 4.30: Examples of A_E distributions in MC for the dark Higgsstrahlung (blue) search final state and the two control samples: $\mu\mu$ (orange) and $e\mu$ (green).

Examples of A_E distributions in data and MC for the two control samples and for some mass points are shown in Figure 4.31 and Figure 4.32. A good general agreement can be deduced.

In order to produce quantitative statements, the shape comparison was carried out through a Kolmogorov-Smirnov (KS) test, which measures the maximum distance between the cumulatives
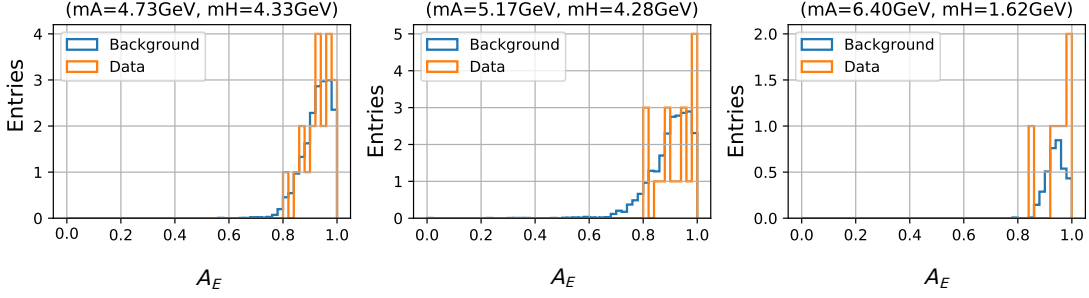
Figure 4.31: Examples of A_E distributions for data (orange) and MC (blue) for the $e\mu$ control sample.
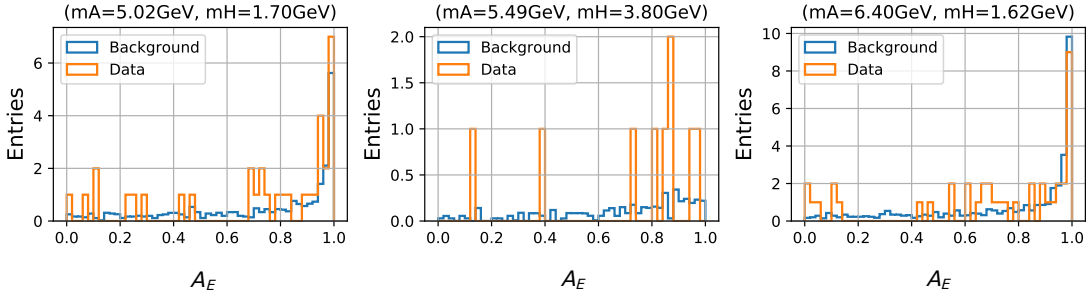
Figure 4.32: Examples of A_E distributions for data (orange) and MC (blue) for the $\mu\mu\gamma$ control sample.

of the distributions being examined. A p-value is associated to such a distance: this was built by producing 1000 pseudo-experiments with fake data generated according to the MC shapes with the data expected statistics and defined as the fraction of cases in which the toy experiment returned a distance larger than the observed one. Kolmogorov-Smirnov distances associated p-values for the two control samples are shown in Figure 4.33. Distributions are reasonably flat, as expected if the shapes agree and their differences are due to statistical fluctuations only, with the exceptions of a peak close to zero. For technical reasons, cases in which an enlarged mass window contained no events, turn out to show a p-value of zero. If these cases are subtracted from the first bin of the p-value histogram, one ends up with a fully flat distribution in the $e\mu$ control sample and with a moderate excess in the $\mu\mu\gamma$ case. This last was closely inspected and turned out to come from cases in which the data and MC distributions were very populated and really close each other (small KS distance), but the severity of the test and probably the imperfect toy MC generation process caused a small p-value. Thus, based on the $e\mu$ control sample a very good data/MC agreement on the shapes of the A_E distributions was deduced.

Finally, the data/MC agreement after the $A_E < A_E^{OPT}$ cut was checked on control samples
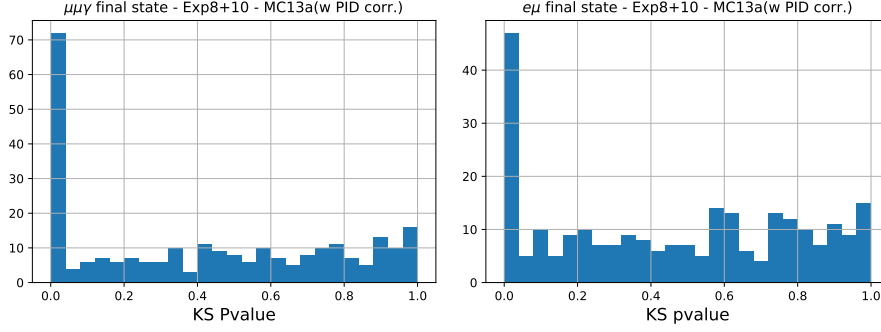
Figure 4.33: Kolmogorov-Smirnov distances associated p-values for the $\mu\mu\gamma$ and $e\mu$ control samples.

at enlarged mass window level. Events in enlarged mass windows belonging to the same macro region were counted and summed up in data and MC. Correlations are negligible, because of the choice of the sub-grid with a 6σ step as explained before. Data/MC ratios results after $A_E < A_E^{OPT}$ selection are shown in Table 4.4: they are almost everywhere compatible or very close to 1, with the exception of the macro region 1, where, however, the statistics is very limited.

Table 4.4: Data/MC ratios in macro regions most relevant for the $\mu\mu\gamma$ and $e\mu$ control samples at enlarged mass window level after $A_E < A_E^{OPT}$ selection. MC has been normalized to an integrated luminosity of 8.339 fb^{-1}.

Macro region	control sample	data/MC A_E cut
1	$e\mu$	0.64 ± 0.16
2	$\mu\mu\gamma$	1.01 ± 0.01
3	$e\mu$	0.99 ± 0.02
3	$\mu\mu\gamma$	1.00 ± 0.02
4	$e\mu$	1.15 ± 0.18
5	$e\mu$	1.02 ± 0.02
7	$\mu\mu\gamma$	1.02 ± 0.01

4.6.2 Systematic uncertainties

There are many systematic uncertainties affecting the dark Higgsstrahlung search: they come either from detector effects, as inefficiencies and resolutions that need to be measured on real data, and from the differences between the simulation, used for the analysis optimization, and data. Both types of contributions need to be estimated with dedicated studies. The most relevant sources are related to trigger, luminosity, tracking efficiency, muonID, effects of analysis preselections, effects of the A_E selection, mass resolution/momentum resolution, dependence of signal efficiency on A' and h' masses, theoretical uncertainties on the model. The evaluation of the systematic uncertainties is closely related to the studies performed with control samples in the previous Section.

Summary from data validation

Uncertainties affecting the background and the signal due to trigger, luminosity, tracking efficiency, muonID, effects of analysis pre-selections are derived from the control sample macro region studies in Sect. 4.6.1 and, more specifically, from the numbers in Tab. 4.3. The measurement of the data/MC ratios in macro regions does not disentangle single contributions, but takes into account all of them globally. Strictly speaking, these studies refer explicitly to the background rather than to the signal. Anyway, being the final state the same and the implied kinematics very similar, they are indeed a very strong constraint on the signal too. As statistical errors are small, the spread of these numbers was assumed as a measure of the systematic contribution due to these sources: a value of $\pm 3\%$ was thus estimated, which apply to both background and signal. The study will be repeated with the final $\mu\mu$ sample after data unblinding and values eventually corrected to take them into account.

Uncertainties affecting the background due to the A_E final suppression are derived from the studies in Sect. 4.6.1 and, more specifically, from the numbers in Tab. 4.4. With the exception of the macro-region 1, whose result is affected by a large statistical error, all the remaining numbers are compatible with 1. Such results were therefore combined and an overall effect of $\pm 5\%$ was conservatively estimated, representing the spread of the data/MC ratio across the macro-regions. This has been considered affecting the background only, as this selection is quite mild on the signal side. Indeed, the shape of the variable is expected to be flat for the signal, and furthermore, differently from the background case, where the A_E cut is very selective and leaves few surviving events, it has a high efficiency on the signal side, typically larger than 50%.

muonID selection

Differences between the *muonID* selection efficiency on data and MC have been estimated by means of a riadiative $\mu\mu\gamma$ sample by Belle II collaboration studies [130]. Its effect has been taken into account by correcting the MC expectations accordingly. The systematic effects arising from the muonID cut can be estimated by assigning an uncertainty of 2% (0.5%) for tracks with momentum value below (above) 1.5 GeV/c. For the kinematic of dark Higgsstrahlung final state muons, the effect has been evaluated to be of the order of 2%. This value has been computed as a check, and results are not used in the total systematic uncertainty evaluation, as they are already included in the macro region studies.

True mass dependence

The signal efficiency used for later on computation (i.e., upper limits estimation on the cross section) has been computed for A' and h' masses generated at the center of the mass window. Uncertainties affecting the signal due to dependence of efficiency on A' and h' masses inside the mass windows are reported here and derive from studies in Appendix B. Signal events were

available only for nominal masses placed at the center of the mass window. Thus, in order to estimate this uncertainty effect, they have been rigidly moved around generic points within the mass window: the operation corresponds to generate the dark photon and dark Higgs nominal masses to these new positions. Then the corresponding signal efficiency has been computed. Signal efficiency of a specific window for different signals samples with true masses across the window is shown as an example in Figure 4.34. In realistic situations, due to the scanning procedure in steps of one mass resolution, only a portion, defining an effective area, of the mass window is interesting, because outside this area the significance will be better in a nearby window (see Appendix B). The distribution of the RMS of such efficiency values within this effective area is typically around 2%, and has been assumed as a systematic contribution.
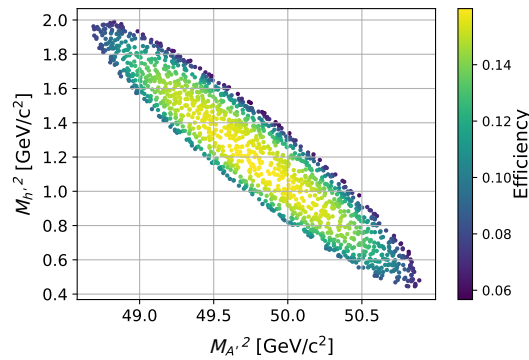
Figure 4.34: Signal efficiency of a specific window (shown as an example) for different signals samples with true masses across the window.

Mass resolution

Systematic effects coming from a data/MC disagreement in dimuon and recoil mass resolutions may affect the estimate of the signal efficiency. They are evaluated in two different ways and then combined: direct measurement of the mass resolutions in data and MC on known resonances, and through measured momentum resolution.

As far as the first method, at the stage of pre-unblinding, the only useful case was the $J/\psi \ \gamma_{ISR}$ final states, with the J/ψ peak in the dimuon spectrum and the associated photon peak resulting from the γ_{ISR} in the recoil spectrum, for which the expectation is zero. Only a few of the selections introduced in Sect. 4.5 have been applied, namely the cosmic veto and selection and the polar angle of both muon tracks to be contained within a reduced ECL barrel region. The presence of a photon with $E_\gamma > 1$ GeV and the `hie` trigger bit fired in data instead of `ffo` were required. When performing the fit on the recoil mass spectrum, it was furthermore required $2.9 < M_{\mu\mu} < 3.3$, $E_{\mu,1} + E_{\mu,2} + E_\gamma > 10.5$ GeV to limit the presence of additional photons which would spoil the expectation of a zero recoil mass.

The kinematic variables, specifically the momenta distributions, are quite different for data and MC J/ψ sample with respect to those of the signal, reflecting the nature of the involved processes, as shown in Figure 4.35. Therefore, a re-weighting technique was performed: the selected events on both data and MC samples are weighted to match the kinematic distribution expected for the signal. The weights have been computed in the bidimensional momentum distribution and then applied to the selected control sample on both MC and data events.
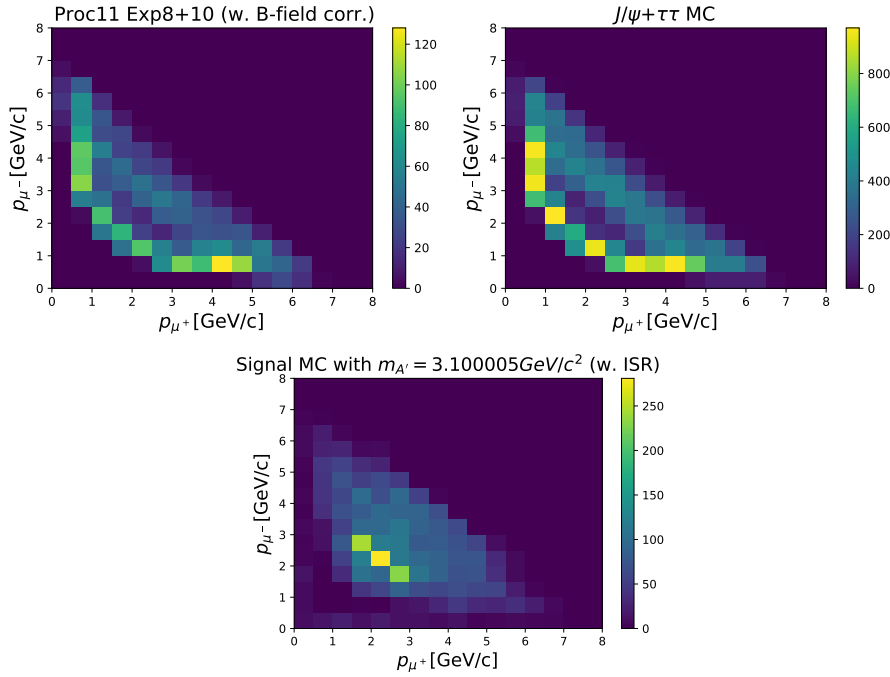
Figure 4.35: Two-dimensional momentum distributions of the two muons for data (top left), J/ψ MC (top right) and signal MC with $m_{A'} = 3.1$ GeV/c^2. The chosen bin size is 0.1 GeV/c × 0.1 GeV/c.

This procedure defines event-by-event weights, then applied when fitting the dimuon and recoil mass distributions. As fit PDF, it was used the sum of a Gaussian and a polynomial of first order to fit the J/ψ peak and the sum of a Crystal Ball and a Gaussian for the photon peak at zero recoil mass. The width of the peaks were estimated as the resulting fit values of the Gaussian (dimuon) sigma and the weighted sigma of the Crystal Ball and the Gaussian according to eq. 3.3. The fitted distributions after the re-weighting technique are shown in Figure 4.36 and 4.37. Discrepancies of the order of $1 \pm 5\%$ (dimuon) and $6 \pm 7\%$ (recoil) are observed. The largest among the measured discrepancies and their errors were kept: 5% for the dimuon mass and 7% for the recoil.

These results need to be somehow extended from the local J/ψ region to the full mass plane. First, the contribution that, added in quadrature to the MC width, reproduce the fitted values in data was estimated. In the absence of additional information, these contributions are assumed
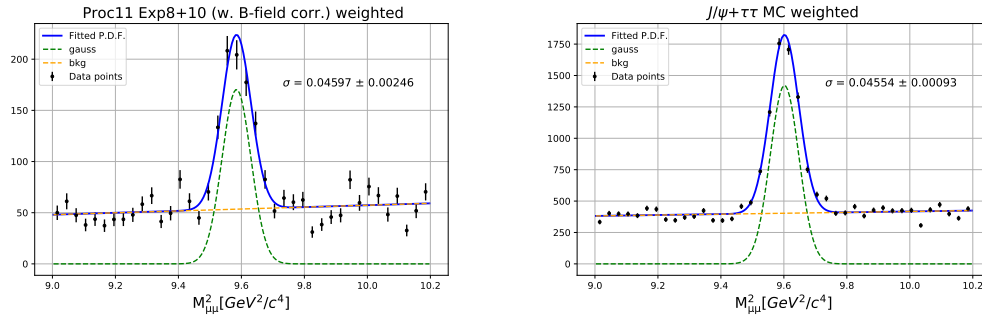
Figure 4.36: Fitted dimuon mass distributions for data (left) and $J/\psi + \tau\tau$ MC (right) with momentum weights applied. The different contributions from the Gaussian and the polynomial are shown in green and yellow respectively. The indicated σ represents the width of the Gaussian.
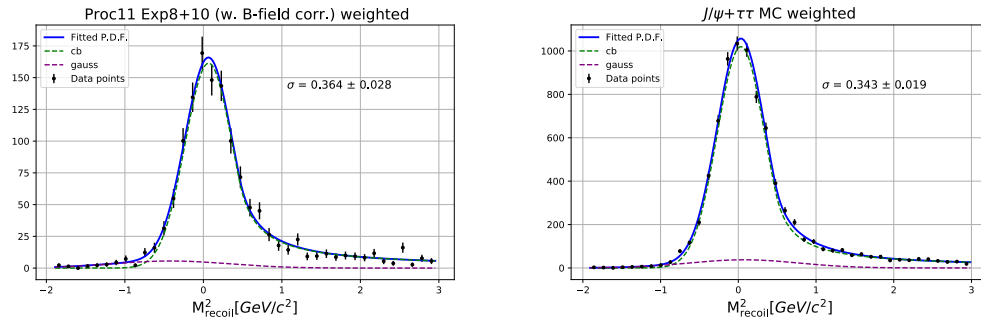
Figure 4.37: Fitted recoil mass distributions for data (left) and $J/\psi + \tau\tau$ MC (right) with momentum weights applied. The different contributions from the Crystal Ball and the Gaussian are shown in green and violet respectively. The indicated σ represents the weighted width of the Crystal Ball and the Gaussian according to Eq. 3.3.

to apply everywhere in the mass plane. Then, a Monte Carlo procedure was set up: on event by event basis, for all signal samples, to each reconstructed mass a value extracted from a Gaussian of expected mean 0 and widths set to the two additional contributions (dimuon and recoil) was added. The analysis selections (particularly the assignment of an event to a specific mass window) are then applied and the variation of efficiency in the mass window is estimated. Results are shown in Figure 4.38 (left).

The mass resolution effect so far estimated suffers from the limitation of having been evaluated in the J/ψ case only and then propagated across the full mass plane, assuming that the same discrepancy holds everywhere. A parallel approach has been developed to overcome this potential issue. Mass resolution is ultimately due to momentum resolution, while other effects being negligible. Momentum resolution has been estimated in two different momentum intervals in other Belle II collaboration studies [131]. For the momentum intervals covered by such a study, an additive term σ_p which, added in quadrature to the Monte Carlo, gives approximately the

measured resolution in data was computed: they are 0.31% and 0.19% for $p_t < 2$ GeV/c and $4.4 < p_t < 5.3$ GeV/c, respectively. For intermediate values in the range $2 < p_t < 4.4$ GeV/c a linear interpolation between 0.31% and 0.19% was used. A Monte Carlo procedure was then put in place, similar to that described in the previous section, by adding to each track momentum a value extracted from a Gaussian of expected mean 0 and width set to σ_p and then recomputing the dimuon and recoil masses, for all signal samples. The analysis selections were then applied and the variation of efficiency in the mass window was estimated. Results are shown in Figure 4.38 (right).
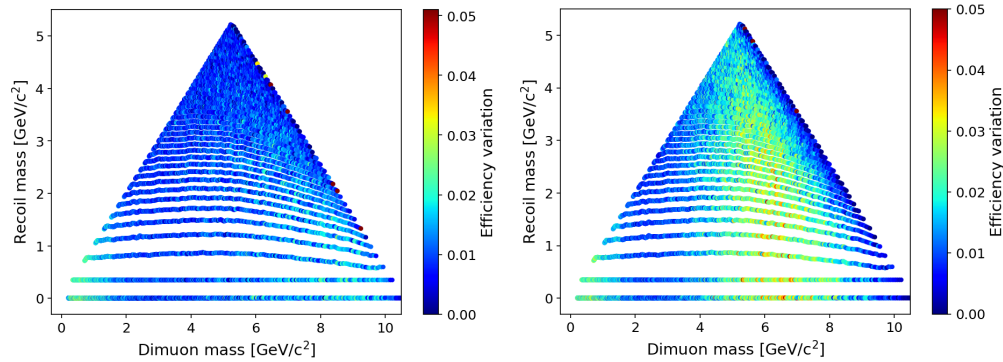
Figure 4.38: Left: Signal efficiency variation due to the mass resolution difference in data and MC, measured at the level of the J/ψ resonance and propagated across the full mass plane. Right: Signal efficiency variation due to the momentum resolution difference in data and MC.

Results estimated in the two previous ways are combined by taking, mass window per mass window, the worst of the two cases, and a flat value of 3% of systematic uncertainties due to the mass resolution was conservatively assumed all across the mass plane.

Systematic uncertainties summary

The main systematic uncertainties affecting the dark Higgsstrahlung measurement are summarized in Table 4.5. A summary of the strategy adopted is given in the following:

- uncertainties affecting the background and the signal due to trigger, luminosity, tracking efficiency, muonID, effects of analysis preselections are collectively evaluated through the control sample macro region studies in Sect. 4.6.1, to be at the order of 3%. Strictly speaking, these studies refer explicitly to the background rather than to the signal. Anyway, being the final state the same and the implied kinematics very similar, they are indeed a very strong constraint on the signal too. They will be repeated on the final $\mu\mu$ sample and the results taken into account;

- uncertainties affecting the background due to the A_E selection are evaluated through the control sample studies in Sect. 4.6.1, to be at the order of 5%. These studies will be

repeated on the final $\mu\mu$ sample and the results taken into account. They haven't been considered for the signal efficiency as this selection is quite mild on the signal side: the shape of the variable is expected to be flat, thus, differently from the background case, where the A_E cut is very selective, it has a high efficiency on the signal, typically larger than 50%;

- uncertainties affecting the signal efficiency due to mass resolution effects have been evaluated to be at the order of 3%. They are related to signal only, as the background distributions are smooth and integrated over areas much larger than the resolution;

- uncertainties affecting the signal due to dependence of efficiency on A' and h' masses inside the mass windows have been evaluated in this section to be at the 2% level;

- theoretical uncertainties on the model enter in the A' branching ratio estimate and affect the sensitivity and the limits expressed in terms of $\epsilon^2 \times \alpha_D$, but not those in terms of the cross section σ_{DH}.

This must be considered as the best effort before data unblinding, and, as such, potentially subject to some revision after data will be fully available and analysed. These values have been used in the sensitivity evaluation in the next Section. Generally speaking, for a statistically dominated analysis with a very low background, systematic uncertainties on the signal efficiency will affect the final results more significantly than those on the background.

Table 4.5: Systematic uncertainty sources, estimate of the effect on signal and background.

Source	estimated effect	target
trigger, lumi, tracking, muonID, presel	3%	background/signal
A_E selection	5%	background
mass resolution	3%	signal
ϵ_{sig} inside mass window	2%	signal
Theory: BR(A')	4%	signal

4.7   Statistical interpretation

In this Section, the statistical treatment of the yields found after the final selection is discussed. As at the moment the analysis is still into a 'blinded' stage, only expected sensitivities can be computed based on the simulated background yields and on the data validation results from control sample. The statistical analysis of the selected events has been implemented in a fully Bayesian approach. Details on the significance test and the upper limits computation procedures to be performed on data after the approval for unblinding, are reported in detail in Appendix B. Particularly relevant is the discussion of the look-elsewhere-effect, which for a 2d mass scan analysis, like the the dark Higgsstrahlung search, must be carefully taken into account.

4.7.1   General strategy

As described in Sect. 4.1, due to the smallness of the expected background (see Fig. 4.21) at the end of the selections a counting procedure was used. The procedure set up relies on comparing the number of observed events with the expected background in mass windows. As described in Appendix B, for each mass window, the following equation holds:

$$N = \sigma_{DH} \times \mathcal{L} \times \epsilon_{\text{sig}} \times \epsilon_{\text{trigger}} + B \qquad (4.8)$$

where N is the observed number of events, ϵ_{sig} is the signal efficiency, B is the MC expected background and σ_{DH} is the cross section of the $e^+e^- \rightarrow A'h'$; $A' \rightarrow \mu^+\mu^-$, $h' \rightarrow$ invisible process.

All the relevant prior distributions have been defined taking into account the following assumptions:

- the likelihood distribution for the model, given the observed number of events, was assumed to be Poissonian;

- the prior distribution for the process cross section was assumed to be flat between 0 and $100 \cdot \sqrt{b}/(\mathcal{L} \times \epsilon_{\text{sig}})$ fb (with the luminosity expressed in fb^{-1}). The effect due to different priors (log-flat, intrinsic, ...) will be investigated, too;

- all the prior distributions related to systematic uncertainties were assumed to be Gaussian, with a width equal to the estimated size of the effect;

- the expected (Monte Carlo) background number of events was assumed to be Poissonian.

The size of the systematic effects is taken from the values in Table 4.5. All the sources are treated as uncorrelated and summed up in quadrature separately for signal and background, with the exception of the uncertainties coming from the macro-region validation studies (accounting for trigger, luminosity, tracking efficiency, muonID and effect of preselection cuts) for which 100% correlation was assumed between signal and background. With the previous assumptions on the

prior distributions, the BAT package [128] was setup to estimate the local/global significance and the 90% credibility level upper limit on the cross section σ_{DH}. Particularly relevant is the discussion of the look-elsewhere-effect, which for a 2d mass scan analysis, like the the dark Higgsstrahlung search, must be carefully taken into account (see App. B.2).

4.7.2 Expected sensitivities

At the moment, as the signal region is still being kept blind due to the ongoing analysis review by the Belle II collaboration, only the expected upper limits on the cross section σ_{DH} have been computed. They are defined as the average upper limits obtained by an ensemble of pseudo-experiments with the expected background B and no signal.

Results for the expected sensitivity to the cross section of the $e^+e^- \to A'h'$; $A' \to \mu^+\mu^-$, $h' \to$ invisible process are shown in the left side of Figure 4.39 as a function of the dimuon and recoil mass, where the MC simulated samples are normalized to an integrated luminosity of 8.339 fb^{-1} and then scaled for the trigger efficiency (89.9%). Cross section results have been translated in terms of upper limits on the product $\epsilon^2 \times \alpha_D$, according to eq. 4.1. They are shown in Figure 4.39 (right) as a function of the dimuon and recoil mass. A smoothed version of the sensitivity in terms of $\epsilon^2 \times \alpha_D$ is shown in Figure 4.40. Results are also shown as a function of the A' mass for fixed values of the h' mass, and as a function of the h' mass for fixed values of the A' mass in Figure 4.41, on the left and the right, respectively.

Belle II is expected to constrain the product $\epsilon^2 \times \alpha_D$ down to $\mathcal{O}(10^{-7})$ in a relevant part of the available phase space.
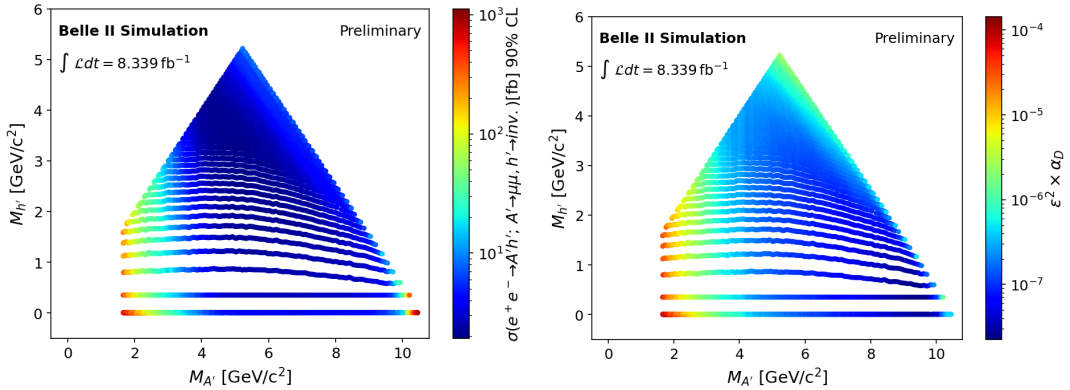
Figure 4.39: 90% CL expected upper limits on cross-section (Left) and on the product $\epsilon^2 \times \alpha_D$ (Right) for the 2019 data-set, corresponding to an integrated luminosity of 8.339 fb^{-1}.

The best ϵ^2 limits available at the moment in the A' mass region covered in this analysis are from BaBar [92] and are roughly flat at the $\sim 5 \times 10^{-7}$ level. As the cross-section of the dark Higgsstrahlung process depends on $\epsilon^2 \times \alpha_D$, one can consider as very interesting regions those for which 90% CL limits $\epsilon^2 \times \alpha_D < 5 \times 10^{-7}$ hold: this is shown in Figure 4.40 as a contour
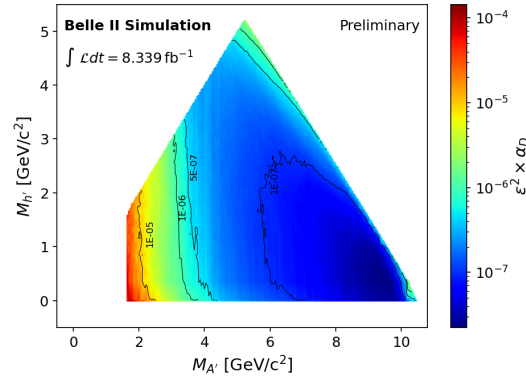
Figure 4.40: 90% CL expected upper limits on the product $\epsilon^2 \times \alpha_D$ for the 2019 data-set, corresponding to an integrated luminosity of 8.339 fb^{-1}. Smoothed version. Contour lines corresponding to $\epsilon^2 \times \alpha_D$ values of 10^{-7}, 5×10^{-7}, 10^{-6} and 10^{-5} are shown.
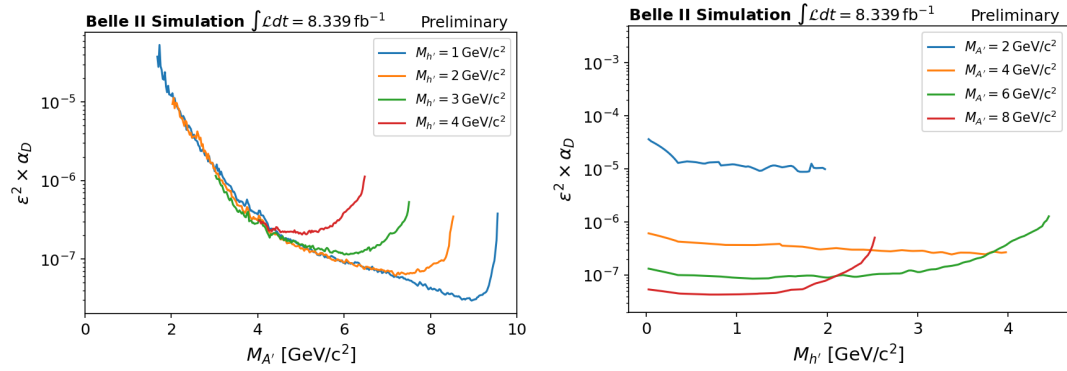
Figure 4.41: 90% CL expected upper limit on the product $\epsilon^2 \times \alpha_D$ versus dark photon mass (left) and dark Higgs boson mass (right) for the 2019 data-set, corresponding to an integrated luminosity of 8.339 fb^{-1}.

line. Alternatively, one can set the coupling α_D to arbitrary values and express the sensitivity in terms of ϵ^2: this is shown in Figure 4.42 for the arbitrary choice $\alpha_D = 0.1$. A sizable region of the accessible phase space turns out to be still below the Babar limits.

It must be remarked that the only measurement in the same topology ($M_{h'} < M_{A'}$) was performed by the KLOE experiment [96], for A' masses up to $\simeq 1$ GeV/c^2, while Belle and BaBar [95, 94] investigated for the orthogonal case ($M_{h'} > M_{A'}$). Therefore, the measurement presented in this work is expected to cover a not yet investigated parameter phase space, significantly extending the mass range investigated by previous experiments.
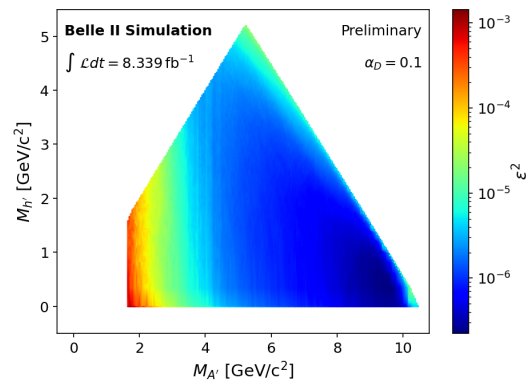
Figure 4.42: 90% CL expected upper limit onϵ^2 for the arbitrary choice $\alpha_D = 0.1$, for the 2019 data-set, corresponding to an integrated luminosity of 8.339 fb^{-1}.

4.8   Future developments

The analysis flow described in the previous section targets a measurement with the 2019 data-set. The next benchmarks for an update of such an analysis may be 80 fb^{-1} and 500 fb^{-1}, corresponding to the luminosity collected during 2020 and to the current estimate of luminosity that can be integrated before the 2022 shutdown (see Sect. 2.6), respectively. Despite the increased luminosity, a major improvement in the measurement is related to the usage of more inclusive low multiplicity trigger lines, which have been activated starting on the 2020 data-taking period. As shown in the previous sections, the signal efficiency (see Fig. 4.22) and then the expected upper limits are strongly limited in the low dimuon mass region due to the `ffo` trigger logic requirements. Events in such a region are expected to have a low opening angle, therefore hardly fulfilling the `ffo` logic, which requires two tracks with an opening angle in the transverse plane exceeding 90°. As an example the transverse plane opening angle distributions of signal for different dark photon masses are reported in Figure 4.43. For masses lower than ~ 4 GeV/c^2 it can be clearly observed how the distribution peaks for angles lower than 90°.
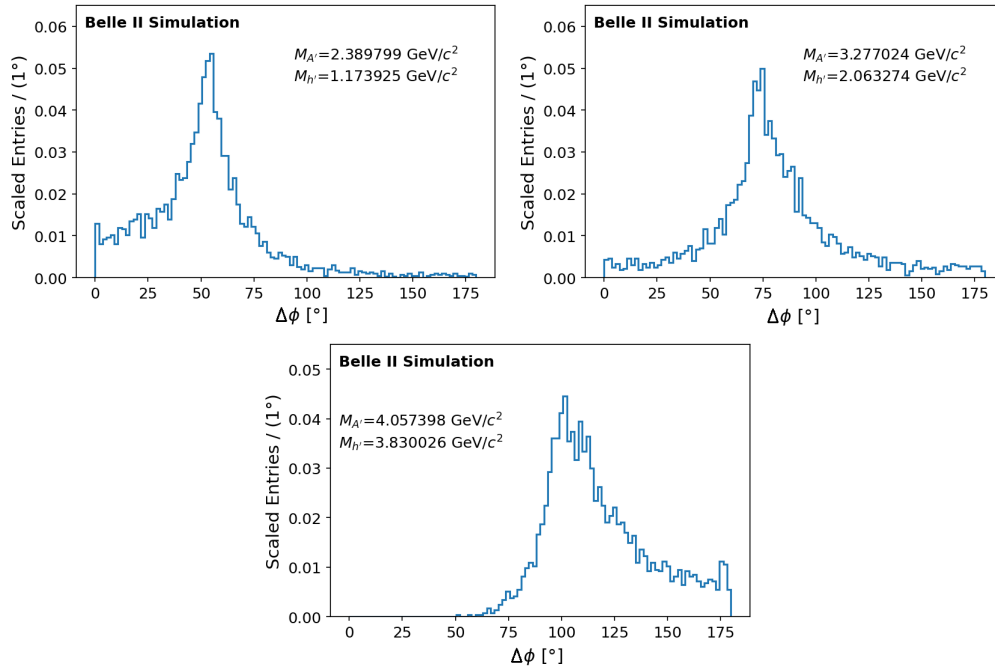
Figure 4.43: Distribution of the two muon opening angle in the transverse plane, for different signal mass hypotheses.

For this mass region, a remarkable improvement is expected with the use of the more inclusive Level 1 triggers that have been activated starting from the 2020 data-taking period. Particularly interesting are the triggers which include information from the CDC and the KLM detectors, namely the `cdcklmX` lines, where `X` is the exact number of CDC tracks matched with fired

barrel KLM sectors, with `X=1,2,3,4`. The interesting lines for the dark Higgsstrahlung analysis are those related to one or two tracks. As a part of this thesis work, the efficiency of the `cdcklm1` line, i.e., the Belle II single muon trigger, has been studied. Details on this study are reported in Appendix A, where the `cdcklm1` efficiency has been measured on μe events from the $e^+e^- \rightarrow \tau^+\tau^-$ reaction. Topologies with more than one muon in the final state can be interpreted using single muon efficiencies as a basis.

Such results have been applied to the dark Higgsstrahlung search case. Specifically, the expected sensitivities for the two benchmark luminosities have been computed by simulating the use of the CDC-KLM triggers in a logical OR with the CDC trigger line `ff30`. The `ff30` efficiency was estimated to be 90% and the effect introduced in Monte Carlo samples by selecting events with an opening angle in the transverse plane (LAB frame) $\Delta\phi > 30°$. The CDC-KLM efficiency and its effect in MC was estimated according to the prescriptions given in Appendix A. The combined efficiency was then estimated as $1 - (1 - \epsilon_{ff30}) \times (1 - \epsilon_{CDCKLM})$, neglecting the effect of correlations: it is typically very high, well above 90%, and almost uniform across the mass plane.

With these assumptions, the expected sensitivities on the cross section for the process $e^+e^- \rightarrow A'h'$; $A' \rightarrow \mu^+\mu^-$, $h' \rightarrow$ invisible in two possible configuration of luminosity have been computed. The same analysis chain, with the same preselections described in Sect. 4.5, was applied to the Monte Carlo samples and the new signal efficiencies and the new surviving background were estimated. The final background suppression selection based on the A_E variable was re-optimized following the same criteria as in Sect. 4.5, and updated to the two luminosity values. Systematic uncertainties estimated through the usage of control samples were reduced according to the square root of the luminosities as dominated by statistics, while the uncertainty due to the mass resolution was reduced to 2%. Finally, the same Bayesian procedure implemented in the previous section was used. Results are show in Figure 4.44 and Figure 4.45
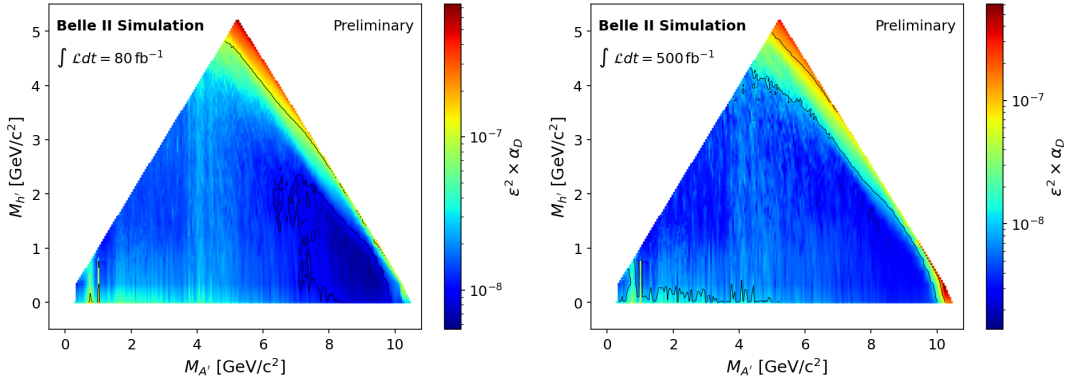
Figure 4.44: 90% CL expected upper limit on the product $\epsilon^2\alpha_D$ for an integrated luminosity of 80 fb^{-1} (left) and 500 fb^{-1}(right). The effect of the trigger lines `ff30` and `cdcklm` is taken into account.
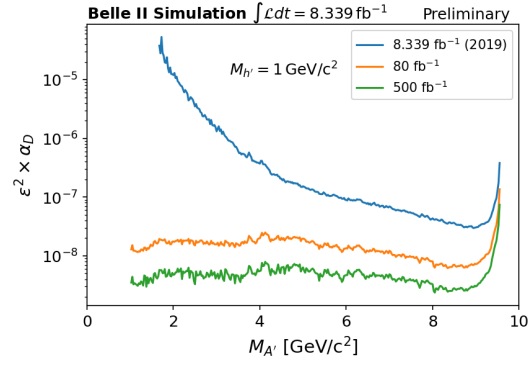
Figure 4.45: 90% CL expected upper limit on the product $\epsilon^2 \times \alpha_D$ versus dark photon mass for the 2019 data-set, and the investigated case of 80 fb^{-1} and 500 fb^{-1}. The effect of the trigger lines `ff30` and `cdcklm` is taken into account.

The effect of the introduction of the new triggers changed drastically the sensitivities for low A' masses, fully recovering the region below 4 GeV/c^2, which was almost blind to the dark Higgsstrahlung analysis with the 2019 data. Elsewhere, the sensitivity is found to scale better than the square root of the luminosity for regions of the mass plane where the background is low, almost approaching a linear scaling for the 80 fb^{-1} case.

Conclusions

The results presented in this thesis concern two searches for dark sector mediators in e^+e^- annihilations at the center-of-mass energy of 10.58 GeV with the Belle II experiment. Two different processes have been investigated, both in a final state with two muons plus missing energy.

The first search presented in this work investigates an invisibly decaying Z' boson (in the framework of a $L_\mu - L_\tau$ symmetry) produced radiatively in the process $e^+e^- \to \mu^+\mu^- Z'$; $Z' \to$ invisible and a Lepton Flavour Violating Z' boson produced in the process $e^+e^- \to e^\pm\mu^\mp Z'$; $Z' \to$ invisible. The data collected during the so-called Phase 2 commissioning run in 2018 have been used, corresponding to an integrated luminosity of 276 pb^{-1}. No anomalies have been observed in data, and 90% CL upper limits on the coupling constant g' in the range $[5 \times 10^{-2} - 1]$ for the former case and to the efficiency times cross section of the order of 10 fb for the latter have been placed. These are the first results for an invisibly decaying Z' and, despite the small data-set used, allowed to explore an interesting new region of the dark sector parameters space. A paper that summarizes the results presented in this work was published in *Physical Review Letters* [1].

A search for a different process has also been presented, consisting in the simultaneous production of a dark photon A' and a dark Higgs h' boson in the Dark Higgsstrahlung process $e^+e^- \to A'h'$; $A' \to \mu^+\mu^-$, $h' \to$ invisible. The full analysis flow, optimized for the 2019 data-set (corresponding to an integrated luminosity of 8.339 fb^{-1}) has been described and the expected sensitivities on the cross section and in terms of the coupling constant product $\epsilon^2 \times \alpha_D$ have been computed. At the moment, the signal region is still being kept blind due to the ongoing review by the Belle II collaboration. Once the permission to unblind the data will be provided, the entire analysis flow studied and optimized in this work will be repeated on data. The only similar measurement was performed by KLOE, for A' masses up to $\simeq 1$ GeV/c^2, thus Belle II is going to provide a sizeable enlargement of the explored region.

Future updates of these analyses are foreseen, as it has been shown throughout this thesis, with the goal to improve constraints on the investigated processes cross sections and on the related dark sector parameters by using larger statistics and detector/analysis improvements.

Appendix A

Measurement of the single-muon trigger efficiency with the 2020 data

As part of this thesis work, the measurement of the efficiency of the Level 1 `cdcklm1` trigger, i.e., the single-muon Belle II trigger, has been performed on the 2020 collision data-set. The use of this and other recently activated triggers, will allow a significant upgrade of the invisible Z' and the dark Higgsstrahlung analyses, improving the sensitivity in the low mass phase space region considerably.

A.1   Overview

Starting from the 2020 data-taking period, new Level 1 triggers which include information from the KLM detector have been activated. Among those, particularly interesting for the analyses described in this work are the `cdcklmX` lines, where `X` is the number of CDC tracks matched with fired barrel KLM sectors, with `X=1,2,3,4`. A KLM sector is fired if the number of layers with hits>0 is greater than 7. The matching is performed only by the ϕ information of the CDC 2D track and fired KLM sector. The `cdcklmX` are exclusive lines, meaning that `cdcklm1` corresponds to exactly one match, `cdcklm2` to exactly two matches, and so on.

In this Chapter, the efficiency measurement of the `cdcklm1` line, i.e., the Belle II single muon trigger, is described. Topologies with more than one muon in the final state may be interpreted using single muon efficiencies as a basis.

The efficiency of the `cdcklm1` line has been measured on data by using an orthogonal trigger as reference. Specifically, it has been used the `hie` line, which requires that the total energy deposition in the barrel and part of the endcap ECL be larger than 1 GeV, and the event not

being classified neither as a Bhabha nor as a $\gamma\gamma$. The trigger efficiency has been defined as:

$$\epsilon_{\text{cdcklm1}} = \frac{N_{\text{cdcklm1}} \& N_{\text{hie}}}{N_{\text{hie}}} \tag{A.1}$$

where N_{hie} is the number of events passing the `hie` reference trigger, while $N_{\text{cdcklmX}} \& N_{\text{hie}}$ is the number of events firing simultaneously the `cdcklm1` and the reference trigger.

A.2   Data sets and event selection

The efficiency of the `cdcklm1` line, has been measured by means of eq. A.1, by using the 2020 Phase 3 collision data. At this purpose, μe events have been used from the $e^+e^- \rightarrow \tau^+\tau^-$ reaction, with τ's decaying to a muon on one side and to an electron on the opposite side, with energy above 1 GeV, thus enough to fire the `hie` trigger line.

In order to reconstruct $e\mu$ events, the following selections have applied:

- two opposite charge tracks originating from the IP, satisfying the following criteria which define the "CleanedTracks" selection: $|dz| < 2$ cm, $|dr| < 0.5$ cm, nCDCHits > 0;

- tracks have been identified as a muon and an electron, by applying a muonID > 0.5 and an electronID > 0.5 cut, respectively;

- both tracks are required to be in the ECL barrel region ($33° < \theta < 128°$), which is wider than the BKLM angular acceptance ($37° < \theta < 130°$, measured at the level of the innermost layer) in the forward direction and almost coincident backward;

- the electron energy deposition in the calorimeter must exceed 1 GeV, in order to selects events able to fire the `hie` trigger line.

A further selection has been applied in order to focus as much as possible on events that come from taus. In principle, this is not necessary, as the presence of an electron and a muon in the final state is enough to measure the trigger efficiency, regardless of the production process. Nevertheless, restricting to $e^+e^- \rightarrow \tau^+\tau^-$ with $\tau \rightarrow \mu$ and $\tau \rightarrow e$ helps in keeping lepton misidentifications, background contaminations and systematics under control. The following additional selections have been applied:

1. all events with a reconstructed photon within a $15°$ cone around the recoil momentum direction are discarded;

2. the transverse momentum of the $e\mu$ pair tracks in the CMS frame satisfies $p_{e\mu}^T > 0.5$ GeV/c.

3. the ROE must have no additional "cdcTracks" and the extra energy in the ECL is required to be less than 0.4 GeV;
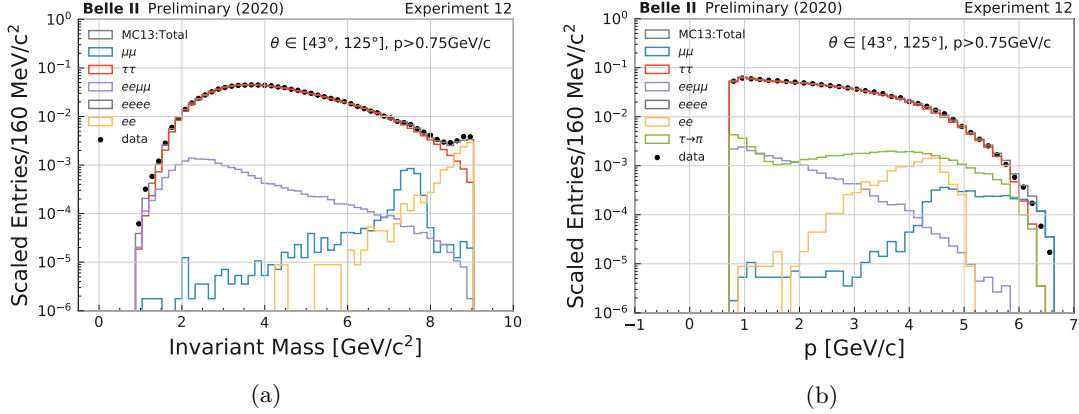
Figure A.1: Invariant mass of the $e\mu$ system after selections (a) and momentum of the muon candidate (b) for data and background sources.

4. the invariant mass of the two candidates must be far from $\sqrt{s}$, specifically less than 9 GeV/c^2;

5. The invariant mass of the two candidates must be above 1 GeV/c^2;

The first four selections are designed to suppress radiative backgrounds, namely $ee\gamma$ and $\mu\mu\gamma$, while the latter is needed in order to suppress a $ee\pi\pi$ background contribution which is ha not been simulated, but appeared evident in the data. The expected sample composition, as evaluated in the simulation, is shown as a function of the invariant mass of the two candidates and as a function of the momentum of the muon candidate in Fig. A.1.

After these selections, various sources of background contribute. The $\mu\mu(\gamma)$ contribution was found to come dominantly from cases in which one of the two muons radiated a hard photon close to the track, producing a cluster eventually associated to it, and then misidentified as an electron. This was checked by verifying that the event recoil momentum was very close to the direction of the muon under scrutiny. The presence of the hard photon explains the invariant mass peak position in Figure A.1 (Left), far from $\sqrt{s}$. Such events are expected to fire the cdcklm2 trigger rather than the `cdcklm1`. Thus, a selection on the invariant mass of the μe system was furthermore performed, excluding the interval between 7 and 8 GeV/c^2, which contains most of the $\mu\mu(\gamma)$ contribution.

The Bhabha $ee(\gamma)$ background was found to come primarily from cases in which one of the two electron directions showed either a polar angle at the border of the forward BKLM acceptance or pointed in azimuth to the regions of separation between adjacent KLM sectors: particles leaking from the electromagnetic showers and traveling along with KLM gaps likely produced some hits in deep KLM layers, which in turn induced high values for the muonID. As the energy depositions in ECL were those expected for electrons (i.e. large), an additional selection to the muon candidate $clusterE < 1.5$ GeV was thus added to easily get rid of this background source.
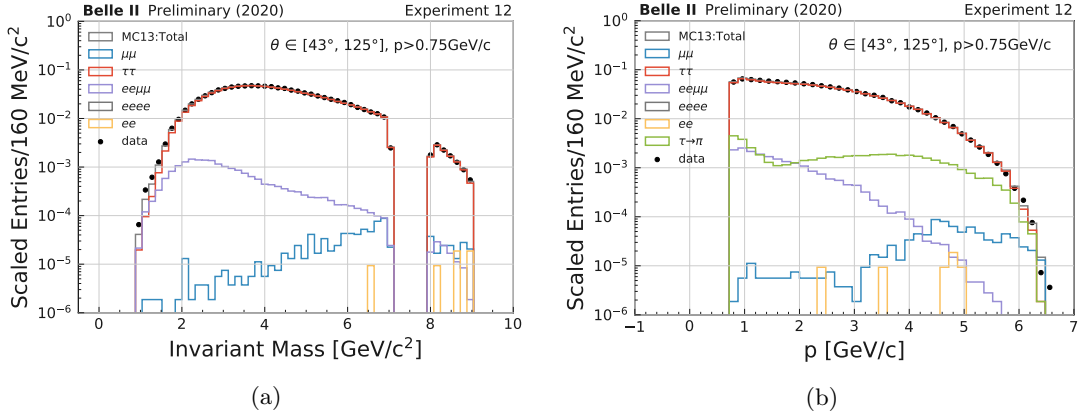
Figure A.2: Invariant mass of the $e\mu$ system after the final selections (a) and momentum of the muon candidate (b) for data and background sources.

The distributions of the μe invariant mass and of the muon candidate momentum after all the above selections are shown in Figure A.2. A very good agreement with data can be observed.

The expected pion contamination in the sample, due to $\tau \to \pi$ decay, is shown in Figure A.3. The bump at low momenta (below 1 GeV) corresponds to the cases of particles not reaching (or barely reaching) the KLM detector, which is the most important device for the muon identification. The contamination grows with increasing momentum due to the kinematics of the $\tau \to \pi$ decay, which has a harder spectrum compared to the leptonic $\tau \to \mu$ case, where two neutrinos are emitted. The overall contamination, averaged over momentum, is 6%. The `cdcklm1` trigger efficiency should be in principle corrected for the pion contamination in the muon sample, but it will not be accounted for in this studies as not trivial. On the other hand, the muonID selection strongly biases the pion distributions to those very similar muons also from the KLM trigger point of view.
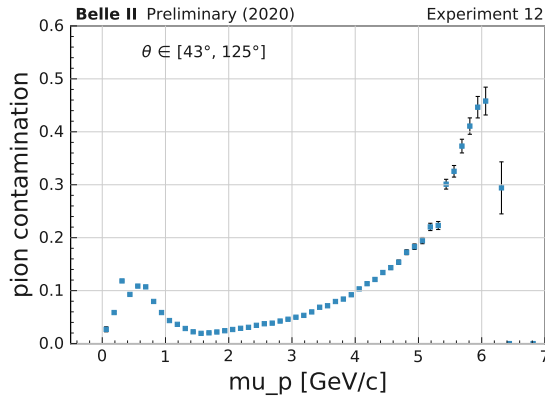
Figure A.3: Pion contamination in the selected muon sample.

A.3   Efficiency dependencies

The `cdcklm1` trigger efficiency has been measured as a function of various kinematic variables, such as the muon polar angle θ, the azimuthal angle ϕ, the muon momentum in the laboratory frame and the track quality.

Dependence on track θ and ϕ

The 2d dependence of the `cdcklm1` trigger efficiency on the polar angle and on the azimuthal angle of the muon for momenta $p > 0.75$ GeV/c (the activation threshold, as explained in the next subsection) is shown in Figure A.4. The inefficiency region corresponding to the presence of the chimney (a KLM detector gap which accommodates solenoid services) is clearly visible in the interval $\theta > 112°$ and $\phi \in [50°, 125°]$
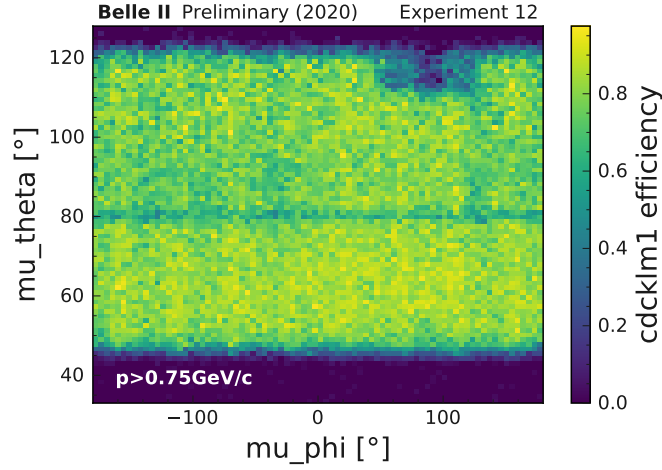
Figure A.4: `cdcklm1` trigger efficiency as a function of the θ and ϕ angles of the muon candidate, for momentum $p > 0.75$ GeV/c.

In Figure A.5a the `cdcklm1` trigger efficiency dependence on the polar angle of the muon is shown, separately for the chimney regions only and for regions in which the chimney has been excluded. One can see the drop on the edges of the BKLM acceptance. The efficiency is zero for polar angles below 43° and above 125° due to geometrical reasons, being impossible for a track with such polar angles to cross eight KLM layers. An approximate plateau region can be recognized for $\theta \in [51°, 117°]$. Also visible is the drop around 80°, corresponding to the separation between the forward and the backward part of BKLM.

The `cdcklm1` trigger efficiency dependence on the azimuthal angle of the muon is shown in Figure A.5b, separately for the chimney regions only and for regions in which the chimney has been excluded. The modulation of the different BKLM sectors is clearly visible.
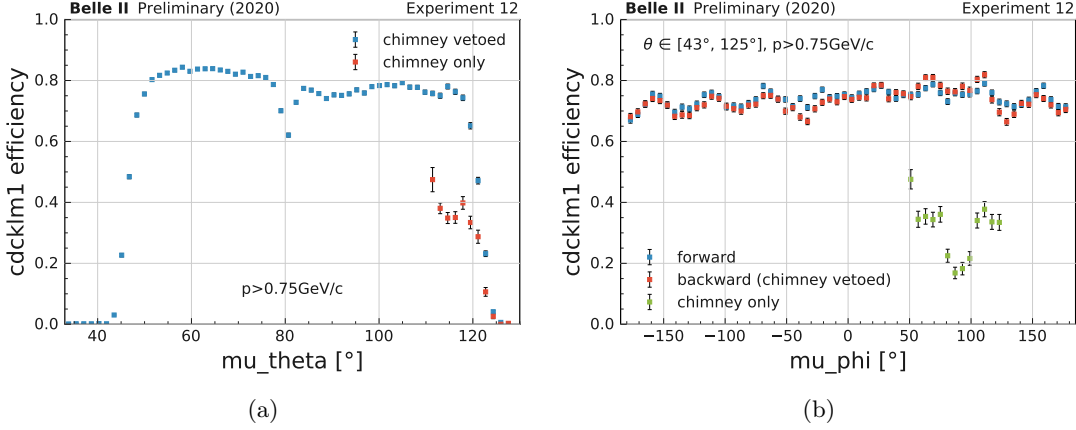
Figure A.5: `cdcklm1` trigger efficiency as a function of the θ (a) and ϕ (b) angle of the muon candidate, for momentum $p > 0.75$ GeV/c. Efficiencies computed separately inside and outside the chimney region. In plot (b) ϕ dependencies are shown separately for the forward and backward BKLM.

Dependence on track momentum

The `cdcklm1` trigger efficiency dependence on the muon momentum measured in the LAB frame is shown in Figure A.6. Efficiencies are here computed excluding the chimney region. Two different situations are shown: tracks with polar angles between $43°$ and $125°$ and tracks in a more restricted region of polar angles between $51°$ and $117°$. The `cdcklm1` trigger efficiency activation is approximately at $p = 0.75$ GeV/c, which corresponds to the minimum momentum for a track to reach the KLM detector. One can distinguish approximate plateau regions extending from 1.2 GeV/c up to 5 GeV/c and 6 GeV/c for the two cases. For the [$43°$-$125°$] range, the efficiency drops above 5 GeV/c due to a momentum-polar angle correlation effect coming from the collision boost (see Fig. A.7). For the [$51°$-$117°$] range, the efficiency stays approximately stable up to 6 GeV/c. The `cdcklm1` trigger efficiency dependence on the muon LAB momentum was deeply studied in different polar angle intervals, each corresponding to approximate plateau regions: this is shown in Fig. A.8a. All the curves activate at about 0.75 GeV/c. Some of them reach the plateau around 1.4 GeV/c, others around 2 GeV/c. This pattern suggests the opportunity to compute integrated `cdcklm1` trigger efficiencies in 2d $p - \theta$ regions of different sizes: results will be shown in Fig. A.11 and in Table A.1. Due to the nature of the selected $e\mu$ sample, the statistics is poor for momenta above 5 GeV/c, where only the forward θ intervals are populated, because of the collision boost.

Dependence on muonID cut

The impact on the muonID cut value on the trigger efficiency for the three reference values (0.5, 0.90, 0.95) has been evaluated, as shown in Figure A.8b. Detailed results are presented in Tab. A.1, A.2 and A.3
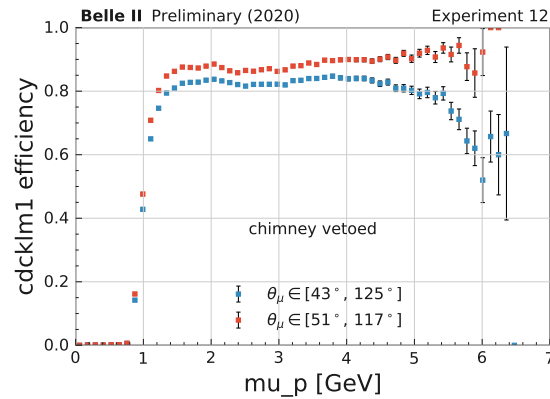
Figure A.6: `cdcklm1` trigger efficiencies as a function of the muon momentum in two different polar angle intervals: [43-125]° (blue points), [51-117]°(red points).

Dependence on track quality

The `cdcklm1` trigger efficiency as a function of the number of the CDC hits is shown in Figure A.9. These results will be later used for a study of the systematic uncertainties affecting these measurements.

Dependence on run number

Furthermore, the efficiency stability over the time has been checked by studying its variation as a function of the run number as shown in Figure A.10. Vertical lines mark a subdivision in seven different data-taking periods, separated by no collisions periods. Efficiencies look roughly consistent along the full data taking, with the exception of the first period, where lower values are clearly visible. Those samples have been excluded from this analysis.

These results will be later used for a study of the systematic uncertainties affecting the trigger efficiency (see sec. A.4.1)
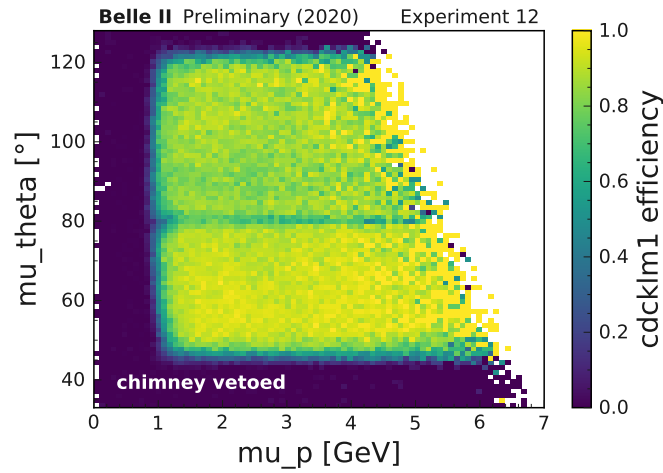
Figure A.7: `cdcklm1` efficiencies as a function of the muon momentum and polar angle. The effect of the collision boost, which allows high momenta to be reached only in the forward directions, is clearly visible.

(a)

(b)
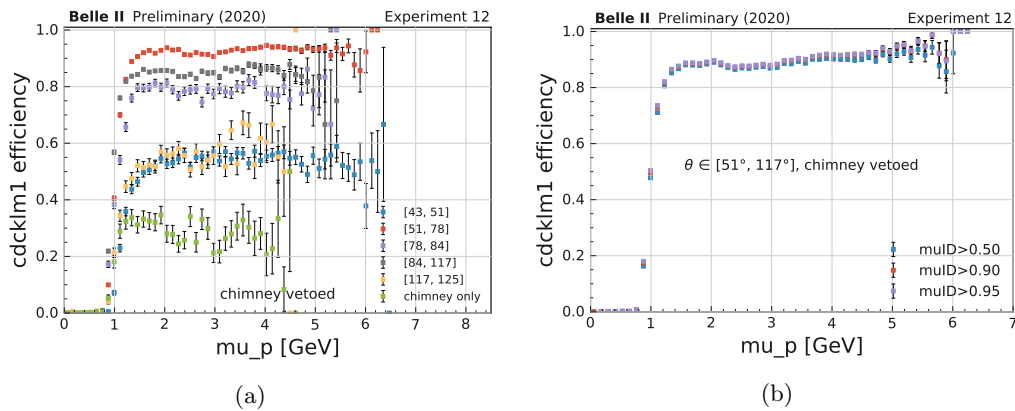
Figure A.8: (a) `cdcklm1` efficiencies as a function of the muon momentum for different polar angle intervals, inside and outside the chimney region. (b)`cdcklm1` trigger efficiencies as a function of the muon momentum for three different values of muonID cut: 0.5 (blue points), 0.9 (red points), 0.95 (magenta points).
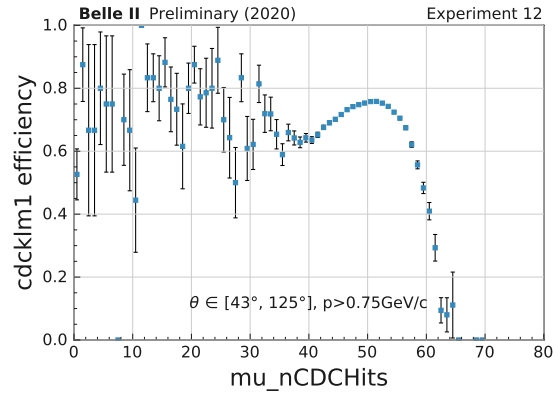
Figure A.9: `cdcklm1` trigger efficiency as a function of $nCDCHits$
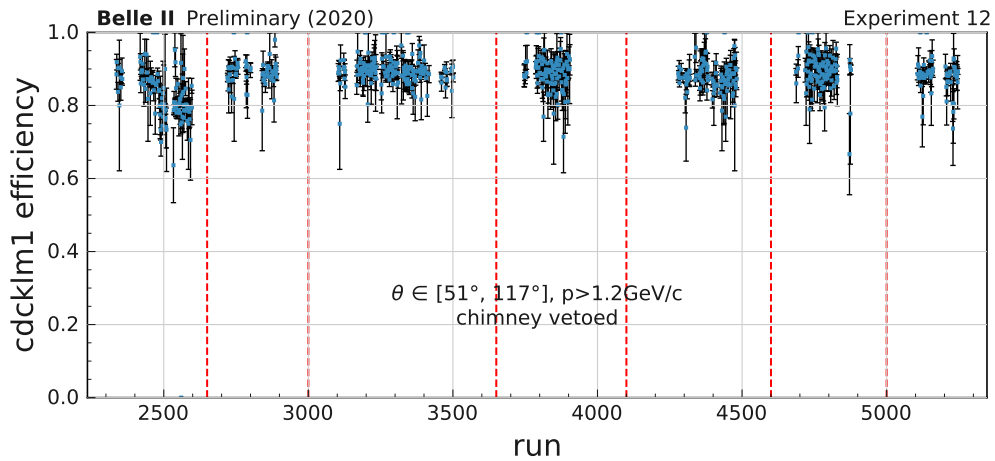
Figure A.10: `cdcklm1` trigger efficiencies, for muon momentum $p > 1.2$ GeV/c and in a polar angle interval 51°-117°, as a function of the run number. Vertical lines mark a subdivision in seven different periods, later used for an evaluation of the systematic uncertainties.

A.4   Results

The `cdcklm1` trigger efficiencies computed in bins of $p - \theta$ of different sizes are shown in Figure A.11 and in Table A.1 for the standard muonID cut ($muonID > 0.5$). Results for the other two muonID reference cuts (0.90 and 0.95) are shown in Table A.2 and A.3.

Furthermore, an integrated efficiency value (for a muonID selection of muonID>0.5 of 0.888 $\pm$ 0.001(stat.) for muons of momentum $p > 1.2$ GeV/c in an angular θ interval [51° - 117°] (marked with id=100 in the tables) is reported. It can be used, if the sensitivity of the analysis case study to the KLM trigger is not too high and a quick approximate efficiency is sufficient.
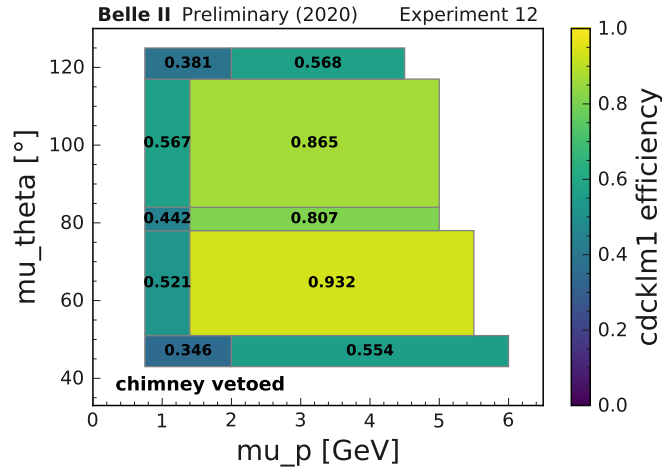
Figure A.11: `cdcklm1` trigger efficiencies in different momentum and polar angle intervals, for muonID>0.5 .

A.4.1   Systematic uncertainties

Several source of systematic uncertainties affect the `cdcklm1` trigger efficiency measurement, namely those coming from the measured dependencies upon polar and azimuthal track angles θ and ϕ (see Sect. A.3), track momentum p (see Sect. A.3), track quality through the number of recorded hits in CDC $nCDChits$ (see Sect. A.3), muonID cut (see Sect. A.3) and run number (see Sect. A.3).

A possible approach is that of estimating variations of the trigger efficiency as a function of all these variables and then summing up in quadrature the different contributions. This procedure unavoidably leads to overestimates of the systematic uncertainties, because (a) actual measurements in most cases are sensitive only to average values of some of these variables and (b) it neglects correlations between them. These are the cases of the contributions coming from the track azimuthal angle ϕ for case (a) and of the $nCDCHits$ induced systematic uncertainties for cases (a) and (b).

id	θ [°]	p [GeV/c]	Efficiency	Systematic Uncertainty				
				θ-p	ϕ	nCDCHits	run	Total*
100	51 - 117	>1.2	0.888±0.001	0.058	0.000	0.006	0.007	0.059
0	43 - 51	0.75 - 2.0	0.346±0.004	0.263	0.049	0.009	0.010	0.264
1	43 - 51	2.0 - 6.0	0.554±0.003	0.275	0.040	0.002	0.008	0.275
2	51 - 78	0.75 - 1.4	0.521±0.003	0.053	0.032	0.005	0.016	0.056
3	51 - 78	1.4 - 5.5	0.932±0.001	0.013	0.019	0.002	0.004	0.014
4	78 - 84	0.75 - 1.4	0.442±0.006	0.060	0.062	0.004	0.019	0.063
5	78 - 84	1.4 - 5.0	0.807±0.003	0.068	0.038	0.008	0.019	0.071
6	84 - 117	0.75 - 1.4	0.567±0.003	0.031	0.050	0.009	0.020	0.038
7	84 - 117	1.4 - 5.0	0.865±0.001	0.024	0.027	0.007	0.007	0.026
8	117 - 125	0.75 - 2.0	0.381±0.006	0.299	0.088	0.008	0.023	0.300
9	117 - 125	2.0 - 4.5	0.568±0.007	0.287	0.057	0.011	0.026	0.289
c	112 - 125	0.75 - 1.2	0.175±0.011	0.110	0.076	0.012	0.014	0.112
c	112 - 125	1.2 - 4.5	0.351±0.007	0.079	0.140	0.016	0.023	0.084

Table A.1: `cdcklm1` trigger efficiencies in different momentum and polar angle intervals, for muonID>0.5. The last two lines, marked with 'c', refer to the chimney region. The error in the efficiency column is statistical only. Also shown are the estimated systematic uncertainties. The region marked with id=100 corresponds to a wider angular and momentum selection.
* Contributions due to the azimuthal angle ϕ shown, but not included in the total.

As most of the processes studied in Belle II have flat distributions in ϕ (notable exceptions are measurements connected with cosmic rays), the contributions due to the track azimuthal angle are not included in the total systematic uncertainties, but provided separately. If needed, it can be added in quadrature or even better, the explicit efficiency dependence on ϕ can be taken into account.

The systematic uncertainties related to $nCDCHits$ deserve special attention. The cdcklm1 trigger efficiency and the tracking efficiency do depend on this quantity (see Figure A.9). Nevertheless, $nCDCHits$ distributions are almost entirely determined by the track polar angle θ and momentum p. This property was checked by comparing $nCDCHits$ distributions in regions selected in narrow intervals $\Delta\theta \times \Delta p$ (approximately 5° × 1 GeV) centered in $(\theta) - (p)$ with analogous regions at $(180 - \theta) - (p)$, in symmetric positions with respect to the CDC vertical axis in the longitudinal plane, where very similar local conditions are expected: three examples are shown in fig. A.13. These distributions turned out to be very similar, with at most a shift of one bin, which was later used to estimate a systematic uncertainty due to this source (see below).

Systematic effects due to θ and p dependencies were computed by subdividing the regions in fig. A.11 in sub-regions of approximate size $\Delta\theta \times \Delta p$ of 5° × 1 GeV. The `cdcklm1` efficiency for each of these sub-regions was computed, within which, as a consequence of our previous con-

id	θ [°]	p [GeV/c]	Efficiency	Systematic Uncertainty				
				θ-p	ϕ	nCDCHits	run	Total**
100	51 - 117	>1.2	0.897±0.001	0.059	0.000	0.006	0.006	0.059
0	43 - 51	0.75 - 2.0	0.376±0.004	0.278	0.055	0.009	0.011	0.278
1	43 - 51	2.0 - 6.0	0.575±0.004	0.291	0.042	0.003	0.004	0.291
2	51 - 78	0.75 - 1.4	0.551±0.003	0.047	0.037	0.005	0.015	0.049
3	51 - 78	1.4 - 5.5	0.940±0.001	0.015	0.017	0.002	0.003	0.015
4	78 - 84	0.75 - 1.4	0.463±0.006	0.060	0.065	0.004	0.020	0.063
5	78 - 84	1.4 - 5.0	0.816±0.003	0.070	0.037	0.008	0.018	0.072
6	84 - 117	0.75 - 1.4	0.588±0.003	0.028	0.049	0.009	0.019	0.035
7	84 - 117	1.4 - 5.0	0.874±0.001	0.027	0.026	0.007	0.005	0.029
8	117 - 125	0.75 - 2.0	0.418±0.006	0.311	0.088	0.008	0.025	0.312
9	117 - 125	2.0 - 4.5	0.593±0.007	0.295	0.058	0.012	0.025	0.296
c	112 - 125	0.75 - 1.2	0.228±0.013	0.090	0.069	0.010	0.019	0.092
c	112 - 125	1.2 - 4.5	0.445±0.009	0.052	0.149	0.021	0.020	0.059

Table A.2: cdcklm1 trigger efficiencies in different momentum and polar angle intervals, for muonID>0.9. The last two lines, marked with 'c', refer to the chimney region. The error in the efficiency column is statistical only. Also shown are the estimated systematic uncertainties. The region marked with id=100 corresponds to a wider angular and momentum selection.
* Contributions due to the azimuthal angle ϕ shown, but not included in the total.

siderations, the $nCDCHits$ dependencies are automatically taken into account almost entirely. The obtained values are shown in Fig. A.12. Systematic uncertainties for each of the regions in Fig. A.11 are computed as the RMS of the values in Fig. A.12. They are included in Table A.1, A.2 and A.3.

The residual effects due to the cdcklm1 efficiency dependence on $nCDCHits$ was then taken into account. First, a differential trigger efficiency as a function of $nCDCHits$ (as in Figure A.9) was computed for each of the subregions in fig. A.12. These curves were then applied, for each of the sub-regions in Fig. A.12, on $nCDCHits$ distributions shifted by one bin to the right and to the left (see above), and new efficiencies were computed. Average variations with respect to the values coming from unshifted distributions were assumed as systematic uncertainties due to this effect. Results are included in Table A.1, A.2 and A.3.

Systematic uncertainties related to the stability of the cdcklm1 efficiency during the data taking were estimated by grouping the run numbers in seven periods, according to the vertical divisions in Fig. A.10. Efficiencies were computed in each period. The first value was consistently below the others, and thus discarded from this study. The last six were thus averaged and the pulls computed. With the usage of a simple toy Monte Carlo technique, variations around the average values beyond the systematic uncertainties were estimated. They were found to be of the order of 0.7% for the wide selection of muons of momentum p>1.2 GeV/c in an angular θ

id	θ [°]	p [GeV/c]	Efficiency	Systematic Uncertainty				
				θ-p	ϕ	nCDCHits	run	Total*
100	51 - 117	>1.2	0.898±0.001	0.059	0.000	0.006	0.005	0.060
0	43 - 51	0.75 - 2.0	0.386±0.005	0.282	0.056	0.009	0.009	0.283
1	43 - 51	2.0 - 6.0	0.581±0.004	0.293	0.042	0.003	0.005	0.293
2	51 - 78	0.75 - 1.4	0.562±0.003	0.045	0.039	0.005	0.014	0.048
3	51 - 78	1.4 - 5.5	0.942±0.001	0.015	0.017	0.003	0.003	0.016
4	78 - 84	0.75 - 1.4	0.471±0.006	0.060	0.064	0.004	0.020	0.064
5	78 - 84	1.4 - 5.0	0.818±0.003	0.070	0.037	0.008	0.018	0.073
6	84 - 117	0.75 - 1.4	0.596±0.003	0.026	0.050	0.009	0.019	0.033
7	84 - 117	1.4 - 5.0	0.875±0.001	0.028	0.026	0.007	0.005	0.029
8	117 - 125	0.75 - 2.0	0.430±0.006	0.313	0.089	0.008	0.025	0.314
9	117 - 125	2.0 - 4.5	0.606±0.007	0.295	0.055	0.011	0.023	0.296
c	112 - 125	0.75 - 1.2	0.244±0.014	0.088	0.070	0.011	0.018	0.091
c	112 - 125	1.2 - 4.5	0.477±0.009	0.047	0.150	0.022	0.021	0.056

Table A.3: cdcklm1 trigger efficiencies in different momentum and polar angle intervals, for muonID>0.95. The last two lines, marked with 'c', refer to the chimney region. The error in the efficiency column is statistical only. Also shown are the estimated systematic uncertainties. The region marked with id=100 corresponds to a wider angular and momentum selection.
* Contributions due to the azimuthal angle ϕ shown, but not included in the total.

interval [51° - 117°] (marked with id=100 in the tables). The same procedure was applied for each of the regions in Fig. A.11. Values are included in Table A.1, A.2 and A.3.

Trigger efficiencies in the activation regions between 0.75 and 2 GeV/c suffer from high systematic errors, being far from plateau conditions. In these regions, functional fits as a function of the track momentum, rather than integrated efficiency values, would be a better option, however not explored in this work.
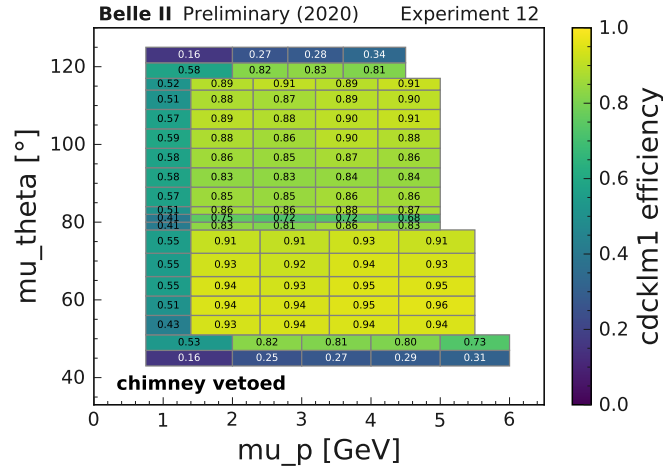
Figure A.12: cdcklm1 trigger efficiencies in different momentum and polar angle intervals, for muonID>0.5 The regions in A.11 are here splitted into subregions of approximate size $\Delta\theta \times \Delta p$ of $5° \times 1$ GeV.
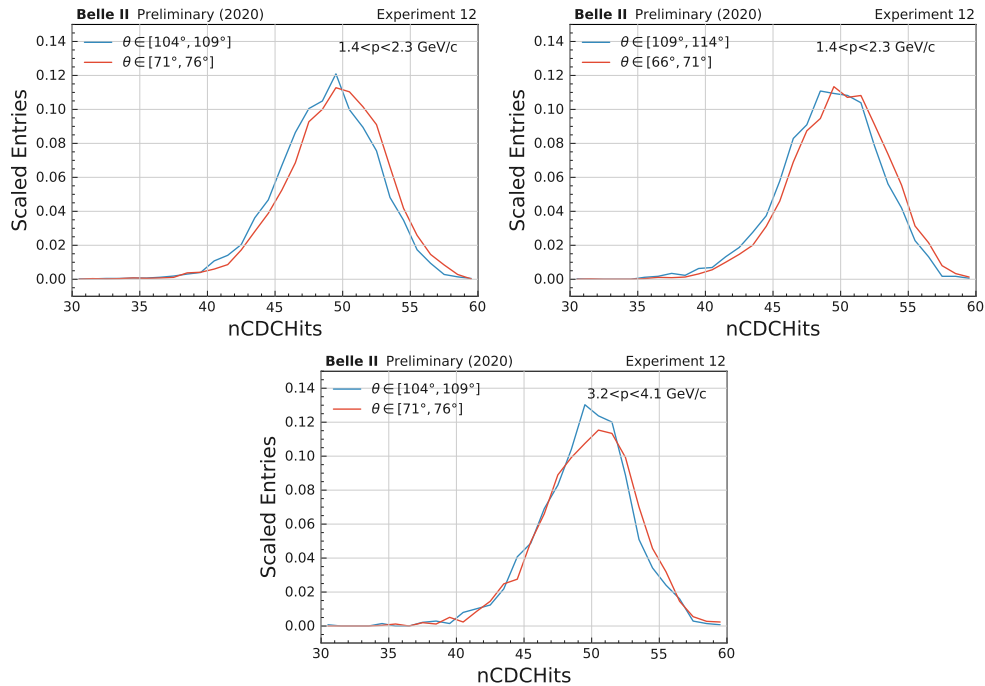
Figure A.13: Distributions of $nCDCHits$ for three specific regions in narrow $\Delta\theta \times \Delta p$ intervals at position $(\theta) - (p)$ compared with their symmetric counterparts at position $(180 - \theta) - (p)$

Appendix B

Statistical interpretation

This Appendix addresses the statistical concepts used in Chapter 3 and Chapter 4 to treat the yields found after the analysis selection in data and MC. The procedures used to look for anomalies in data in both a frequentist and a Bayesian approach, and to setting an upper limit on the signal cross section with a Bayesian approach are illustrated. Furthermore, the treatment of the look-elsewhere-effect, which is strictly needed for the case of the dark Higgsstrahlung search, is deeply investigated here.

B.1 The hypothesis test

In the following, the background only hypothesis is indicated with H_0 while the signal+background hypothesis with H_1. The expected signal yield s can be expressed as $s = \epsilon \times L \times \sigma_{dark}$ where σ_{dark} is the cross section for the process of interest (Z' production or dark Higgsstrahlung), ϵ_{sig} the signal efficiency after all the selections and L the integrated luminosity. Thus, in the H_1 hypothesis, the following relation holds:

$$N_{\text{obs}} = \sigma_{dark} \times L \times \epsilon_{\text{sig}} + B \tag{B.1}$$

where N_{obs} is the number of observed events in data. As in the presented analyses a counting technique within a predefined set of bins is used, the previous relation must be intended as computed bin by bin.

B.1.1 p-value

After applying all the analysis selections, observed event on real data and MC expectation can be compared in order to look for possible anomalies. In a freqentist approcah, this is done by checking the null hypothesis H_0 only, with a significance test based on the p-value frequentist concept. Given the number of observed events N_{obs} and the number of expected background

events B, the p-value is defined as:

$$p\text{-value} = \sum_{j=N_{obs}}^{\infty} P(j|B) = 1 - \sum_{j=0}^{N_{obs}-1} P(j|B) \tag{B.2}$$

where $P(j|B)$ is the Poissonian probability for j events when expected B.

The p-value, thus, gives the probability to get a result greater or equal than the observed one. The above definition holds for a known background B, only. As the number of expected background events is defined with an uncertainty δ_{bkg}, a so-called "marginalized p-value", i.e., integrated over the background to account for systematics and MC statistics uncertainties, has been adopted. This is achieved by considering for N_{obs} a Poissonian distribution convoluted with a Gaussian that summarizes the effects of all the systematic uncertainties:

$$I(N_{obs}|B, \delta_{bkg}) = \int_{\delta_{min}}^{\delta_{max}} P(N_{obs}|B \cdot (1+x)) \cdot Gauss(x; 0, \delta_{bkg}) \, dx \tag{B.3}$$

where $\delta_{min} = -5\,\delta_{bkg}$ or -1 if $-5\,\delta < -1$ and $\delta_{min} = +5\,\delta_{bkg}$, and $Gauss(x; 0, \delta)$ is a Gaussian function with zero mean and width equal to δ_{bkg} [132]. The p-value is then defined as following:

$$p\text{-value} = 1 - \sum_{j=0}^{N_{obs}-1} I(j|B, \delta_{bkg}) \tag{B.4}$$

If no anomalies are observed at a given significance, the signal hypothesis is rejected at the corresponding confidence level and the upper limits are, thus, computed. Such procedure has been applied to the invisible Z' analysis, as described in Sect. 3.7.

B.1.2   Bayes factor

The Bayesian approach for the significance test and the upper limits computation is based on the Bayes theorem. In a general context, it states that the probability of the model M_λ given the data-set D (called *posterior* probability) is given by:

$$h(\lambda|D) = \frac{P(D|\lambda)\,\pi(\lambda)}{\int_{-\infty}^{\infty} P(D|\lambda)\,\pi(\lambda)\,d\lambda}. \tag{B.5}$$

where $P(D|\lambda)$ is the probability of having the data-set given the model (known as *likelihood*), while $\pi(\lambda)$ is the initial probability for the model (called *prior*). The denominator on the right hand side of the equation is called *evidence*, and it is the integral of the numerator over the allowed region of the model parameter, ensuring that the posterior probability is normalized. The above formula can also be interpreted as a learning process: the knowledge about the model before the experiment, is updated by using the probability of the new data for different values of the parameters, resulting in the posterior knowledge.

To account for the uncertainty associated with the model approximation/idealization, one can

allow for additional dependencies on unknown parameters (called *nuisance* parameters) in the model. These values are unknown and uninteresting but do influence the results. The Bayesians approach reduces the problem dimensionality by "averaging" over the space of the unknown nuisance parameters: assuming a prior for any of the nuisance parameters, an integration (often called "marginalization") over the nuisance parameters is performed to obtain a posterior that no longer depend on them.

Moving to the specific case of the analyses described in this work, under the H_1 hypothesis, eq. B.1 holds. The following assumptions were furthermore taken into account:

- the likelihood of the observed number of events $P(N_{obs}|s+B)$ was assumed to be Poissonian;

- all the prior distributions related to systematic uncertainties were assumed to be Gaussian, with a width equal to the estimated size of the effect;

- the expected (Monte Carlo) background number of events was assumed to be Poissonian.

The hypothesis testing in a pure Bayesian approach is formalized through the usage of the Bayes factors. Differently from p-values, which are based on background-only features, Bayes factors compare two different hypotheses through the ratio of Bayesian evidences, i.e., the prior-weighted average of the likelihood over the parameter space according to their relative hypothesis.

Given the Poissonian likelihood of data for N observed events and predicted background B in the signal + background case,

$$P(N|s+B) = \frac{(s+B)^N e^{-(s+B)}}{N!},$$ (B.6)

the Bayes factor testing H_1 versus H_0 is defined as:

$$B_{10} = \frac{E_1}{E_0} = \frac{\int_0^\infty (s+B)^N e^{-(s+B)} \pi_1(B,s)\,ds}{b^N e^{-B}}; \quad s = \epsilon \times L \times \sigma_{dark}$$ (B.7)

where $\pi_1(b,s)$ is the prior probability for a signal s given the background B. These expressions hold for an exactly known background B. In the real case, each time B appears, in numerator or denominator, a further marginalization is implied, to take into account systematic uncertainties and Monte Carlo statistics of B. The same apply for uncertainties on s. This is never shown in equations, for the sake of simplicity. The interpretation of B_{10} is straightforward: it quantifies how the hypothesis H_1 of signal+background is stronger than the background-only hypothesis H_0. This is a major difference with respect to the frequentist case, where p-values are based on H_0 only. When $B_{10} > 1$, the data favour model H_1 over model H_0, while when $B_{10} < 1$ is the viceversa. Another major difference resides in the fact that Bayes factors depend only on the number of observed events N, while p-values involve the probability content even for number of events larger than N, which are actually not observed.

The choice of the prior $\pi_1(b,s)$ is non-trivial and deserves some care. As it will be shown in the next Section for limit estimation procedure, a common choice is a flat prior $\pi_{flat}(s) = \frac{1}{s_1 - s_0}$

for the signal in the interval $s_1 - s_0$ (with s_0 usually set to zero). This can be interpreted as a representation of the "ignorance" about the signal strength. On the other hand, it is well known that in Bayesian hypothesis testing, contrarily to Bayesian upper limit case, the usage of flat (or, more generally, "improper") priors must be avoided: one can easily see, by using $\pi_{flat}(s)$, that the Bayes factor would become arbitrary, depending directly upon the interval chosen through $\frac{1}{s_1 - s_0}$ (which does not depend on s and can get out of the integration). As a consequence, for hypotheses testing, the so called intrinsic prior for $\pi_1(b, s)$, which has solid justifications [133, 134, 135] has been used. It is defined as:

$$\pi_i(s) = \frac{b}{(s + b)^2} \tag{B.8}$$

An interpretation of the Bayes factor outcome is given in Ref. [136] and reported here in Tab. B.1.

B_{10}	Evidence in favour of H_1
1-3	weak
3-20	moderate
20-150	strong
≥ 150	very strong

Table B.1: Interpretation of Bayes factors.

A parallelism between p-values and Bayes Factors has been performed, by studying the relation holding in the case of Poissonian distributions for the background B with three different expected values. This is shown in Figure B.1, where, for each of the three distributions, p-values and Bayes Factors are computed for a set of hypothetically observed number of events and then interpolated. The relation is far from universal, being the two quantities very different in terms of mathematical definition and statistical meaning, as previously discussed, however a certain trend can be understood.

As consolidated traditions in the HEP field, based in the framework of the frequentist approach, one would require minimum significances of 3σ to claim an 'evidence' and 5σ to claim a 'discovery'. Based on Figure B.1, the two threshold correspond to a Bayes Factor of ~ 20 and $\mathcal{O}(10000)$, respectively.

The full numerical calculation of B_{10} has been implemented by using the Bayesian Analysis Toolkit (BAT) package, a software package specifically designed to solve Bayesian statistical problems with the use of Markov Chain MC [128].

Such a procedure has been exploited for the dark Higgsstrahlung search. As this analysis relies on a counting technique within a predefined set of mass windows, the previous consideration must be intended as computed window by window. After data unblinding, the Bayes factors B_{10} for each mass window will be provided. The above procedure must be complemented with the discussion on the look-elsewhere-effect described in the next Section.
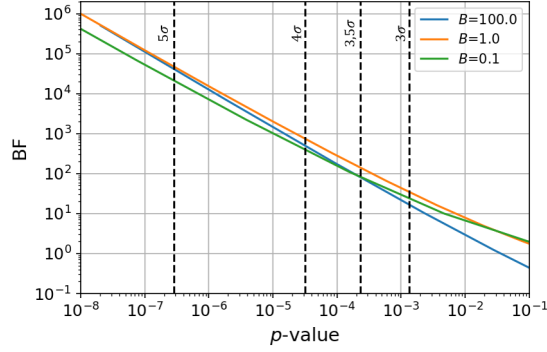
Figure B.1: Relationship between the Bayes Factor and the p-value for three different Poissonian distributions of expected values 0.1 (green), 1 (red), 100 (blue). Also shown are vertical lines indicating significance values most conventionally used of 3σ, 3.5σ, 4σ and 5σ.

B.2   The look-elsewhere-effect

A common problem in statistical analysis in high energy physics is to find evidence for a physical signal over a large and continuous parameter space, where the true position of the signal is not known a priori. When searching over a wide parameter space one increases the probability of finding large signals caused by random statistical fluctuations: this is known as look-elsewhere-effect (LEE) and must be accounted for when performing a hypothesis test [137]. Indeed, ignoring this effect would lead to an overestimation of the statistical significance and thus incorrectly concluding the detection of a physical sign.

The Bayes factor computation described in the previous Section must be seen as a result of a local hypothesis testing. The crucial step towards a global (multiple, in Bayesian language) hypothesis testing, is the full evaluation of the look-elsewhere-effect as it will be described in this section. The look-elsewhere-effect is pretty common in many usual applications where test hipoteses are performed, and can be understood as following: the larger the number of tests, the larger the chance of a false positive arising due to a statistical fluctuation. With 9003 mass windows used to search for a signal, the Dark Higgsstrahlung analysis is potentially subject to a large look-elsewhere-effect. As an example, just to quantify the size, the probability for a background-only fluctuation to give a one-sided 3σ excess is $\sim$0.135%. Thus $\sim$12 mass windows with such an effect are expected, bringing the global probability of observing a significance of this size to practically 100%.

To avoid making false claims of detection, one must account for this effect when assigning the statistical significance of an anomaly. There are several possible approaches which can be performed to take the look-elsewhere-effect into account. Methods such as the Bonferroni [138] and Sidák correction [139] correction use the trials factor to correct the conclusions of a hypothesis test in light of this effect. There is however no unique definition of the trials factor when searching a continuous parameter space for a signal. This is typically accomplished via poten-

tially expensive numerical simulations. Any case, the trial factor for the dark Higgsstrahlung analysis is expected to be of the order of the number of mass windows $O(10^4)$.

The approach described here to take into account look-elsewhere effect follows a Bayesian logic. The crucial step towards a global hypothesis testing, with full evaluation of the look-elsewhere-effect, is the introduction of the true signal mass dependencies into the Bayes Factor computation: in a Bayesian approach, the global evidence is equal to the prior-weighted average of the likelihood over the masses parameter space. This integration over the prior accounts for the look-elsewhere effect by penalizing large prior volumes, thus searches over large masses phase space. This is done by adding to eq. B.7 the dark photon mass $M_{A'}$ and the dark Higgs mass $M_{h'}$ as nuisance parameters, with a related prior probability distribution. The following notation is used: $M = (M_{A'}, M_{h'})$ with $\pi(M)$ as the associated prior. Thus a global Bayes factor $B_{10}^G(W)$ can be defined for a generic mass window W, meaning that the full true mass probability distribution is taken into account. As the mass windows have been defined in the squared mass space, the previous considerations apply to the squared masses, as follow:

$$B_{10}^G(W) = \frac{\int dM^2 \int_0^\infty ds\,(s+b)^N e^{-(s+b)}\pi_i(b,s)\pi(M^2)}{b^N e^{-b}} \quad ; s = \epsilon_W(M) \times L \times \sigma_{dark} \quad (B.9)$$

A flat probability was chosen as prior for the true signal mass M. The search space of the dark Higgsstrahlung analysis is triangular, with base $\sqrt{s}$ and height $\sqrt{s}/2$. Furthermore, the phase space below the dimuon threshold must be discarded. The prior $\pi(M)$ can thus be written as:

$$\pi(M) = \frac{1}{A_T} = FLAT \quad (B.10)$$

where A_T is phase space are defined according to previous prescriptions. The resulting prior in the squared masses plane $\pi(M^2)$, computed by the usual transformation rules of probability distribution functions for a change of variable, is:

$$\pi(M^2) = \pi(M)\frac{1}{2\sqrt{M_{A'}^2}}\frac{1}{2\sqrt{M_{h'}^2}} = \frac{1}{4A_T}\frac{1}{\sqrt{M_{A'}^2}}\frac{1}{\sqrt{M_{h'}^2}} \quad (B.11)$$

The global Bayes factor for the generic mass window W can thus be written as:

$$B_{10}^G(W) = \frac{\int dM^2 \frac{1}{A_T}\frac{1}{2\sqrt{M_{A'}^2}}\frac{1}{2\sqrt{M_{h'}^2}}\int_0^\infty ds\,(s+b)^N e^{-(s+b)}\pi_i(b,s)}{b^N e^{-b}} \quad (B.12)$$

In this last expression, the result of the integration over ds of the Poissonian term does not depend on the efficiency $\epsilon_W(M)$ and thus on the mass M. As a consequence, the global Bayes

factor can be factorized as:

$$B_{10}^G(W) = B_{10}(W)\frac{1}{A_T}\int dM^2 \frac{1}{2\sqrt{M_{A'}^2}}\frac{1}{2\sqrt{M_{h'}^2}} \tag{B.13}$$

where $B_{10}(W)$ has been defined in eq. B.7.

This result establish a direct connection between local and global Bayes factors, by means of the product for a suppression factors:

$$\frac{1}{A_T}\int dM^2 \frac{1}{2\sqrt{M_{A'}^2}}\frac{1}{2\sqrt{M_{h'}^2}} \tag{B.14}$$

Another interesting case holds for a different choice of the signal mass prior probability, which can be assumed to be flat in M^2 rather than in M. The search space in M^2 has no longer a triangular shape, but has an irregular shape (see Figure B.2).
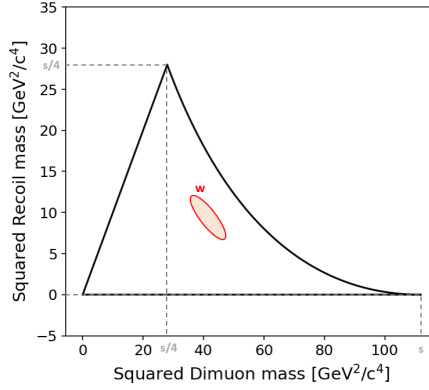
Figure B.2: Squared mass plane, with a mass window W displayed for illustration only (not to scale).

Thus:

$$\pi(M^2) = \frac{1}{A_{T^2}} = FLAT \tag{B.15}$$

where A_{T^2} is the area of the search space.

By now, the integration domain over the mass M of eq. B.13 has not been defined. Anyway, it is understood that it can extend only up to the region where the signal efficiency is larger than zero. However, a further step towards a more realistic situation emerging after data unblinding can be done. At that moment, as a consequence of the scanning strategy, the attention is limited to the cases of mass windows showing local Bayes factors which are local maxima among neighbouring windows in the mass plane and with values above some pre-defined threshold of interest. This condition (high local maximum) acts as a constraint to the integration operations in eq. B.13, restricting the integration domain effectively to a region where the condition holds. The integration space is defined by the condition $A_M \equiv \ \ M : (B_{10} > B_{10}^T) \cap B_{10} \ max$, where

B_{10}^T is a pre-defined threshold on the local Bayes factor. Thus eq. B.13 transform to:

$$B_{10}^G(W) = B_{10}(W) \frac{1}{A_T} \int_{A_M} dM^2 \frac{1}{2\sqrt{M_{A'}^2}} \frac{1}{2\sqrt{M_{h'}^2}}$$ (B.16)

The area of the integration domain defined by the A_M condition around the local maximum, compared to the full initial search space, gives the size of the look-elsewhere-effect, with the mass dependent expression acting as a weight.

The condition A_M is expected to be valid in regions smaller than the mass window W, because of window overlap: a signal with true mass in one mass window can give rise to a larger Bayes Factor in another nearby mass window in which such a signal is also contained, located there in a more central position, thus resulting into a higher signal efficiency. The problem is therefore that of finding a portion of the mass window, with its expected background, within which a signal with true mass therein would give rise to the maximum local Bayes Factor over a specified threshold, and restricting the integration to that region. This has been done with a Monte Carlo simulation, which is described in some detail here. As a first step, a specific mass window, called "central" mass window in the following, and the 48 surrounding ones, corresponding to three levels of neighbours, have been set. The next step is filling all the mass windows with a realization of the background: events have been extracted according to Poissonian distributions with as expected values those computed after the final background suppression in Sect. 4.5 (see Figure 4.21). Then the signal was injected. At this stage, i.e., before unblinding, fixed signal yield in a set of predefined values (0.1, 1, 3, 10, 30, 100) was used. The number of signal events N_S has been extracted by a Poissonian distribution with the aforementioned expected values. Then N_S events from the available generated signal distribution in the central mass window that passed all the selections were extracted randomly.

Signal events were available only for nominal masses placed at the center of the mass window. In order to allow the procedure to probe the A_M one need to move them around in generic points M. In order to do that, 1000 points are uniformly generated across a rectangular region with an area corresponding to twice that of the central mass window. The signal distribution (N_S events) is shifted by amounts corresponding to the distance between these points and the center of the window: the operation corresponds to generate the dark photon and dark Higgs nominal masses to these new positions. Signal and background events are counted in each of the 49 mass windows, and the corresponding Bayes Factors are computed on the base of the total number of events (generated background + generated signal) versus the expected background. The crucial step of the procedure is to check for the A_M condition, by identifying the cases in which the Bayes Factor of the central mass window is the largest among the 49 selected and over threshold. The cases in which this condition holds define an effective area which typically lies within the central window and corresponds to core geometric shapes of size $\approx 2\sigma \times 2\sigma$, where σ is the mass resolution. An example of the procedure is shown in Figure B.3. The result looks very reasonable and expected, due to the 1σ step of the scanning procedure and the window overlap.

The fraction of cases, out of the 1000 generated points, in which the condition A_M is fulfilled, is a measure of the area of this region. Within the same Monte Carlo procedure the integrals in eq. B.16 and the equivalent for a flat $\pi(M^2)$ prior can be numerically computed. The entire procedure has been repeated 300 times (trials) for each signal level, to get distributions of areas and suppression factors. The number of trials is increased to 3000 for the cases with 1 and 0.1 signal events.
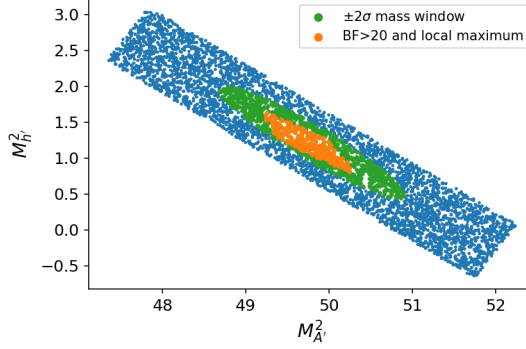

Figure B.3: Example of the toy Monte Carlo procedure applied on a central mass window. In blue, the rectangular region in which the A_M condition is checked. In green, the mass window. In orange, the region in which the A_M condition is fulfilled, with a Bayes Factor larger than the 48 surrounding ones and over threshold.

Results are shown in Figure B.4 for the mass window in Figure B.3 and for the 6 signal levels studied. Bayes Factors are required to exceed a threshold of 20 (which has been assumed as threshold). The distributions show the fraction of area in which the A_M condition is fulfilled, normalized to mass window area. Mean values converge to an asymptotic value as the signal increases, with distributions progressively shrinking, according to expectations. For low signal injections, the background acquires more importance and there are less and less cases (trials) in which the A_M condition is fulfilled. The effect of changing the threshold was also investigated, by repeating these studies with values of 20, 100 and 1000: results were qualitatively similar, with faster convergence to the asymptotic value for high signal injections, and with smaller contribution for low signals. As the whole procedure requires a lot of resources from a computational point of view, it has not been performed for all the mass windows. However, alternative mass points in different regions of the mass plane were checked, with similar results. The picture which seems to emerge is that, given a mass window with a Bayes Factor which is large (over threshold) and locally maximum, the mass integrals in eq. B.16 (and the equivalent for a flat $\pi(M^2)$ prior) will likely be dominated by the asymptotic condition (signal much larger than the background), because low signals will be heavily downweighted by the small fraction of cases in which the A_M condition is fulfilled.

All this work is useful to understand how the system reacts for signal injections of various sizes. The final step now needed is to build a procedure that, starting from the above considerations,
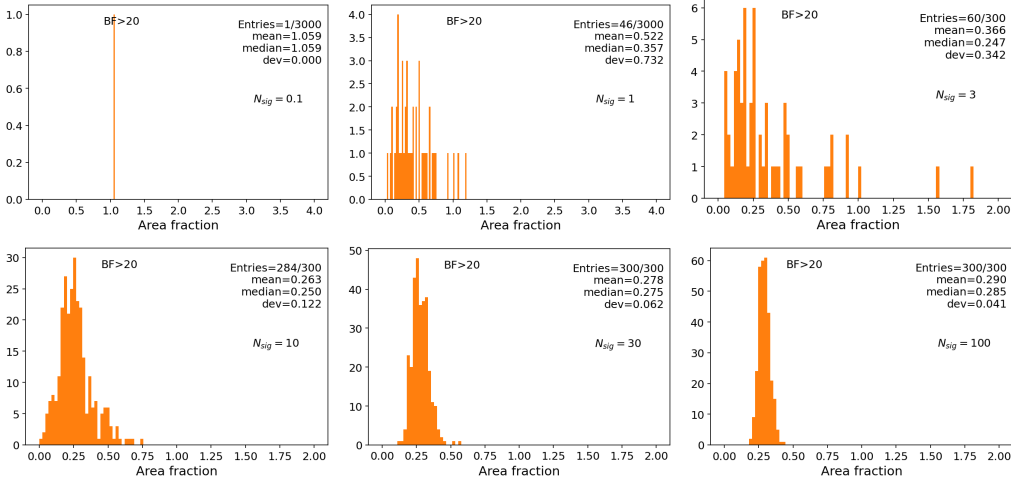
Figure B.4: Fraction of area in which the A_M condition is fulfilled, normalized to the standard mass window area, for six different signal injections of 0.1, 1, 3, 10, 30 and 100 events. Mean values approximately converge to an asymptotic value and distributions shrink with the signal increase. For weak signals the statistics is low because in less and less cases (trials) the A_M condition is fulfilled.

estimates the local to global suppression factors in eq. B.16 (and the equivalent for a flat $\pi(M^2)$ prior) in the closest possible situation to that observed after unblinding on data. The entire procedure can be repeated by injecting signal according to the posterior distribution obtained after N_{obs} events have been observed in a mass window for which the expected background is known. As a proof of feasibility, it was simulated the case of one mass window with an expected background of 0.3 events and three different outcomes for the number of observed events: 4, 5 and 7 events, for which the corresponding Bayes Factors are of the order of $\sim$100, $\sim$1000 and $\sim$2.5$\times10^5$, respectively. The three posterior distributions, which have been numerically computed by means of BAT, are shown in Figure B.5. They are expressed in terms of the dark Higgsstrahlung cross section, easily converted in number of events by multiplying them for the integrated luminosity L. The above described toy Monte Carlo procedure is then modified in the part that relates to signal injection. A cross section σ is extracted according to the distributions in Figure B.5. The quantity $R = \sigma \times L$ is used as the expected parameter of a Poisson distribution, after which a number of events N_s is generated. A number N_s of randomly chosen events generated in the central mass window is picked up and all the analysis selections applied. The rest of the procedure proceeds along the lines previously described, with randomization of the mass M, check of the A_M condition and so on. The final averages will automatically incorporate the effect of having injected signal in the right expected relative amounts. Results are shown in Figure B.6 for the three different outcomes and for a threshold set at 20 on the Bayes Factor: the area fractions are very similar in the three cases and compatible with the asymptotic value.

The existence of a plateau (asymptotic value) is a guarantee of stability, though not strictly

necessary, as the procedure is able to compute the area in which the A_M condition is fulfilled and therefore the local to global suppression factors even in cases where the asymptotic condition is not reached.

After unblinding the data, this procedure will be applied on the few interesting cases, if any, with high and locally maximun Bayes Factors that will emerge after unblinding. At that time, the precision of the procedure can be improved by increasing by one order of magnitude both the number of points introduced to study the effects related to the true mass M position (presently one thousand) and the number of trials (presently three hundred).
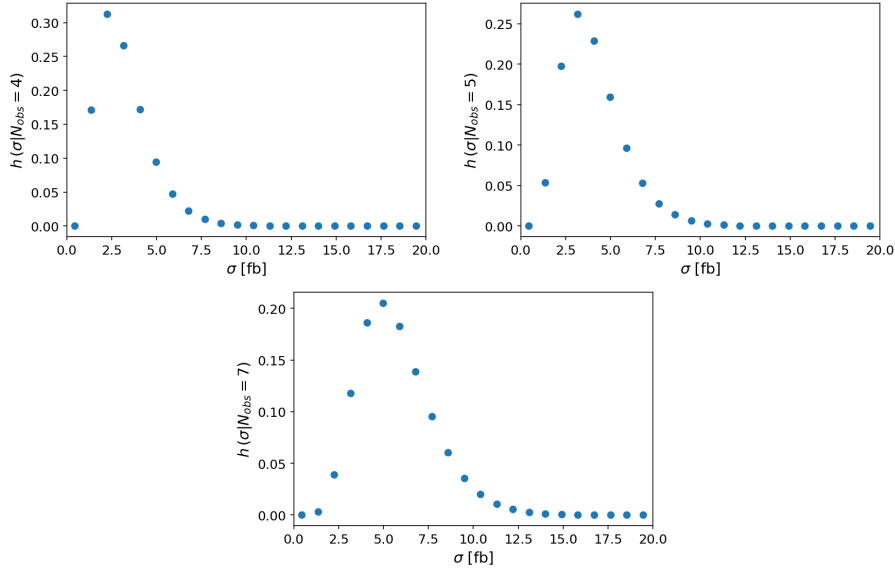
Figure B.5: Cross-section posterior distributions for a mass window with an expected background of 0.3 events and for a number of observed events of 4, 5 and 7, respectively

While waiting for data to be available, a less computing demanding procedure which, with some approximations, allows the local to global suppression factors was performed. In presence of a low and smoothly varying background, the local significance and thus the Bayes factor, is expected to be driven by the signal efficiency. Under this hypothesis, the condition that the Bayes factor in a mass window is a local maximum among neighbouring windows, can be reduced to the condition that the signal efficiency has a local maximum in that window: $(\epsilon_W(M) > 0) \cap \epsilon_W(M) \ max$. Analogously to the condition A_M, it is expected and found to be valid in regions smaller than the mass window W, because of window overlap: a signal with true mass in one mass window can be detected with a larger efficiency in another nearby mass window in which such a signal is also contained, located there in a more central position. The problem is therefore that of finding portions of the mass window within which a signal with true mass therein would give the maximum local efficiency $\epsilon_W(M)$ and restricting the integration to this region. This is done with a Monte Carlo simulation very similar to that described above, but much
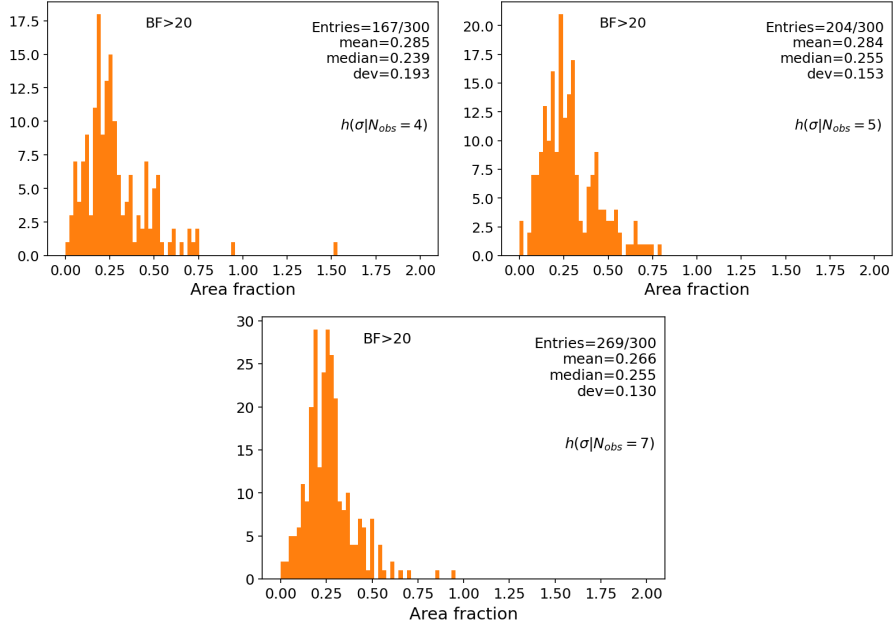
Figure B.6: Fraction of area in which the A_M condition is fulfilled, normalized to the rectangular area of the initial search, for continuous signal injection according to the posterior distributions in Figure B.5. Mean values approximately converge to asymptotic values.

simpler, because it does not need the introduction of the background and does not make use of signal injections at different levels, being the efficiency the only relevant parameter. Results for a specific mass window are shown in Figure B.7. An effective area inside the central mass window is found, where the signal efficiency of the central window for signals with masses belonging to this region is the largest among all the neighbours. This is almost identical, in shape and size, to that found while checking for the A_M condition. As before, the same Monte Carlo procedure is used to compute numerically the integrals in eq. B.16 with the new integration domain and the equivalent for a flat $\pi(M^2)$ prior. The resulting suppression factors relating local to global Bayes factors are shown in Figure B.8 for the two prior hypotheses: they are of the order of 10^{-4}, as expected. The suppression factors computed in the two prior mass hypotheses differ on average by about 20%. They can be used to get a very good idea of the size of the look-elsewhere-effect across the full mass plane, before real data are available. A useful spinoff of this procedure is that it allows to estimate the variation of the signal efficiency inside the effective area where this efficiency is the largest among the neighboring windows. This procedure has been used in Sect. 4.6.2 to have an estimate on the systematic on the signal efficiency, as upper limit estimates and local Bayes Factor calculations are performed using the efficiency for a signal placed at the center of the mass window.
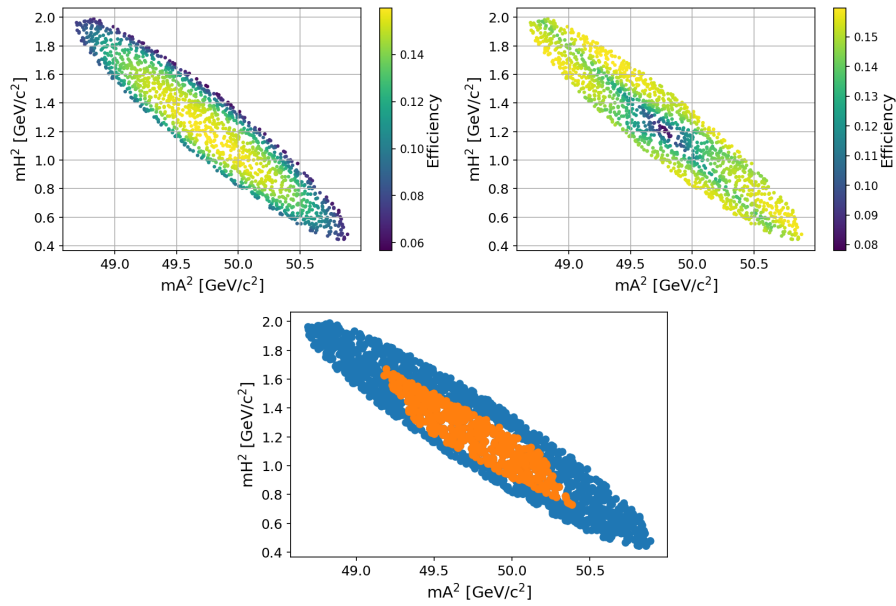
Figure B.7: Left: signal efficiency of a specific central window (shown as an example) for signals with true masses inside the window. Right: largest signal efficiency among all the neighbouring windows for signals with true masses inside the central window. Bottom: In orange, the region in which the signal efficiency of the central window for signals with masses belonging to this region is the largest among all the neighbours.
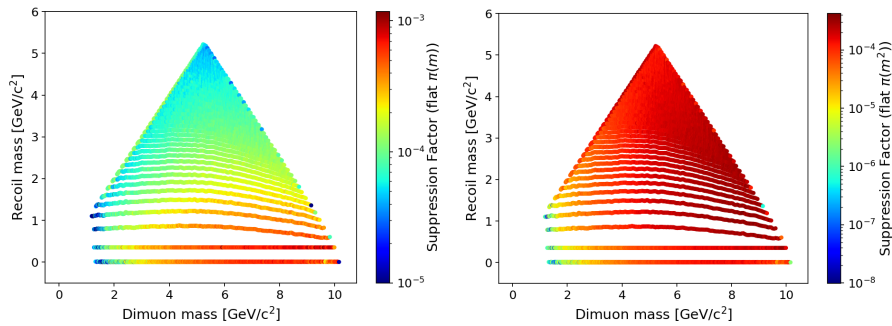
Figure B.8: Suppression factors relating local to global Bayes factors under the flat prior mass hypothesis (left) and flat prior squared mass hypothesis (right).

B.3 Bayesian upper limits computation

An upper limit is a probabilistic statement bounding unknown parameters determining the observed data. Setting upper limits on parameters in a Bayesian framework is straightforward, and just requires the integration of the posterior probability. For example, setting a 90% upper limit on the parameter λ for a model M_λ would require solving the following equation in λ^{UP}:

$$\int_{-\infty}^{\lambda^{\mathrm{UP}}} h(\lambda|D)\, d\lambda = 1 - \alpha = 0.9 \tag{B.17}$$

The parameter value λ^{UP} defines the 90% Credibility Level upper limit on λ. It can be interpreted as following: "*Given the observed data and the model M_λ, the size of the parameter λ is less or equal than λ^{UP} with the 90% probability*" [140].

Moving to the specific case of the analyses described in this work, under the H_1 hypothesis, eq. B.1 holds. According to the assumption introduced in Sect. B.1.2, for a generic mass window, the Poissonian likelihood of data for N observed events is:

$$P(N|s+B) = \frac{(s+B)^N e^{-(s+B)}}{N!} \tag{B.18}$$

while the posterior probability is given by:

$$h(s|N) = \frac{(s+b)^N e^{-(s+b)} \pi(s)}{\int_0^\infty (s+b)^N e^{-(s+b)} \pi(s)ds}; \quad s = \epsilon \times L \times \sigma_{dark}. \tag{B.19}$$

The prior distribution for σ_{dark} was assumed to be flat between 0 and $200 \cdot \sqrt{b}/(\mathcal{L} \times \epsilon_{\mathrm{sig}})$ fb (with the luminosity expressed in fb^{-1}). Furthermore, each time B and s appears, in numerator or denominator, a marginalization is implied, to take into account systematic uncertainties and Monte Carlo statistics uncertainties.

In order to compute the posterior probability and then set the upper limits, the BAT package has been used.

Bibliography

[1] I. Adachi et al. "Search for an Invisibly Decaying Z' Boson at Belle II in $e^+e^- \rightarrow \mu^+\mu^-(e^\pm\mu^\mp)$ Plus Missing Energy Final States". In: *Phys. Rev. Lett.* 124.14 (2020), p. 141801. DOI: 10.1103/PhysRevLett.124.141801. arXiv: 1912.11276 [hep-ex].

[2] M. Campajola. "Dark Sector first results at Belle II". In: *Physica Scripta* (2021). DOI: 10.1088/1402-4896/abfef2. URL: https://doi.org/10.1088/1402-4896/abfef2.

[3] M. Campajola. "First results and prospects for dark sector searches at Belle II". In: *Submitted to Nuovo Cim. C* (2021).

[4] F. Zwicky. "Die Rotverschiebung von extragalaktischen Nebeln". In: *Helv. Phys. Acta* 6 (1933), pp. 110–127. DOI: 10.1007/s10714-008-0707-4.

[5] F. Zwicky. "On the Masses of Nebulae and of Clusters of Nebulae". In: *Astrophys. J.* 86 (1937), pp. 217–246. DOI: 10.1086/143864.

[6] V. C. Rubin and W. K. Ford Jr. "Rotation of the Andromeda Nebula from a Spectroscopic Survey of Emission Regions". In: *Astrophys. J.* 159 (1970), pp. 379–403. DOI: 10.1086/150317.

[7] K. G. Begeman, A. H. Broeils, and R. H. Sanders. "Extended rotation curves of spiral galaxies: dark haloes and modified dynamics". In: *Monthly Notices of the Royal Astronomical Society* 249.3 (Apr. 1991), pp. 523–537. ISSN: 0035-8711. DOI: 10.1093/mnras/249.3.523. URL: https://doi.org/10.1093/mnras/249.3.523.

[8] R. Massey, T. Kitching, and J. Richard. "The dark matter of gravitational lensing". In: *Rept. Prog. Phys.* 73 (2010), p. 086901. DOI: 10.1088/0034-4885/73/8/086901. arXiv: 1001.1739 [astro-ph.CO].

[9] R. Massey et al. "Dark matter maps reveal cosmic scaffolding". In: *Nature* 445 (2007), p. 286. DOI: 10.1038/nature05497. arXiv: astro-ph/0701594.

[10] M. Colless et al. "The 2dF Galaxy Redshift Survey: spectra and redshifts". In: *Monthly Notices of the Royal Astronomical Society* 328.4 (Dec. 2001), pp. 1039–1063. ISSN: 0035-8711. DOI: 10.1046/j.1365-8711.2001.04902.x. eprint: https://academic.oup.com/mnras/article-pdf/328/4/1039/3780131/328-4-1039.pdf. URL: https://doi.org/10.1046/j.1365-8711.2001.04902.x.

[11] M. Tegmark et al. "The Three-Dimensional Power Spectrum of Galaxies from the Sloan Digital Sky Survey". In: *The Astrophysical Journal* 606.2 (May 2004), pp. 702–740. DOI: 10.1086/382125. URL: https://doi.org/10.1086/382125.

[12] Volker Springel et al. "Simulating the joint evolution of quasars, galaxies and their large-scale distribution". In: *Nature* 435 (2005), pp. 629–636. DOI: 10.1038/nature03597. arXiv: astro-ph/0504097.

[13] Wayne Hu and Naoshi Sugiyama. "Small scale cosmological perturbations: An Analytic approach". In: *Astrophys. J.* 471 (1996), pp. 542–570. DOI: 10.1086/177989. arXiv: astro-ph/9510117.

[14] Arno A. Penzias and Robert Woodrow Wilson. "A Measurement of excess antenna temperature at 4080-Mc/s". In: *Astrophys. J.* 142 (1965), pp. 419–421. DOI: 10.1086/148307.

[15] George F. Smoot. "COBE observations and results". In: *AIP Conf. Proc.* 476.1 (1999). Ed. by L. Maiani, F. Melchiorri, and N. Vittorio, pp. 1–10. DOI: 10.1063/1.59326. arXiv: astro-ph/9902027.

[16] C. L. Bennett et al. "Nine-Year Wilkinson Microwave Anisotropy Probe (WMAP) Observations: Final Maps and Results". In: *Astrophys. J. Suppl.* 208 (2013), p. 20. DOI: 10.1088/0067-0049/208/2/20. arXiv: 1212.5225 [astro-ph.CO].

[17] N. Aghanim et al. "Planck 2018 results. VI. Cosmological parameters". In: *Astron. Astrophys.* 641 (2020), A6. DOI: 10.1051/0004-6361/201833910. arXiv: 1807.06209 [astro-ph.CO].

[18] P. A. R. Ade et al. "Planck 2013 results. XVI. Cosmological parameters". In: *Astron. Astrophys.* 571 (2014), A16. DOI: 10.1051/0004-6361/201321591. arXiv: 1303.5076 [astro-ph.CO].

[19] Samuel D. McDermott, Hai-Bo Yu, and Kathryn M. Zurek. "Turning off the Lights: How Dark is Dark Matter?" In: *Phys. Rev. D* 83 (2011), p. 063509. DOI: 10.1103/PhysRevD.83.063509. arXiv: 1011.2907 [hep-ph].

[20] Santiago De Lope Amigo et al. "Cosmological Constraints on Decaying Dark Matter". In: *JCAP* 06 (2009), p. 005. DOI: 10.1088/1475-7516/2009/06/005. arXiv: 0812.4016 [hep-ph].

[21] David Harvey et al. "The non-gravitational interactions of dark matter in colliding galaxy clusters". In: *Science* 347 (2015), pp. 1462–1465. DOI: 10.1126/science.1261381. arXiv: 1503.07675 [astro-ph.CO].

[22] Edward W. Kolb and Michael S. Turner. *The Early Universe*. Vol. 69. 1990. ISBN: 978-0-201-62674-2.

[23] P. S. Bhupal Dev, Anupam Mazumdar, and Saleh Qutub. "Constraining Non-thermal and Thermal properties of Dark Matter". In: *Front. in Phys.* 2 (2014), p. 26. DOI: 10.3389/fphy.2014.00026. arXiv: 1311.5297 [hep-ph].

[24]   Jonathan L. Feng. "Dark Matter Candidates from Particle Physics and Methods of Detection". In: *Ann. Rev. Astron. Astrophys.* 48 (2010), pp. 495–545. DOI: 10.1146/annurev-astro-082708-101659. arXiv: 1003.0904 [astro-ph.CO].

[25]   Gerard Jungman, Marc Kamionkowski, and Kim Griest. "Supersymmetric dark matter". In: *Physics Reports* 267.5 (1996), pp. 195–373. ISSN: 0370-1573. DOI: https://doi.org/10.1016/0370-1573(95)00058-5. URL: http://www.sciencedirect.com/science/article/pii/0370157395000585.

[26]   Benjamin W. Lee and Steven Weinberg. "Cosmological Lower Bound on Heavy-Neutrino Masses". In: *Phys. Rev. Lett.* 39 (4 July 1977), pp. 165–168. DOI: 10.1103/PhysRevLett.39.165. URL: https://link.aps.org/doi/10.1103/PhysRevLett.39.165.

[27]   G. W. Bennett et al. "Final Report of the Muon E821 Anomalous Magnetic Moment Measurement at BNL". In: *Phys. Rev. D* 73 (2006), p. 072003. DOI: 10.1103/PhysRevD.73.072003. arXiv: hep-ex/0602035.

[28]   Michel Davier et al. "Reevaluation of the Hadronic Contributions to the Muon g-2 and to alpha(MZ)". In: *Eur. Phys. J. C* 71 (2011). [Erratum: Eur.Phys.J.C 72, 1874 (2012)], p. 1515. DOI: 10.1140/epjc/s10052-012-1874-8. arXiv: 1010.4180 [hep-ph].

[29]   Rouven Essig, John A. Jaros, and William Wester. "Dark Sectors and New, Light, Weakly-Coupled Particles". In: 2013.

[30]   Mauro Raggi and Venelin Kozhuharov. "Results and perspectives in dark photon physics". In: *Riv. Nuovo Cim.* 38.10 (2015), pp. 449–505. DOI: 10.1393/ncr/i2015-10117-9.

[31]   Bob Holdom. "Two U(1)'s and Epsilon Charge Shifts". In: *Phys. Lett. B* 166 (1986), pp. 196–198. DOI: 10.1016/0370-2693(86)91377-8.

[32]   Bob Holdom. "Searching for ϵ Charges and a New U(1)". In: *Phys. Lett. B* 178 (1986), pp. 65–70. DOI: 10.1016/0370-2693(86)90470-3.

[33]   Peter Galison and Aneesh Manohar. "TWO Z's OR NOT TWO Z's?" In: *Phys. Lett. B* 136 (1984), pp. 279–283. DOI: 10.1016/0370-2693(84)91161-4.

[34]   L. B. Okun. "LIMITS OF ELECTRODYNAMICS: PARAPHOTONS?" In: *Sov. Phys. JETP* 56 (1982), p. 502.

[35]   Brian Batell, Maxim Pospelov, and Adam Ritz. "Probing a Secluded U(1) at B-factories". In: *Phys. Rev. D* 79 (2009), p. 115008. DOI: 10.1103/PhysRevD.79.115008. arXiv: 0903.0363 [hep-ph].

[36]   Brian Shuve and Itay Yavin. "Dark matter progenitor: Light vector boson decay into sterile neutrinos". In: *Phys. Rev. D* 89.11 (2014), p. 113004. DOI: 10.1103/PhysRevD.89.113004. arXiv: 1403.2727 [hep-ph].

[37]   Wolfgang Altmannshofer et al. "Explaining dark matter and B decay anomalies with an $L_\mu - L_\tau$ model". In: *JHEP* 12 (2016), p. 106. DOI: 10.1007/JHEP12(2016)106. arXiv: 1609.04026 [hep-ph].

[38] R Aaij et al. "Measurement of Form-Factor-Independent Observables in the Decay $B^0 \rightarrow K^{*0}\mu^+\mu^-$". In: *Phys. Rev. Lett.* 111 (2013), p. 191801. DOI: 10.1103/PhysRevLett.111.191801. arXiv: 1308.1707 [hep-ex].

[39] David Curtin et al. "Illuminating Dark Photons with High-Energy Colliders". In: *JHEP* 02 (2015), p. 157. DOI: 10.1007/JHEP02(2015)157. arXiv: 1412.0018 [hep-ph].

[40] D. S. Akerib et al. "Results from a search for dark matter in the complete LUX exposure". In: *Phys. Rev. Lett.* 118.2 (2017), p. 021303. DOI: 10.1103/PhysRevLett.118.021303. arXiv: 1608.07648 [astro-ph.CO].

[41] Xiangyi Cui et al. "Dark Matter Results From 54-Ton-Day Exposure of PandaX-II Experiment". In: *Phys. Rev. Lett.* 119.18 (2017), p. 181302. DOI: 10.1103/PhysRevLett.119.181302. arXiv: 1708.06917 [astro-ph.CO].

[42] E. Aprile et al. "First Dark Matter Search Results from the XENON1T Experiment". In: *Phys. Rev. Lett.* 119.18 (2017), p. 181301. DOI: 10.1103/PhysRevLett.119.181301. arXiv: 1705.06655 [astro-ph.CO].

[43] Marc Schumann. "Direct Detection of WIMP Dark Matter: Concepts and Status". In: *J. Phys. G* 46.10 (2019), p. 103003. DOI: 10.1088/1361-6471/ab2ea5. arXiv: 1903.03026 [astro-ph.CO].

[44] R. Bernabei et al. "Final model independent result of DAMA/LIBRA-phase1". In: *Eur. Phys. J. C* 73 (2013), p. 2648. DOI: 10.1140/epjc/s10052-013-2648-7. arXiv: 1308.5109 [astro-ph.GA].

[45] David Tucker-Smith and Neal Weiner. "Inelastic dark matter". In: *Phys. Rev. D* 64 (2001), p. 043502. DOI: 10.1103/PhysRevD.64.043502. arXiv: hep-ph/0101138.

[46] L. Accardo et al. "High Statistics Measurement of the Positron Fraction in Primary Cosmic Rays of 0.5–500 GeV with the Alpha Magnetic Spectrometer on the International Space Station". In: *Phys. Rev. Lett.* 113 (2014), p. 121101. DOI: 10.1103/PhysRevLett.113.121101.

[47] Aous A. Abdo et al. "Measurement of the Cosmic Ray e+ plus e- spectrum from 20 GeV to 1 TeV with the Fermi Large Area Telescope". In: *Phys. Rev. Lett.* 102 (2009), p. 181101. DOI: 10.1103/PhysRevLett.102.181101. arXiv: 0905.0025 [astro-ph.HE].

[48] Oscar Adriani et al. "An anomalous positron abundance in cosmic rays with energies 1.5-100 GeV". In: *Nature* 458 (2009), pp. 607–609. DOI: 10.1038/nature07942. arXiv: 0810.4995 [astro-ph].

[49] O. Adriani et al. "Cosmic-Ray Positron Energy Spectrum Measured by PAMELA". In: *Phys. Rev. Lett.* 111 (2013), p. 081102. DOI: 10.1103/PhysRevLett.111.081102. arXiv: 1308.0133 [astro-ph.HE].

[50] R. J. Protheroe. "ON THE NATURE OF THE COSMIC RAY POSITRON SPECTRUM". In: *Astrophys. J.* 254 (1982), pp. 391–397. DOI: 10.1086/159743.

[51]   M. Aguilar et al. "First Result from the Alpha Magnetic Spectrometer on the International Space Station: Precision Measurement of the Positron Fraction in Primary Cosmic Rays of 0.5–350 GeV". In: *Phys. Rev. Lett.* 110 (2013), p. 141102. DOI: `10.1103/PhysRevLett.110.141102`.

[52]   M. G. Aartsen et al. "Search for annihilating dark matter in the Sun with 3 years of IceCube data". In: *Eur. Phys. J. C* 77.3 (2017). [Erratum: Eur.Phys.J.C 79, 214 (2019)], p. 146. DOI: `10.1140/epjc/s10052-017-4689-9`. arXiv: `1612.05949 [astro-ph.HE]`.

[53]   S. Adrian-Martinez et al. "Limits on Dark Matter Annihilation in the Sun using the ANTARES Neutrino Telescope". In: *Phys. Lett. B* 759 (2016), pp. 69–74. DOI: `10.1016/j.physletb.2016.05.019`. arXiv: `1603.02228 [astro-ph.HE]`.

[54]   K. Choi et al. "Search for neutrinos from annihilation of captured low-mass dark matter particles in the Sun by Super-Kamiokande". In: *Phys. Rev. Lett.* 114.14 (2015), p. 141301. DOI: `10.1103/PhysRevLett.114.141301`. arXiv: `1503.04858 [hep-ex]`.

[55]   Bumseok Kyae and Jong-Chul Park. "130 GeV Fermi gamma-ray line from dark matter decay". In: *Phys. Lett. B* 718 (2013), pp. 1425–1429. DOI: `10.1016/j.physletb.2012.12.041`. arXiv: `1205.4151 [hep-ph]`.

[56]   A.A. Abdo et al. "Constraints on Cosmological Dark Matter Annihilation from the Fermi-LAT Isotropic Diffuse Gamma-Ray Measurement". In: *JCAP* 04 (2010), p. 014. DOI: `10.1088/1475-7516/2010/04/014`. arXiv: `1002.4415 [astro-ph.CO]`.

[57]   J. Albert et al. "Observation of Gamma Rays from the Galactic Center with the MAGIC Telescope". In: *The Astrophysical Journal* 638.2 (Jan. 2006), pp. L101–L104. DOI: `10.1086/501164`. URL: `https://doi.org/10.1086/501164`.

[58]   A. Abramowski et al. "Search for Photon-Linelike Signatures from Dark Matter Annihilations with H.E.S.S." In: *Phys. Rev. Lett.* 110 (2013), p. 041301. DOI: `10.1103/PhysRevLett.110.041301`. arXiv: `1301.1173 [astro-ph.HE]`.

[59]   S. Archambault et al. "Dark Matter Constraints from a Joint Analysis of Dwarf Spheroidal Galaxy Observations with VERITAS". In: *Phys. Rev. D* 95.8 (2017), p. 082001. DOI: `10.1103/PhysRevD.95.082001`. arXiv: `1703.04937 [astro-ph.HE]`.

[60]   Thomas Siegert et al. "Search for 511 keV Emission in Satellite Galaxies of the Milky Way with INTEGRAL/SPI". In: *Astron. Astrophys.* 595 (2016), A25. DOI: `10.1051/0004-6361/201629136`. arXiv: `1608.00393 [astro-ph.HE]`.

[61]   Alexey Boyarsky et al. "Checking the Dark Matter Origin of a 3.53 keV Line with the Milky Way Center". In: *Phys. Rev. Lett.* 115 (2015), p. 161301. DOI: `10.1103/PhysRevLett.115.161301`. arXiv: `1408.2503 [astro-ph.CO]`.

[62]   Nico Cappelluti et al. "Searching for the 3.5 keV Line in the Deep Fields with Chandra: the 10 Ms observations". In: *Astrophys. J.* 854.2 (2018), p. 179. DOI: `10.3847/1538-4357/aaaa68`. arXiv: `1701.07932 [astro-ph.CO]`.

[63] Esra Bulbul et al. "DETECTION OF AN UNIDENTIFIED EMISSION LINE IN THE STACKED X-RAY SPECTRUM OF GALAXY CLUSTERS". In: *The Astrophysical Journal* 789.1 (June 2014), p. 13. DOI: `10.1088/0004-637x/789/1/13`. URL: `https://doi.org/10.1088/0004-637x/789/1/13`.

[64] Joerg Jaeckel, Javier Redondo, and Andreas Ringwald. "3.55 keV hint for decaying axionlike particle dark matter". In: *Phys. Rev. D* 89 (2014), p. 103511. DOI: `10.1103/PhysRevD.89.103511`. arXiv: `1402.7335 [hep-ph]`.

[65] Yuri Gershtein et al. "Discovering hidden sectors with mono-photon Z'o searches". In: *Phys. Rev. D* 78 (2008), p. 095002. DOI: `10.1103/PhysRevD.78.095002`. arXiv: `0809.2849 [hep-ph]`.

[66] Frank J. Petriello, Seth Quackenbush, and Kathryn M. Zurek. "The Invisible Z' at the CERN LHC". In: *Phys. Rev. D* 77 (2008), p. 115020. DOI: `10.1103/PhysRevD.77.115020`. arXiv: `0803.4005 [hep-ph]`.

[67] Björn Penning. "The pursuit of dark matter at colliders—an overview". In: *J. Phys. G* 45.6 (2018), p. 063001. DOI: `10.1088/1361-6471/aabea7`. arXiv: `1712.01391 [hep-ex]`.

[68] Oliver Buchmueller, Caterina Doglioni, and Lian Tao Wang. "Search for dark matter at colliders". In: *Nature Phys.* 13.3 (2017), pp. 217–223. DOI: `10.1038/nphys4054`. arXiv: `1912.12739 [hep-ex]`.

[69] Antonio Boveia and Caterina Doglioni. "Dark Matter Searches at Colliders". In: *Ann. Rev. Nucl. Part. Sci.* 68 (2018), pp. 429–459. DOI: `10.1146/annurev-nucl-101917-021008`. arXiv: `1810.12238 [hep-ex]`.

[70] Mariangela Bondi. "Searching for light dark matter at fixed target experiments". In: *J. Phys. Conf. Ser.* 1561.1 (2020). Ed. by Antonio Trifiró, Giuseppe Mandaglio, and Marina Trimarchi, p. 012005. DOI: `10.1088/1742-6596/1561/1/012005`.

[71] Patrick deNiverville. "Searching for Sub-Gev Dark Matter at Fixed Target Neutrino Experiments". In: *Phys. Procedia* 61 (2015). Ed. by Frank Avignone and Wick Haxton, pp. 55–60. DOI: `10.1016/j.phpro.2014.12.010`.

[72] Natalia Borodatchenkova, Debajyoti Choudhury, and Manuel Drees. "Probing MeV dark matter at low-energy e+e- colliders". In: *Phys. Rev. Lett.* 96 (2006), p. 141802. DOI: `10.1103/PhysRevLett.96.141802`. arXiv: `hep-ph/0510147`.

[73] Pierre Fayet. "U-boson production in e+ e- annihilations, psi and Upsilon decays, and Light Dark Matter". In: *Phys. Rev. D* 75 (2007), p. 115017. DOI: `10.1103/PhysRevD.75.115017`. arXiv: `hep-ph/0702176`.

[74] Rouven Essig, Philip Schuster, and Natalia Toro. "Probing Dark Forces and Light Hidden Sectors at Low-Energy e+e- Colliders". In: *Phys. Rev. D* 80 (2009), p. 015003. DOI: `10.1103/PhysRevD.80.015003`. arXiv: `0903.3941 [hep-ph]`.

[75] Rouven Essig et al. "Constraining Light Dark Matter with Low-Energy e^+e^- Colliders". In: *JHEP* 11 (2013), p. 167. DOI: 10.1007/JHEP11(2013)167. arXiv: 1309.5084 [hep-ph].

[76] Matthew Reece and Lian-Tao Wang. "Searching for the light dark gauge boson in GeV-scale experiments". In: *JHEP* 07 (2009), p. 051. DOI: 10.1088/1126-6708/2009/07/051. arXiv: 0904.1743 [hep-ph].

[77] Peng-Fei Yin and Shou-Hua Zhu. "Light dark sector searches at low-energy high-luminosity e^+ e colliders". In: *Front. Phys. (Beijing)* 11.5 (2016), p. 111403. DOI: 10.1007/s11467-016-0541-1.

[78] Dong Woo Kang, P. Ko, and Chih-Ting Lu. "Exploring properties of long-lived particles in inelastic dark matter models at Belle II". In: (Jan. 2021). arXiv: 2101.02503 [hep-ph].

[79] Michael Duerr et al. "Invisible and displaced dark matter signatures at Belle II". In: *JHEP* 02 (2020), p. 039. DOI: 10.1007/JHEP02(2020)039. arXiv: 1911.03176 [hep-ph].

[80] Matthew J. Dolan et al. "Revised constraints and Belle II sensitivity for visible and invisible axion-like particles". In: *JHEP* 12 (2017). [Erratum: JHEP 03, 190 (2021)], p. 094. DOI: 10.1007/JHEP12(2017)094. arXiv: 1709.00009 [hep-ph].

[81] F. Abudinén et al. "Search for Axion-Like Particles produced in e^+e^- collisions at Belle II". In: *Phys. Rev. Lett.* 125.16 (2020), p. 161806. DOI: 10.1103/PhysRevLett.125.161806. arXiv: 2007.13071 [hep-ex].

[82] M. Campajola. "Dark Sector Physics with Belle II". In: *PoS* LeptonPhoton2019 (2019), p. 063. DOI: 10.22323/1.367.0063.

[83] J. P. Lees et al. "Search for a Dark Photon in e^+e^- Collisions at BaBar". In: *Phys. Rev. Lett.* 113.20 (2014), p. 201801. DOI: 10.1103/PhysRevLett.113.201801. arXiv: 1406.2980 [hep-ex].

[84] D. Babusci et al. "Search for light vector boson production in $e^+e^- \to \mu^+\mu^-\gamma$ interactions with the KLOE experiment". In: *Phys. Lett. B* 736 (2014), pp. 459–464. DOI: 10.1016/j.physletb.2014.08.005. arXiv: 1404.7772 [hep-ex].

[85] A. Anastasi et al. "Limit on the production of a new vector boson in $e^+e^- \to U\gamma$, $U \to \pi^+\pi^-$ with the KLOE experiment". In: *Phys. Lett. B* 757 (2016), pp. 356–361. DOI: 10.1016/j.physletb.2016.04.019. arXiv: 1603.06086 [hep-ex].

[86] A. Anastasi et al. "Combined limit on the production of a light gauge boson decaying into $\mu^+\mu^-$ and $\pi^+\pi^-$". In: *Phys. Lett. B* 784 (2018), pp. 336–341. DOI: 10.1016/j.physletb.2018.08.012. arXiv: 1807.02691 [hep-ex].

[87] J. R. Batley et al. "Search for the dark photon in π^0 decays". In: *Phys. Lett. B* 746 (2015), pp. 178–185. DOI: 10.1016/j.physletb.2015.04.068. arXiv: 1504.00607 [hep-ex].

[88] Roel Aaij et al. "Search for Dark Photons Produced in 13 TeV pp Collisions". In: *Phys. Rev. Lett.* 120.6 (2018), p. 061801. DOI: 10.1103/PhysRevLett.120.061801. arXiv: 1710.02867 [hep-ex].

[89] E Kou et al. "The Belle II Physics Book". In: *Progress of Theoretical and Experimental Physics* 2019.12 (Dec. 2019). 123C01. ISSN: 2050-3911. DOI: 10.1093/ptep/ptz106. eprint: https://academic.oup.com/ptep/article-pdf/2019/12/123C01/32693980/ptz106.pdf. URL: https://doi.org/10.1093/ptep/ptz106.

[90] J. P. Lees et al. "Search for a muonic dark force at BABAR". In: *Phys. Rev. D* 94.1 (2016), p. 011102. DOI: 10.1103/PhysRevD.94.011102. arXiv: 1606.03501 [hep-ex].

[91] Albert M Sirunyan et al. "Search for an $L_\mu - L_\tau$ gauge boson using Z→ 4μ events in proton-proton collisions at $\sqrt{s} = 13$ TeV". In: *Phys. Lett. B* 792 (2019), pp. 345–368. DOI: 10.1016/j.physletb.2019.01.072. arXiv: 1808.03684 [hep-ex].

[92] Wolfgang Altmannshofer et al. "Neutrino Trident Production: A Powerful Probe of New Physics with Neutrino Beams". In: *Phys. Rev. Lett.* 113 (9 Aug. 2014), p. 091801. DOI: 10.1103/PhysRevLett.113.091801. URL: https://link.aps.org/doi/10.1103/PhysRevLett.113.091801.

[93] S. R. Mishra et al. "Neutrino tridents and W-Z interference". In: *Phys. Rev. Lett.* 66 (24 June 1991), pp. 3117–3120. DOI: 10.1103/PhysRevLett.66.3117. URL: https://link.aps.org/doi/10.1103/PhysRevLett.66.3117.

[94] J.P. Lees et al. "Search for Low-Mass Dark-Sector Higgs Bosons". In: *Phys. Rev. Lett.* 108 (2012), p. 211801. DOI: 10.1103/PhysRevLett.108.211801. arXiv: 1202.1313 [hep-ex].

[95] I. Jaegle. "Search for the dark photon and the dark Higgs boson at Belle". In: *Phys. Rev. Lett.* 114.21 (2015), p. 211801. DOI: 10.1103/PhysRevLett.114.211801. arXiv: 1502.00084 [hep-ex].

[96] A. Anastasi et al. "Search for dark Higgsstrahlung in $e^+e \to \mu^+\mu$ and missing energy events with the KLOE experiment". In: *Phys. Lett. B* 747 (2015), pp. 365–372. DOI: 10.1016/j.physletb.2015.06.015. arXiv: 1501.06795 [hep-ex].

[97] Makoto Kobayashi and Toshihide Maskawa. "CP Violation in the Renormalizable Theory of Weak Interaction". In: *Prog. Theor. Phys.* 49 (1973), pp. 652–657. DOI: 10.1143/PTP.49.652.

[98] A. J. Bevan et al. "The Physics of the B Factories". In: *Eur. Phys. J. C* 74 (2014), p. 3026. DOI: 10.1140/epjc/s10052-014-3026-9. arXiv: 1406.6311 [hep-ex].

[99] M. Tanabashi et al. "Review of Particle Physics". In: *Phys. Rev. D* 98.3 (2018), p. 030001. DOI: 10.1103/PhysRevD.98.030001.

[100] Bernard Aubert et al. "Measurement of CP violating asymmetries in B^0 decays to CP eigenstates". In: *Phys. Rev. Lett.* 86 (2001), pp. 2515–2522. DOI: 10.1103/PhysRevLett.86.2515. arXiv: hep-ex/0102030.

[101]   Kazuo Abe et al. "Observation of large CP violation in the neutral B meson system". In: *Phys. Rev. Lett.* 87 (2001), p. 091802. DOI: `10.1103/PhysRevLett.87.091802`. arXiv: `hep-ex/0107061`.

[102]   Bernard Aubert et al. "Evidence for $D^0 - \overline{D}^0$ Mixing". In: *Phys. Rev. Lett.* 98 (2007), p. 211802. DOI: `10.1103/PhysRevLett.98.211802`. arXiv: `hep-ex/0703020`.

[103]   S. Kurokawa and Eiji Kikutani. "Overview of the KEKB accelerators". In: *Nucl. Instrum. Meth. A* 499 (2003), pp. 1–7. DOI: `10.1016/S0168-9002(02)01771-0`.

[104]   Yukiyoshi Ohnishi et al. "Accelerator design at SuperKEKB". In: *PTEP* 2013 (2013), 03A011. DOI: `10.1093/ptep/pts083`.

[105]   Kazunori Akai, Kazuro Furukawa, and Haruyo Koiso. "SuperKEKB Collider". In: *Nucl. Instrum. Meth. A* 907 (2018), pp. 188–199. DOI: `10.1016/j.nima.2018.08.017`. arXiv: `1809.01958 [physics.acc-ph]`.

[106]   The Belle II Collaboration. "Super KEKB and Belle II". In: (). https://www.belle2.org/.

[107]   P. Raimondi. "Status of the SuperB Effort". In: *2nd Workshop on SuperB Factory, LNF-INFN, Frascati* (2006). DOI: `10.1016/S0168-9002(01)02013-7`.

[108]   P. M. Lewis et al. "First Measurements of Beam Backgrounds at SuperKEKB". In: *Nucl. Instrum. Meth. A* 914 (2019), pp. 69–144. DOI: `10.1016/j.nima.2018.05.071`. arXiv: `1802.01366 [physics.ins-det]`.

[109]   A. Abashian et al. "The Belle Detector". In: *Nucl. Instrum. Meth. A* 479 (2002), pp. 117–232. DOI: `10.1016/S0168-9002(01)02013-7`.

[110]   T. Abe et al. "Belle II Technical Design Report". In: (Nov. 2010). arXiv: `1011.0352 [physics.ins-det]`.

[111]   C. Marinas. "The Belle II pixel detector: High precision with low material". In: *Nucl. Instrum. Meth. A* 731 (2013). Ed. by Yoshinobu Unno et al., pp. 31–35. DOI: `10.1016/j.nima.2013.03.025`.

[112]   K. Adamczyk et al. "The Belle II silicon vertex detector assembly and mechanics". In: *Nucl. Instrum. Meth. A* 845 (2017). Ed. by G. Badurek et al., pp. 38–42. DOI: `10.1016/j.nima.2016.03.100`.

[113]   H. Ikeda et al. "A detailed test of the CsI(Tl) calorimeter for BELLE with photon beams of energy between 20-MeV and 5.4-GeV". In: *Nucl. Instrum. Meth. A* 441 (2000), pp. 401–426. DOI: `10.1016/S0168-9002(99)00992-4`.

[114]   Andreas Moll. "Comprehensive study of the background for the Pixel Vertex Detector at Belle II". PhD thesis. Munich U., 2015. DOI: `10.5282/edoc.19106`.

[115]   T. Aushev et al. "A scintillator based endcap K_L and muon detector for the Belle II experiment". In: *Nucl. Instrum. Meth. A* 789 (2015), pp. 134–142. DOI: `10.1016/j.nima.2015.03.060`. arXiv: `1406.3267 [physics.ins-det]`.

[116]   Satoru Yamada et al. "Data Acquisition System for the Belle II Experiment". In: *IEEE Trans. Nucl. Sci.* 62.3 (2015), pp. 1175–1180. DOI: 10.1109/TNS.2015.2424717.

[117]   Yoshihito Iwasaki et al. "Level 1 trigger system for the Belle II experiment". In: *IEEE Trans. Nucl. Sci.* 58 (2011). Ed. by Sascha Marc Schmeling, pp. 1807–1815. DOI: 10.1109/TNS.2011.2119329.

[118]   S. Agostinelli et al. "GEANT4–a simulation toolkit". In: *Nucl. Instrum. Meth. A* 506 (2003), pp. 250–303. DOI: 10.1016/S0168-9002(03)01368-8.

[119]   F. Abudinén et al. "Measurement of the integrated luminosity of the Phase 2 data of the Belle II experiment". In: *Chin. Phys. C* 44.2 (2020), p. 021001. DOI: 10.1088/1674-1137/44/2/021001. arXiv: 1910.05365 [hep-ex].

[120]   J. Alwall et al. "The automated computation of tree-level and next-to-leading order differential cross sections, and their matching to parton shower simulations". In: *JHEP* 07 (2014), p. 079. DOI: 10.1007/JHEP07(2014)079. arXiv: 1405.0301 [hep-ph].

[121]   Tomasz Skwarnicki. "A study of the radiative CASCADE transitions between the Upsilon-Prime and Upsilon resonances". PhD thesis. Cracow, INP, 1986.

[122]   F. Pedregosa et al. "Scikit-learn: Machine Learning in Python". In: *Journal of Machine Learning Research* 12 (2011), pp. 2825–2830.

[123]   Giovanni Punzi. "Sensitivity of searches for new signals and its optimization". In: *eConf* C030908 (2003). Ed. by L. Lyons, R. P. Mount, and R. Reitmeyer, MODT002. arXiv: physics/0308063.

[124]   Ilya Komarov and Gianluca Inguglia. "Performance of the CDC trigger for very low multiplicity studies in Phase 2 data". BELLE2-NOTE-TE-2018-017. 2018.

[125]   Ilya Komarov. "Comparison of electron tracking efficiency in data and simulations using radiative Bhabha events in Phase2". BELLE2-NOTE-TE-2018-020. 2018.

[126]   Laura Zani and Professor Francesco Forti. "Search for an invisible Z' in $\mu^+\mu^-$ plus missing energy events at Belle II". Presented on 24 01 2020. PhD thesis. Pisa: Pisa, University of Pisa, Physics Department E. Fermi, 2020.

[127]   Ilya Komarov, Alberto Martini, and Giacomo De Pietro. "Study of muon identification performance in Phase 2 using ECL variables". BELLE2-NOTE-TE-2018-019. 2018.

[128]   Allen Caldwell, Daniel Kollar, and Kevin Kroninger. "BAT: The Bayesian Analysis Toolkit". In: *Comput. Phys. Commun.* 180 (2009), pp. 2197–2209. DOI: 10.1016/j.cpc.2009.06.026. arXiv: 0808.2552 [physics.data-an].

[129]   Paul Feichtinger, Gianluca Inguglia, and Christoph Schwanda. "Search for an invisibly decaying Z' boson and study of particle identification at the Belle II experiment". Presented on 16 03 2021. PhD thesis. Vienna: Vienna, TU Wien, 2021.

[130]   Alberto Martini. "Description and performances of the ID". Jan. 2020.

[131]   R. Garg et al. "Track momentum resolution using dimuon sample in the phase 3 data".
        July 2020.

[132]   Giacomo De Pietro, Paolo Branchini, and Enrico Graziani. "Search for an invisibly de-
        caying Z' dark boson at Belle II in $e^+e^- \to \mu^+\mu^-(e^\pm\mu^\mp)$ + missing energy final states".
        Presented on 16 03 2020. PhD thesis. Rome: Rome, Università degli Studi Roma Tre,
        2020.

[133]   James Berger. "The Bayesian Approach to Discovery". In: *PHYSTAT 2011*. Geneva:
        CERN, Jan. 2011. DOI: `10.5170/CERN-2011-006.17`.

[134]   James Berger. "A comparison of testing methodologies". In: *PHYSTAT-LHC Workshop
        on Statistical Issues for LHC Physics*. 2007.

[135]   James Berger et al. "Objective Bayesian Methods for Model Selection: Introduction and
        Comparison". In: *Lecture Notes-Monograph Series* 38 (Jan. 2001), pp. 135–207. DOI: `10.
        2307/4356165`.

[136]   Adrian E. Raftery. "Bayesian Model Selection in Social Research". In: *Sociological Method-
        ology* 25 (1995), pp. 111–163. ISSN: 00811750, 14679531. URL: `http://www.jstor.org/
        stable/271063`.

[137]   Adrian E. Bayer and Uros Seljak. "The look-elsewhere effect from a unified Bayesian and
        frequentist perspective". In: *JCAP* 10 (2020), p. 009. DOI: `10.1088/1475-7516/2020/
        10/009`. arXiv: `2007.13821 [physics.data-an]`.

[138]   C. E. Bonferroni. "Teoria statistica delle classi e calcolo delle probabilit". In: *Teoria
        statistica delle classi e calcolo delle probabilita, Pubblicazioni del R Istituto Superiore di
        Scienze Economiche e Commerciali di Firenze* (1936)).

[139]   Z. idák. "Rectangular Confidence Regions for the Means of Multivariate Normal Distri-
        butions". In: *Journal of the American Statistical Association* 62 (1967), pp. 626–633.

[140]   Christian Rover, Chris Messenger, and Reinhard Prix. "Bayesian versus frequentist upper
        limits". In: *PHYSTAT 2011*. Geneva: CERN, 2011, pp. 158–163. DOI: `10.5170/CERN-
        2011-006.158`. arXiv: `1103.2987 [physics.data-an]`.